In vitro Models of the Bacterial Outer Membrane for Antibiotic Research

A Thesis Submitted by

Nicolò Paracini

For the Degree of Doctor of Philosophy

Institute for Cell and Molecular Biosciences

Faculty of Medical Sciences

Newcastle University

May 2019

ABSTRACT

Antibiotic resistance is rapidly becoming a global health threat and the proportion of bacteria capable of evading the effects of antibiotics is progressively rising. In the case of Gram-negative bacteria this phenomenon is exacerbated by the outermost layer of their cellular envelope, the outer membrane (OM), an asymmetric lipid bilayer which represents an impenetrable barrier for many antibiotics. The defining characteristic of the OM is lipid asymmetry, with an inner leaflet of phospholipids and an outer layer of lipopolysaccharides (LPS), which confers on it its peculiar barrier properties. Due to its complexity, obtaining high-resolution structural information about the OM directly on the surface of bacteria is a challenging task. Thus, a reductionist approach to the problem consists of reconstituting OM components *in vitro* to create models that mimic the OM natural structure and composition, enabling its investigation under controlled conditions. Here, asymmetric OM models were used to investigate the effects of two antimicrobials, the last resort drug polymyxin B (PmB) and the bacterial toxin colicin N (ColN), providing insights into their mode of action and demonstrating the potential of these models as powerful research tools. The only structural technique capable of resolving the asymmetry of these 5 nm thin layers is neutron reflectometry, which was the key tool used throughout this work. The differential sensitivity of neutrons towards hydrogen (^{1}H) and deuterium (^{2}H), applied to the study of isotopically asymmetric OM model bilayers, enabled accurate determination of the lipid asymmetry of these systems which would not have been possible with any other biophysical technique. The studies on the effects of PmB clearly revealed the correlation between the antibiotic's effect and the transition of the OM from a gel to a fluid phase confirming the previously disputed existence of a liquid crystalline phase in the OM. Furthermore, a comparison between different OM models highlighted the requirement for accurate systems to reproduce the behaviour displayed *in vivo*. The structural investigation of ColN binding to OM models led to the identification of two separate membrane-bound toxin conformations determined by the specificity of the interaction. Additionally, a disordered loop region of ColN responsible for both LPS binding and toxicity was identified. Finally, complex OM models integrating LPS from pathogenic bacteria were assembled and characterised, opening up new possibilities to study more realistic models of the Gram-negative bacterial outer membrane.

ACKNOWLEDGEMENTS

First and foremost, I want to thank Jeremy, for his endless support and guidance throughout these four years. There has not been a single occasion in which, at the end of a meeting, I haven't felt motivated to do more and do better. It has been a pleasure working with you.

I would also like to thank Luke for setting the ground upon which this project was built. Thank you for all the help and support throughout the countless neutron experiments of these four years, no matter what day of the week or time of the day. Thanks also to all the people that I met at ISIS in these four years, you all taught me a lot and helped me get things done in so many occasions, Mario, Max, Becky, Josh, Nina, and the sample environment team, Tom, Andy, Richie and Jeff, I have a feeling we'll see each other relatively soon.

I am deeply grateful to Helen, for doing the job of three people in the lab, making sure everything works at all times, always helping us with all sorts of experiments and growing the smelliest bacteria known to man, in order to keep people from coming use our stuff all the time. Thank you for everything you do every day. Dan, you were always the first to hear about my problems and never failed to help me sort things out, I will miss sitting next to you. Thanks to Tim for all the shared beers and pool games, I am coming over to Sweden mate, you'll have a chance to try beat me over there. Thanks to Majeed, who I truly admire for hammering a PhD whilst having two kids and losing his passport, all without ever stop smiling. You are a real hero. Thanks to Tonia, who had to go through the experience of being the first research project I supervised but nevertheless managed to do an excellent job. Thanks to Azzeldin for his unlimited wisdom, which rescued me from dark places several times. Thanks to Hayat for always making sure we're not short of coffee in the lab and to Mouna for making sure we're never short of drama.

A special thanks goes to Magdalena, who stood by my side during the tough times that come with a PhD. You always had words of encouragement that gave me the strength and confidence to get to this point, whether we were close or far apart.

Thanks to my family who has always been close to me even if I was far away. Thanks to Agnese and Sara for their continuous support even when we didn't see each other for a long time, but when we get back together it's just like we've never left home. Finally, I would not have done any of this without the care and support of my mum and dad to whom goes the biggest acknowledgement, thank you for your love and encouragement.

CONTENTS

ABSTRACT i
ACKNOWLEDGEMENTS ii
CONTENTS iii
TABLE OF FIGURES vi
LIST OF TABLES viii
LIST OF ABBREVIATIONS x
1 INTRODUCTION 2
1.1 The Gram-negative bacterial outer membrane 3
1.1.1 Lipopolysaccharides 5
1.1.2 Outer membrane proteins 10
1.2 *In vitro* OM models for biophysical studies 13
1.2.1 LPS monolayers 14
1.2.2 Phospholipid/LPS asymmetric bilayers 17
1.2.3 Protein containing OM models 18
1.3 Antibiotic resistance and the barrier function of the OM 20
1.3.1 Polymyxin B 21
1.3.2 Colicin N 23
1.4 Neutron reflectometry 25
1.4.1 Theoretical aspects 25
1.4.2 Experimental aspects 29
1.4.3 Data analysis 32
1.5 Aims 33
2 MATERIALS AND METHODS 35
2.1 Materials 36
2.2 Microbiology 36
2.2.1 Bacterial strains 36
2.2.2 Media 37
2.2.3 Transformation 38
2.2.4 Large scale protein expression 38
2.2.5 Liquid culture survival assay for ColN mutants 38
2.3 General and biochemical protocols 39
2.3.1 Size exclusion chromatography (SEC) 39
2.3.2 Sodium dodecylsulphate polyacrylamide gel electrophoresis (SDS PAGE) 39

2.3.3 Thin layer chromatography (TLC) 41
2.3.4 UV spectrophotometry of proteins and DNA 41
2.3.5 Lipopolysaccharide vesicles preparation 42
2.3.6 Assessment of protein secondary structure by Circular Dichroism (CD) 42
2.4 Molecular biology 43
2.4.1 Inverse polymerase chain reaction (PCR) and vector isolation 43
2.4.2 Sequence and ligation independent cloning (SLIC) reaction and plasmid preparation 45
2.4.3 Sequence analysis 45
2.5 Protein and lipopolysaccharide purification 46
2.5.1 Deuterated RaLPS production and purification 46
2.5.2 E183C OmpF (^{cys}OmpF) purification 47
2.5.3 Colicin N mutants purification 48
2.6 Preparation of model membranes for NR and ATR-FTIR 48
2.6.1 Substrates for membrane assembly 48
2.6.2 Surface cleaning 49
2.6.3 Deposition of self-assembled monolayers (SAM) 50
2.6.4 Langmuir-Blodgett (LB) and Langmuir-Schaefer (LS) deposition of asymmetric phospholipid/LPS bilayers 51
2.6.5 Assembly of DPPTE-^{cys}OmpF OM model 53
2.7 Neutron reflectometry (NR) 54
2.7.1 Experimental setup 54
2.7.2 NR measurements 56
2.7.3 Data reduction 57
2.7.4 Data analysis 57
2.8 Other biophysical techniques 61
2.8.1 Infrared spectroscopy (IR) 61
2.8.2 Surface plasmon resonance (SPR) 64
3 INTERACTION OF POLYMYXIN B WITH OUTER MEMBRANE MODELS 67
3.1 Introduction 68
3.2 Results 70
3.2.1 Self-assembled LPS hybrid bilayer membranes ($_{LPS}$HBM) 70
3.2.2 Isotopically asymmetric OM model bilayers ($_{dPL/hLPS}$OMM) 84
3.2.3 Fully deuterated OM model bilayers ($_{dPL/dLPS}$OMM) 91
3.2.4 Phase behaviour of OM models 99

3.3 Discussion 101
4 Interaction of Colicin N with Outer Membrane Models 106
4.1 Introduction 107
4.2 Results 109
4.2.1 Effect of core oligosaccharide size on electrostatic binding of ColN to asymmetric OM models 109
4.2.2 Core oligosaccharide packing affects specific ColN binding 117
4.2.3 LPS binding and toxicity of ColN are regulated by a loop region within the R-domain 120
4.3 Discussion 127
5 Development of Novel Outer Membrane Models 133
5.1 Introduction 134
5.2 Results 138
5.2.1 Asymmetric OM models containing smooth LPS 138
5.2.2 Floating OM models 147
5.2.3 Effect of EDTA on floating and silicon supported smooth LPS OM models 152
5.2.4 OM model containing LPS and OmpF 154
5.3 Discussion 162
6 Conclusions and Future Work 168
6.1 Conclusions 168
6.2 Future work 170
6.3 Final Remarks 171
7 Bibliography 172

TABLE OF FIGURES

Figure 1.1 | Cell envelope of Gram-negative bacteria 4
Figure 1.2 | LPS structure 6
Figure 1.3 | Synthesis and transport of LPS. The basis of *E. coli* OM asymmetry 8
Figure 1.4 | Structure of OmpF 12
Figure 1.5 | Experimental setup to study lipid monolayers using the Langmuir trough 16
Figure 1.6 | Assembly of asymmetric phospholipid/LPS bilayers via LB/LS deposition 18
Figure 1.7 | Reconstitution of ^{cys}OmpF onto a gold surface for AFM and NR studies 20
Figure 1.8 | Physicochemical properties of antibiotics highlight the shared route across the OM 21
Figure 1.9 | Chemical structure and variability of polymyxin B 23
Figure 1.10 | Structures of pore-forming colicins 24
Figure 1.11 | Specular reflection of a neutron wave 26
Figure 1.12 | Specular neutron reflection from a multi-layered material 28
Figure 1.13 | Solid-liquid cell setup for neutron reflection studies of the solid liquid interface. 31
Figure 2.1 | Water drainage on a clean surface from a NR silicon substrate 49
Figure 2.2 | Silicon substrates after deposition of an OTS monolayer 50
Figure 2.3 | LB and LS deposition of asymmetric phospholipid/LPS bilayers 52
Figure 2.4 | Assembly of the NR solid-liquid cell 53
Figure 2.5 | Solid-liquid beamline set up. 55
Figure 2.6 | ATR-FTIR setup 62
Figure 2.7 | Approaches to study lipid-protein interactions by SPR 65
Figure 3.1 | Models of the Gram-negative outer membrane and structure of PmB. 70
Figure 3.2 | ATR-FTIR of RaLPS and DMPC adsorption on OTS coated substrate. 72
Figure 3.3 | SPR sensorgram of $_{DMPC}$HBM formation. 74
Figure 3.4 | SPR sensorgram of $_{LPS}$HBM formation. 75
Figure 3.5 | NR of $_{LPS}$HBM formation. 77
Figure 3.6 | ATR-FTIR spectra of PmB adsorption of $_{LPS}$HBM and $_{DMPC}$HBM. 80
Figure 3.7 | SPR sensorgrams of PmB and PmBN binding to $_{LPS}$HBM. 81
Figure 3.8 | NR of PmB interaction with $_{LPS}$HBM. 82
Figure 3.9 | NR of $_{dPL/hLPS}$OMM at room temperature. 85

Figure 3.10 | Lack of PmB effects on $_{dPL/hLPS}$OMM at RT. 86
Figure 3.11 | PmB effect on $_{dPL/hLPS}$OMM at 37°C. 88
Figure 3.12 | Temperature and concentration dependence of PmB effects on $_{dPL/hLPS}$OMM. 90
Figure 3.13 | Effects of PmBN on $_{dPL/LPS}$OMM. 91
Figure 3.14 | Characterisation of deuterium labelled RaLPS. 93
Figure 3.15 | NR of $_{dPL/dLPS}$OMM at RT. 94
Figure 3.16 | Lack of PmB effect on $_{dPL/dLPS}$OMM at RT. 95
Figure 3.17 | PmB effect on $_{dPL/dLPS}$OMM at 37°C. 96
Figure 3.18 | Temperature and concentration dependence of PmB effects on $_{dPL/dLPS}$OMM. 98
Figure 3.19 | Phase transition of OM models measured by ATR-FTIR. 100
Figure 3.20 | Summary of PmB effects at 37°C. 103
Figure 4.1 | Structure of ColN and LPS. 108
Figure 4.2 | NR of OM models containing Ra and RdLPS. 110
Figure 4.3 | NR of ColN binding to OM models containing Ra and RdLPS. 112
Figure 4.4 | NaCl titration of the LPS-ColN complexes. 115
Figure 4.5 | Cartoon representation of the salt dependent binding of ColN from asymmetric OM models. 116
Figure 4.6 | NR of ColN binding to EDTA treated RaLPS OM model. 118
Figure 4.7 | Structure and localisation of loop^R within ColN. 121
Figure 4.8 | Characterisation of ColN loop^R mutants. 123
Figure 4.9 | Toxicity of loop^R mutants tested by liquid culture killing assay. 124
Figure 4.10 | RaLPS binding ability of loop^R mutants. 126
Figure 4.11 | Specificity of ColN WT and mutants binding to Ra and RdLPS. 127
Figure 4.12 | X-ray structure of a porin-RdLPS complex. 129
Figure 4.13 | Cartoon of the proposed role of loop^R in the first steps of ColN binding. 132
Figure 5.1 | Schematic cartoon of current OM models and novel versions described in this chapter. 136
Figure 5.2 | DOC PAGE banding pattern of LPS. 139
Figure 5.3 | NR of asymmetric OM models containing smooth LPS. 141
Figure 5.4 | Distribution of O-antigen chains of the OM models containing smooth LPS. 142
Figure 5.5 | DOC PAGE of fractions collected from SEC from the separation of LPS O111. 144

Figure 5.6 | NR of O-antigen containing asymmetric OM models. 146
Figure 5.7 | NR of floating OM model containing low-MW fraction LPS. 149
Figure 5.8 | NR of floating OM model containing smooth LPS. 150
Figure 5.9 | Effect of EDTA on floating and silicon supported OM model containing smooth LPS. 153
Figure 5.10 | SDS PAGE of the purification of ^{cys}OmpF from *E. coli* BZB1107 cells. 155
Figure 5.11 | MCNR characterisation of a ^{cys}OmpF-DPPTE monolayer adsorbed on gold. 157
Figure 5.12 | MCNR characterisation of the ^{cys}OmpF-DPPTE monolayer after the assembly of a hydrogenous RaLPS outer leaflet. 159
Figure 5.13 | MCNR characterisation of the ^{cys}OmpF-DPPTE monolayer after the assembly of a deuterated RaLPS outer leaflet. 161
Figure 5.14 | O-antigen structures characterised by NR. 165

LIST OF TABLES

Table 1.1 | Scattering lengths of the most common elements in biology 28
Table 2.1 | List of specialist chemicals and suppliers 36
Table 2.2 | List of bacterial strains 37
Table 2.3 | Recipe of minimal media for the production of deuterium labelled rough LPS 37
Table 2.4 | Molecular weight and extinction coefficient of proteins used in this study 42
Table 2.5 | Forward and reverse primers used to introduce mutations in the ColN gene 44
Table 2.6 | Components in the PCR mix 44
Table 2.7 | PCR conditions 45
Table 2.8 | 1000x protein inhibitor cocktail 48
Table 2.9 | SLD and composition of isotopic contrast solutions 56
Table 2.10 | Layers used to model the reflectivity from a silicon supported OM model used in this work 58
Table 2.11 | SLD values for the chemically distinct layers in the model membranes 59
Table 2.12 | IR absorbance of some stretching vibrations relevant in the studies performed in Chapter 3. 63
Table 3.1 | Parameters derived from the fitting of the reflectivity data from the $_{LPS}$HBM. 78
Table 3.2 | Parameters derived from the fitting of the reflectivity data from the $_{LPS}$HBM after the addition of PmB 83

Table 3.3 | Parameters derived from the fitting of the reflectivity data from the $_{dPL/hLPS}$OMM. 89

Table 3.4 | Parameters derived from the fitting of the reflectivity data from the $_{dPL/dLPS}$OMM. The substrate parameters describe the silicon surface and are assumed not to vary with temperature or PmB addition. 97

Table 4.1 | Parameters derived from the fitting of the NR data from the Ra and RdLPS OM models and corresponding adsorbed ColN layers. 113

Table 4.2 | Volume fractions of ColN adsorbed on Ra and RdLPS OM models as a function of [NaCl] calculated from the fitted SLD of the protein layer under each salt condition . 116

Table 4.3 | Parameters derived from the fitting of the NR data from the EDTA treated RaLPS OM model and associated ColN layers in the absence and the presence of NaCl.119

Table 4.4 | List of Colicin N mutants produced and characterised by CD and SDS-PAGE. 122

Table 4.5 | List of mutants tested in this study showing the effects on toxicity and LPS binding. 131

Table 5.1 | Parameters derived from the fitting of the NR data from the O-antigen containing OM models assembled from smooth LPS. 142

Table 5.2 | Parameters derived from the fitting of the NR data from the OM models containing fractionated smooth LPS. 147

Table 5.3 | Parameters derived from the fitting of the NR data from the floating OM models containing low-MW fractionated and smooth O111 LPS..... 151

Table 5.4 | Parameters derived from the fitting of the NR data from the silicon supported OM model containing O111 LPS in the presence of 3 mM EDTA. 154

Table 5.5 | Parameters derived from the fitting of the MCNR data from the ^{cys}OmpF-DPPTE monolayer assembled on the gold substrate. 158

Table 5.6 | Parameters derived from the fitting of the MCNR data from the ^{cys}OmpF-DPPTE monolayer assembled on the gold substrate in the presence of hydrogenous and deuterated RaLPS outer leaflets. 162

LIST OF ABBREVIATIONS

AFM - Atomic force microscopy

ATR-FTIR - Attenuated total internal reflection Fourier transform infrared spectroscopy

AuMW - Gold SLD matched water

BME - β-mercaptoethanol

C16NEtOH - N-(2-Hydroxyethyl)-16-mercaptohexadecanamide

CD - Circular dichroism

ColN - Colicin N

^{cys}OmpF - OmpF bearing the E183C mutation

D_2O - Deuterium oxide

d_{62}DPPC - Tail deuterated DPPC

DAB - Di-amino-butyric-acid

DMPC - 1,2-dimyristoyl-sn-glycero-3-phosphocholine

DOC - Deoxycholate

DPPC - 1,2-dipalmitoyl-sn-glycero-3-phosphocholine

DPPTE - 1,2-dipalmitoyl-sn-glycero-3-phosphothioethanol

EDTA - Ethylenediaminetetraacetic acid

EM - Electron microscopy

E. coli - Escherichia coli

FSB - Free standing bilayer

HBM - Hybrid bilayer membrane

HG - Head group

IM - Inner membrane

IPTG - Isopropyl-β-D-thiogalactopyranoside

IR - infrared

LB - Langmuir Blodgett

LB (when referred to media) - Lysogeny broth

LPS - Lipopolysaccharide

LS - Langmuir Schaefer

MCNR - Magnetic contrast neutron reflectometry

MIC - Minimum inhibitory concentration

MW - Molecular weight

NR - Neutron reflection

OG - Octyl glucopyranoside

OM - Outer membrane

OMM - Outer membrane model

OMP - Outer membrane protein

OmpF - Outer membrane protein F

OTS - Octadecyltrichlorosilane

PAGE -Polyachrylamide gel electrophoresis

PCP - Phenol/chloroform/petroleum spirit (2:5:8 v:v:v)

PCR - Polymerase chain reaction

PL - Phospholipid

PMB - Polymyxin B

PmBN - Polymyxin B nonapeptide

RU - Response units

SAM - Self assembled monolayer

SDS - Sodium dodecylsulphate

SEC - Size exclusion chromatography

SLD - Scattering length density

SLIC - Sequence and ligation independent cloning

SMW - Silicon SLD matched water

SPR - Surface plasmon resonance

TCEP - Tris(2-carboxyethyl) phosphine hydrochloride

TLC - Thin layer chromatography

TOF - Time of flight

UV - Ultraviolet

WT - Wild type

XR - X-ray reflection

ω-thioPC - 1-oleoyl-2-(16-thiopalmitoyl)-sn-glycero-3-phosphocholine

I am afraid neutrons will not be of any use to anyone.

Sir James Chadwick, February 29th, 1932

1 INTRODUCTION

1.1 THE GRAM-NEGATIVE BACTERIAL OUTER MEMBRANE

Cellular membranes define the boundaries of all living cells. The ubiquitous protein-containing bilayer structure, held together by the hydrophobic effect of its lipid component, creates a semi-permeable barrier that regulates the exchange of solutes and information between cells and their surrounding environment. Bacteria are classified in two main groups according to the architecture of their cellular envelopes: Gram-positive organisms possess a cytoplasmic membrane enclosed by a thick cell wall of peptidoglycan. Gram-negative bacteria, on the other hand, are surrounded by two membranes with a thin layer of cell wall sandwiched in the periplasm between them. In both types of bacteria, the cytoplasmic membrane consists of a mixture of glycerophospholipids that form a fluid matrix in which lipids and embedded membrane proteins can diffuse laterally resembling a "fluid mosaic", according to the classic model proposed by Singer and Nicolson in 1972 (Singer and Nicolson, 1972).

In addition to the cytoplasmic (inner) membrane (IM), Gram-negative bacteria possess an outer membrane (OM) that constitutes the outermost layer of the cell envelope, at the interface with the surrounding habitat. The OM is a uniquely robust, asymmetric lipid membrane that protects the cell from noxious molecules and harsh environments (**Fig. 1.1**) (Nikaido, 2003). The inner leaflet of the OM has a composition similar to that of the IM, which contains ~70% phosphatidylethanolamine, ~15% phosphatidylglycerol and ~15% cardiolipin, whilst the outer leaflet contains unique glycolipids known as lipopolysaccharides (LPS). In enteric bacteria this lipid asymmetry is substantial and the outer leaflet of the OM contains almost exclusively LPS (Kamio and Nikaido, 1976). Due to the high level of phosphorylation of LPS, divalent cations such as Ca^{2+} and Mg^{2+} play a key role in stabilising the OM by bridging and crosslinking together LPS molecules in the outer leaflet. The effective barrier function of the OM relies heavily on its asymmetric lipid distribution, which is established by the LPS transport (Lpt) protein system (Okuda *et al.*, 2016) and constantly preserved by the specialist maintenance of lipid asymmetry (Mla) family of OM proteins (Abellon-Ruiz *et al.*, 2017), along with several other OM proteins and lipoproteins (Henderson *et al.*, 2016). The peculiar properties of LPS make the lipid matrix of the OM about two orders of magnitude less permeable to hydrophobic solutes compared to the canonical phospholipid bilayer of cytoplasmic membranes (Plesiat and Nikaido, 1992; Plesiat *et al.*, 1997). Due to the low permeability of the OM, nutrient uptake relies on water filled β-barrel OM proteins (OMPs) that form trimeric channels in the OM

lipid matrix, allowing the diffusion of small hydrophilic molecules (<600 Da) with various degrees of substrate specificity (Koebnik *et al.*, 2000). OM proteins also represent, by far, the main route of entrance exploited by antibiotics to cross the OM and enter the Gram-negative cell (O'Shea and Moser, 2008; Tommasi *et al.*, 2015). Due to its low permeability, OM penetration is now recognized as the limiting factor in the development of antimicrobials effective against Gram-negative organisms (Pages *et al.*, 2008). The OM is difficult to precisely address by biophysical methods *in vivo* (i.e. directly on whole bacteria), due to the close proximity of the inner membrane and the small size of bacterial cells. However, understanding its properties and interactions with antibiotics, is critical for the development of new effective antimicrobials, critically needed to face the growing threat of antibiotic resistance (Ventola, 2015). Models of the OM reconstituted *in vitro* have been shown to provide a promising platform for the investigation of this crucial biological barrier at a molecular level (Clifton *et al.*, 2015a).

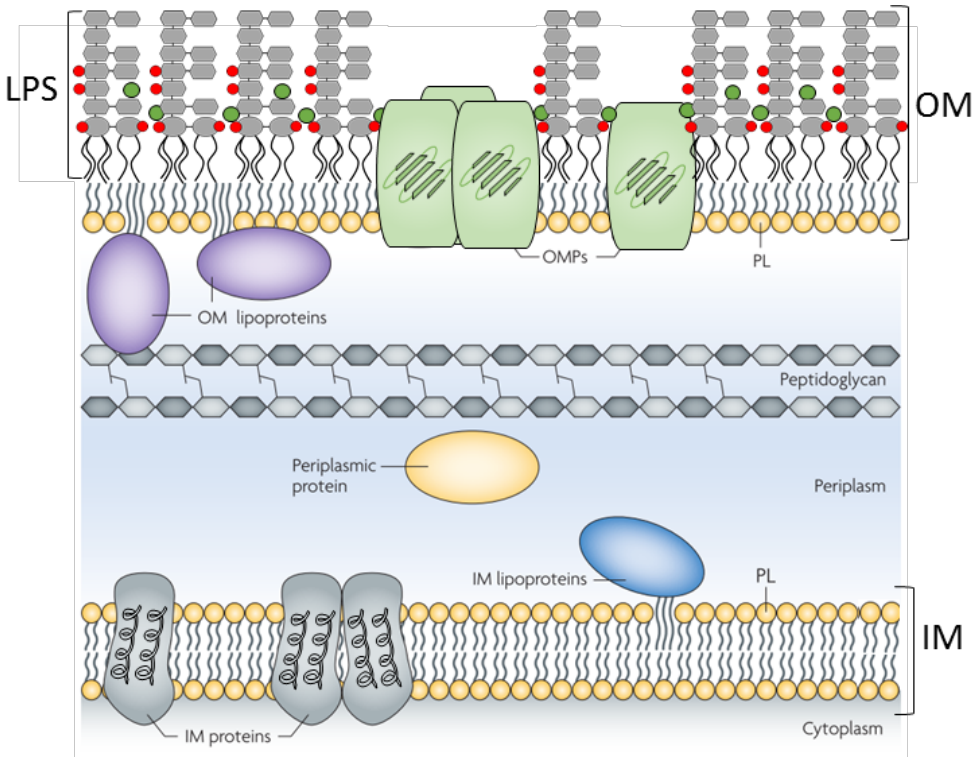

Figure 1.1 | Cell envelope of Gram-negative bacteria

Cartoon of the cell envelope of Gram-negative bacteria. The outer membrane (OM) is an asymmetric lipid bilayer containing phospholipids (PL) in the inner leaflet and lipopolysaccharide (LPS) in the outer leaflet forming the outermost layer of the cell. Red circles represent negatively charged phosphate groups and green circles divalent cations. Embedded in the OM, water filled OM proteins (OMPs) allow the passage of small hydrophilic molecules. The periplasm separates the OM from the inner membrane (IM) and contains the cell wall made of peptidoglycan as well as periplasmic proteins. Integral OM proteins have a β-barrel structure whilst IM proteins are typically α-helical in their transmembrane region. Redrawn from (Ruiz *et al.*, 2009).

1.1.1 Lipopolysaccharides

The LPS molecule can be divided into three covalently linked sections: the lipid A, the core oligosaccharide and the O-antigen (**Fig. 1.2a**) (Raetz and Whitfield, 2002). The lipid A is the hydrophobic region of LPS, responsible for anchoring it to the OM lipophilic interior. It is composed of a tetra-acylated di-glucosamine which bears phosphate groups at position 1 and position 4' of the amino sugar di-saccharide. In *Escherichia coli* (*E. coli*), the four acyl chains linked to the disaccharide unit are 3-hydroxymyristoyl moieties which are further acylated with secondary lauroyl and myristoyl chains on the non-reducing sugar of the di-glucosamine yielding a hexa-acylated lipid A (Molinaro *et al.*, 2015).

Attached to the lipid A glucosamine, the core oligosaccharide region is composed of a branched oligosaccharide of 10-12 sugars which extends towards the extracellular environment (Heinrichs *et al.*, 1998b). The core oligosaccharide can be further divided in two chemically distinct parts: an inner core region composed of heptose residues and an outer core region of hexose sugars, typically glucose and galactose. The heptose residues of the inner core are often phosphorylated and are linked to the lipid A non-reducing glucosamine via a 3-deoxy-D-manno-oct-2-ulosonic acid (Kdo) disaccharide. In *E. coli* there are five variants of core oligosaccharide structures, R1-R4 and K12, which display minor differences mainly in the type and arrangement of the hexose residues in the outer core region (**Fig. 1.2b**) (Amor *et al.*, 2000). The inner core is conserved amongst different core types, but it can contain non-stoichiometric modifications depending on the core type (**Fig. 1.2c**).

The terminal part of the LPS molecule is a polymeric glycan known as the O-antigen. Whilst lipid A and the core oligosaccharide are largely conserved structures, there are more than 180 different O-antigen types in *E. coli*. The size of the repeating oligosaccharide units varies from 2 to 6 sugars and can be linear or branched (Stenutz *et al.*, 2006). The number of O-antigen units attached to each LPS molecule is highly variable within each cell, spanning from 0 to up to 100 units. Most laboratory adapted strains of *E. coli* lose the ability to synthesise the O-antigen and their LPS is composed only of the lipid A and core oligosaccharide (Stevenson *et al.*, 1994). LPS lacking the O-antigen is termed rough LPS in contrast with the O-antigen-containing LPS of wild type bacteria which is referred to as smooth LPS.

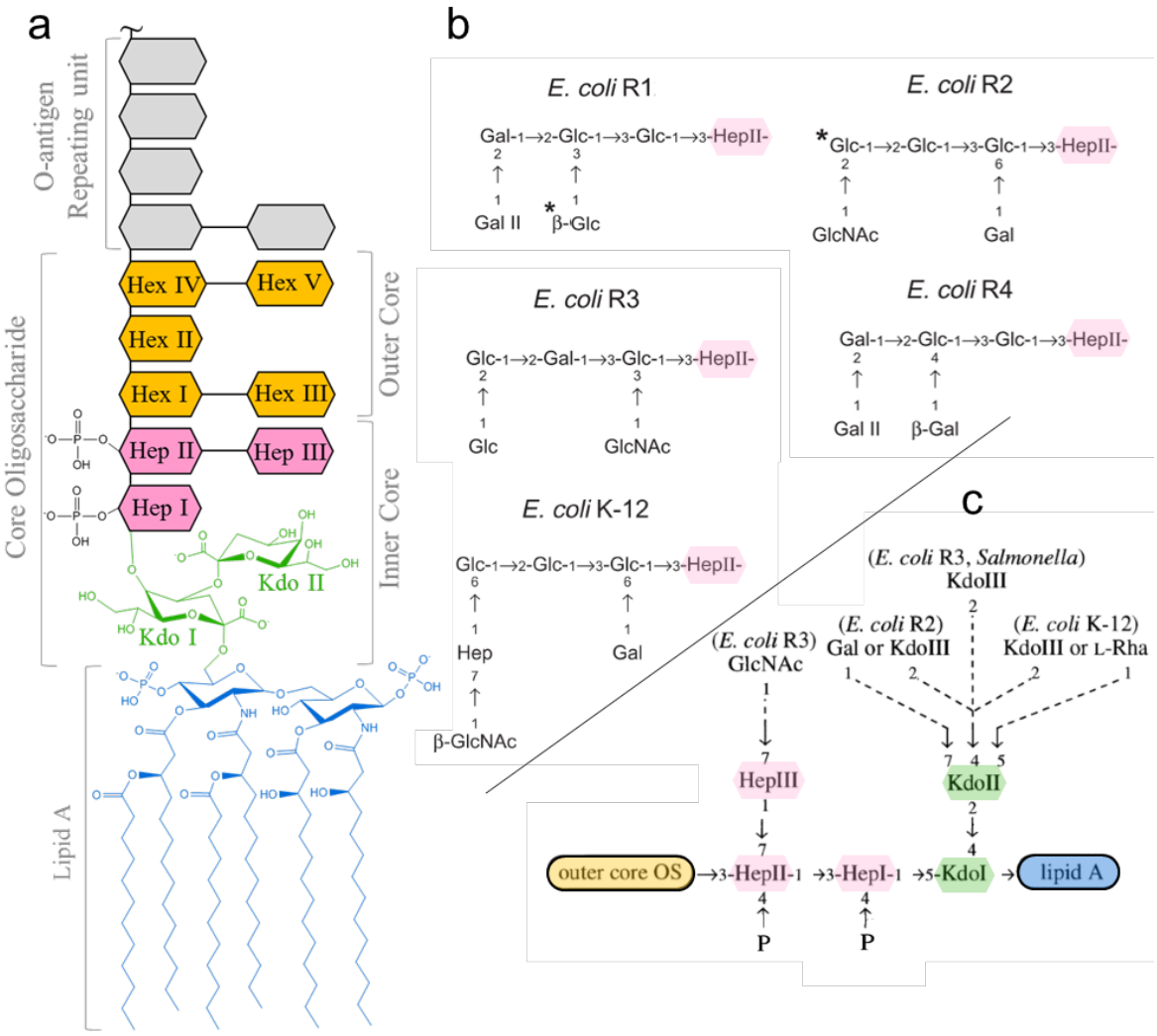

Figure 1.2 | LPS structure

(**a**) General structure of LPS. The hydrophobic lipid A (blue) anchors LPS to the OM. The core oligosaccharide is divided in an inner and an outer region. The inner region is composed of Kdo (green) and heptoses (pink) whilst the outer core is composed of hexoses (yellow). The O-antigen repeating unit (grey) is absent in rough LPS and is present in highly variable numbers in smooth LPS. (**b**) Outer core variability in *E. coli.* Glc = glucose, Gal = galactose, GlcNAc = acetyl-glucosamine. Asterisks indicate the known positions where the O-antigen is attached (Heinrichs *et al.*, 1998a). (**c**) Inner core variability in *E. coli.* Dashed lines indicate non-stoichiometric substitutions found in the respective core types. Hep = heptose, Kdo = 3-deoxy-D-manno-oct-2-ulosonic acid, Rha = rhamnose (adapted from (Heinrichs *et al.*, 1998b)).

This nomenclature derives from the appearance of the edges of bacterial colonies expressing the two types of LPS when grown on solid media. Notably, as a consequence of the highly variable number of O-antigen units, up to 40-50% of the total LPS content of smooth strains is represented by lipooligosaccharide (LOS), term which refers to LPS with either no or a single O-antigen unit (Peterson and McGroarty, 1985; Hitchcock *et al.*, 1986). Due to the high density of negative charges on the lipid A and inner core oligosaccharide regions, the

stability of the OM relies on divalent cations, such as Ca^{2+} and Mg^{2+}, to bridge together and cross-link LPS molecules in the outer leaflet. The stabilising effects of divalent cations is a fundamental aspect of the OM as it is responsible for both the strengths and weaknesses of its barrier function (Vaara, 1992). Removal or displacement of divalent cations by exposure to polyamines or chelating agents such as EDTA, causes the release of large quantities of LPS and destabilisation of the OM *in vivo* and *in vitro* (Bayer and Leive, 1977; Clifton *et al.*, 2015b).

1.1.1.1 LPS synthesis and transport

Elucidation of the pathway responsible for the synthesis and transport of LPS from the cytoplasm to the extreme periphery of the cell involved numerous groups and over 50 years of research (Ruiz *et al.*, 2009). LPS synthesis starts with a 9-step enzymatic sequence, known as the Raetz pathway, which begins with soluble enzymes in the cytoplasm and terminates on the cytoplasmic side of the IM with the synthesis of Kdo_2-lipid A, formed by the lipid A scaffold bearing the Kdo disaccharide (**Fig. 1.3a**) (Raetz *et al.*, 2007). Except in rare cases(Zhang *et al.*, 2013), the Kdo_2-lipid A is the minimal LPS viable structure in Gram-negative bacteria and the genes encoding for the enzymes involved in the Raetz pathway are nearly completely conserved (Henderson *et al.*, 2016). The core oligosaccharide is sequentially added by a series of cytoplasmic glycosyltransferases to the newly synthesised Kdo_2-lipid A (Heinrichs *et al.*, 1998b). Selectively silencing glycosyltransferases involved in the core oligosaccharide synthesis allows production of mutant LPS types with truncated core regions. Rough LPS with a complete core region is termed RaLPS and species with increasingly large truncations are Rb, Rc, Rd and ReLPS where the latter corresponds to the Kdo_2-lipid A structure (**Fig. 1.3b**). Once the core oligosaccharide synthesis is complete, LPS is flipped to the periplasmic side of the IM by the MsbA membrane protein (Mi *et al.*, 2017). The O-antigen is added to the rough LPS structure on the periplasmic side of the IM. Contrary to the core oligosaccharide, the synthetic pathway responsible for the assembly of the O-antigen cannot be controlled to produce LPS with a specific length of the O-antigen polysaccharide (Samuel and Reeves, 2003). Finally, once the LPS structure is completed and anchored to the periplasmic side of the IM, it is transported across the periplasm and inserted into the outer leaflet of the OM by the lipopolysaccharide transport (Lpt) system comprising seven different proteins (Henderson *et al.*, 2016). With a series of elegant experiments, Sherman *et al* have recently shown that LPS molecules are not shuttled to the OM but pushed

through a physical bridge that connects the IM and the OM and is formed by the assembly of LptA proteins across the periplasm (Sherman *et al.*, 2018).

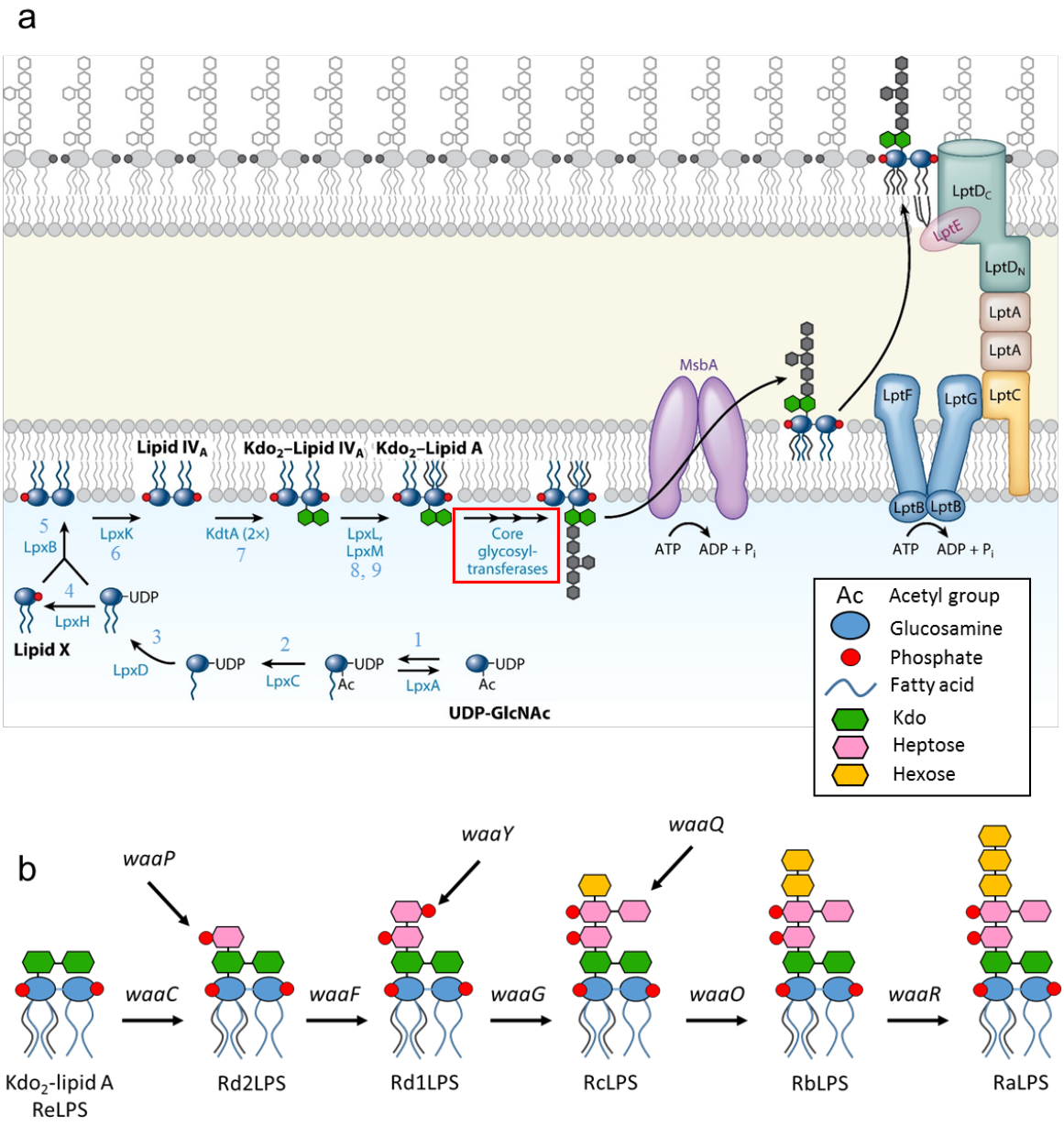

Figure 1.3 | Synthesis and transport of LPS. The basis of *E. coli* OM asymmetry

(**a**) Biosynthetic pathway of LPS. Numbered in blue the first 9 steps forming the Raetz pathway which leads to the synthesis of Kdo$_2$-lipid A. After the addition of the core oligosaccharide (red square, shown in **b**, LPS is flipped to the periplasmic space by MsbA and transported to the outer leaflet of the OM by the six protein Lpt complex (adapted from (Henderson *et al.*, 2016)) (**b**) Assembly of the conserved residues of the core oligosaccharide, the genes encoding the enzymes responsible for the addition of residues are labelled (redrawn from (Johnson *et al.*, 2014)).

1.1.1.2 OM physical state

The unusually low permeability of the OM, particularly towards hydrophobic molecules, has led to an open debate on whether the LPS hydrocarbon interior is in a liquid-crystalline fluid state, similar to that of phospholipids in cytoplasmic membranes, or whether it remains in a gel-like state (Brandenburg and Seydel, 1991). Brandenburg *et al* have used infrared spectroscopy (IR) and differential scanning calorimetry (DSC) to measure the gel to liquid ($L_\alpha \leftrightarrow L_\beta$) phase transition of various types of rough and smooth LPS. The data showed that most LPS species underwent a transition from the gel to the fluid state within a range of temperatures between 30°C and 36°C under a series of different conditions (Brandenburg and Seydel, 1990). After analysing the effects of divalent cations, water content and pH on the LPS phase transition they concluded that the acyl chains of LPS exist in a fluid state at physiological temperatures. A different scenario is that described by Hiroshi Nikaido in the most cited review about the OM in the literature (Nikaido, 2003). According to Nikaido the low permeability of the OM is a direct consequence of the low fluidity of the OM outer leaflet due to LPS being in the gel state at physiological temperatures. This interpretation is built upon several lines of evidence discussed in the review. The main points in favour of the gel state of the OM are based on the elevated number and high level of saturation of the acyl chains of LPS compared to phospholipids and the observation that in the presence of mM levels of divalent cations the melting temperatures of negatively charged lipids substantially increases. Part of the reason why the physical state of the OM is still unclear is the difficulty of probing the state of LPS directly in a native like environment. Measurements of lateral mobility by fluorescence recovery after photobleaching (FRAP) have shown that LPS is able to diffuse laterally in the OM of *S. typhimurium* with a diffusion rate in the order of $\sim 10^{-10}$ cm^2/sec (Schindler *et al.*, 1980). This value is comparable to that of phospholipids in the gel phase, whilst fluid phase phospholipids diffuse at a faster rate of $\sim 10^{-8}$ cm^2/sec (Fahey and Webb, 1978; Metcalf *et al.*, 1986). However, in the OM, the high protein content has been suggested to considerably slow down lipid diffusion (Goose and Sansom, 2013). Moreover, the strong interaction of LPS with OM proteins is likely to restrict its mobility (Arunmanee *et al.*, 2016) making the correlation between diffusion rates and the physical state of LPS acyl chains more complicated than for phospholipids. Although the low permeability and slow LPS diffusion rates could result from a gel-like state of the OM, Gram-negative bacteria have been shown to synthesise lower-melting-point LPS when grown at low temperature, supporting the idea that homeoviscous adaptation contributes to

maintain a fluid phase OM (Li *et al.*, 2012). A clear demonstration of the physiological relevance of the LPS phase transition is however still missing.

1.1.2 Outer membrane proteins

OM proteins (OMPs) are estimated to cover a large fraction of the OM, with studies suggesting that, in some species, up to 75% of the OM surface is occupied by proteins (Jaroslawski *et al.*, 2009). OMPs are fundamentally different from membrane proteins found in cytoplasmic membranes, due to their secondary structure. Whilst the transmembrane domain of proteins embedded in cytoplasmic membranes are α-helical, except in rare cases (Dong *et al.*, 2006), virtually all integral OM proteins are barrels composed of antiparallel β-strands (Koebnik *et al.*, 2000). There are 3 main types of OMPs: (i) diffusion channels, (ii) energy-dependent transporters (iii) structural proteins.

(i) Diffusion channels are β-barrels proteins formed of 8-18 β-strands which allow the passive diffusion of molecules across the OM following the inwardly-directed concentration gradient (Nikaido, 1992). There are two types of diffusion channels: porins and substrate-specific channels. Substrate-specific channels contain stereospecific ligand-binding sites within their lumens which allow only the diffusion of a specific substrate. Examples of specific porins are the maltose-specific channel LamB (Schirmer *et al.*, 1995) from *E. coli* and the sucrose-specific ScrY from *S. typhimurium* (Forst *et al.*, 1998). Non-specific porins, on the other hand, only discriminate between solutes on the basis of their size and partially its charge, allowing non-specific diffusion of solutes usually below 600 Da. Examples of porins found in *E. coli* are OmpF and PhoE with preferences for cations and anions respectively (Cowan *et al.*, 1992). The presence of a binding site within the lumen of specific channels with affinities in the μM-mM range, substantially affects the rate of diffusion (Nikaido, 1993). Diffusion through non-specific porins increases linearly with solute concentration making porins more efficient at high solute concentrations. Specific channels display a faster diffusion at low solute concentration which saturates at higher solute concentrations, making these channels more efficient at low substrate concentrations (Nikaido, 1992).

(ii) Energy-dependent transporters (or TonB-dependent transporters, TBDT) are capable of transporting specific substrates against their concentration gradient across the OM. Since the periplasm is devoid of ATP, the energy required by this family of proteins is transduced from the IM to the OM by the TonB protein. All TBDT are 22-stranded

β-barrels in which the N-terminal domain forms a plug that occludes the channel on the periplasmic side of the barrel (Bolam and van den Berg, 2018). TonB is a periplasm-spanning IM protein coupled with the ExbBD complex which transduces energy by exploiting the proto-motive force across the IM. The energy is then used by TonB to "unplug" the TBDT and drive the active transport of the substrate across the OM. TBDT are highly efficient transporters and bind their substrates, which include ferric chelates (siderophores), vitamin B12 and carbohydrates, with nM affinities. Examples of TBDT are FhuA which transports ferric siderophores (Ferguson *et al.*, 1998) and SusC which transports complex carbohydrates (Glenwright *et al.*, 2017).

(iii) Structural proteins are crucial for the stability of the OM and the Gram-negative cell envelope. The major structural protein in the OM of *E. coli* is OmpA which together with Braun's lipoprotein links the OM to the underlying peptidoglycan cell wall (De Mot and Vanderleyden, 1994; Koebnik, 1996). Bacteria expressing non-functional versions of OmpA and Braun's lipoprotein become spherical, losing the classic rod-like shape and are significantly more sensitive to osmotic shocks (Sonntag *et al.*, 1978).

In addition to these three major families there are several other integral OM proteins with important functions. Amongst these are: proteins responsible for LPS insertion in the OM (LptD of the Lpt complex) (Sherman *et al.*, 2018); the BAM complex which assists OMPs folding in the OM (Noinaj *et al.*, 2017); phospholipase A which hydrolyses mislocalized phospholipids in the OM outer leaflet and contributes to maintaining the OM asymmetry (May and Silhavy, 2018); enzymes such PagP PagL and LpxR which remodel the lipid A moiety of LPS by adding or removing acyl chains (Needham and Trent, 2013);

1.1.2.1 Outer membrane protein F (OmpF)

Porins are of particular interest since they represent one of the most abundant protein species of the OM and are the major route of entrance exploited by antibiotics (O'Shea and Moser, 2008; Pages *et al.*, 2008). The major porin of *E. coli* OM is OmpF, which is present at 100.000 copies per cell and constitutes 7% of the total protein mass of the bacterium (Rosenbusch, 1974). Because of its abundance and stability OmpF was the first membrane protein to be crystallised and one of the first for which a high-resolution structure was

determined (Garavito *et al.*, 1983; Cowan *et al.*, 1992). OmpF is a homotrimeric protein composed of three identical 340-amino acid residue β-barrels of 16 antiparallel β-strands (**Fig. 1.4a**). The 16 β-strands are linked by 8 tight turns on the periplasmic side and 8 long loops on the extracellular side of the barrel. Loop 2, which connects strands 3 and 4, folds outwards over the barrel of the neighbouring monomer unit, stabilising the trimeric form of the protein. Loop 3, connecting strand 5 and 6, folds inward into the lumen of the barrel narrowing the diameter of the channel to create the "eyelet region" (**Fig. 1.4b**). The size of the eyelet region is ~7 Å by ~11 Å and allows the diffusion of hydrophilic solutes smaller than 600 Da with a preference for cationic molecules.

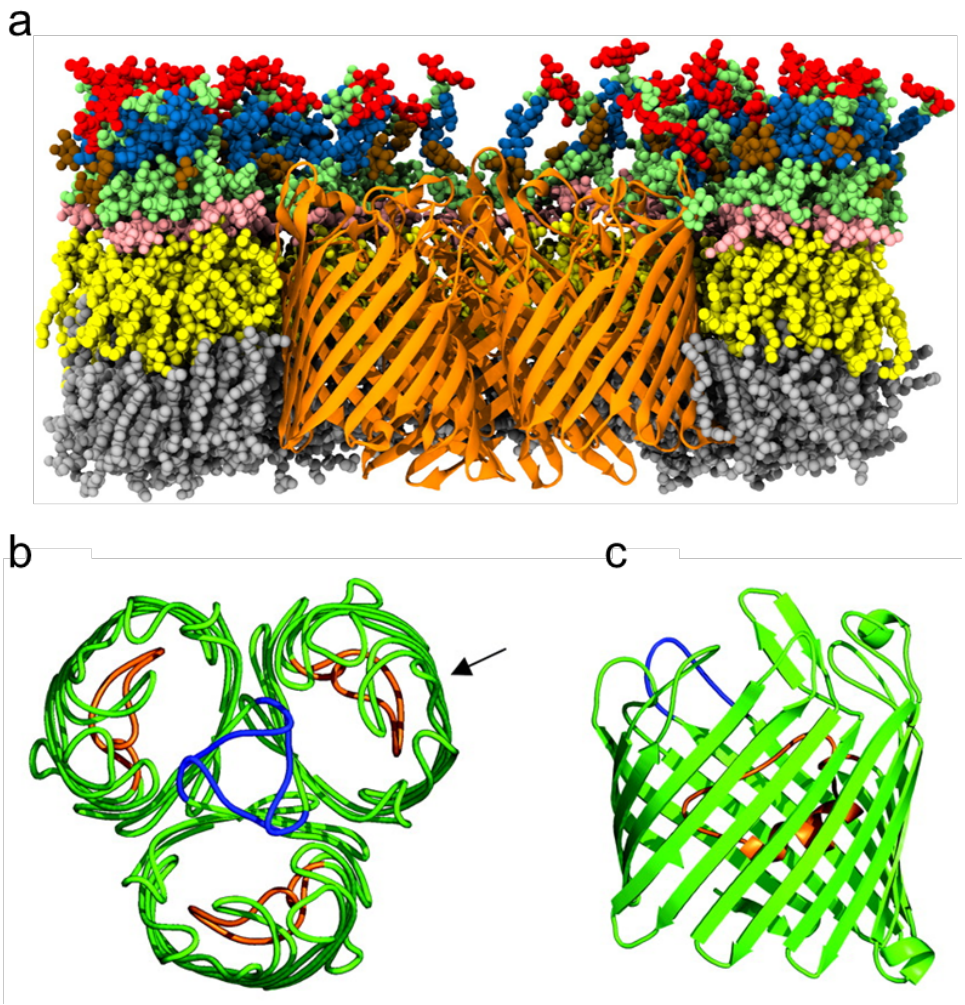

Figure 1.4 | Structure of OmpF

(**a**) Front view of an OmpF trimer (orange) embedded in an asymmetric phospholipid/LPS bilayer. Phospholipids are shown in grey and LPS tails in yellow. Image obtained from a snapshot of an MD simulation. Adapted from (Pothula *et al.*, 2016). (**b**) Top view of the OmpF trimer, loop 2 (blue) laces the monomers together whilst loop 3 (orange) folds inwards inside the barrel crating a constriction region. (**c**) Side view of an OmpF monomer, roughly in the direction of the arrow shown in **b**.

The elevated number of H-bonds and the tight packing allowed by the β-barrel structure of OmpF enables it to be highly resistant to harsh pH and temperature conditions. The trimeric porin remains intact and folded in detergents unless heated above 75°C whilst at room temperature it can withstand pH levels between 1.6 and 12 without deteriorating (Schindler and Rosenbusch, 1984). The high stability and chemical resistance make OmpF an ideal candidate for reconstituting it in OM models.

1.2 *IN VITRO* OM MODELS FOR BIOPHYSICAL STUDIES

The investigation of structural and biophysical aspects of the OM started in the 1960's with electron microscopy (EM) studies on sections of Gram-negative cells. These were the first to provide a clear picture of the double membrane envelope surrounding Gram-negative bacteria (Bladen and Mergenhagen, 1964; Mergenhagen *et al.*, 1966). EM allowed localisation of OM components such as the surface exposed O-antigen chains using ferritin labelled antibodies (Shands, 1965) and provided visual evidence for the large scale morphological changes caused by membrane damaging agents such as polymyxins and EDTA (Koike *et al.*, 1969; Lounatmaa *et al.*, 1976; Bayer and Leive, 1977). After these initial promising results however, the insufficient resolution and lack of contrast limited the use of EM in OM studies, even though cryo-EM, particularly tomography, has continued to make important progress in the imaging of the bacterial cell envelope (Milne and Subramaniam, 2009). The development of atomic force microscopy (AFM) has allowed higher resolution imaging of the OM on whole bacteria, with the advantage of not requiring the invasive fixation steps typical of EM (Louise Meyer *et al.*, 2010). Although this enabled the investigation of the OM on intact bacteria under conditions close to their native environment, the high resolution necessary to highlight molecular details of the OM could only be obtained on purified OM fragments (Yamashita *et al.*, 2012). To this date, the highest resolution of the OM under nearly native conditions was obtained on purified OM fragments by Jarosławski *et al* which resolved the structure of individual trimeric porins by AFM, showing highly ordered porin arrays in the OM of the bacterium *R. denitrificans* (Jaroslawski *et al.*, 2009). At the highest end of the resolution spectrum, diffraction techniques achieve atomic resolution structures of crystallised OM proteins and LPS bilayer stacks (Snyder *et al.*, 1999). However the physiological conditions have to be sacrificed, in order to form the highly ordered repeating structures required for diffraction studies such as protein crystals

and lipid bilayer stacks (Foglia *et al.*, 2015). The efforts to obtain atomic resolution information whilst also preserving physiological conditions, have led to the development of several *in vitro* OM models, reconstituted using LPS and OM proteins. Several studies have used X-ray and neutron scattering techniques, such as reflectometry and grazing incidence diffraction, for the structural characterisation of these OM models. Below is a brief review of OM models, from simpler LPS monolayers to asymmetric phospholipid-LPS bilayers to reconstituted models containing OMPs.

1.2.1 LPS monolayers

A single layer of LPS molecules is the simplest mimic of the Gram-negative surface. LPS monolayers have been created at the air-water interface and at the solid-liquid interface for biophysical studies.

Monolayers at the air-water interface

The study of molecular monolayers at the air-water interface was pioneered by Irving Langmuir who was awarded the Nobel Prize for his work on surface chemistry in 1932. The Langmuir-Blodgett film balance (or Langmuir trough) is the instrument at the basis of the study of lipid monolayers at the air-water interface. It consists of a Teflon trough filled with an aqueous solution (subphase), which is enclosed between two movable barriers (**Fig. 1.5a**). When spread on the water surface, lipids dissolved in an organic solvent form an insoluble molecular monolayer, oriented with the hydrophilic heads in the aqueous solution and the hydrophobic tails in the air (Stefaniu *et al.*, 2014). The monolayer can be compressed using the movable barriers and the lateral pressure that builds up in the monolayer is measured by the reduction in surface tension of the subphase according to:

$$\Pi = \gamma_0 - \gamma \qquad (1.1)$$

Where Π is the surface pressure, γ_0 is the surface tension of the pure subphase and γ is the surface tension of the subphase with the monolayer. This technique enables the measurement of the area per molecule of the lipids whilst providing a reliable platform for monolayer studies using scattering and fluorescence techniques. Furthermore, the ability to control the lateral pressure of the monolayer can be used to recreate the lipid packing found in biological membranes (Marsh, 2007) and monitor the insertion of molecules such as antimicrobial peptides added to the subphase.

Monolayers of lipid A (Gidalevitz *et al.*, 2003; Neville *et al.*, 2006), Re (Oliveira *et al.*, 2010; Schneck *et al.*, 2010; Jeworrek *et al.*, 2011), Rc (Le Brun *et al.*, 2013), Ra (Oliveira *et al.*, 2009; Abuillan *et al.*, 2013) and only recently smooth LPS (Micciulla *et al.*, 2019) have been studied at the air-water interface using X-rays and neutrons. In all cases LPS formed stable insoluble monolayers at the air-water interface. Upon compression the tilt angle of the LPS molecules decreased and the overall thickness of the monolayer increased. The monolayer thickness determined by X-ray reflectometry (XR) and neutron reflectometry (NR) consistently revealed a 11-14 Å thick acyl chain region, and a core oligosaccharide that varied between ~10 and ~28 Å from Re to RaLPS, according to the level of truncation of the core, in agreement with X-ray diffraction measurements (Snyder *et al.*, 1999). In a recent study, a combination of XR and NR was used to characterise smooth LPS monolayers, which revealed and extension of the polysaccharide chains of of the O-antigen of ~200 Å (Micciulla *et al.*, 2019) . Divalent cations were shown to regularly displace monovalent cations from the monolayers, displaying a higher affinity for the LPS head groups and localising in the inner core region, regardless of the truncation level of the core (Oliveira *et al.*, 2009; Schneck *et al.*, 2010). This resulted in the condensation of the monolayers, indicated by a consistent reduction in the area per molecule when the subphase contained mM levels of Ca^{2+} (Oliveira *et al.*, 2010; Hwang *et al.*, 2018). In the presence of divalent cations, LPS monolayers were also shown to be less susceptible to the insertion of antimicrobial peptides such as protamine and polymyxin B (Zhang *et al.*, 2000; Oliveira *et al.*, 2009). Herrmann *et al* showed how divalent cations also promoted the formation of a crosslinked 2D LPS network and were able to measure the effect of divalent cations on the viscoelastic properties of Re and RaLPS monolayers (Herrmann *et al.*, 2015).

Hybrid bilayer membranes (HBM)

Hybrid bilayer membranes are model membranes formed by a lipid monolayer deposited on a solid substrate covalently modified with a hydrophobic monolayer (Cooper *et al.*, 1998). LPS HBM have been characterised, although there are significantly fewer studies on these LPS monolayer systems compared to those at the air-water interface. HBM formation can be achieved either via self-assembly from liposome fusion (Schneck *et al.*, 2009) or by transferring a monolayer from the air-water interface (Rodriguez-Loureiro *et al.*, 2018). The latter is performed using Langmuir-Blodgett (LB) or Langmuir-Schaefer (LS) transfer techniques (**Fig. 1.5b** and **c**). An early study used mixed phospholipid-lipid A monolayers deposited by self-assembly to measure the interaction of various LPS-binding antimicrobial

peptides by surface plasmon resonance (Thomas *et al.*, 1999). However, the study provided little information on the formation of the mixed monolayer.

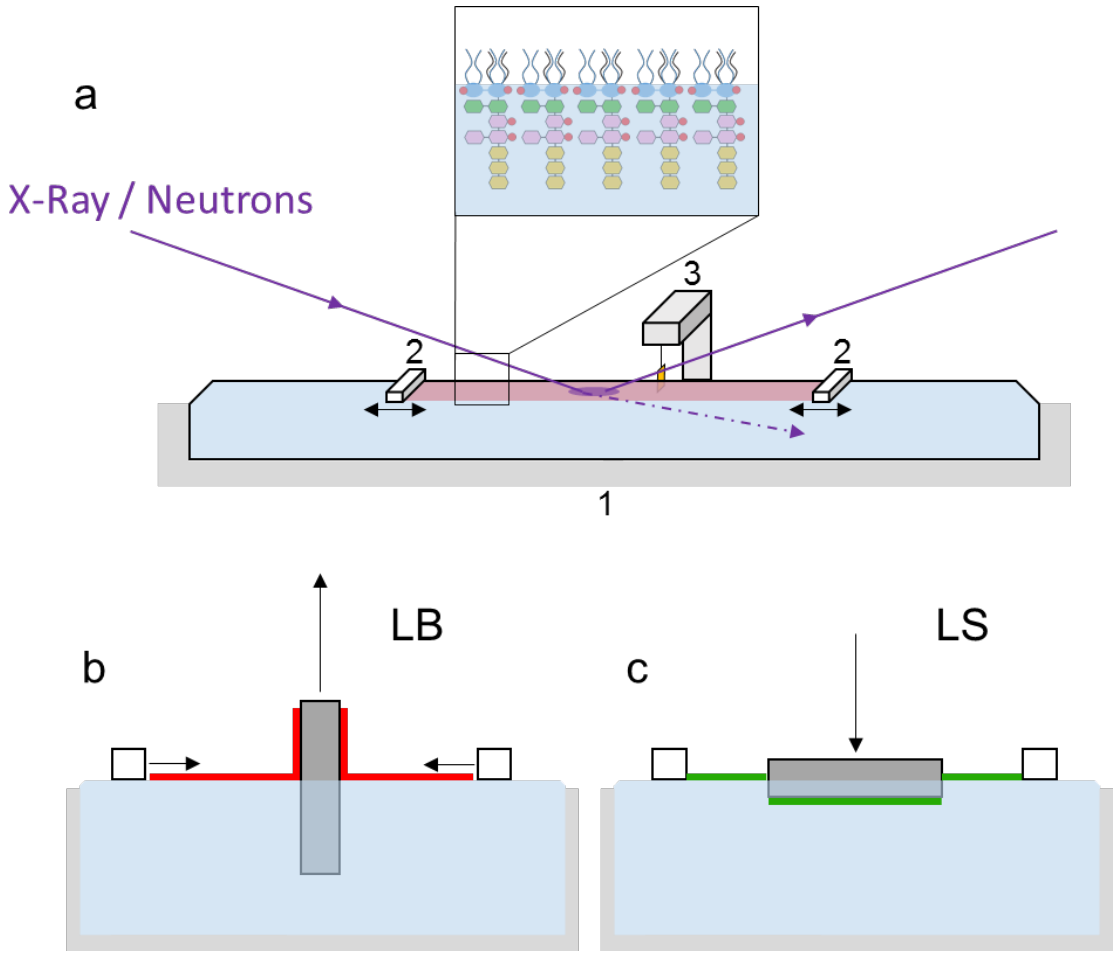

Figure 1.5 | Experimental setup to study lipid monolayers using the Langmuir trough

(**a**) Components of a Langmuir trough. The Teflon container (1) contains the water subphase. The LPS monolayer (red area, magnified in the inset) is enclosed between the two movable Teflon barriers (2) that control the lateral pressure exerted on the 2D lipid film. The surface pressure is measured using a Wilhelmy plate (orange) attached to a film balance (3). The monolayer can be investigated by neutron and X-ray scattering techniques, especially reflectometry and grazing incidence diffraction. (**b**) Langmuir-Blodgett deposition. A submerged solid substrate (grey), is slowly lifted vertically out of the subphase, transferring the lipid monolayer (red) onto the solid surface, whilst the barriers maintain a constant lateral pressure. (**c**) Langmuir-Schaefer deposition. The substrate is aligned horizontal to the water surface and pushed through the monolayer allowing its transfer onto the solid surface.

In a different study, a smooth LPS monolayer was self-assembled on a silanised silicon surface and the effects of calcium ions on the conformation of the O-antigen were investigated by XR (Schneck *et al.*, 2009). Calcium ions displaced monovalent cations, in line with what was observed in experiments at the air-water interface and caused the collapse

of the O-antigen polysaccharide into a more condensed layer. More recently smooth LPS monolayers have been assembled on silanised silicon surfaces by LB transfer and characterised by NR (Rodriguez-Loureiro *et al.*, 2018). This was the first study to provide an accurate structural characterisation of smooth LPS and its distribution of O-antigen polymeric chains.

1.2.2 Phospholipid/LPS asymmetric bilayers

The transfer of a phospholipid monolayer followed by a monolayer of LPS, via sequential LB and LS depositions onto a solid substrate, can been used to create OM model bilayers that reproduce the asymmetric lipid distribution of the OM (**Fig. 1.6a**).

Most of the work done on the development of asymmetric phospholipid (PL)/LPS OM models ($_{PL/LPS}$OMM) has been carried out by Clifton and co-workers in the last six years (Fragneto *et al.*, 2018). A key aspect in the development of these model membranes is the use of NR to characterise the structure of the bilayers (Clifton *et al.*, 2013b). By exploiting the differential sensitivity of neutrons for hydrogen and its isotope deuterium (see section 1.4.1 below) they resolved the structure of the two leaflets of the asymmetric bilayer by NR, through the use of perdeuterated phospholipids and hydrogenous rough LPS in the inner and outer leaflet respectively. This approach enables the quantification of the asymmetry and the monitoring of the changes in the bilayer structure to study the effect of perturbing agents such as EDTA under near physiological conditions (Clifton *et al.*, 2015b). Building upon the initial work of Hughes *et al* (Hughes *et al.*, 2008; Hughes *et al.*, 2014) on floating lipid bilayers, the same LB/LS approach described for the fabrication of the silicon supported $_{PL/LPS}$OMM was applied to a gold coated silicon crystal functionalised with a grafted monolayer of ω-thiolipids (**Fig. 1.6b**). This yielded asymmetric $_{PL/LPS}$OMM floating above a 20 Å thick water reservoir that separates the substrate from the bilayer (Clifton *et al.*, 2015a). These asymmetric free-standing bilayers (FSB) were used to test the effect of Ca^{2+} removal and the interaction with the antimicrobial proteins lysozyme and lactoferrin. The effect of the EDTA mediated Ca^{2+} removal caused the mixing of the inner and outer leaflet leading to a reduced asymmetry of the FSB similar to what was observed on the silicon supported $_{PL/LPS}$OMM (Clifton *et al.*, 2015b). Both the antimicrobial proteins tested were shown to interact with the bilayer. However, lactoferrin caused a more substantial disruption of the model membrane, in line with that observed on the natural OM. These experiments provided a solid proof of principle for the biological significance of these model membranes in the structural investigation of biologically relevant processes involving the OM and its

interaction with antimicrobial molecules. Along with the work of Clifton *et al*, Mei-Ling *et al* used a similar approach to create $_{PL/LPS}$OMM containing lipid A from *P. aeruginosa* in the outer leaflet to investigate the effects of polymyxin derivatives on the bilayer structure (Han *et al.*, 2017; Han *et al.*, 2018). Notably, no $_{PL/LPS}$OMM containing smooth LPS has been reported yet, which would represent an important step towards mimicking the cell envelope of wild type bacteria.

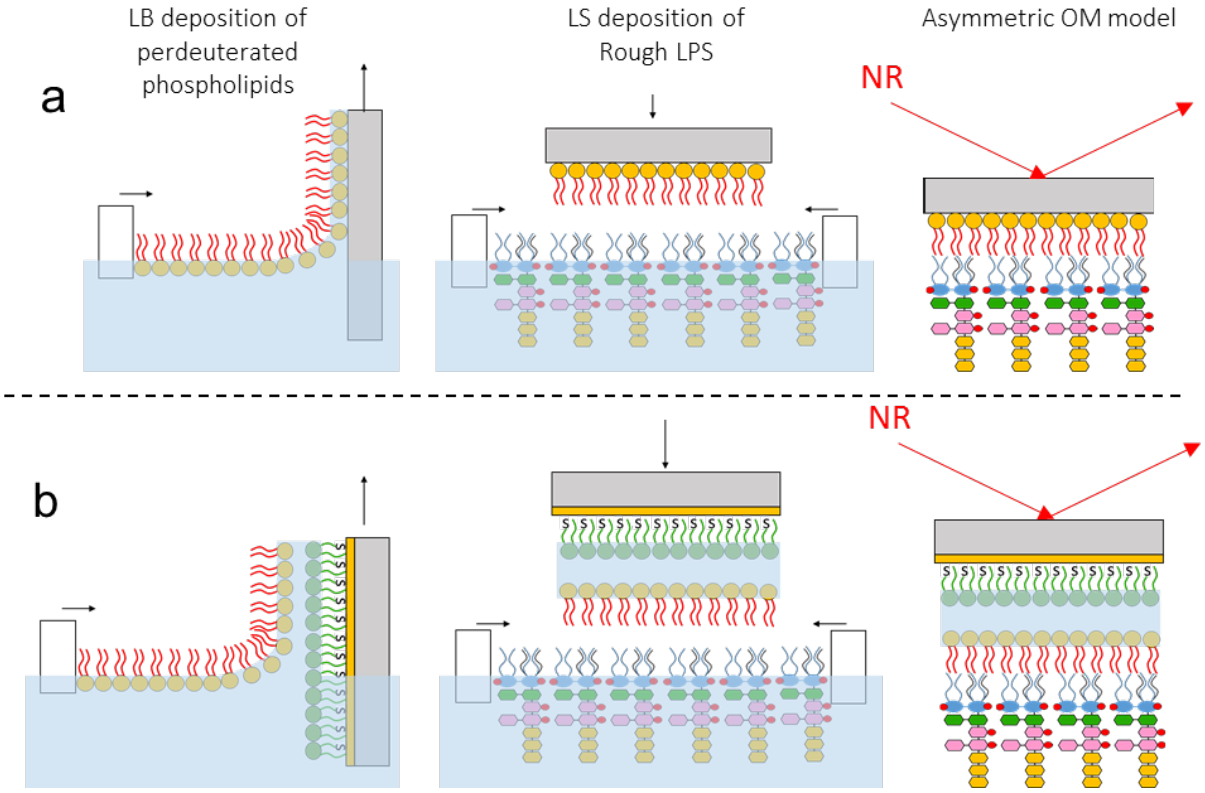

Figure 1.6 | Assembly of asymmetric phospholipid/LPS bilayers via LB/LS deposition

Assembly of (**a**) silicon supported and (**b**) floating asymmetric phospholipid/LPS bilayers like those developed by Clifton *et al* for neutron reflectivity studies. The deposition procedure of the asymmetric bilayer is identical in **a** and **b** and it consists of an LB deposition to transfer the phospholipid inner leaflet (left) followed by a LS deposition to deposit the LPS outer leaflet (middle) yielding the asymmetric bilayer (right). In **a**, the starting substrate is a bare silicon crystal whilst in **b** it's a gold coated silicon crystal functionalised with a ω-thiolipid grafted layer (green) that allows the incorporation of a water reservoir between the substrate and the bilayer.

1.2.3 Protein containing OM models

OmpF represents one of *E. coli*'s most abundant OM proteins and due to its remarkable stability, it has been reconstituted *in vitro* in several OM models, however only a few of them has been intended for structural studies. Clifton *et al* reconstituted OmpF into

phospholipid monolayers at the air-water interface to study the insertion of the antimicrobial protein colicin N, which is known to bind OmpF as part of its translocation process through the OM, which is essential for its toxic function (Clifton *et al.*, 2012). The presence of OmpF in the monolayer was shown to significantly facilitate the insertion of colicin N and the structure of the OmpF-ColN complex at the interface of the phospholipid monolayer was determined by NR and complemented by the OmpF-ColN solution structure obtained by small angle neutron scattering. Another approach to characterise the structure of reconstituted OmpF is that adopted by Cisneros *et al*, which used AFM to image OmpF trimers immobilised on a gold surface via an engineered cysteine residue (E183C) introduced in the fifth periplasmic short turn of OmpF (^{cys}OmpF) (Terrettaz *et al.*, 2002). After the addition of 1,2-dipalmitoyl-sn-glycero-3-phosphothioethanol (DPPTE), a filler thiolipid molecule, around the immobilised ^{cys}OmpF trimers, high resolution AFM imaging showed the successful immobilisation of oriented individual protein trimers on the gold surface, with unprecedented resolution (Cisneros *et al.*, 2006) (**Fig. 1.7a** and **b**). The same OmpF immobilisation approach was extended by Holt *et al*, who went a step further by assembling a phospholipid outer leaflet on top of the assembled DPPTE-^{cys}OmpF monolayer (**Fig. 1.7c**) (Holt *et al.*, 2009). They determined the structure of the protein-phospholipid layer by NR showing reproducible assembly and consistent coverage of the surface by the protein of ~30% of the surface area across multiple samples. An alternative method to reconstitute a membrane model that displays the native protein-lipid composition of the OM is to use outer purified OM vesicles to reconstitute a planar bilayer on a polymer coated surface (Hsia *et al.*, 2016). The innovative approach of Hsia *et al* yields a molecularly complete OM model which reproduces closely the composition of the natural OM and has the potential to be a promising platform for interaction studies and bio-sensing applications. However, the inherent randomness of the vesicle fusion process does not provide control neither on the final orientation of proteins nor on the lipid asymmetry of the model. Asymmetric OM models containing both oriented proteins and LPS are still lacking and would represent a valuable platform for OM studies.

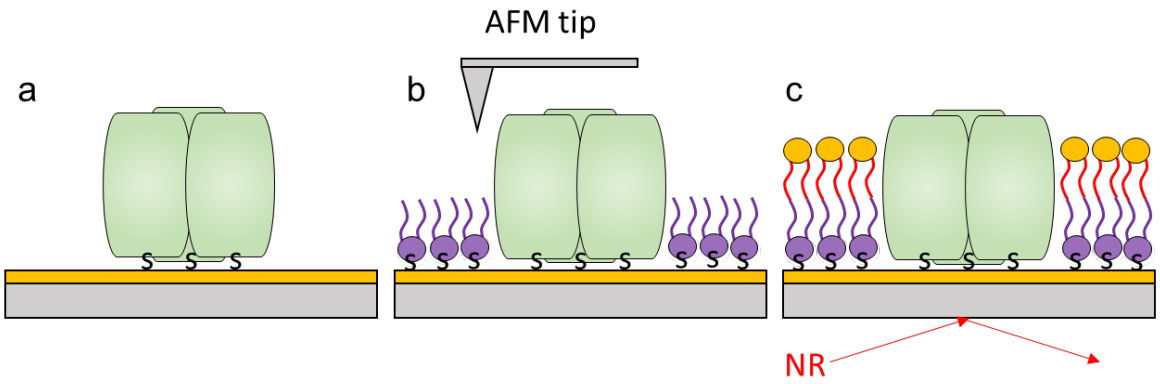

Figure 1.7 | Reconstitution of ^{cys}OmpF onto a gold surface for AFM and NR studies

(**a**) Immobilisation of ^{cys}OmpF (green) on a gold coated surface, (**b**) after the addition of the filler thiolipid DPPTE (purple) and (**c**) after the addition of the phospholipid outer leaflet.

1.3 ANTIBIOTIC RESISTANCE AND THE BARRIER FUNCTION OF THE OM

In 2008 the ESKAPE acronym first appeared in the Journal of infectious diseases, describing a group of pathogens responsible for most hospital acquired infections which are becoming increasingly resistant to available antibiotics. These are: *Enterococcus faecium, Staphylococcus aureus, Klebsiella pneumoniae, Acinetobacter baumanni, Pseudomonas aeruginosa* and *Enterobacter* species (Rice, 2008). Notably, four out of six pathogens in the ESKAPE list are Gram-negative bacteria which have the critical advantage of being shielded by the OM. For the vast majority of drug molecules active against Gram-negatives, the lipid matrix formed by the external LPS leaflet of the OM constitutes an impenetrable barrier, leaving porins the only route of access to the cell (Pages *et al.*, 2008). This shared pathway of entry makes antibiotic efficacy susceptible to small mutation of the channel region of porins, leading to a rapid development of antibiotic resistance (Tommasi *et al.*, 2015). A comparison between the physicochemical properties of antibiotics active against Gram-positives with those active against Gram-negative bacteria, highlights the effect that the shared porin access route has on the characteristics of these drug molecules (**Fig 1.8**). 95% of antibiotics active against Gram-negative bacteria have a MW below 600 Da and are more hydrophilic compared to other drugs (O'Shea and Moser, 2008). This is due to the size constraint imposed by the lumen of porins through which they must pass and the fact that they have to be water soluble enough to diffuse through the water-filled channels. Antibiotics

active against Gram-positive bacteria, on the other hand, span a much larger range of sizes and chemistries. The restricted antibiotic influx through the OM indirectly increases the effectiveness of a wide range of other resistance strategies which either degrade, actively pump out, or alter the target of clinically important drugs. Therefore, understanding how antibiotics that cross the OM by avoiding the porin route are able to do so is an important step towards the development of new drug molecules capable of overcoming the current limitations.

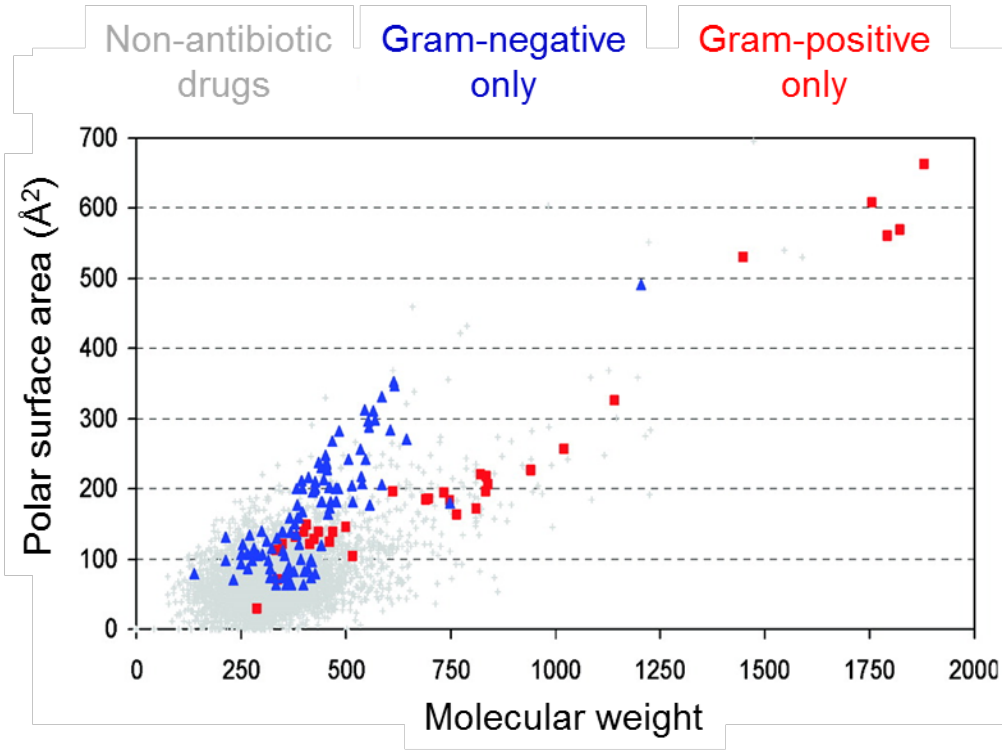

Figure 1.8 | Physicochemical properties of antibiotics highlight the shared route across the OM

A comparison between the properties of antibiotics active against Gram-positives (red), Gram-negatives (blue) and non-antibiotic drug molecules (grey). The sharp cut-off at 600 Da which differentiates antibiotics active against Gram-negatives from those active against Gram-positives is the result of the size limit imposed by the channel region of porins. Exceptions with higher MW are azithromycin (749 Da) and polymyxin B (1203 Da). Adapted from (O'Shea and Moser, 2008).

1.3.1 Polymyxin B

An exception to the commonly exploited porin pathway through the OM is represented by polymyxins. Polymyxins are a family of cationic lipopeptides produced by the Gram-positive bacterium *Paenibacillus polymyxa* which currently represent the last resort antibiotics for the treatment of Gram-negative infections resistant to all available drugs (Falagas and Kasiakou, 2005; Zavascki *et al.*, 2007). Polymyxin B (PmB) (**Fig 1.9**) is a

mixture of closely related compounds composed of a cyclic decapeptide scaffold containing 5 positively charged di-amino-butyric acid (DAB) moieties (Velkov *et al.*, 2010). An acyl tail, attached to the decapeptide unit, together with a phenylalanine and a leucine residue in the decapeptide are responsible for the amphipathic properties of the molecule. The first steps of its antimicrobial action involve a direct interaction with LPS and the disruption of the OM integrity, which allows PmB molecules to penetrate the Gram-negative cell avoiding the porin-mediated translocation (Schroeder *et al.*, 1992). Resistance mechanisms involve LPS modifications aimed at reducing LPS net negative charge (Gunn *et al.*, 1998; Needham and Trent, 2013), increasing the strength of its hydrophobic core by supplementary lipid A acylation (Boll *et al.*, 2015) or, in extreme cases, complete loss of LPS from the OM (Moffatt *et al.*, 2010; Vila-Farres *et al.*, 2015). The molecular details of PmB interaction with LPS and the OM have not been fully elucidated. *In vivo*, PmB kills sensitive bacteria with a minimum inhibitory concentration (MIC) of ~1-2 μg/ml (Velkov *et al.*, 2014) and it releases periplasmic and cytoplasmic proteins as well as large amounts of LPS (Sahalan and Dixon, 2008). It has long been known that PmB causes extensive membrane damage (Koike *et al.*, 1969), and, *in vitro*, it breaks up and disperse LPS aggregates (Lopes and Inniss, 1969). As with other membrane active antimicrobials, the effects of PmB on LPS are inversely related to the concentration of divalent cations present in the media. PmB insertion into LPS monolayers at the air-water interface has been shown to gradually decrease in the presence of increasing amounts of Mg^{2+} in the subphase (between 0 and 5 mM) (Zhang *et al.*, 2000). Similarly, the fluorescence of the PmB derivative dansyl-PmB, which develops upon binding to LPS, decreases as Mg^{2+} ions are added to the solution containing the PmB-LPS complex whilst it is restored upon further addition of the chelating agent EDTA (Moore *et al.*, 1986). Although the cationic nature of PmB is central to its mechanism of action, its deacylated analogue, PmB nonapeptide (PmBN) (**Fig 1.9b**), which lacks the fatty acid tail but retains four out of the five cationic DAB residues, is not bactericidal (Duwe *et al.*, 1986; Sahalan and Dixon, 2008). Hydrophobic interactions, mediated by the acyl moiety, are therefore important for PmB antibiotic activity. PmB toxicity and LPS-binding have both been shown to be markedly temperature dependent. Several reports demonstrated that PmB kills *E. coli* in a temperature dependent manner (Teubner and Bader, 1977; Katsu *et al.*, 1984), with some studies showing a striking difference in PmB's killing rates, which dropped from ~98% to ~5% between 35°C and 18°C (Hodate and Bito, 1982). In the same temperature range, the thermodynamics of the binding of PmB to LPS *in vitro* was shown to change from strongly endothermic to exothermic for bacteria sensitive to PmB, whilst remaining endothermic in

the case of bacteria resistant to PmB (Brandenburg *et al.*, 2002; Brandenburg *et al.*, 2005; Howe *et al.*, 2007). Several of these studies suggest a connection between the temperature dependent effects of PmB and the transition of LPS in the OM from the gel to the fluid phase that has been suggested to take place in the same temperature range (Brandenburg and Seydel, 1990). However, direct evidence for the link between LPS phase transition and PmB membrane damage is still missing.

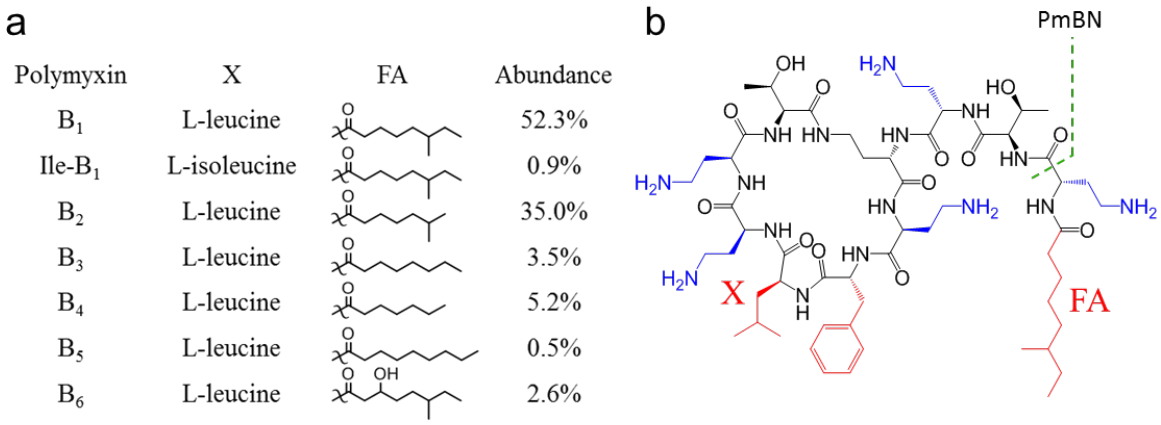

Figure 1.9 | Chemical structure and variability of polymyxin B

(**a**) Variability amongst PmB components and relative abundances (Orwa *et al.*, 2001). (**b**) Chemical structure of polymyxin B_1, the most abundant component of PmB. In blue the cationic di-amino-butyric acid and in red the hydrophobic moieties. The part to the left of the dashed green line is missing in the nonapeptide derivative of PmB, PmBN. FA = fatty acid

1.3.2 Colicin N

Another example of antimicrobials that translocate through the OM in a non-canonical way is represented by colicins, which are large bactericidal proteins (>40 kDa) (Kim *et al.*, 2014). Unlike polymyxins, colicins are not used to treat Gram-negative infections, but are secreted by *E. coli* to target and kill closely related competing strains. Colicins perform their lethal function by either forming a pore in the IM, degrading nucleic acids or interfering with the cell wall synthesis (Cascales *et al.*, 2007). All colicins are composed of three functional domains which are responsible for the three steps of the colicins mechanism of action (**Fig. 1.10a**). The receptor binding (R-) domain is responsible for the initial interaction of the antimicrobials with the OM and anchors the colicin typically to a specific OMP (Kleanthous, 2010). The translocation (T-) domain is responsible for mediating the translocation through the OM into the periplasm by exploiting a second OMP, termed the translocon. This process is still poorly understood but it revolves around the binding of the T-domain either to the

Ton or the Tol families of IM proteins which then leads to the translocation of the entire protein in the periplasm. The cytotoxic domain, or, in the case of pore forming colicins, the pore forming (P-) domain carries the toxic activity by forming a pore in the cytoplasmic membrane. ColN is the smallest pore forming colicin with a size of 42 kDa (**Fig 10b**). Its uniqueness resides in being the only known colicin that does not use an OMP as its primary receptor but instead recognises specific sugars in the LPS outer core oligosaccharide via its R-domain (Sharma *et al.*, 2009; Johnson *et al.*, 2014). Its translocon is OmpF but it has been shown that translocation does not occur through the barrel lumen (Bainbridge *et al.*, 1998). Instead it has been suggested that ColN translocation through the OM takes place at the interface between OmpF and LPS (Baboolal *et al.*, 2008; Clifton *et al.*, 2012). Two important open questions about ColN concern the initial steps of its mechanism of action: the residues of the R-domain responsible for LPS recognition have not yet been identified and there is no information so far on the structural aspects of its interaction with LPS.

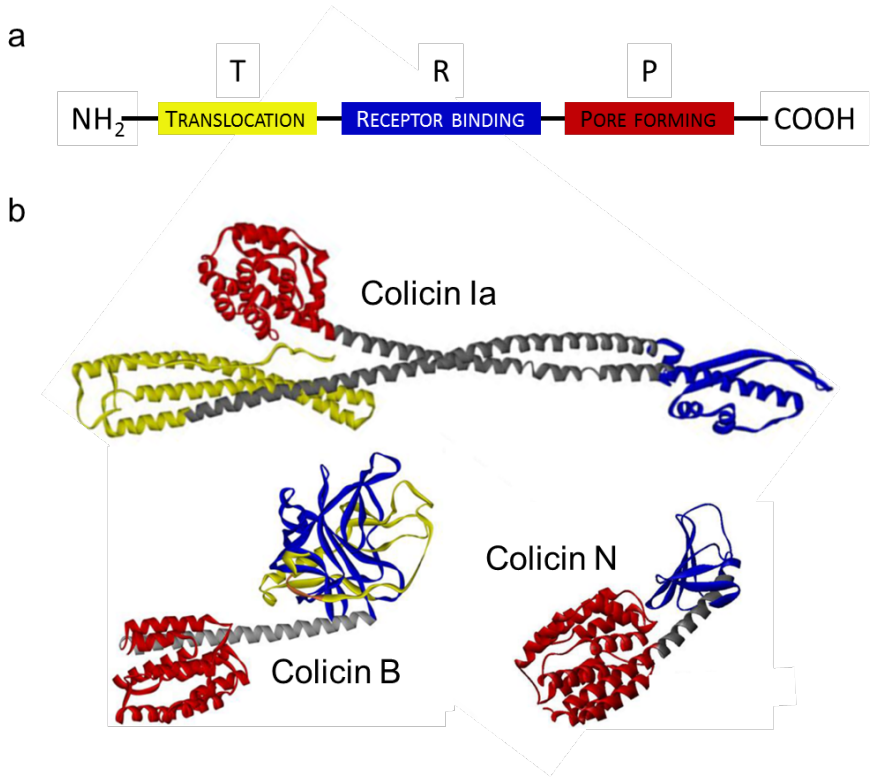

Figure 1.10 | Structures of pore-forming colicins

(**a**) General three domain organisation of colicins. (**b**) Crystal structures of three pore forming colicins: colicin Ia (PDB 1Cll) colicin B (PDB 1RH1) and colicin N (PDB 1A87). The T domain of ColN is not visible in the crystal structure due to its disordered nature. The same applies to residues 1-22 in the structure of ColIa and 1-10 and 29-43 in ColB.

1.4 NEUTRON REFLECTOMETRY

Neutron reflectometry (NR) is an established technique for the study of thin films, which can probe the structure of molecular layers as thin as a few Å (Penfold and Thomas, 1990). Historically, neutron scattering has been the realm of physicists and chemists but in the last two decades the applications of neutrons to investigate biological systems have grown substantially (Lakey, 2009). In particular, neutron reflectometry has been shown to be a powerful tool for structural studies of reconstituted biological membranes (Wacklin, 2010; Foglia *et al.*, 2015; Lakey, 2019). This is due to a set of unique properties of neutrons which include the capacity to penetrate deep into complex sample environments and the ability to clearly differentiate between hydrogen (^{1}H) and its isotope deuterium (^{2}H).

1.4.1 Theoretical aspects

Neutrons are uncharged subatomic particles with a mass m_n of 1.675 x 10^{-27} kg which, according to the de Broglie relation, can be treated as waves with a wavelength λ equal to

$$\lambda = \frac{h}{m_n v} \tag{1.2}$$

Where, v is the speed of the particle and h is Planck's constant (6.63 x 10^{-34} J s). It follows that the wavelength of a neutron is related to its kinetic energy by:

$$\mathrm{E} = \frac{1}{2} m_n v^2 = \frac{h^2}{2 m_n \lambda^2} \tag{1.3}$$

To be useful in studies of biological membranes and similar structures, the energy of a beam of neutrons, and therefore its wavelength, must be adjusted to be in a range useful to probe molecular distances (1-20 Å). This is achieved by reducing the speed of neutrons produced by a source, through a process called moderation, in which neutrons lose some of their energy by passing through a cold medium made of hydrogen, solid methane or deuterium oxide (D_2O). Neutrons in thermal equilibrium with their surrounding have an energy corresponding to:

$$\mathrm{E} \approx K_B \mathrm{T} \tag{1.4}$$

Where k_B is Boltzmann's constant (1.38 x 10^{-23} J K^{-1}) and T the absolute temperature in degrees Kelvin. So called cold neutrons, have wavelengths between 0.5 and 17Å, similar to X-rays, which makes them ideal to study phenomena at a molecular length scale.

Unlike X-rays, however, the main interaction of neutrons with matter takes place with the nucleus of atoms rather than with the electron cloud surrounding it. Compared to its wavelength (~10^{-10} m), the scattering of a neutron by a nucleus takes place at a much smaller scale (~10^{-14} m), which means that neutrons are essentially scattered by point sources, regardless of the mass and size of the atoms involved. The ability of an atom to coherently scatter a neutron is therefore an intrinsic property of the nucleus which is termed scattering length (b). The value of b determines the magnitude of the scattering and has two important characteristics: (i) it shows no systematic trend across the periodic table, appearing to vary randomly from one element to the other and (ii) it is isotope specific. A key consequence is that hydrogen and deuterium scatter neutrons with very different magnitudes (**Table 1.1**). This enables the use of selective deuteration of molecules to highlight their location within a complex hydrogen rich structure, providing a way to add "contrast" to the sample.

In scattering theory, neutrons are treated like electromagnetic radiation and are described by a wave vector **k** with modulus $k=2\pi/\lambda$ and an orientation equal to the direction of propagation of the neutron wave. When a neutron is reflected by an interface, the difference between the incident and reflected wave vectors is the wave vector transfer Q.

$$Q = k_i - k_r \tag{1.5}$$

In the elastic scattering regime, no energy is exchanged between the neutron and the sample, thus $|k_i|=|k_r|=2\pi/\lambda$ and the wave vector transfer is given by

$$Q = \frac{4\pi sin\theta}{\lambda} \tag{1.6}$$

Where θ is the angle made between the incoming neutron and reflecting surface, as exemplified by the geometrical representation of an ideal specular reflection event shown in **Figure 1.11**

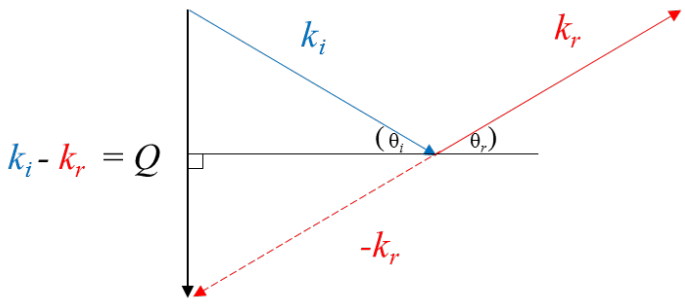

Figure 1.11 | Specular reflection of a neutron wave

Q is given by the difference between the incident (k_i) and the reflected (k_r) wave vectors and its direction is perpendicular to the reflecting interface. In specular reflection, $\theta_i = \theta_r$

In a standard reflectometry experiment, the intensity of the reflected neutron beam is measured as function of Q, which, as shown by **Equation 1.6**, is just a combination of the angle of incidence and the wavelength of the neutron. Depending on the type of instrument used, the desired Q range is achieved by either varying the incident angle, the neutron wavelengths or a combination of the two.

The phenomenon of thin film interference, which lies at the heart of NR, is the neutron analogue of the iridescent colours that appear on the surface of a soap bubble or on a puddle covered by a thin layer of oil. When electromagnetic radiation is reflected by a film of a thickness comparable to the wavelength of the impinging radiation, an interference pattern emerges which encodes information about the structure of the film. Neutron reflection is governed by the same laws of optics that describe the reflection and refraction of light. Each time a neutron beam crosses an interface between two regions with different neutron refractive indices, part of the beam is reflected, and part is refracted at an angle determined by the change in refractive index according to Snell's law

$$n_0 cos\theta_0 = n_1 cos\theta_1 \tag{1.7}$$

Where n_0 and n_1 are the refractive indices of the two media whilst θ_0 and θ_1 are the angles between the wave vectors and the interface (**Fig 1.12**). The fraction of neutrons reflected and refracted at a given interface can be calculated using the same Fresnel equation used to describe electromagnetic radiation (Born and Wolf, 1970). If the reflecting interface is made of layers with a thickness comparable to the neutron wavelength, the interference arising from the waves reflected from the boundaries between different layers, can be used to obtain information on the layer thickness and refractive indices.

The neutron refractive index relates to the elemental composition of the medium through:

$$n \approx 1 - \frac{\lambda^2 Nb}{2\pi} \tag{1.8}$$

Where Nb is the scattering length density (SLD) of the material defined as:

$$Nb = \frac{\sum b_j}{V} \tag{1.9}$$

With b_j being the scattering length of each atom in the material and V the total volume these atoms occupy. A list of scattering lengths of the most common elements found in biological molecules is given in **Table 1.1**

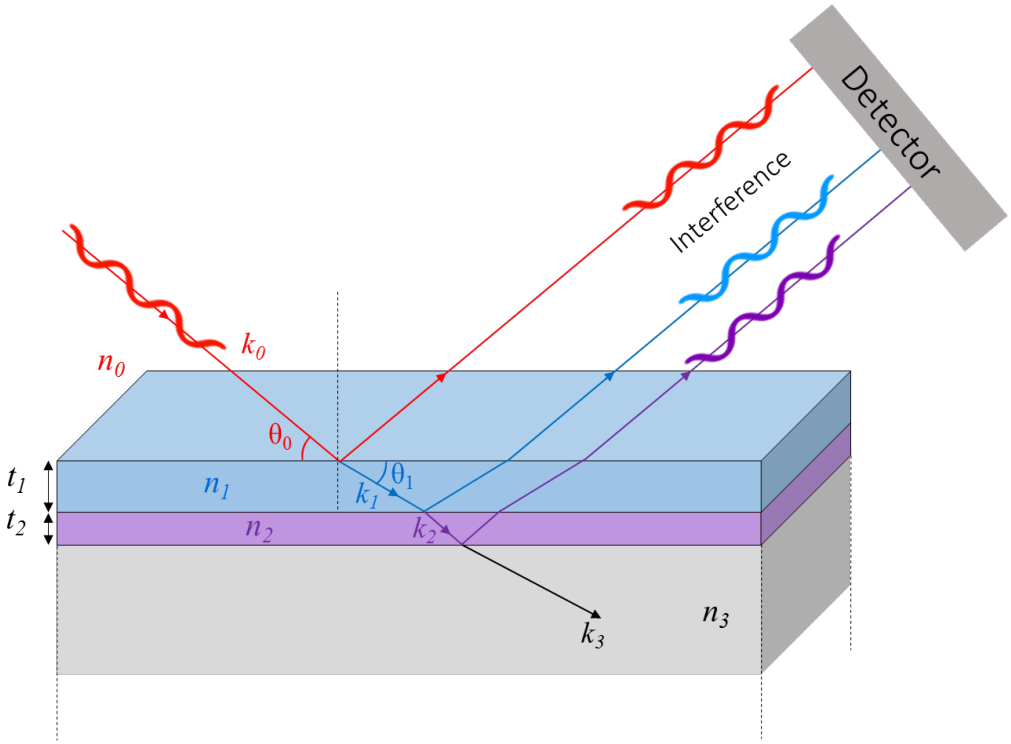

Figure 1.12 | Specular neutron reflection from a multi-layered material

Specular reflection of a beam of neutrons represented by its wave vector *k* from an interface containing two layers of thickness *t* and refractive index *n*. The path travelled by the refracted beam through the layers, before re-emerging from the interface, shifts the wave out of phase with the incident beam by an amount determined by the thickness and refractive index of the layers. According to Bragg's law, when this extra distance is equal to an integer multiple of the wavelength, constructive interference will occur.

Table 1.1 | Scattering lengths of the most common elements in biology

The sign of the scattering length value indicates whether the interaction of the neutron with that nucleus produces a positive or a negative shift in the phase of the scattered wave. Positive b values result in negative phase shifts whilst the opposite is true for negative b values.

Element	Scattering length b ($x10^{-5}$ Å)
Hydrogen (^{1}H)	-3.74
Deuterium (^{2}H)	6.67
Carbon	6.65
Nitrogen	9.36
Oxygen	5.80
Sulphur	2.58
Phosphorus	5.13

For most materials, the refractive index for neutrons is less than 1, thus below a critical angle θ_c the neutron beam will be totally reflected. The value of θ_c depends on the difference in SLD between the bulk phases (n_0 and n_3 in **Fig. 1.12**) and is given by:

$$\theta_c = \sqrt{16\pi\,(Nb_{out} - Nb_{in})} \tag{1.10}$$

Where Nb_{out} and Nb_{in} are the SLD of the two bulk phases traversed by the beam.

For a simple interface, where the scattering is weak (a condition known as the kinematic approximation), the reflectivity can be calculated as a function of Q as follows:

$$R(Q) = \frac{16\pi^2}{Q^4}\left|\int_{+\infty}^{-\infty} \frac{dNb}{dz} e^{-iQz} dz\right|^2 \tag{1.11}$$

Where the part highlighted in red is the Fourier transform of the derivative of the SLD distribution profile across the interface. *R(Q)* and the SLD profile along the normal to the surface are therefore mathematically linked by a Fourier transform. An important consequence is that due to the mathematical nature of the Fourier transform, there is an inverse correlation between the spacing of the interfacial layers and the spacing of the features in the reflectivity curve that these generate. This is a useful correlation which allows to infer changes in the interfacial structure, directly from the reflectivity, before the data is analysed by fitting it to a model (see below).

1.4.2 Experimental aspects

Neutrons can be created by two processes: nuclear fission and spallation. In the first case a continuous flux of neutrons is generated by the nuclear chain reaction in a reactor, where the fission of each nucleus of ^{235}U produces on average 2.5 neutrons according to:

$$^{235}\mathrm{U} + \mathrm{n} \longrightarrow \mathrm{X} + \mathrm{Y} + 2.5\mathrm{n} \tag{1.12}$$

Where n is a neutron, and X and Y are nuclei produced by the fission of uranium. Spallation sources, such as the ISIS Neutron and Muon source in the UK, do not rely on nuclear material but produce neutrons by bombarding a heavy element, like tungsten or mercury, with pulses of a proton beam accelerated to >80% the speed of light in a particle accelerator. For each pulse of protons hitting the target, a "white" beam of neutrons is produced which is made of a packet of neutrons with a distribution of wavelengths. Since the neutron wavelength is inversely related to its speed by **Equation 1.2**, the time it takes for each neutron to reach the detector after they are released from the source, is used to determine the wavelength of each

neutron in the packet and therefore determine the *Q* range. This is known as Time of Flight (TOF) technique. The requirement for either a nuclear reactor or a particle accelerator to produce a beam of neutrons, restricts neutron experiments to large scale facilities with limited access, which is partly the reason why the use of neutrons in biophysics has progressed at a slow pace.

The highly penetrating nature of neutrons makes them ideal to study buried interfaces such as the interface between a solid and a liquid (**Fig. 1.13**) (Welbourn and Clarke, 2019). This enables biological model membranes reconstituted on a solid surface, to be studied in an aqueous environment that closely mimics physiologically relevant conditions using neutron reflectometry. The typical setup used to study the solid liquid interface is shown in **Figure 1.13.** The neutron beam easily penetrates the bulk silicon substrate and is reflected from the buried solid-liquid interface where the lipid bilayer sits. In a TOF instrument, the reflectivity is measured at multiple glancing angles, between 0.25° and 2.5°, until the desired *Q* range is covered, usually between ~0.01 and ~0.3 $Å^{-1}$. As the *Q* vector lies perpendicular to the surface (**Fig 1.11**), the reflectivity curve encodes the SLD distribution along the normal across the surface which describes the elemental composition of the chemically distinct layers of the membrane (e.g. lipid head groups and tails). The ability to exchange the solution bathing the membrane within the solid-liquid cell, allows control of the SLD of the bulk solution by using buffers made by mixing H_2O and deuterium oxide (D_2O). This enables the measurement of reflectivity curves under different solution isotopic conditions, termed contrasts, which yields different datasets that are then constrained to fit to a shared model of the interface where the only independent variable that determine differences in the reflectivity is the SLD of the solution. This approach provides accurate information on the interfacial structure of the layered sample, such as the thickness of the distinct layers, chemical composition and level of penetration of water within each layer (Clifton *et al.*, 2013a).

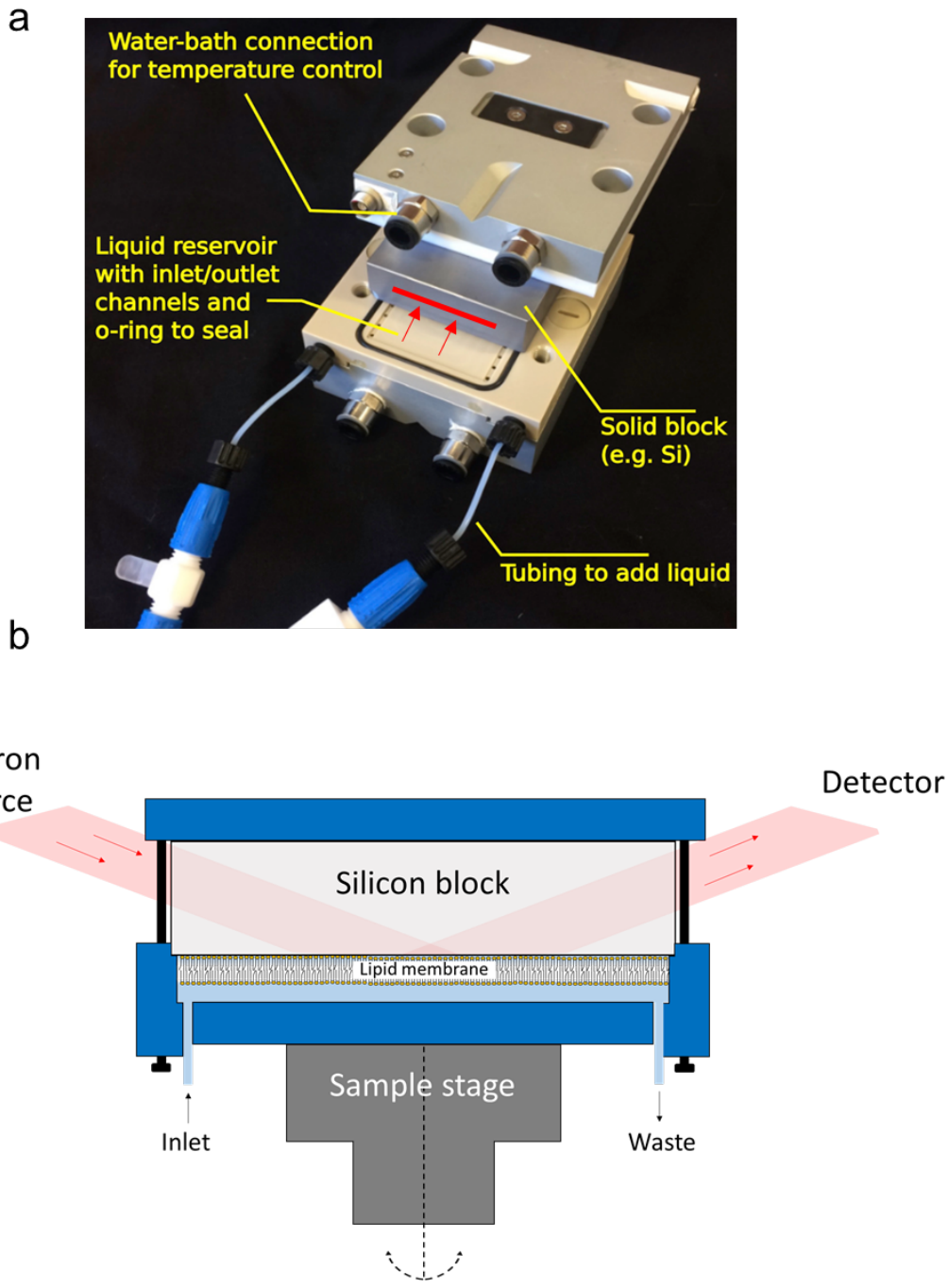

Figure 1.13 | Solid-liquid cell setup for neutron reflection studies of the solid liquid interface.

(**a**) Picture of a solid liquid cell used to study membranes at the solid liquid interface. Silicon is often used as a substrate as it is nearly transparent to neutrons. The tubing can be connected to a computer controlled HPLC pump to exchange aqueous buffers in the liquid reservoir. Red arrows indicate the direction of the beam across the silicon and the red line is the approximate width of the incident beam. The silicon block shown in the picture is 8x5x1.5 cm (adapted from (Welbourn and Clarke, 2019)) (**b**) Cartoon of a membrane sample in a reflectometry experiment. The neutron beam penetrates the silicon block and is reflected at the solid liquid interface where the lipid bilayer sits. The angle of incidence is determined by a rotating stage which holds the sample in the path of the beam.

1.4.3 Data analysis

The aim of a NR experiment is to correlate the reflected intensity, measured as a function of Q, with the structure of the sample. This yields a measure of the thickness and SLD of each chemically distinct layer stacked at the interface.

To obtain an SLD profile from reflectivity data, there are two main approaches. One is based on the kinematic approximation (**Eq. 1.11**) and describes the interface in terms of the contribution of each layer to the total reflectivity, yielding partial structure factors that describe the distribution of the SLD of each chemically distinct component along the normal to the surface. This approach has been used extensively for monolayers systems at the air-liquid interface (Lu *et al.*, 2000).

The second method is based on the treatment of the reflectivity according to the classical laws of optics, using the Fresnel equations to calculate the reflection and refraction of neutrons at the boundaries of each successive layer of a stratified interface. Mathematically, this can be done either using the matrix formalism described by Abeles (Abeles, 1950) or with the recursive formula proposed by Parratt (Parratt, 1954). Although with different approaches, both methods model the interface as a series of stacked layers, each with a defined SLD and thickness from which the reflectivity is calculated. The sharpness of the interface between each successive layer is then modulated using a Gaussian function allowing to model a more realistic diffuse interface rather that an ideal flat boundary (Nevot and Croce, 1980).

This approach is at the basis of the algorithm implemented by fitting programs such as RasCal (Hughes, 2013), which allows fitting of the reflectivity to that calculated from a user defined model of the interface by using the Parratt recursive formula (Parratt, 1954). The model consists of a series of layers each of which is described by three parameters that define the thickness, SLD and interfacial roughness of the layer. The calculated reflectivity from the user-defined model, is compared to the experimental reflectivity and the parameters of the model adjusted until the difference between the model and the data is minimised. This allows the determination of the SLD profile of the interface (Clifton *et al.*, 2013a). The information content of the reflectivity profile however is limited by the relatively small Q range available and the phase problem which derives from the ability to only measure the amplitudes of the reflected neutrons but not their phases. Thus, to impose constraints on the model, multiple reflectivity curves from the same sample, measured at different solution

isotopic contrasts, are simultaneously fitted to a shared model of the interface, which differs only in the SLD of the solution, and has to generate a calculated reflectivity that satisfies all datasets simultaneously. Once the simulated reflectivity has been fitted to the measured data, a 95% confidence interval on the values obtained is estimated using error analysis approaches such as bootstrap (Efron, 1979) resampling or Bayesian analysis methods (Sivia and Webster, 1998).

1.5 AIMS

The challenges imposed by the complexity of the natural OM, the proximity to the IM and the small size of bacterial cells, complicate its biophysical study *in vivo*. Asymmetric OM models reconstituted in vitro from phospholipids and LPS, represent a promising tool for the investigation of the properties of the Gram-negative cell envelope. The possibility of achieving near atomic resolution of these models, under near-physiological conditions, makes them ideal to probe the molecular aspects of their interaction with antimicrobials. Furthermore, the use of NR combined with selective deuteration of components of the OM model provides a key advantage in resolving the structure of this uniquely asymmetric structure. This approach could provide relevant information on the biophysics of the OM and its interactions with antimicrobial compounds that would not be possible to achieve with other methods. A more detailed understanding of the mechanism of OM penetration of non-conventional antimicrobials is essential for the design of much needed, new effective antibiotics. The project behind this thesis focused on three main questions:

- How do the physicochemical properties of OM models affect their interaction with the last resort antimicrobial polymyxin B and how does this relate to its known *in vivo* effects?
- How does colicin N bind selectively bind to the core oligosaccharide of LPS and what is the basis of this specificity?
- Is it possible to increase the complexity of existing OM models to achieve a more realistic replica of the OM by (i) including smooth LPS in asymmetric floating OM models and (ii) creating a platform which displays both OmpF and LPS in an oriented manner?

2 MATERIALS AND METHODS

2.1 MATERIALS

Most of the chemicals used in the work for this thesis were sourced from Sigma-Aldrich (UK) or Melford (UK) unless otherwise stated. Chemicals obtained from different suppliers are listed in **Table 2.1**

Table 2.1 | List of specialist chemicals and suppliers

Chemical	Supplier
Tail deuterated 1,2-dipalmitoyl(d62)-sn-glycero-3-phospohocholine (d_{62}DPPC)	Avanti Polar Lipids (USA)
1,2-Dipalmitoyl-sn-Glycero-3-Phosphothioethanol (DPPTE)	Avanti Polar Lipids (USA)
Octyl β-D-glucopyranoside (OG)	Anatrace (USA)
Deuterated octadecyltrichlorosilane (dOTS)	Kind gift of Dr. Peixun Li (STFC, UK) and Prof R. K. Thomas (Univ. of Oxford, UK)
N-(2-Hydroxyethyl)-16-mercaptohexadecanamide	Kind gift of Dr. Martynas Gavutis (Centre for Physical Sciences and Technology, LTU)
Silver staining Kit	Bio Rad (UK)
Chelex-100 resin	Bio Rad (UK)
Phusion polymerase	NEB (UK)
T4 polymerase	NEB (UK)

2.2 MICROBIOLOGY

2.2.1 Bacterial strains

The *E. coli* strains used throughout this thesis are listed in table 2.2 together with their source and use in the experiments

Table 2.2 | List of bacterial strains

Strain	Genotype	Use
E. coli TURBO (NEB, UK)	F' $proA^{+}B^{+}$ $lacI^{q}$ ΔlacZM15 / fhuA2 Δ(lac proAB) glnV galK16 galE15 R(zgb-210::Tn10)Tet^{S} endA1 thi-1 Δ(hsdS-mcrB)5	ColN WT and mutants transformation
E. coli BL21-AI (Invitrogen, UK)	F- *ompT* $hsdS_B$ ($r_B^- m_B^-$) gal dcm araB::T7RNAP-tetA	ColN WT and mutants expression
E. coli BE3000 (kind gift of J. Rosenbusch)	$OmpA^-$ (BZB6/3)	Liquid culture survival assay
E. coli BZB 1107 (kind gift of J. Rosenbusch)	OmpF::Tn5 (Kan^r)	OmpF E183C expression
E. coli K-12 BW25113 (kind gift of A. Egan)	rrnB3 ΔlacZ4787 hsdR514 Δ(araBAD)567 Δ(rhaBAD)568 rph-1	Deuterated LPS production

2.2.2 Media

For standard protein production the media was Lysogeny Broth (LB) which consists of 10 g/L tryptone, 5 g/L granulated yeast extract and 10 g/L NaCl. LB agar plates were obtained by mixing LB with 20g/L agar. Media and plates were sterilised by autoclaving before use. Filter sterilised ampicillin solution was added to a final concentration of 0.1 mg/ml

For deuterated LPS production the media was prepared according to (Meilleur *et al.*, 2009) with the final composition shown in **table 2.3.** The media prepared in deuterium oxide (D_2O) was sterilised by filtration and no antibiotic was added to the media.

Table 2.3 | Recipe of minimal media for the production of deuterium labelled rough LPS

Component	Concentration (g/L)	Concentration (molarity)
$(NH_4)_2SO_4$	6.86 g/L	52 mM
KH2PO4	1.56 g/L	11 mM
Na2HPO4	6.48 g/L	46 mM
$(NH_4)_2$-H-citrate	0.49 g/L	2 mM
MgSO4	0.25 g/L	2 mM
Glycerol	20.0 g/L	217 mM
Trace metal solution*	1.0 ml/L	

*Trace metal solution: 0.5 g/L $CaCl_2.2H_2O$, 16.7 g/L $FeCl_3.6H_2O$, 0.18 g/L $ZnSO_4.7H_2O$, 0.16 g/L $CuSO_4.5H_2O$, 0.15g/L $MnSO_4.4H_2O$, 0.18 g/L $CoCl_2.6H_2O$, 20.1 g/L EDTA

2.2.3 Transformation

E. coli cells were transformed by heat shock. 100 µl of competent cells were incubated on ice for 30 minutes in the presence of 3 µl of DNA. The cells were heated to 42°C for 1 minute and placed on ice for 5 minutes. 500 µl of SOC media (NEB) were added and the cells incubated at 37°C for 45 minutes with shaking. 400 µl of cells were then spread on an agar plate containing 0.1 mg/ml ampicillin and incubated at 37°C overnight. A single colony was grown in 5 ml LB overnight and the culture was divided in 200 µl aliquots in Eppendorf tubes and diluted 1:1 with 60% glycerol. The tubes were flash frozen in liquid nitrogen and stored in a -80°C freezer.

2.2.4 Large scale protein expression

Transformed *E. coli* cells were streaked on a LB agar plate containing 0.1 mg/ml ampicillin and incubated overnight at 37°C. A single colony was grown overnight in 5ml LB and used to inoculate 2x250 ml flask containing 50 ml LB and grown overnight at 37°C in an orbital shaker at 180 rpm. The cultures were harvested by centrifugation at 2350xg and resuspended in 6 ml of fresh LB media. 6x2 L sterilised baffled flasks containing 750 ml of LB media and 0.1 mg/ml ampicillin were inoculated with 1 ml of the resuspended cells and grown at 37°C in the orbital shaker (when growing OmpF E183C the media was supplemented with 0.5% (w:v) glucose to repress expression of the maltoporin LamB). Once the OD_{600nm} reached 0.8, protein expression was induced by adding IPTG to a final concentration of 1 mM for pMS119 expression and arabinose to a final concentration of 0.2% (w:v) for pET3a. The cells were then grown for 2 h reaching an OD_{600nm} between 2 and 2.5. Samples of the cultures were taken every 30 min to monitor protein expression by SDS PAGE. Cells were harvested by centrifugation at 6000xg for 8 minutes at 4°C.

2.2.5 Liquid culture survival assay for ColN mutants

5 ml of sterile LB medium were inoculated with a single colony of *E. coli* BE3000 and grown at 37°C overnight in an orbital shaker at 180 rpm. 1 ml of the starter culture was used to inoculate 50 ml of LB medium which was grown under the same conditions until it reached an OD_{600nm} of 0.5. The culture was then mixed 1:1 with a cold solution containing 10 mM sodium phosphate pH 7.0 and 300 mM NaCl and left on ice for 30 min to halt bacterial growth. 75 µl of ColN WT and mutants dissolved in sterile LB media were aliquoted in a 96-well plate (COSTAR) to give a final concentration of protein of 10 nM. 75 µl of *E. coli*

BE3000 suspension were added to the 96-well plate using a multichannel pipette and the plate was incubated at 37°C for 30 min in a FLUOstar Optima plate reader (BMG Labtech) shaking at 180 rpm to allow for cell killing. The content of each well was then diluted 1:100 by 2x1:10 sequential dilutions performed with a multichannel pipette by transferring 15 µl of cell suspension into 135 µl of fresh LB and then 15 µl of the diluted cells into a second well containing 135 µl of fresh LB. The final plate containing the diluted solution of ColN treated cells was incubated for 23 h at 37°C and the growth monitored by recording the OD_{600nm} over time. The lag phase elapsed before the rise in OD_{600nm} was taken as a relative measure of the toxicity of ColN.

2.3 GENERAL AND BIOCHEMICAL PROTOCOLS

2.3.1 Size exclusion chromatography (SEC)

Size exclusion chromatography was performed on an ÄKTA purification system (GE Healthcare). A ProteoSec 16/60 3-70 column (Generon) was equilibrated with 2 column volumes (CV) of running buffer containing 0.25% (w/v) deoxycholate, 200 mM NaCl, 1 mM EDTA, 10 mM Tris-HCl pH 8.2 at a flow rate of 1 ml/min. 50 mg of smooth LPS from *E. coli* O111:B4 (Sigma Aldrich) were dissolved in 1 ml of running buffer and vortexed and bath sonicated until the LPS was fully dissolved. The sample was loaded in a 2 ml capillary loop previously filled with the running buffer and eluted with 1.5 CV of the same buffer at a flow rate of 0.2 ml/min. 1 ml fractions were collected in 96 well plates. Detection of LPS in the eluted fraction was done by DOC PAGE analysis followed by silver staining.

2.3.2 Sodium dodecylsulphate polyacrylamide gel electrophoresis (SDS PAGE)

Analysis of proteins by SDS-PAGE followed the standard protocol based on a two-part discontinuous acrylamide gel described by Laemmli (Laemmli, 1970). The resolving (lower) gel contained a buffer made of 375 mM Tris-HCl pH 8.8, 0.1% (w/v) SDS and 12% (v/v) acrylamide. 10% ammonium persulphate and tetramethylethylenediamine (TEMED) were added to catalyse the polymerisation reaction and a layer of water saturated butanol was applied to the top of the solution contained in the glass cast to obtain a defect free interface. Once the lower gel had set the butanol layer was rinsed away and the stacking gel was applied. This contained a buffer made of 125 mM Tris-HCl pH 6.8, 0.1% (w/v) SDS and 4% (v/v) acrylamide and was polymerised the same way as the lower gel after a comb was inserted in the gel. 10 µl of sample were mixed 1:1 with a loading dye containing 15% (v/v)

glycerol 125 mM Tris-HCl, 2% (v/v) SDS 0.1% (w/v) bromophenol blue, 1% (v/v) mercaptoethanol pH 6.8. 10-20 µl of sample-dye mix were loaded into the wells of the loading gel. The SDS PAGE was resolved using 180 V current in a buffer containing 25 mM Tris-HCl, 192 mM glycine, 0.1% (w/v) SDS pH 8.0 in a mini PROTEAN tetra cell (Bio-Rad) and protein band were visualised by Coomassie staining.

2.3.2.1 Deoxycholate polyacrylamide gel electrophoresis (DOC PAGE)

DOC PAGE was used to separate LPS and was performed following the protocol described for SDS PAGE with the following modifications: The stacking and resolving gels contained 7% and 15% acrylamide respectively and SDS was replaced by 0.25% deoxycholate (DOC) in the gel preparation and in the running buffer (Guard-Petter *et al.*, 1995). LPS was visualised using silver staining

2.3.2.2 Coomassie staining

The protein gels were stained using Coomassie staining. The gel was immersed in a staining solution containing 0.05% (w/v) Coomassie brilliant blue 10% (v/v) glacial acetic acid, 10% (v/v) propan-2-ol, microwaved for 30 seconds and left to incubate for 15 min. The gel was destained in 10% (v/v) glacial acetic acid and 10% (v/v) propan-2-ol until the bands developed. The protein MW was determined by comparison with a standard protein marker (Precision plus dual colour protein standard from Bio-Rad). Gels were imaged on a Gel Doc XR+ (Bio-Rad)

2.3.2.3 Silver staining

The LPS gels were stained using a silver stain kit (Bio-Rad) according to the manufacturer protocol with some modifications. Briefly, once the gel was run, it was left overnight in 100 ml of a solution containing 50 ml of MeOH, 30 ml of deionised water, 10 ml of glacial acetic acid and 10 ml of the fixative enhancer provided in the kit. After the overnight incubation, the gel was thoroughly rinsed with deionised water and incubated with a spatula of Chelex-100 resin for 20 minutes. The staining solution was prepared by mixing 0.625 g of the development accelerator reagent in 12.5 ml of distilled water and, separately, 8.75 ml of distilled water with 1.25 ml of silver stain complex reagent, 1.25 ml of reduction moderator solution and 1.25 ml of image development reagent. Before staining the gel, the Chelex-100 resin was removed, and the gel thoroughly rinsed with deionised water. The development accelerator solution was mixed with the remaining staining solution just before adding the mix to the gel which was left rocking until the bands developed. The staining was stopped

by adding 5% acetic acid to the staining solution before the background developed a dark colour. Gels were imaged on a Gel Doc XR+ (Bio-Rad)

2.3.3 Thin layer chromatography (TLC)

TLC analysis of hydrogenous and deuterated lipid A and RaLPS species was performed on silica coated plates (Sigma Aldrich) and eluted with a mobile phase containing $CHCl_3$, MeOH, H_2O 60:39:1 (v:v:v) Lipid A was obtained from hydrogenous and deuterated RaLPS by mild acid hydrolysis as described by Henderson *et al* (Henderson *et al.*, 2013). 15 µl of a $CHCl_3$ 1 mg/ml solution of lipid A were spotted with a glass capillary on the silica plate whilst the same amount of RaLPS was spotted from a $CHCl_3$, MeOH, H_2O 60:39:1 (v:v:v). The spots were dried under a stream of air and the plate placed in the TLC tank equilibrated with the mobile phase vapours until the solvent front reached a distance of 1 cm from the top of the plate. The plate was dried in the fume hood and immersed in a 10% ethanolic solution of H_2SO_4 for 1 minute, then dried and charred using a Bunsen burner until the spots developed.

2.3.4 UV spectrophotometry of proteins and DNA

Protein and nucleic acid absorbance were measured using a nanodrop ND-1000 (Labtech) at 260 nm (DNA) and 280 nm (proteins) after blanking the instrument with the buffer in which the samples were dissolved. The concentration of the species in solution was obtained using the Lambert-Beer law, which relates the attenuation of light at a certain wavelength to the properties of the solution which the light is travelling through by:

$$A = \epsilon c l \tag{2.1}$$

Where A is the measured absorbance, ε is the molar extinction coefficient ($M^{-1}cm^{-1}$), c is the concentration of protein (M) and l is the path length (cm). **Table 2.4** shows the extinction coefficient of OmpF E183C and colicin N which were used in this study

Table 2.4 | Molecular weight and extinction coefficient of proteins used in this study

Protein	Molecular Weight (kDa)	Extinction coefficient at 280 nm ($M^{-1}cm^{-1}$)
OmpF (E183C)	37.2	54210
Colicin N	42.7	49500

2.3.5 Lipopolysaccharide vesicles preparation

Rough LPS (Ra or Rd) was suspended in a small volume (<1 ml) of $CHCl_3$, MeOH, H_2O 60:39:1 (v:v:v) solution in a flat-bottom glass vial. The suspension was repeatedly vortexed and bath sonicated at 50°C until no large aggregates were visible. The solution was evaporated under a stream of dry nitrogen to create a lipid cake which was left under vacuum overnight to eliminate any trace of solvent. The dry lipid cakes were then resuspended at 1 mg/ml in a buffer containing 5 mM $CaCl_2$, 20 mM HEPES pH 7.4 buffer unless otherwise specified, and bath sonicated until the lipid cake was completely suspended. The suspension was then transferred to a 15 ml falcon tube and tip sonicated at an amplitude of 80% until the suspension became clear. The tube was then centrifuged at 2350xg for 10 minutes to eliminate metal nanoparticles detached from the sonicator's tip and the vesicles transferred to a clean falcon tube.

2.3.6 Assessment of protein secondary structure by Circular Dichroism (CD)

Protein samples for CD analysis were exchanged into 20 mM phosphate buffer pH 7.0 using a Sephadex G25 PD-10 desalting column (GE Healthcare) and transferred into a 0.2 mm quartz cuvette (Hellma) at a final concentration of 0.5 mg/ml. CD spectra were collected on a JASCO J-810 spectropolarimeter (JASCO) between 250 and 185 nm at a speed of 2 nm/min, with a bandwidth of 2 nm, a response time of four 4 s and a data pitch of 0.2 nm. Six spectra were collected for each protein sample, averaged and corrected by subtracting the background from a 20 mM phosphate buffer blank solution. The CD signal was converted to molar differential extinction coefficient $\Delta\varepsilon$ ($M^{-1}cm^{-1}$) to account for differences in protein concentration.

2.3.6.1 Thermal stability by CD

Protein samples at a concentration of 0.1 mg/ml in a buffer containing 50 mM sodium phosphate pH 7.0 and 300 mM NaCl were loaded in a 1 mm path length quartz cuvette (Hellma). The CD signal was measured at 222 nm while heating the solution at 2°C per minute between 25°C and 95°C. The thermal transition temperature was obtained by the peak maxima of the first order derivative of the intensity signal as a function of temperature.

2.4 MOLECULAR BIOLOGY

Colicin N (ColN) mutants were produced via sequence and ligation independent cloning (SLIC) (Jeong *et al.*, 2012) besides the ColN^{6A} mutant which was produced in a previous study. The ColN gene was previously synthesised and subcloned into vector pET3a (Novagen) by GeneArt (Regensburg, Germany) (Johnson *et al.*, 2014). The ColN gene contained a C-terminal hexahystidine –SSHHHHHH tag to allow for its purification by immobilised metal affinity chromatography (IMAC) and its immobilisation on NTA functionalised gold surfaces for surface plasmon resonance experiments.

2.4.1 Inverse polymerase chain reaction (PCR) and vector isolation

Oligonucleotide primers designed to introduce mutations in the ColN gene (GenBank accession number HM449003) were synthesised by Eurofins (**Table 2.5**). A description of the mutants is given in **Table 4.4**. Mutants were designed by using the Serial Cloner software (Perez, 2004). The optimal annealing temperature for each set of primers (**Table 2.5**) was determined by performing a gradient PCR on 10 µl of PCR reaction mix (**Table 2.6**) following the steps described in **Table 2.7**. The preparative PCR was performed on 2x20 µl of PCR reaction mix at the annealing temperature determined by gradient PCR.

Table 2.5 | Forward and reverse primers used to introduce mutations in the ColN gene

In lower case letters, the complementary 15 bp sequence that forms the overhangs required for the final circularisation of the vector. Nucleotide sequences are shown 5' to 3'

Mutant	Forward primer	Reverse primer	Annealing temperature
K171E	ccgaaatataacaatgaaCTTGTGAA GAGGTTTGTGAGC	ATTGTTATATTT CGGTCCCTTCC	62°C
K167E	aactggaagggaccggaaTATAACA ATAAACTTGTGAAGAGG	CGGTCCCTTCC AGTTCAC	70°C
K164E	gattatgtgaactgggaaGGACCGAA ATATAACAATAAACTTG	CCAGTTCACAT AATCAACTCTC	62°C
$ColN^{3A}$	tgggcaggaccggcaTATAACAAT GCACTTGTGAAGAGGTTTG TGAGC	tgccggtcctgcccaG TTCACATAATC AACTCTC	62°C
$ColN^{3E}$	tgggagggaccggagTATAACAAT GAGCTTGTGAAGAGGTTTG TGAGC	ctccggtccctcccaGT TCACATAATCA ACTCTC	67°C
$ColN^{\Delta 6}$	agagttgattatgtgTATAACAATAA ACTTGTGAAGAGGTTTGTG	CACATAATCAA CTCTCATTTTAT CAATATTAC	67°C

Table 2.6 | Components in the PCR mix

The primer mix contains equal amounts of the forward and reverse primer

Component	Volume (µl)
Nanopure water	55
GC buffer (5x)	20
Primer mix (10 µM)	10
dNTP nucleotide mix (2 mM)	10
DMSO	3
ColN pET3a plasmid (10 ng/µl)	1
Phusion polymerase (2 ng/µl)	1
	Tot: 100

Table 2.7 | PCR conditions

For gradient PCR the annealing temperatures tested were 50.0°C, 57.5°C, 62.0°C, 65.9°C and 70.0°C

PCR step	Temperature (°C)	Time	N° of cycles
Denaturation	98	3 min	1
Denaturation	98	10 s	35
Annealing	For gradient PCR see legend	30 s	
	For prep PCR see Table 2.5		
Elongation	72	150 s	
Elongation	72	10 min	1
Cooling	4	infinite	-

PCR product were separated by electrophoresis on a 0.8% agarose gel containing 1 µg/ml ethidium bromide and the band corresponding to the desired PCR product, visualised under UV light, were excised from the gel with a scalpel. The linear vector was extracted from the gel with a Monarch DNA gel extraction kit (NEB) according to the protocol provided by the manufacturer.

2.4.2 Sequence and ligation independent cloning (SLIC) reaction and plasmid preparation

1-5 µl of the extracted DNA were incubated with 1 µl of NEB buffer 2.1 (10x) (NEB) and diluted with water at a concentration of 10 ng/ml. 0.5 µl of T4 polymerase were added to the mix and incubated at room temperature for 2.5 min. The mixture was then placed on ice to halt the SLIC reaction. *E. coli* TURBO cells were transformed with the SLIC reaction mixture as described in section 2.2.3. A single colony of transformed cells was grown in 5 ml of LB containing 0.1 mg/ml ampicillin overnight and the plasmid was extracted using the Monarch Plasmid Miniprep kit (NEB) according to the manufacturer instructions.

2.4.3 Sequence analysis

Plasmids were sent for Sanger sequencing at GATC Biotech and the results aligned using Serial Cloner.

2.5 PROTEIN AND LIPOPOLYSACCHARIDE PURIFICATION

2.5.1 Deuterated RaLPS production and purification

Cell growth

E. coli K12 BW25113 was used to extract LPS as it produces rough LPS with a complete core oligosaccharide region. Deuteration of cells was carried out as described by Meilleur *et al* (Meilleur *et al.*, 2009) with some modifications. The recipe of the minimal used is listed in **Table 2.3**. Cells were first adapted to grow in the presence of deuterium oxide (D_2O) by initially inoculating a single colony of cells grown on Agar into 5 ml minimal media made containing 25% D_2O and 75%H_2O (v:v). After an overnight growth at 37°C, 0.1 ml of culture was used to inoculate a minimal media solution made with 50% H_2O and 50% D_2O and the cells were grown overnight. The process was iterated by successively inoculating the resulting cultures in media containing 75%, 90%, and 98% D_2O over the course of 3 days. 3x250 ml flasks containing 50 ml of minimal media made with 98% D_2O were then inoculated with 1 ml of the 98% D_2O-adapted cells and grown overnight. The cultures were harvested by centrifugation at 2350xg at room temperature, resuspended in 10 ml of fresh 98% D_2O minimal media and used to inoculate a 1.5-litre Minifors1 fermentation vessel (INFORS) containing 1 L of 98% D_2O minimal media at 37°C. The fermenter was set in cascade mode to maintain a fixed pO_2 of 40% by adapting the stirring speed between 200 and 1000 rpm. The pH was not controlled. Cell growth was monitored by measuring the OD_{600nm} in a UV-spectrophotometer (Shimadzu) until it reached at least 10.0. The cells were then harvested by centrifugation at 8000xg for 10 min at 4°C. The cell pellet was then washed twice with Nanopure water and freeze dried until all the water was removed.

LPS extraction

Rough LPS was extracted following the method by Galanos *et al* (Galanos *et al.*, 1969). The freeze-dried cell pellets were gently homogenised in phenol/$CHCl_3$/petroleum ether 2:5:8 (v:v:v) (PCP) using 10 ml for every gram of dry cells for three hours with gentle stirring. To prepare the PCP solvent, $CHCl_3$ was mixed with a solution of $CHCl_3$, phenol, isoamyl alcohol 49.5:49.5:1 (v:v:v) and petroleum ether (boiling point (40-60°C). The cell suspension was centrifuged in glass tubes at 2350xg for 15 minutes. The supernatant was kept and the pellet re-homogenized in the organic mixture for three more hours. The supernatant from each extraction was pooled and vacuum filtered using coarse filter paper.

The filtered solution was then transferred to a glass round bottom flask and the chloroform and petroleum ether removed by rotary evaporation at 55°C for 1 h. LPS was precipitated out of the remaining phenol solution by dropwise adding a 1:1 solution of diethyl ether and acetone (v:v) until a white precipitate formed. The solution was left overnight at room temperature to allow for complete precipitation. The precipitate was centrifuged a 2350xg for 15 min and washed three times with water saturated phenol equilibrated in a separating funnel to avoid excess water, followed by three washes of diethyl ether to remove traces of phenol. The obtained white pellet was dried under a stream of air and used with no further purification.

2.5.2 E183C OmpF (^{cys}OmpF) purification

E. coli BZB1107 cells were transformed with the pMS119 plasmid containing the OmpF E183C gene (Terrettaz *et al.*, 2002; Cisneros *et al.*, 2006) as described in section 2.2.3 and ^{cys}OmpF was expressed as described in section 2.2.4. Harvested cells were resuspended in 30 ml of 20 mM sodium phosphate buffer (pH 6.8) containing 2 mM dithiothreitol (DTT) and supplemented with 2 mg of DNAse, 2 mg of RNAse and a 1:1000 dilution of a stock solution of protease inhibitor cocktail (**Table 2.8**). The cells were disrupted in a One Shot (Constant Systems) at 20 Kpsi and the cell debris was removed by centrifugation at 2350xg for 15 min. The supernatant was centrifuged at 118000xg using a 45-Ti rotor in a Beckman L7-80 centrifuge to sediment the membrane pellet containing the protein. The supernatant was discarded and the membrane pellet was resuspended in wash buffer (20 mM TRIS, 2% SDS (w:v), 2 mM DTT pH7.4) and homogenised at 55°C for 1 h to eliminate components loosely associated with the pellets. The solution was centrifuged again as described above at 118000xg, the supernatant was discarded, and the pellets washed a second time by homogenising at 55°C for 1 h in wash buffer. Membrane pellets were isolated again by centrifugation at 118000xg and ^{cys}OmpF was extracted from the pellets by homogenising for 1 h at 45°C in wash buffer supplemented with 500 mM NaCl. The centrifugation step was repeated, and the supernatant was collected whilst the membrane pellets extracted a second time to increase the protein yield. The supernatants from the two extractions were pooled and dialysed against 5 mM $NaHCO_3$, 0.1% SDS (w:v), 2mM DTT pH 7.4 overnight at 37°C. ^{cys}OmpF was precipitated from the solution by adding ethanol pre chilled at -80°C to a final concentration of 90% and incubating at -20°C overnight. The precipitated protein was centrifuged at 17000xg for 1h and dried under a stream of air. The protein was finally resuspended in 20 mM Tris 300 mM NaCl 1% Octylglucoside.

Table 2.8 | 1000x protein inhibitor cocktail

Component	Concentration (mg/ml)
4-(2-aminoethyl)-benzenesulphonylfluoride	100
Aprotinin	0.5
Benzamidine	1
Pepstatine	1
Leupeptine	1

2.5.3 Colicin N mutants purification

E. coli BL21-AI cells were transformed with the plasmid pET3a carrying either ColN WT or a mutant, as described in section 2.2.3 and the protein was expressed as described in section 2.2.4. Harvested cells were resuspended in loading buffer (50 mM sodium phosphate, 300 mM NaCl, pH 7.0) supplemented with 2 mg/ml DNAse, 2 mg/ml RNAse, a 1:1000 dilution of the protease inhibitor cocktail and then disrupted in a One Shot at 20 Kpsi. Lysed cells were centrifuged at 17000xg at 4°C and the supernatant was loaded onto a column containing 3 ml of Ni-NTA affinity resin (Novagen) pre equilibrated with 15 ml of loading buffer. The column was washed with 15 ml of the same buffer and then with 30 ml of loading buffer supplemented with 25 mM imidazole. The protein was eluted with loading buffer supplemented with 350 mM imidazole and analysed by SDS PAGE. All the purification steps were performed at 4°C and proteins were stored on ice at 4°C

2.6 PREPARATION OF MODEL MEMBRANES FOR NR AND ATR-FTIR

2.6.1 Substrates for membrane assembly

Bare silicon crystals for neutron reflectometry (NR) and attenuated total internal reflection Fourier transform infrared spectroscopy (ATR-FTIR) were obtained from Crystran (UK). NR substrates were rectangular silicon wafers, 8x5x1.5 cm, polished on a single major face to a root mean squared (rms) roughness <3 Å and with a curvature <1 μm (**Fig 2.1**). For ATR-FTIR the crystals were trapezoidal with four out of six faces (those traversed by or reflecting the infrared beam) polished to a rms roughness of <3 Å (shown in **Figue 2.3** and **2.3**).

Gold substrates for NR were obtained by sequentially sputtering on a 5x8x1.5 cm silicon crystal a binding layer of permalloy (Ni:Fe 4:1) and a layer of gold. The thickness of the layers was between 130-150 Å and the substrates were prepared by Dr. Frank Heinrich at the National Institute of Standards and Technology (NIST) as described in (Hughes *et al.*, 2014).

2.6.2 Surface cleaning

Gold

Gold surfaces for NR were cleaned by UV/ozone treatment for 20 minutes, followed by rinsing with nanopure water and drying under a nitrogen stream. The process was repeated twice just before the surfaces were used for the sample preparation steps.

Silicon

Silicon surfaces used for NR and ATR-FTIR were cleaned using piranha solution made of H_2SO_4, 30% H_2O_2, H_2O (4:1:5). The crystals were immersed in a glass beaker filled with piranha solution and heated to 90°C for 30 minutes. The surfaces were then thoroughly rinsed with Nanopure water and dried under a nitrogen stream. Before the sample preparation step, the surfaces were further exposed to a 20 min cycle of UV/ozone cleaning, rinsed with Nanopure water, and the cleanliness of the surface was assessed by visual inspection of the water drainage from the polished face (**Fig 2.1**)

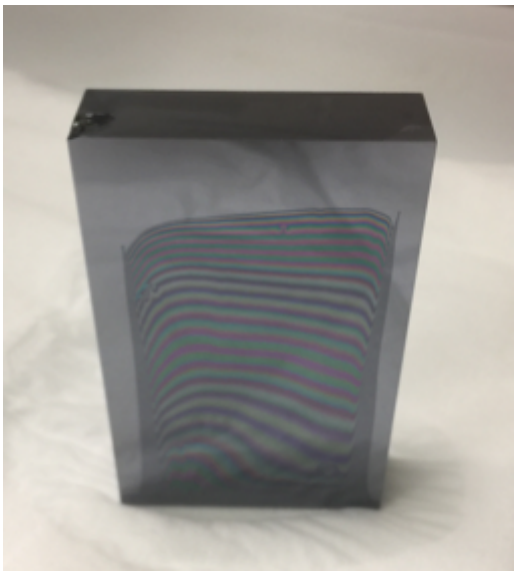

Figure 2.1 | Water drainage on a clean surface from a NR silicon substrate

The coloured fringes are due to the thin film interference of light from the water layer draining from the surface. Uniform draining is an indicator of a clean and defect-free hydrophilic surface.

2.6.3 Deposition of self-assembled monolayers (SAM)

Octadecyltrichlorosilane (OTS) on silicon crystals for ATR-FTIR and NR

Octadecyltrichlorosilane (OTS) monolayers (hydrogenous or deuterated) were deposited on silicon wafers for NR and ATR-FTIR experiments. A spatula of $MgSO_4$ was added to 500 ml of hexane to eliminate any residual water and a solution of 1 mM OTS was prepared with the dry hexane in a beaker. Clean silicon substrates were completely immersed in the hexane solution which was placed in a desiccator for 1 h. As the silicon substrates were extracted from the hexane solution, fresh hexane was poured on the surface to wash away residual OTS and avoid formation of patches on the surface. The coated silicon wafers were dried and stored under nitrogen. Successful deposition of a hydrophobic monolayer was assessed by visual inspection of the contact angle (**Fig 2.2**)

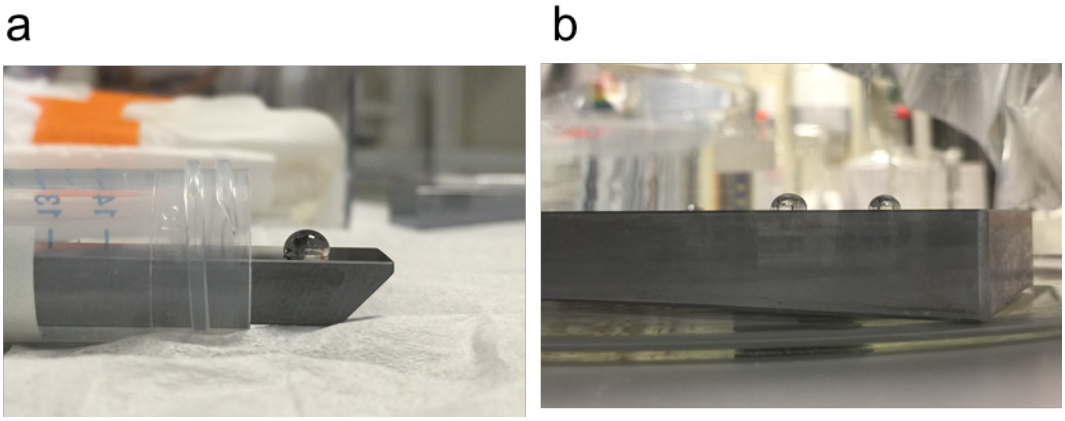

Figure 2.2 | Silicon substrates after deposition of an OTS monolayer

(**a**) Silicon substrate for ATR-FTIR experiments and (**b**) silicon substrate for NR experiments. The high contact angle of the water droplet on the surface

N-(2-Hydroxyethyl)-16-mercaptohexadecanamide (C16NEtOH) on gold coated silicon crystals for NR

N-(2-Hydroxyethyl)-16-mercaptohexadecanamide (C16NEtOH) monolayers were deposited on gold substrates for NR experiments by incubating clean substrates in a 50 µM ethanolic solution of the thiols. Substrates were left incubating for at least 24 h in the dark to ensure complete adsorption. The gold surface was then thoroughly rinsed with ethanol and dried under a nitrogen stream.

2.6.4 Langmuir-Blodgett (LB) and Langmuir-Schaefer (LS) deposition of asymmetric phospholipid/LPS bilayers

Asymmetric phospholipid-LPS bilayers were deposited via Langmuir-Blodgett (LB) and Langmuir-Schaefer (LS) deposition as described previously (Clifton *et al.*, 2013b; Clifton *et al.*, 2015a; Clifton *et al.*, 2015b) (**Fig 2.3**). Asymmetric bilayers were deposited on three types of substrates:

For NR

- Bare silicon crystals were used to create silicon supported asymmetric bilayers
- Gold coated silicon crystals functionalised with a C16NEtOH monolayer were used to create floating bilayers

And for ATR-FTIR

- Trapezoidal ATR silicon crystals were used to create silicon supported asymmetric bilayers

In all cases the procedure was identical, differing only in the substrate used and, therefore, the type of solid liquid cell required for housing the substrate.

For the LB deposition, the Langmuir trough (NIMA, UK) was filled with Nanopure water and the air/water interface cleaned by aspirating the water surface with a nozzle connected to a vacuum pump. The substrate for the deposition was attached to an automated dipping arm through a holder and submerged in the central well of the trough with its polished face perpendicular to the water surface. The water surface was cleaned again, and a monolayer of tail deuterated 1,2-dipalmitoyl-sn-glycero-3-phosphocholine (d_{62}DPPC) was spread on the water surface from a 2 mg/ml $CHCl_3$ solution using a Hamilton syringe. The $CHCl_3$ was left to evaporate for 15 min and the monolayer was subject to two compression decompression cycles between 0 and 38 mN/m, using the movable barriers of the trough to assess monolayer stability. The monolayer was then compressed to 37 mN/m and the LB was performed by lifting the silicon substrate through the interface at a speed of 2 mm/min whist the surface pressure was held constant at 37 mN/m (**Fig 2.3a**). Once completely emerged, the substrate was stored under a clean glass beaker.

For the LS deposition of the LPS leaflet, the trough was cleaned, and a solid-liquid cell was placed in the well of the trough, to receive and house the substrate. The trough was cooled

to 10°C using a water bath and filled with pre chilled Nanopure water, containing 5 mM $CaCl_2$. Rough LPS monolayers were spread on the surface from a 1 mg/ml suspension in $CHCl_3$, MeOH, H_2O 60:39:1 (v:v:v) whilst smooth LPS was spread from a 1 mg/ml phenol, $CHCl_3$, petroleum ether (PCP) 2:5:8 (v:v:v) solution using a Hamilton syringe. The solutions were left to evaporate for 15 min and the LPS monolayer was subject to two compression decompression cycles between 0 and 38 mN/m to assess its stability. The substrate was placed in the holder with its polished face parallel to the water surface and aligned to the air-water interface using a custom built Level'O'Matic laser system (this was not possible for the ATR crystal which was aligned manually). The LPS monolayer was compressed to 37 mN/m and the LS deposition was performed by lowering the substrate onto the monolayer and through the water interface into the solid liquid cell placed at the bottom of the trough at a speed of 2 mm/min (**Fig 2.3 b**).

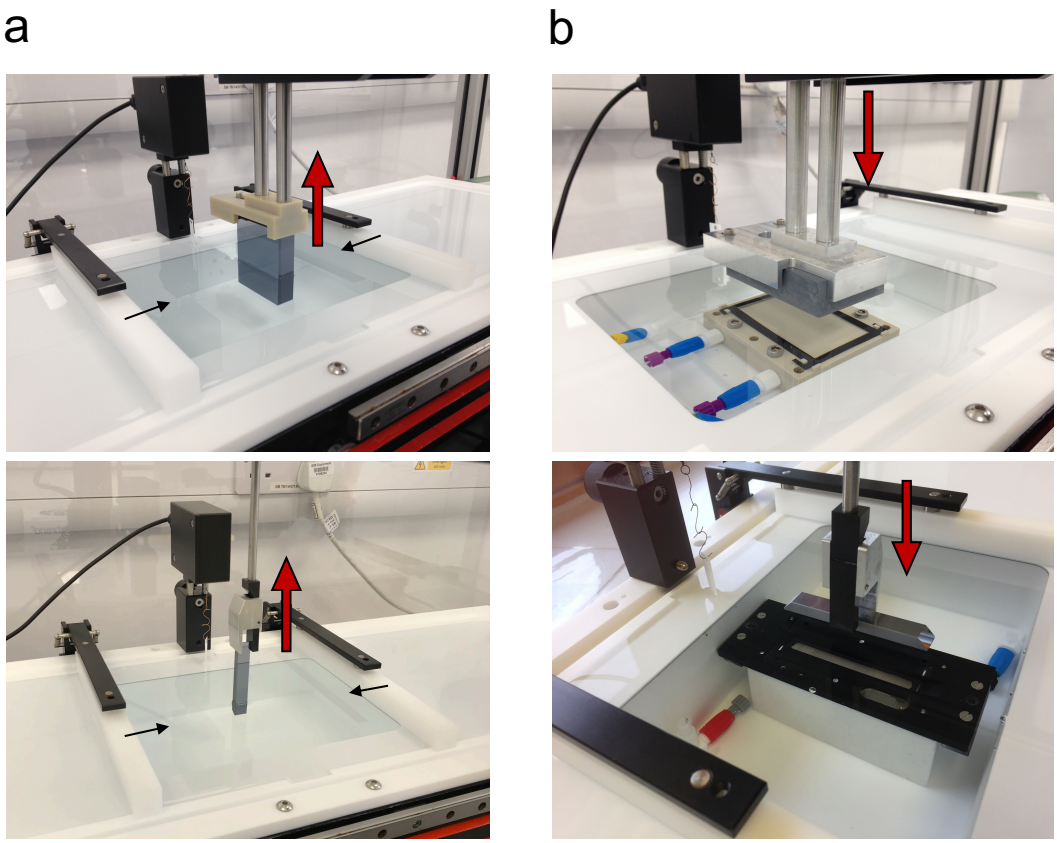

Figure 2.3 | LB and LS deposition of asymmetric phospholipid/LPS bilayers

(**a**) LB deposition on a NR substrate (top) and an ATR-FTIR substrate (bottom). Red arrows indicate the direction of motion of the dipping arm whilst black arrows indicate the direction of the movable barriers. As the monolayer is transferred onto the substrate, the barriers maintain a constant lateral pressure on the monolayer. (**b**) LS deposition on a NR substrate (top) and an ATR-FTIR substrate (bottom).

Once the substrates were housed in the respective solid-liquid cells, these were sealed under water by attaching the rear part of the cell with metal screws, yielding the final sample (see **Figure 2.4c** for an example of assembled NR solid-liquid cell).

2.6.5 Assembly of DPPTE-^{cys}OmpF OM model

Assembly of 1,2-dipalmitoyl-sn-glycero-3-phosphothioethanol (DPTTE)-^{cys}OmpF monolayers has been described by Holt *et al* (Holt *et al*., 2009) and repeated here with some modifications. A clean gold-coated silicon crystal was incubated in a 1 mM β-mercaptoethanol (BME) ethanolic solution for 1 h inside a clean glass dish. The substrate was then washed with pure ethanol and dried under a stream of nitrogen. The gold coated substrate was manually housed in a solid-liquid cell placed inside a glass dish filled with water to avoid trapping air in the cell and the cell sealed under water (**Fig 2.4**).

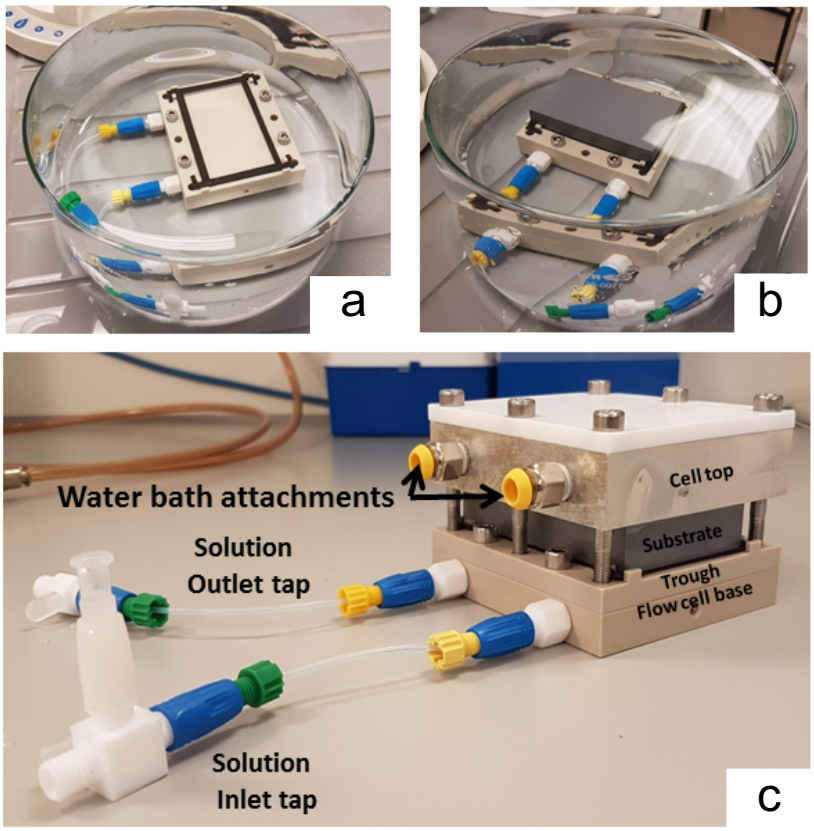

Figure 2.4 | Assembly of the NR solid-liquid cell

(**a**) Solid-liquid cell prepared inside a water-filled glass dish. (**b**) Housing of the gold coated silicon block. (**c**) Assembled cell.

The cell was flushed with a "rinse" buffer containing 300 mM NaCl, 1% OG, 50 mM TRIS pH 7.4 and the cell was connected to a water bath and heated to 37°C for the protein deposition. A solution of 0.3 mg/ml of ^{cys}OmpF in "deposition" buffer (rinse buffer

supplemented with 1 mM tris (2-carboxyethyl) phosphine hydrochloride (TCEP)) was injected in the cell via the inlet line with a syringe mounted on a syringe pump, at a speed of 1 ml/min.

The solution was collected from the outlet line using another syringe which was then used to re-inject the solution in the opposite direction to repeat the deposition and maximise the amount of immobilised protein. The cell was kept under bi-directional flow for 2 h, washed with rinse buffer and the protein deposition repeated for another extra hour. The cell was thus washed with rinse buffer and heated to 45°C for the DPPTE deposition. DPPTE 0.1 mg/ml in deposition buffer was injected following the same steps described for ^{cys}OmpF. After DPPTE deposition the temperature was returned to 37°C and kept stable for the rest of the experiment.

After the characterisation of the DPPTE-^{cys}OmpF monolayer, the substrate was incubated with 0.25 mg/ml of RaLPS vesicles made in 5 mM $CaCl_2$, 20 mM HEPES pH 7.4 for 8 hours to guarantee comprehensive adsorption. After NR characterisation of the DPPTE-^{cys}OmpF-RaLPS, the RaLPS monolayer was removed by thoroughly washing the cell with rinse buffer. The same procedure was adopted for the deposition of the deuterated RaLPS monolayer.

2.7 NEUTRON REFLECTOMETRY (NR)

All neutron reflectometry (NR) experiments were carried out at the ISIS Neutron and Muon source, (Oxford, UK) using the INTER (Webster *et al.*, 2006), OFFSPEC (Dalgliesh *et al.*, 2011), SURF (Penfold *et al.*, 1997), CRISP (Penfold *et al.*, 1987) and POLREF (Webster *et al.*, 2011) reflectometers.

2.7.1 Experimental setup

Figure 2.5 shows a picture of the experimental set up generally used in the NR experiments described here. Solid-liquid cells housing the silicon wafers were docked on the sample stage of the reflectometer using magnetic mounts. For polarised neutron reflectometry on POLREF, the magnetic mount was replaced with adhesive tape as the magnets would interfere with the magnetic field applied to the sample. A computer-controlled high-performance liquid chromatography (HPLC) pump (Hitachi) with four mixing lines was cleaned with ethanol and primed with the experimental buffer solutions which contained 20 mM HEPES pH/pD 7.4 and 5 mM Ca^{2+}, in addition to other components, where specified in

the text. Buffers were filtered and degassed by sonication at the beginning of each experiment. The HPLC pump was connected to the inlet line of the solid-liquid cell via a 6-channel switch (Knauer) (**Fig. 2.5a**) whilst the outlet lines of the cells were connected to a waste collection beaker (**Fig. 2.5b**). The temperature of the cell was controlled using a water bath (Julabo) connected via the heating and cooling dedicated lines (**Fig 2.5c**) and the temperature measured with a probe thermometer attached to the silicon substrate. For contrast changes, buffers with the same composition were made in H_2O and D_2O and the intermediate contrasts, such as silicon matched water (SMW) and gold matched water (AuMW) were obtained by using the HPLC pump to mix the solutions at the appropriate ratios. **Table 2.5** lists the composition and SLD of the solvents used for the isotopic contrast exchange. To ensure a complete solution exchange, between 15 and 18 ml of solution were pumped at a speed of 1 ml/min through the solid liquid cell, which has a capacity of 2 ml.

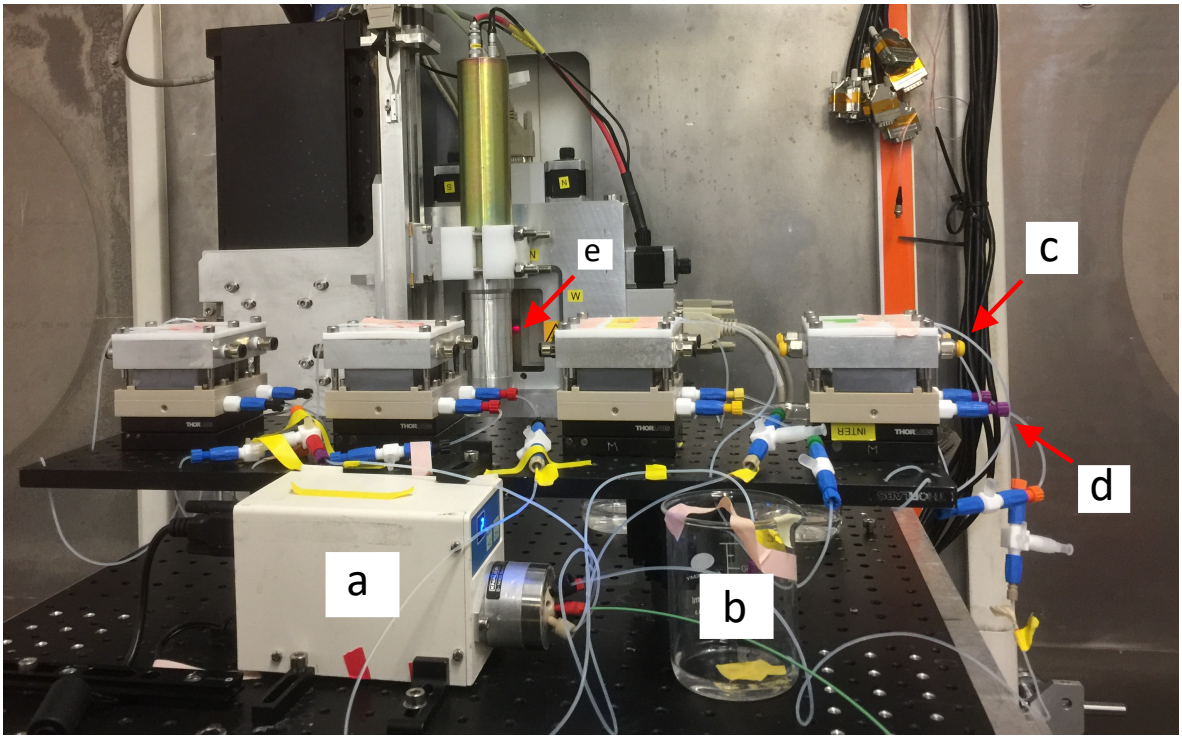

Figure 2.5 | Solid-liquid beamline set up.

(**a**) Computer-controlled 6-way switch enabling the selection of the target cell to which the HPLC pumps solution through. (**b**) Waste beaker collecting the waste solution from the cells. (**c**) Water bath connections for the temperature control of the cells. (**d**) Inlet and outlet lines for exchanging the solution in the cells. (**e**) Slit through which the incoming neutron beam emerges. The detector is situated behind the observer from this point of view.

Table 2.9 | SLD and composition of isotopic contrast solutions

Solvent	SLD ($Å^{-2}*10^{-6}$)
100% H_2O	-0.56
SMW (38% D_2O)	2.07
AuMW (75% D_2O)	4.66
100% D_2O	6.35

2.7.2 NR measurements

Before the start of the reflectivity experiments, a direct beam was measured in transmission mode through the silicon which was then subtracted from the reflectivity data to account for any absorption or scattering from the silicon crystal. As the neutron beam emerges from the source at a fixed angle, the samples were then aligned on the path of the beam so that the reflected neutrons would hit the detector by adjusting the sample stage height and tilt angles. Alignment was performed at the lowest angle used in the measurements and with the cell filled with the D_2O buffer to obtain the highest reflected intensity. Reflectivity measurements were performed at two angles on INTER (0.7°, 2.3°) and OFFSPEC (0.7° and 2.0°), three on SURF and CRISP (0.35°, 0.65° and 1.5°) and four angles were used on POLREF for polarise measurements (0.25°, 0.5°, 1.2°, 2.5°). These angles, combined with the distribution of neutron wavelengths on each instrument, yield a Q range between 0.012 and 0.3 $Å^{-1}$ which covers the range between the critical edge of total reflection at low Q and the background at high Q. The slits, which determine the shape of the beam, where automatically adjusted at each angle to keep the area illuminated by the beam constant.

Polarised neutron reflectometry

Polarised neutron reflectometry measurements were carried out on the POLREF beamline for magnetic contrast neutron reflectometry (MCNR) experiments (Holt *et al.*, 2009). For MCNR, samples were prepared on a substrate containing a magnetic layer of ferromagnetic permalloy (Ni:Fe 4:1) incorporated between the gold layer and the silicon oxide of a gold coated silicon wafer. The sample was placed on the sample stage within a magnetic field aligned with the direction of the neutron beam which was generated by magnets placed on the side of the sample. In the POLREF reflectometer neutrons are polarised by passing the neutron beam through a supermirror which reflects only neutrons with one spin state out of the beam. The obtained polarised neutron beam then passes through a flipper which is used to invert the spin of the neutron and obtain the second spin state. Reflectivity curves were

measured with neutrons polarised parallel (↑↑) and antiparallel (↑↓) with the magnetic field surrounding the sample which are conventionally referred to as spin down and spin up respectively. At each angle, the sample was measured with each spin state alternating between up and down spin every 3000 frames collected until adequate statistics were obtained.

2.7.3 Data reduction

Data reduction and stitching was performed using the MantidPlot software (Arnold *et al.*, 2014). Time of flight reflectivity data at each angle was converted in intensity vs neutron wavelength and then intensity vs. wave vector transfer (Q) profiles that were normalised by a direct beam measurement taken at the beginning of the experimental beam time. Datasets collected at different angles were stitched together in Mantid, which scales the datasets and matches the overlaps between one angle and the next to yield a final single reflectivity curve. Data was rebinned at a resolution δQ/Q between 2 and 4% to account for angular uncertainty in the neutron beam defined by the instrumental collimation slit settings. The rebinning process consists in grouping data points in the reflectivity curve in small packets, or "bins" the size of which determines the final resolution. The intensity of the data points within each bin is averaged and the obtained data points have an error equal to the standard error of the mean intensity of the points in the bin.

2.7.4 Data analysis

NR data was analysed using the Rascal software (Hughes, 2013). Rascal allows to fit reflectivity curves collected under multiple isotopic solutions (i.e. contrasts) to a single model of the interface composed of a stack of layers using the Parratt formalism (Parratt, 1954). Each layer in the model is described by three parameters which define the thickness, SLD and interfacial roughness. The multiple datasets, collected under different solution contrasts, arise from the same bilayer structure, with the only difference being the SLD of the surrounding solution. Thus, the thickness and roughness parameters of each layer in the model must remain the same in different contrasts whilst the SLD is allowed to vary due to water penetration in the layers. Comparing the SLD of a layer measured under multiple contrasts, enables the determination of its hydration (i.e. its water content) using simple linear equations (Clifton *et al.*, 2013a; Clifton *et al.*, 2013b). Here, rather than using hydration to describe the water penetration, layers are described in terms of their coverage. These definitions are complementary as the sum of the coverage of material in a layer and

its hydration is assumed to be 100% of the volume of the layer, thus saying that a layer has a coverage of 30% or a hydration of 70% is equivalent.

Once a user-defined model of the interface is established (e.g. number of layers and sensible initial parameters), the datasets are fed to an algorithm which adjusts the parameters of the model to minimise the differences between the calculated and the experimental reflectivity, quantified by the reduced χ^2 value (the weighted sum of squared deviations divided by the system's degrees of freedom). This yields a calculated reflectivity, and corresponding SLD profile, that best represents the measured reflectivity, and therefore the interfacial structure that generated it.

The initial selection of the model is therefore important to achieve meaningful results from the fits. Here, the simplest possible models (i.e. least number of parameters and layers), which adequately described the data, were selected. **Table 2.10** shows the layers used to fit the asymmetric phospholipid/LPS silicon supported bilayer. The SLD of the various membrane components described in this thesis, calculated from their elemental composition, is shown in **Table 2.11**

Table 2.10 | Layers used to model the reflectivity from a silicon supported OM model used in this work

Example of a layer structure used to fit data on asymmetric OM models containing deuterated phospholipids in the inner leaflet and hydrogenous LPS in the outer leaflet.

Silicon Oxide
d_{62}DPPC HG
d_{62}DPPC tails
LPS tails
LPS HG

NR data was fitted using Rascal's Simplex algorithm which is based on the Nelder-Mead method (Nelder and Mead, 1965). The error estimation on the fitted parameters was done using Rascal's Bayesian error analysis routine which uses Bayesian probability theory to determine 95% confidence intervals of the parameters relative to the fits. Priors were set to be uniform unless indicated in the text, meaning that no prior information on the bilayer structure was used during the error estimation. A description of the Bayesian approach to neutron reflectivity data analysis can be found in (Sivia and Webster, 1998).

Table 2.11 | SLD values for the chemically distinct layers in the model membranes

Values for the bilayer lipid components were from a recent study (Clifton *et al*., 2015a) whilst values from the proteins were calculated from their amino acid content using the Biomolecular Scattering Length Density Calculator online tool (http://psldc.isis.rl.ac.uk/Psldc/)

Material	SLD ($Å^{-2}x10^{-6}$)
Silicon	2.07
Silicon Oxide	3.41
Gold	4.66
DPPC head group	1.98
dDPPC tails	7.45
LPS tails	-0.39
LPS head group in D_2O	4.28
LPS head group in H_2O	2.01
^{cys}OmpF in D_2O	3.21
^{cys}OmpF in H_2O	2.04
ColN in D_2O	3.33
ColN in H_2O	1.87

The C16NEtOH and DPPTE SAM layers, were parameterised in terms of partial lipid volumes obtained from (Armen *et al.*, 1998) as described previously (Hughes *et al.*, 2014). The lipid asymmetry was determined from the SLD of the tail regions of the bilayer by using the linear equations described by Clifton *et al.* (Clifton *et al.*, 2013a; Clifton *et al.*, 2013b). The amount of d_{62}DPPC in the inner leaflet was calculated according to:

$$\%dDPPC_{inner} = \frac{SLD_{exp} - SLD_{LPSTails}}{SLD_{dPCTails} - SLD_{LPSTails}} \quad (2.2)$$

Whilst the amount of LPS in the outer leaflet was calculated according to

$$\%LPS_{outer} = \frac{SLD_{dPCTails} - SLD_{exp}}{SLD_{dPCTails} - SLD_{LPSTails}} \quad (2.3)$$

Where $\%dDPPC_{inner}$ and $\%LPS_{outer}$ are the percentages of d_{62}DPPC and LPS in the inner and outer leaflet respectively, SLD_{exp} is the SLD determined experimentally for the tail region of interest and $SLD_{dPCTails}$ and $SLD_{LPSTails}$ are the calculated values for the regions from **Table 2.11.** The SLD of layers that contain a significant amount of labile hydrogens (e.g. proteins,

carbohydrates) was fitted as a single value (the SLD in D_2O) which for the other contrasts was adjusted in the following way:

$$SLD = (SLD_{D2O} * \varphi_{D2O}) + (1 - \varphi_{D2O}) * (\mathrm{SLD_{ratio}} * SLD_{D2O}) \quad (2.4)$$

Where *SLD* is the value that the layer takes in the different solution contrasts, SLD_{D2O} is the SLD value in D_2O, φ_{D2O} is the volume fraction of D_2O in the buffer and SLD_{ratio} is the ratio of the calculated SLD in H_2O to that in D_2O given in **Table 2.11**. This was done in order to constrain the SLD of these components so that it would not fluctuate independently in the various isotopic contrasts. To further constrain the fitting, when experiments required the same substrate to be measured under different conditions (e.g. when studying the interaction with antimicrobials) the parameters of the substrate were shared across the multiple conditions for consistency across different conditions.

Barycentric mean calculation

The shift in Q of the Kiessig fringe of isotopically asymmetric phospholipids/LPS bilayers caused by PmB was quantified by the shift in the barycentric mean of the fringe. This was done to obtain model independent information of the structural changes occurring in the bilayer as a function of temperature in the presence of the antimicrobial. The barycentric mean represents the shift on the x axis of the centre of mass of a peak and is defined as:

$$\lambda_m = \frac{\sum I(\lambda) * \lambda}{\sum I(\lambda)} \quad (2.5)$$

Where *I* is the intensity of the curve and λ is the coordinate on the x axis, usually wavelength, as this type of data treatment is common in spectral analysis to measure the shift of intensity peaks (Chalton and Lakey, 2010). This approach was used here to analyse the shift of the Kiessig fringe. The Q range of the datasets was 0.012 to 0.12, which goes from the critical edge to the maximum intensity of the undulation at high Q in the IxQ^4 vs Q plot. The barycentric mean was then calculated for each dataset on the reciprocal of the curve, obtained by dividing 1 by IxQ^4 over the specified Q range.

Estimation of the volume fraction of water in a solvated Colicin N model for NR data evaluation

MD simulations were performed by Dr. Filip Ciesielski (Clifton *et al.*, 2016). To estimate the chain volume fraction of a film of ColN proteins on a surface of a lipid bilayer at full coverage, the contribution of water molecules that solvate the protein must be taken into

account. The ColN-RP structure (PDB id. 1A87) was obtained from Protein Data Base (www.rscb.org) and a box with minimum possible dimensions was defined (76.9 × 41.0 × 35.1 $Å^3$), such that all protein atoms were contained within. ColN-RP in the box was able to accommodate 2202 molecules of SPC water model added using Gromacs 5.0 MD simulation software. Density of water was assumed to be d_{H2O} = 0.987 g/cm^3 and used to calculate the volume of a single water molecule V_{H2O} = 29.98 $Å^3$. Relative volume fraction of protein in the unit box was then found by the difference between the volume of the box and the total volume occupied by water molecules. This yielded a volume fraction of protein within the box of ~40%.

2.8 OTHER BIOPHYSICAL TECHNIQUES

2.8.1 Infrared spectroscopy (IR)

Infrared spectroscopy measurements were taken on a Nicolet iS50 spectrometer (Thermo Fisher Scientific)

2.8.1.1 Attenuated total internal reflection Fourier transform infrared spectroscopy (ATR-FTIR)

In ATR-FTIR the IR beam reflects multiple times from the interface containing the sample to be analysed. Part of the infrared radiation generates an evanescent wave which is absorbed by the stretching, vibrational and rotational modes of the chemical bonds within the molecules in the sample (Coates, 2006). The absorption spectra are therefore indicative of the functional groups present at the interface. The IR absorbance values of functional groups relevant here are given in **Table 2.12**. General information about the use of this setup in solid–liquid interfacial studies is given by Arteta *et al* (Arteta *et al.*, 2015).

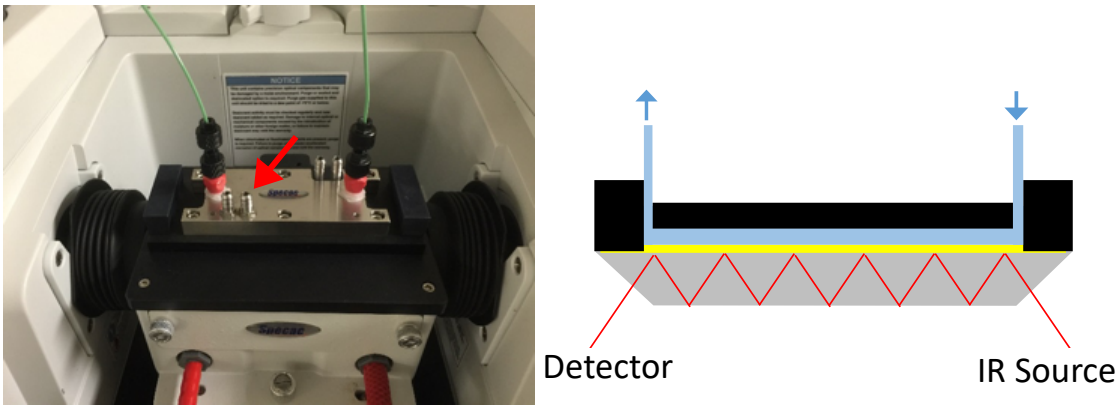

Figure 2.6 | ATR-FTIR setup

On the left a picture of the solid liquid cell fitted to the infrared spectrometer, the green tubing are the inlet and outlet lines whilst the red arrow indicates the water bath lines for the temperature control. On the right a schematic representation of the path of the beam through the silicon prism, from the source to the detector. In yellow the sample deposited on the silicon surface, bathed by the solution in blue. Arrows indicate inlet and outlet lines.

ATR-FTIR data was collected using a mercury-cadmium-telluride detector cooled with liquid nitrogen. The spectrometer was fitted with the solid-liquid cell (Specac) containing the prism with the sample, and the inlet line was connected to a syringe placed on a peristaltic pump (**Fig 2.6**). Asymmetric d_{62}DPPC (inner leaflet) RaLPS (outer leaflet) bilayers were assembled on ATR silicon crystals as described above. The solid–liquid cell containing the silicon crystal, with the bilayer deposited on its surface, was then placed into the sample chamber of the spectrometer, a buffer containing 5 mM Ca^{2+}, 20 mM HEPES pD 7.4 prepared in D_2O was pumped into the cell. Solution flow was controlled by a peristaltic pump. The sample chamber was allowed to purge of H_2O vapor and CO_2 for at least 1 h before spectra were acquired. For data collection, 128 individual spectra were summed. Once the IR measurements were taken, the cell was cleaned with ethanol and 1% Hellmanex to remove the bilayer from the silicon surface. The cell was rinsed with water, filled with the D_2O buffer, and a background measurement was taken which was then subtracted from the initial measurements.

Table 2.12 | IR absorbance of some stretching vibrations relevant in the studies performed in Chapter 3.

All the values are from (Coates, 2006) except those for the stretching of CD_2 (carbon-deuterium) that were from (Liang *et al.*, 1960)

Functional Group	Stretching mode	Wavenumber (cm^{-1})
Alkyl groups		
CH_2	Asymmetric	2935-2915
	Symmetric	2865-2845
CH_3	Asymmetric	2970-2950
	Symmetric	2880-2860
CD_2	Asymmetric	∽2175
	Symmetric	∽2085
Carbonyl groups		
Ester		1750-1725
Carboxylic acid		1725-1700
Amide		1680-1630

For the IR measurements of LPS monolayers deposited by vesicle rupture, silicon ATR crystals were coated with a monolayer octadecyltrichlorosilane as described above and placed in the solid–liquid cell. A background measurement was taken once the solid–liquid cell was mounted on the spectrometer and filled with a buffer containing 5 mM Ca^{2+}, 20 mM HEPES pD 7.4. Vesicles were prepared as described above in the same buffer and injected at 0.25 mg/ml in the solid liquid cell. The monolayer formation from the vesicle suspension was monitored over time until the IR signal reached saturation, after about 2 h.

2.8.1.2 Transmission infrared spectroscopy

For the deuterated LPS characterisation, the IR absorption was measured in transmission mode, with the beam passing directly through the sample. A 1 mg/ml suspension of deuterated LPS in $CHCl_3$, MeOH, H_2O 60:39:1 (v:v:v) was spread on a calcium fluoride window and the solvent was allowed to evaporate under a nitrogen stream and left for 2h under vacuum to remove traces of solvent. Measurements were taken with a deuterated-triglycin-sulfate detector.

2.8.2 Surface plasmon resonance (SPR)

Surface plasmon resonance (SPR) is a versatile surface sensitive technique for the characterisation of molecular interactions, in particular receptor-ligand binding events (Nguyen *et al.*, 2015). The SPR phenomenon arises when light interacts with the electrons in the conductance band of thin gold films (~50 nm). This causes a minimum in the reflected intensity of a laser beam at an incident angle that is related to the refractive index of the medium above the gold (**Fig 2.7e**) Therefore the amount of material bound to the gold – buffer interface of a microfluidic system can be accurately quantified by relating the change of refractive index on the gold surface to the amount of material absorbed at the interface. Two approaches have been used here to investigate the interaction of LPS with antimicrobials by SPR. One consists of depositing an LPS monolayer onto a gold surface coated with a hydrophobic SAM and measuring the interaction of a binding partner flowed over the monolayer (**Fig 2.7a** and **b**) (Cooper *et al.*, 1998). A second approach, which can be used when studying proteins, is that of immobilising a protein onto a nitrilotriacetate (NTA) functionalised gold surface via histidine tag and measuring the binding to lipid vesicles flowed over the protein layer (**Fig 2.7c** and **d**) (Nieba *et al.*, 1997).

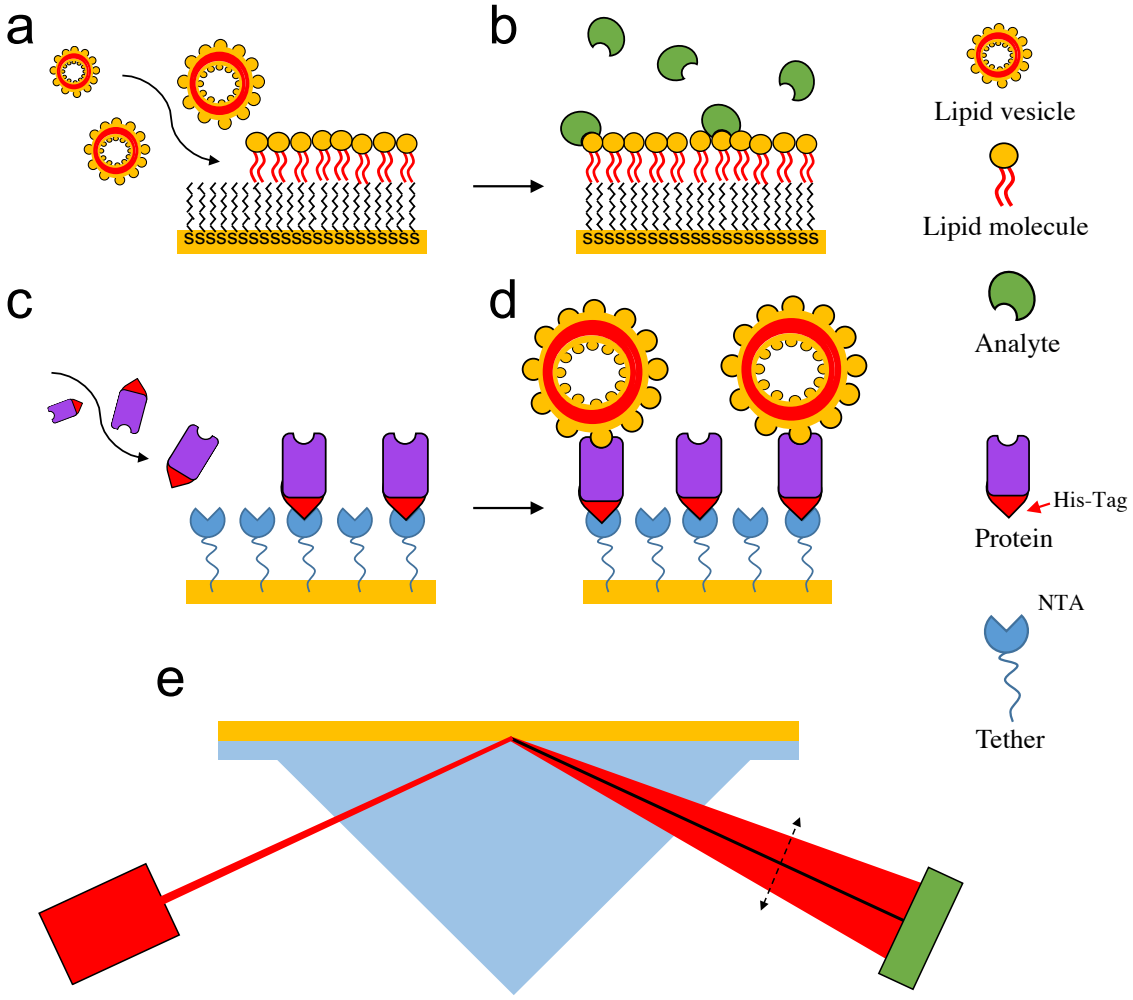

Figure 2.7 | Approaches to study lipid-protein interactions by SPR

(**a**) Deposition of a lipid monolayer on a gold sensor functionalised with a hydrophobic thioalkane monolayer and (**b**) binding of the ligand to the monolayer. (**c**) Immobilisation of His-tagged protein on NTA chip and (**d**) interaction with lipid vesicles. (**e**) Kretschmann configuration typical of SPR instruments such as the BIAcore X100 used in this work. A laser passes through a prism and is reflected by the gold layer which contains the sample on its surface on the other side of the glass. In the reflected beam, the SPR on the gold surface causes a dip in the intensity (black line).

PmB interaction with LPS monolayers

Gold surfaces used for SPR experiments were cleaned using a modified RCA procedure (Kern, 1990). The gold surfaces (SIA kit Au, GE healthcare) were initially sonicated for 15 minutes in ethanol to remove any particulate from the surface. The gold was then rinsed and incubated in a solution of H_2O, NH_4Cl and 30% H_2O_2 (5:1:1) and bath sonicated at 50°C for 10 minutes. The surface was thoroughly rinsed with Nanopure water and dried under a

stream of nitrogen. 1-undecanethiol monolayers were deposited onto the gold sensors by incubating a clean gold chip in a 1 mM ethanolic solution of 1-undecathiol. The incubated sensor was left on a rocker overnight to ensure complete adsorption and the container was kept in the dark. Once the incubation was complete the sensor was thoroughly rinsed with ethanol and the surface dried under a stream of nitrogen. SPR experiments were performed on a Biacore X100 (GE Healthcare).

The hydrophobic gold surface was mounted on the Biacore X100 machine, which was primed with a running buffer containing 150 mM NaCl, 1 mM $CaCl_2$ 20 mM HEPES pH 7.4. LPS vesicles were prepared by sonication and diluted to 0.25 mg/ml in the same buffer used for priming the instrument. The lipid deposition and following interaction with polymyxin B and polymyxin B nonapeptide were carried out as described in the result section.

ColN interaction with Ra and RdLPS

Buffers used:

- Regeneration buffer: 200 mM NaCl 10 mM HEPES 350 mM EDTA pH 8.3
- Running buffer: 200 mM NaCl 10 mM HEPES 50 μM EDTA pH 7.0

Histidine-tagged (His-Tag) ColN mutants, purified as described 2.5.3, were immobilised on a carboxymethylated dextran surface functionalised with nitrilotriacetc acid (NTA) (GE Healthcare), After docking the NTA chip in the Biacore primed with running buffer, the surface of the chip was rinsed for 120 s with regeneration buffer, followed by 60 s of 200 mM NaOH and 60 s of 0.5% SDS. A 0.5mM solution of $NiCl_2$ was flowed onto the NTA chip to activate its binding ability, 0.5μM His-Tag ColN mutants dissolved in running buffer were flowed over the active flow cell for 20s whilst a control flow cell was treated with buffer. Ra or RdLPS vesicles suspended in running buffer supplemented with 5 mM $CaCl_2$ were then flowed over both the flow cells and the signal from the control cell without protein was subtracted from the active cell that contained the His-Tag ColN. His-Tag ColN was removed by flowing regeneration buffer for 120 s, followed by 100 mM NaOH for 60 s and 0.5% SDS for 60 s.

3 INTERACTION OF POLYMYXIN B WITH OUTER MEMBRANE MODELS

3.1 INTRODUCTION

The effective barrier function of the Gram-negative outer membrane (OM), relies heavily on the asymmetric distribution of its lipid components across the bilayer (**Fig 3.1a**). In particular, the dense lipopolysaccharide (LPS) film that constitutes the outer leaflet, constitutes an impermeable layer which, in the presence of divalent cations, forms a tightly cross linked network (Herrmann *et al.*, 2015). To kill Gram-negative bacteria, the vast majority of antimicrobials in use today avoid the hydrophobic core of the OM by entering the cell via water-filled protein pores, named porins, which normally enable the uptake of small, water soluble nutrients (Nikaido, 2003; Delcour, 2009; Tommasi *et al.*, 2015; Arunmanee *et al.*, 2016). This provides Gram-negative bacteria with a significant advantage in developing antibiotic resistance in two ways. Firstly, the cut-off size channels of porins (~600 Da), dictates a strict upper limit for the size of drug molecules effective against these pathogens, limiting the chemical space of the useful antibiotic pool. Secondly, mutations in the lumen region of porins that prevent antibiotic entry become a critical cause of antibiotic resistance. A random single point mutation has the potential to prevent whole classes of antibiotics from reaching their cellular targets, rendering them harmless towards Gram-negatives (Pages *et al.*, 2008).

Cases of Gram-negative infections resistant to all commonly used antibiotics are increasingly reported and are currently treated with the last resort antibiotic Polymyxin B (PmB). PmB is a mixture of closely related LPS-binding amphiphilic antibiotics which combine a hydrophobic acyl tail with a hydrophilic cyclic cationic peptide (Orwa *et al.*, 2001) **(Fig 3.1d)**. Its status of last resort treatment against pan-resistant Gram-negative infections has reinforced interest in the molecular basis of PmB's unique ability to penetrate the Gram-negative cell envelope. PmB has been shown to cause a large scale disruption of the OM *in vivo* due to its ability to bind directly to LPS allowing it to enter the cell via a "self-promoted uptake" pathway (Velkov *et al.*, 2010; Deris *et al.*, 2014). However, molecular data and structural information on the PmB-OM interaction, necessary to clarify the mechanism of action and inform future drug development, is still lacking. This is largely due to the fact that the OM is difficult to precisely address *in vivo* by biophysical methods. Realistic *in vitro* OM models can thus provide a useful tool to study the interaction of antibiotics, such as PmB, with the outer bacterial surface and to better understand antibiotic penetration through the OM (Clifton *et al.*, 2015a; Clifton *et al.*, 2015b).

The aim of this study was to characterise the interaction of PmB with two types of OM models reconstituted *in vitro* using two different approaches:

- $_{LPS}$HBM

The first type of OM model is a hybrid bilayer membrane (HBM) composed of a monolayer of RaLPS deposited via vesicle fusion onto a hydrophobic self-assembled monolayer (SAM) of linear alkanes (**Fig 3.1b**). The RaLPS containing HBM ($_{LPS}$HBM) has the advantage of being relatively easy to assemble, not requiring specialist equipment, versatile and amenable to characterisation by a range of biophysical techniques. On the other hand, the $_{LPS}$HBM reproduces only the outer surface of the OM as the inner phospholipid leaflet is replaced by a SAM covalently linked to an underlying solid surface which only provides a hydrophobic substrate and has limited physiological relevance.

- $_{PL/LPS}$OMM

The second, more complex model, is an asymmetric phospholipid-RaLPS outer membrane model ($_{PL/LPS}$OMM). This is an OM-like lipid bilayer which reproduces the lipid asymmetry characteristic of the Gram-negative cell envelope with an inner phospholipid leaflet and an outer RaLPS leaflet (**Fig 3.1c**) (Clifton *et al.*, 2013b). Its fabrication requires the sequential assembly of a monolayer of phospholipids and a monolayer of RaLPS using Langmuir-Blodgett and Langmuir-Schaefer deposition techniques. The procedure provides full control of the composition and lipid packing of each of the two leaflets. The higher complexity of the sample preparation required for the $_{PL/LPS}$OMM however makes it more complicated and time consuming to assemble.

As elsewhere in this thesis, neutron reflectometry (NR) was the key technique used in this study. The distinctive sensitivity of neutrons for hydrogen and the ability to differentiate it from its isotope deuterium, combined with the selective use of deuterated molecules, makes them a unique tool to investigate biological systems. Here, the combination of NR with the use of deuterated lipids, enabled the structural characterisation of OM models and the determination of PmB effects on the bilayer structure and asymmetry. Infrared spectroscopy, which is also sensitive to the difference between hydrogenous and deuterated components, provided complementary information on the chemical and dynamic changes occurring in the model membranes. Part of the results of this chapter have been published during the course of my PhD (Paracini *et al.*, 2018). The NR data presented here has been re-analysed in order for it to be coherent with the methods used in the rest of this work.

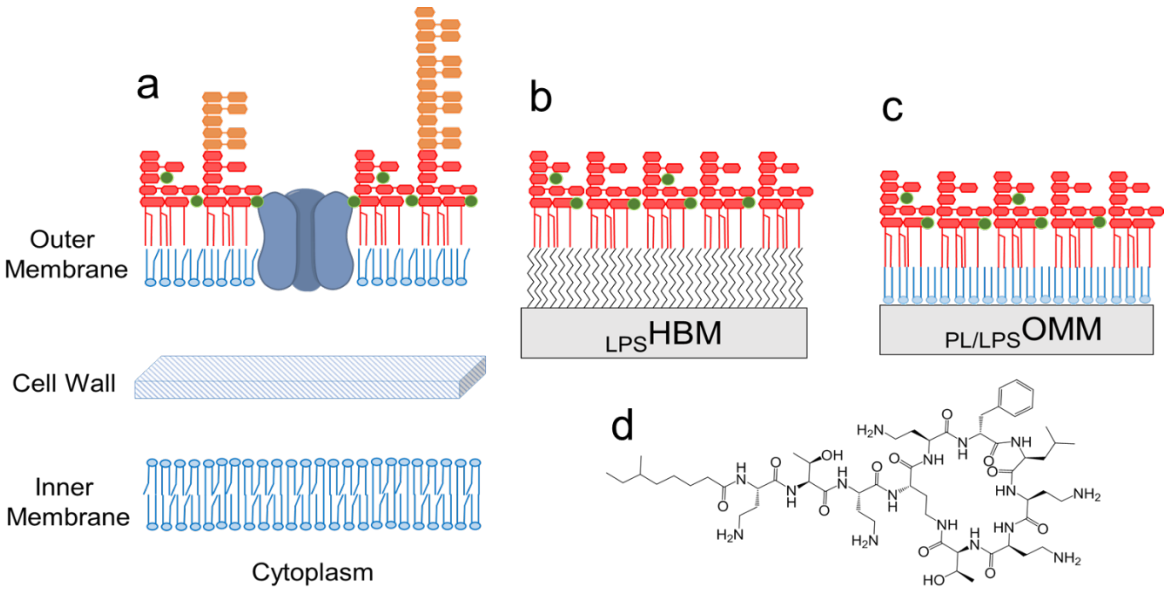

Figure 3.1 | Models of the Gram-negative outer membrane and structure of PmB.

(**a**) Schematic representation of the Gram-negative cell envelope displaying the phospholipid inner membrane, the peptidoglycan cell wall and the asymmetric outer membrane. (**b**) Simplified OM model formed by a hybrid bilayer membrane (HBM) containing a monolayer of RaLPS (red) self-assembled on a hydrophobic monolayer (black) (**c**) Asymmetric OM model assembled *in vitro* on a silicon substrate by sequential deposition of synthetic phospholipids (blue) and purified RaLPS using a Langmuir trough. (**d**) Chemical structure of polymyxin B (PmB).

3.2 Results

3.2.1 Self-assembled LPS hybrid bilayer membranes ($_{LPS}$HBM)

A molecular monolayer of RaLPS adsorbed onto a hydrophobic solid substrate provides the simplest mimic of a model of the Gram-negative outer surface amenable for biophysical characterisation. HBM composed of phospholipids are routinely used in membrane science (Plant *et al.*, 1995; Cooper *et al.*, 1998; Stahelin, 2013), however the self-assembly of RaLPS monolayers on hydrophobic surfaces ($_{LPS}$HBM) has not been previously characterised in depth. A combination of three surface sensitive biophysical techniques was used here to assess different aspects of the $_{LPS}$HBM formation via fusion of RaLPS vesicles onto a solid surface functionalised with a self-assembled monolayer (SAM) of linear alkanes. The self-assembly of RaLPS was compared to that of phosphatidylcholine, widely used in membrane reconstitution studies.

3.2.1.1 Infrared spectroscopy

Attenuated total internal reflection Fourier-transform infrared spectroscopy (ATR-FTIR) yields information on the amount and chemical nature of species at an interface by measuring the infrared absorbance of the molecules adsorbed on a substrate. A polished silicon crystal was functionalised with a hydrophobic SAM of octadecyltrichlorosilane (OTS) and enclosed in a sealed solid liquid cell equipped with inlet and outlet lines to allow for the exchange of the solution contained in the cell as described in the Methods. RaLPS and 1,2-dimyristoyl-sn-glycero-3-phosphocholine (DMPC) vesicles were prepared by rehydration and tip sonication of dry lipid cakes as described in the Methods and injected at 0.25 mg/ml onto OTS coated surfaces whilst monitoring changes in the IR spectra. For both lipid species, the IR signal characteristic of the CH_2 and CH_3 symmetric and asymmetric stretching vibrations, between 2850 cm^{-1} and 3000 cm^{-1} developed above background over time, indicating the adsorption of the lipid's acyl chains onto the hydrophobic OTS SAM. At the same time a range of peaks developed between 1600 cm^{-1} and 1750 cm^{-1}, a region characteristic of the carbonyl stretching absorbance (**Fig. 3.2**). DMPC displayed an expectedly narrow distribution of signals between 1700 cm^{-1} and 1750 cm^{-1} generated by the carbonyls of esters which link the two fatty acid chains to the glycerol moiety of the phospholipid. RaLPS, on the other hand, generated a variety of peaks reflecting the several types of carbonyl-containing groups present in the headgroup of RaLPS (i.e. carboxylic acids, esters and amides) and the different chemical environments that surround them. Although it is hard to attribute each peak generated by the carbonyl stretching vibrations to the specific chemical entities of RaLPS, due to chemical heterogeneity and overlap of the signals, the peaks were visibly divided into two major groups: those between 1700 cm^{-1} and 1750 cm^{-1}, characteristic of carboxylic acids and esters and those between 1600 cm^{-1} and 1680 cm^{-1} typical of the carbonyls of amides (Coates, 2006). The additional peaks between 1600 cm^{-1} and 1680 cm^{-1} arise from the amide linkages connecting two LPS acyl chains to the diglucosamine residue. Furthermore, a variety of ester linkages and carboxylic acids present in the LPS structure contributed to generate a broader signal between 1700 cm^{-1} and 1750 cm^{-1} compared to that of the phospholipid.

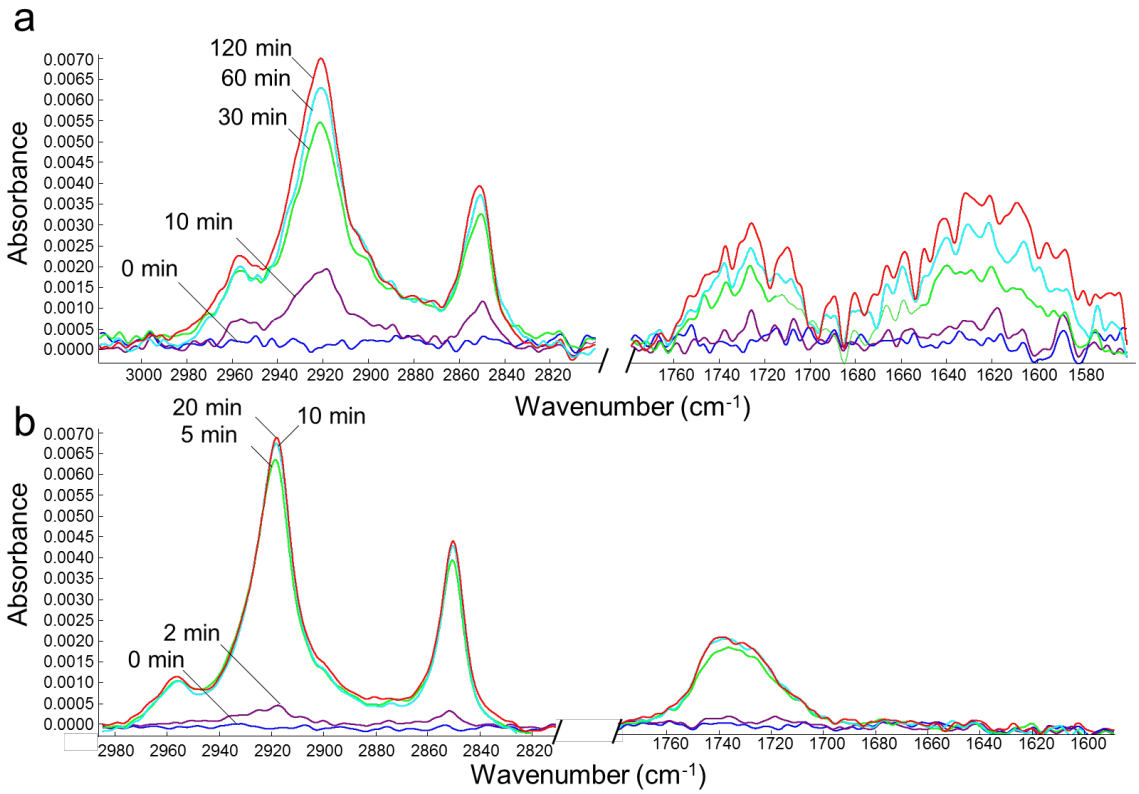

Figure 3.2 | ATR-FTIR of RaLPS and DMPC adsorption on OTS coated substrate.

Infrared absorption spectra of RaLPS (**a**) and DMPC (**b**) adsorbing onto an OTS coated substrate over time. The two main peaks on the left are the C-H bond vibrations of the asymmetric (~2920 cm^{-1}) and symmetric (~2850 cm^{-1}) CH_2 stretching modes, arising from the acyl chains of LPS and DMPC. On the right, the carbonyl stretches of esters (1700-1750 cm^{-1}) and amides (1600-1680 cm^{-1}) groups.

The saturation of the signal occurred within 20 min of DMPC vesicle addition whilst for RaLPS the adsorption was slower, generally requiring at least 2 h for the signal to reach its maximum intensity. It is likely that the larger nature of the LPS molecule is responsible for its slower adsorption kinetics compared to DMPC, however, after reaching saturation, both lipid species displayed signals with comparable intensities.

3.2.1.2 Surface plasmon resonance

Surface plasmon resonance (SPR) was chosen to gain a quantitative understanding of the RaLPS monolayer assembly. SPR quantifies changes in mass adsorbed onto a gold surface by measuring variations in the resonant oscillation of conduction electrons stimulated by incident light. This causes a minimum in the reflected intensity at an incident angle that is related to the refractive index of the medium above the gold. Refractive index variations on a sensor surface, caused by adsorption of molecules at the interface, produce a shift in the

minimum proportional to the amount of mass deposited. Hydrophobically coated gold substrates for the assembly of lipid monolayers, such as the BIAcore HPA sensor chip, are commercially available, however, in this study, gold surfaces were functionalised in-house with a hydrophobic monolayer. The gold sensors (SIA kit Au, GE Healthcare) were cleaned using a modified RCA procedure and a SAM of 1-undecanehiol deposited by exploiting the gold-thiol chemistry as described in the Methods (Strong and Whitesides, 1988)

$_{DMPC}$HBM

To assess whether the in-house coated surface was a suitable substrate for lipid monolayer formation, DMPC was deposited on the surface and the data compared with published results obtained with the HPA sensor chip. Monolayer formation and surface coverage were assayed by analysing the SPR response and the extent of BSA binding, which adsorbs non-specifically onto exposed hydrophobic surfaces and is used routinely to assess the completeness of HBM coverage (Cooper *et al.*, 1998). A 0.25 mg/ml suspension of small unilamellar vesicles of DMPC in 150 mM NaCl 1 mM $CaCl_2$, 20 mM HEPES pH 7.4 obtained by sonication, was injected onto the coated gold chip at a low flow rate (5 µl/min) followed by buffer. This resulted in an unstable signal of 2858 ± 290 relative units (RU) above the baseline which settled to 1416 ± 69 after washing the surface with two short injections of NaOH 100 mM (**Fig. 3.3a**). The process was repeated 10 times in order to maximise the lipid coverage, leading to a final value of 2572 ± 213 RU (**Fig. 3.3b**). After 10 injections, DMPC saturated the surface as indicated by the marginal gains in signal following the last injection which amounted to less than 1% of the total RU (**Fig. 3.3c**). The coverage of the monolayer was assessed by adding 0.1 mg/ml bovine serum albumin (BSA) at a flow rate of 5 µl/min. Only a minor increase of 19 ± 3 RU followed the BSA injection, indicating comprehensive coverage of the hydrophobic surface by the lipid monolayer. The DMPC monolayer was then removed by an injection of 40 mM octyl-β-D-glucopyranoside (OG) which regenerated the hydrophobic surface allowing repetition the process on the same surface. Assuming an area per molecule of DMPC of ~47 $Å^2$ (Hughes *et al.*, 2002) it is possible to estimate the SPR response produced by the formation of a complete DMPC monolayer by using the relationship 1 RU = 1 pg of lipids per mm^2 (Nakajima *et al.*, 2001). This yields a calculated response of about 2400 RU for a DMPC monolayer in line with the experimental value obtained. An estimate of the lipid layer thickness can also be obtained by the magnitude of the SPR signal. A 1000 RU increase corresponds to a 0.1° change in resonant angle and a thickness increase of 7.6 Å for a lipid with a refractive index of 1.45

(Hughes *et al.*, 2014). Therefore an increase of 2570 RU corresponds to a thickness of 19.5 Å, which is about half the thickness of a DMPC bilayer as determined by X-ray diffraction measurements (40.1 ± 0.1 Å) (Tristram-Nagle *et al.*, 2002). Overall, SPR indicated the formation of a complete phospholipid monolayer on the in-house coated sensor which compared well with published SPR data on the formation of phosphatidylcholine monolayers on the commercial HPA sensor chips (Cooper *et al.*, 1998).

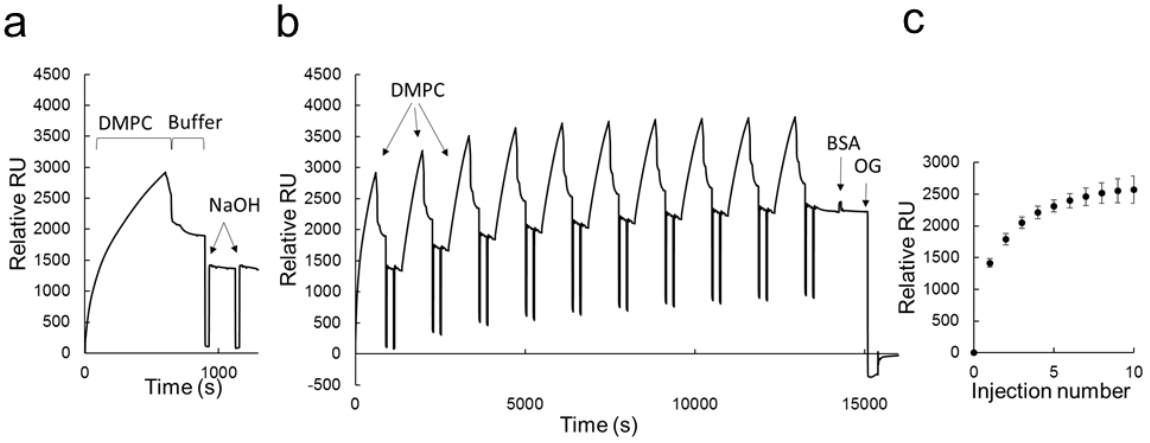

Figure 3.3 | SPR sensorgram of $_{DMPC}$HBM formation.

(**a**) Representative SPR response showing DMPC adsorption onto the alkane-thiol collated gold surface. DMPC was injected for 600s at a flow rate of 5 µl/min followed by 300s of buffer and 2x30s injection of 100 mM NaOH at 10 µl/min. (**b**) Sequential DMPC depositions following the procedure described in **a**. (**c**) Plot of the relative increase in RU after each DMPC injection showing saturation of the signal (values taken after the second NaOH injection). Error bars are from triplicate experiments.

$_{LPS}$HBM

LPS vesicles were prepared by resuspension and sonication of RaLPS lipid cakes and monolayer depositions followed the same procedure described for DMPC. Injection of a 0.25 mg/ml suspension of RaLPS vesicles in 150 mM NaCl 1 mM $CaCl_2$, 20 mM HEPES pH 7.4 onto the alkanethiol coated gold sensor led to an increase in the SPR signal of 4240 ± 224 RU above the baseline (**Fig. 3.4a**). Washing the surface with 100 mM NaOH, removed loosely bound material in a similar fashion to that observed with phosphatidylcholine, lowering the signal to 2439 ± 46 RU after the two sequential NaOH injections. After 10 injections, the increase in RU plateaued, levelling at 3104 ± 63 RU (**Fig. 3.4b** and **c**). The calculated value for a complete RaLPS monolayer, assuming an area per molecule of 150 $Å^2$ (Hwang *et al.*, 2018), is about 4320 RU, noticeably higher than the 3104 ± 63 RU

measured by SPR. As with DMPC, the addition of BSA resulted in a minor increase of 27 ± 6 RU. Both the saturation of the surface and low BSA binding indicated a near complete coverage of the hydrophobic surface by the RaLPS monolayer. However, the RU response was lower than that calculated for an ideal LPS monolayer. Considering that the SPR response is dependent both on the mass and the thickness of the adsorbed layer, a possible explanation that reconciles the saturation observed with the lower-than-expected response is the formation of a thinner monolayer due to a sub-optimal orientation of the LPS molecules. Therefore, to evaluate the structural aspects of the formation of $_{LPS}$HBM, the monolayer was examined by NR.

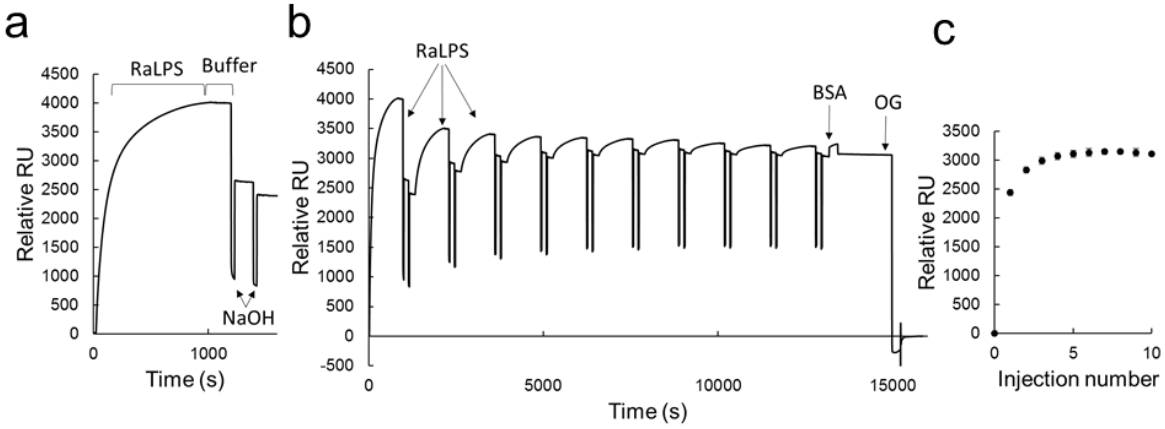

Figure 3.4 | SPR sensorgram of $_{LPS}$HBM formation.

(**a**) Representative SPR response showing RaLPS adsorption onto the alkane-thiol coated gold surface. RaLPS was injected for 900s at 5 µl/min followed by 300s of buffer and 2x30s injection of 100 mM NaOH at 10 µl/min. (**b**) Sequential RaLPS depositions following the procedure described in **a**. (**c**) Plot of the relative increase in RU after each RaLPS injection showing saturation of the signal after the 5th injection (values taken after the second NaOH injection). Error bars are from triplicate experiments

3.2.1.3 Neutron Reflectometry

NR was used to characterise the structural features of the $_{LPS}$HBM. In NR, the intensity of neutrons reflected from an interface is measured as a function of the wave vector transfer (Q) as described in **section 1.4**. Reflectivity curves were measured under three solution isotopic contrasts and fitted to the reflectivity calculated from a stack of distinct chemically homogeneous layers using the Rascal software (Hughes, 2013). Neutron reflectivity was measured under three solution isotopic contrasts: H_2O, D_2O and silicon-SLD matched water (SMW), composed of 38% D_2O and 62% H_2O and the three data sets constrained to fit

simultaneously to a common model of the interface. To further exploit the differential sensitivity of neutrons for hydrogen and deuterium, the hydrophobic SAM coating the silicon substrate was assembled using deuterated OTS (dOTS) thus creating contrast (i. e. differentiating) between the structure of the OTS and that of the acyl tails of LPS. The reflectivity from the dOTS coated silicon wafer was measured before the addition of RaLPS vesicles to characterise the structure of the substrate functionalised with the deuterated SAM. **Figure 3.5a** shows the reflectivity curves, best fit lines and relative SLD profiles for the SAM measured in three solution contrasts. The model used to fit the data was composed of two layers, one representing a silicon oxide layer and the other representing the dOTS SAM. The reflected signal is shown as the product of the measured intensity multiplied by Q^4 (IxQ^4) to account for the intrinsic decay of the reflectivity which falls as a function of Q^{-4}, as shown by **Equation 1.11**. This way of displaying the reflectivity enhances the features in the curves and aids the interpretation of the data. The structure of the deuterated alkane layer was clearly resolved, yielding a thickness of ~26 Å and a surface coverage of ~94% (**Table 3.1**), in excellent agreement with previous measurements and with the predicted thickness of a highly ordered layer of fully extended C18 alkyl chains (Saner *et al.*, 2012). The coverage parameter showed that ~6% of the total volume of the SAM was occupied by water molecules, indicating the presence of minor defects in the monolayer. Given the covalent nature of the substrate-SAM interaction and the relatively simple structure of the dOTS molecule, the roughness of the two layers was coupled to a single value to keep a minimal number of parameters in the model and was found to be 3 Å. The fits indicated an SLD of the dOTS layer of $6.67x10^{-6}$ $Å^{-2}$ which is lower of that of fully deuterated hydrocarbons ($7.45x10^{-6}$ $Å^{-2}$). This discrepancy can be attributed to a deuteration level lower than 100% or a density of OTS in the monolayer lower than 1 g/cm^3, or more likely, a combination of the two. The substrate was therefore used to deposit an RaLPS monolayer. After incubating of the SAM with a 0.25 mg/ml suspension of RaLPS vesicles in 5 mM $CaCl_2$, 20 mM HEPES pH 7.4, the reflectivity curves displayed a sharp change, particularly evident in the D_2O contrast (**Fig 3.5b**) which indicated the adsorption of material at the interface.

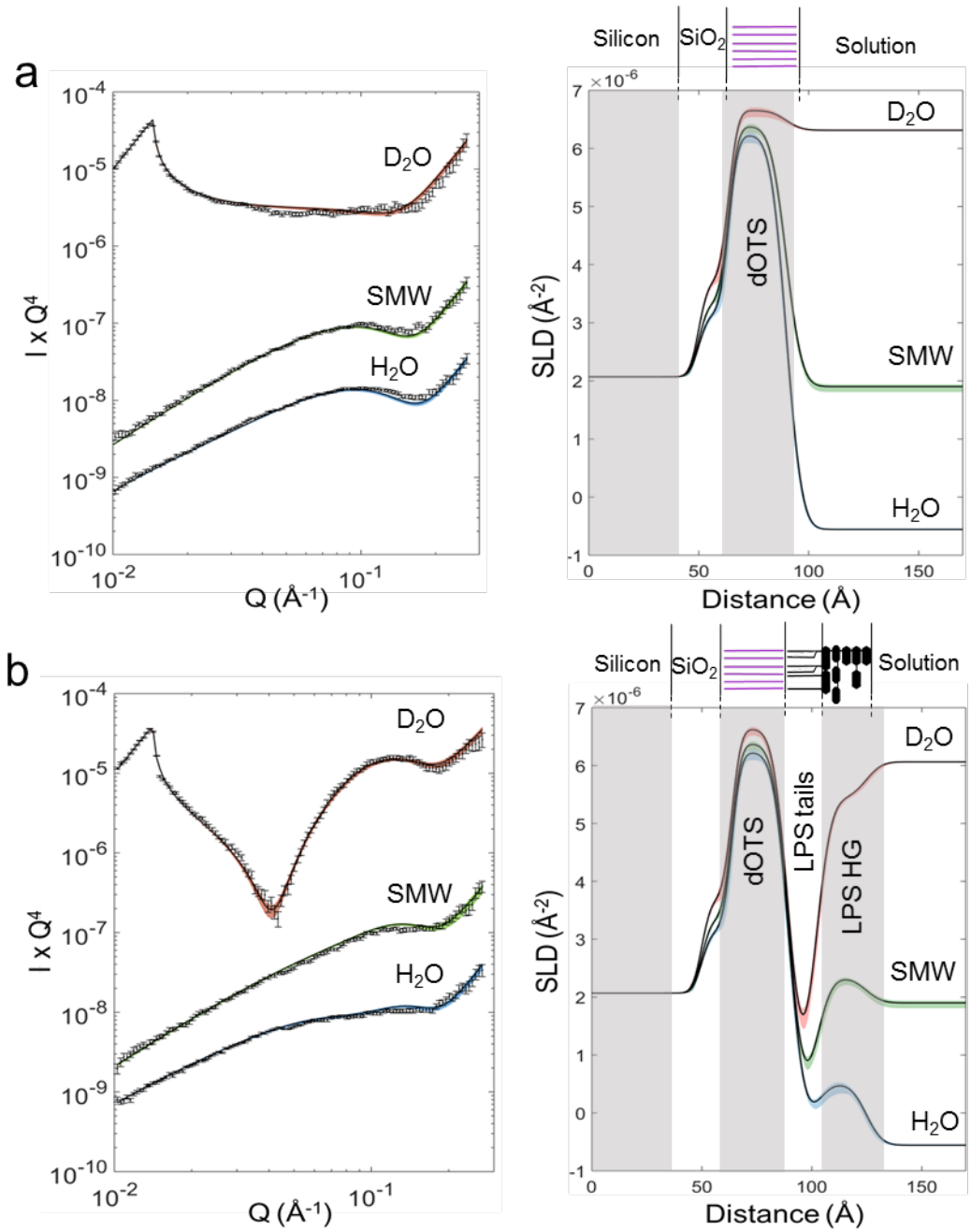

Figure 3.5 | NR of $_{LPS}$HBM formation.

Neutron reflectivity data points, best fit lines (left) and corresponding SLD profiles (right) for the dOTS coated silicon substrate before (**a**) and after (**b**) the deposition of RaLPS on the surface. Data was collected in three isotopic contrasts: D_2O, H_2O and SMW and constrained to fit a common model of the interface. The coloured shading around the lines represents the 95% confidence intervals obtained from the Bayesian error analysis. A cartoon of the interface is shown above each set of SLD profiles with dOTS in purple and LPS in black. Alternate shading indicates the positioning of the layers over the SLD profile. HG = head group. Reflectivity curves are offset vertically for clarity

The sharp dip that appears in the reflectivity measured in D_2O upon formation of the LPS monolayer is known as a Kiessig fringe. This sharp feature is characteristic of the presence

at the interface of a low SLD layer, in this case the hydrogen-rich LPS acyl tails, sandwiched in between two high SLD regions, such as the deuterated SAM and the bulk D_2O solution (Clifton *et al.*, 2013b). To fit the data, two additional layers, corresponding to the chemically distinct regions of the LPS acyl tails and to the core oligosaccharide were added to the model used for the substrate. The SLD of the components of these two regions was fixed to the calculated value based on the estimated elemental composition of each component (**Table 2.11**). The LPS tails were found to have a coverage of ~97% and a thickness of ~11 Å while the core oligosaccharide was ~24 Å thick with a coverage of ~38% (**Table 3.1**). The coverage parameter indicates that ~3% and ~62% of the volume fraction in the LPS tails and head group layers, respectively, are occupied by water molecules. The near absence of water in the hydrophobic LPS tails region confirmed the comprehensive fusion of LPS vesicles on the surface and the absence of major defects in the monolayer, in agreement with the surface saturation observed by SPR and ATR-FTIR.

Table 3.1 | Parameters derived from the fitting of the reflectivity data from the $_{LPS}$HBM.

The substrate parameters describe the dOTS coated silicon surface and are assumed not to vary upon addition of LPS. The parameters fixed to the SLD value calculated from the chemical composition of the component in the layer are shaded in grey. These were regions that were assumed to correspond entirely to their exact chemical composition. In brackets are the 95% confidence intervals derived from the Bayesian error analysis. HG = head group.

Substrate parameters	**Fitted value**
Substrate roughness (Å)	3.3 (2.8, 3.8)
Silicon oxide thickness (Å)	13.6 (13.0, 14.2)
Silicon oxide SLD ($Å^{-2}x10^{-6}$)	3.41
Silicon oxide hydration (%)	8.3 (6.9, 9.4)
dOTS thickness (Å)	26.2 (25.6, 26.7)
dOTS SLD ($Å^{-2}x10^{-6}$)	6.67 (6.61, 6.75)
dOTS coverage (%)	93.9 (93.1, 94.7)
LPS parameters	**Fitted value**
LPS tails thickness (Å)	11.4 (11.1 11.8)
LPS tails SLD ($Å^{-2}x10^{-6}$)	-0.39
LPS tails coverage (%)	97.5 (93.7 99.9)
LPS HG thickness (Å)	23.6 (22.4, 24.7)
LPS HG SLD in D_2O ($Å^{-2}x10^{-6}$)	4.28
LPS HG coverage (%)	37.8 (35.2, 40.4)
LPS roughness (Å)	5.6 (5.3 5.9)

The higher water content in the head group layer is due to water molecules associated with the hydrophilic oligosaccharide forming the LPS head group. Comparison of the total LPS thickness measured here by NR (~35 Å) with that measured by X-ray lamellar diffraction (~48 Å) (Snyder *et al.*, 1999) and by NR on densely packed OM models (~45 Å) (Clifton *et al.*, 2013b; Clifton *et al.*, 2015a), indicated a lower than expected overall thickness of the monolayer. Overall the results confirmed the formation of a high coverage LPS monolayer from vesicle fusing onto the hydrophobic SAM, as suggested by the surface saturation observed by SPR and ATR-FTIR. Crucially, the use of deuterated OTS enabled the clear determination of the thickness of the tail region of LPS. However, when compared to data on highly packed LPS layers, NR revealed a thinner than expected structure the monolayer, which corroborated the SPR results and suggested a sub optimal arrangement of the self-assembled LPS molecules.

3.2.1.4 Interaction of PmB with $_{LPS}$HBM

The approaches used to characterise the assembly of the $_{LPS}$HMB were employed to study the effects of the interaction of PmB with the LPS monolayers at room temperature. All the interaction studies were performed in a buffer containing 20 mM HEPES pH 7.4 and 5 mM C^{2+}. Addition of 100 μg/ml PmB to the $_{LPS}$HBM monitored by ATR-FTIR, resulted in a large increase in the IR absorbance of the spectral region corresponding to the amide bond, around 1650 cm^{-1}, indicating the binding of the peptide moiety of PmB to the LPS monolayer. The binding of the antimicrobial also shifted the C-H stretching vibrations towards higher wavenumbers, an effect linked to a decrease in the ordering of the acyl chain region of the monolayer (**Fig. 3.6a**) (Brandenburg and Seydel, 1990; Coates, 2006). The acyl tail of PmB has been shown to exhibit independent, rapid motion in solution (Meredith *et al.*, 2009) suggesting that the increase in disorder displayed by the hydrophobic core of the RaLPS monolayer was correlated with the intercalation of PmB's alkyl chain moiety. Given the amphiphilic nature of PmB, and therefore its tendency to adsorb at interfaces, the antimicrobial was added under the same conditions to the $_{DMPC}$HBM as a control for possible non-specific interactions. The addition of PmB to the phosphatidylcholine monolayer resulted in none of the changes observed with LPS (**Fig. 3.6b**).

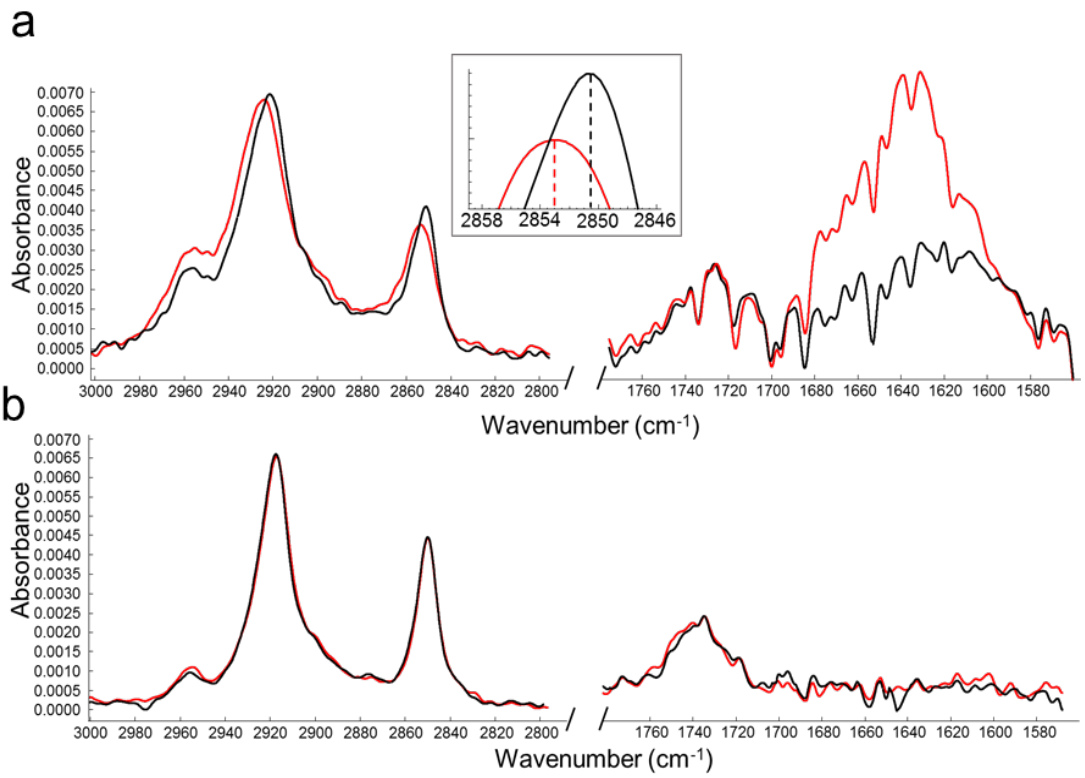

Figure 3.6 | ATR-FTIR spectra of PmB adsorption of $_{LPS}$HBM and $_{DMPC}$HBM.

Infrared absorption spectra of $_{LPS}$HBM (**a**) and $_{DMPC}$HBM (**b**) before (black) and after (red) the addition of 100 µg/ml PmB to the lipid monolayers at room temperature. The inset in **a** shows the shift of the symmetric CH_2 stretching vibrations towards higher wavenumbers indicating an increase in the disorder of the hydrocarbon region

A quantitative assessment of the PmB-$_{LPS}$HBM interaction was carried out by SPR. The RaLPS monolayer was incubated in increasing concentrations of PmB for 300s, followed each time by a buffer wash. This resulted in a concentration dependent binding of the antibiotic to the $_{LPS}$HBM which remained stable under buffer flow conditions and which saturated above 10 µg/ml PmB (**Fig. 3.7a**). Polymyxin B nonapeptide (PmBN), an analogue of PmB which lacks the hydrophobic tail and does not possess bactericidal activity (Duwe *et al.*, 1986; Sahalan and Dixon, 2008) was added the $_{LPS}$HBM for a comparison. Although PmBN caused an initial concentration dependent response during the injection phase, the interaction did not result in a stable binding under buffer flow and the peptide rapidly dissociated from LPS (**Fig. 3.7b**). No saturation was observed up to a concentration of 100 µg/ml, contrary to what observed with PmB, suggesting a less specific, electrostatic binding. Notably, the PmB concentrations that displayed an interaction with the LPS monolayer were consistent with the range of concentrations typically required for PmB activity *in vivo* (Vaara, 1992).

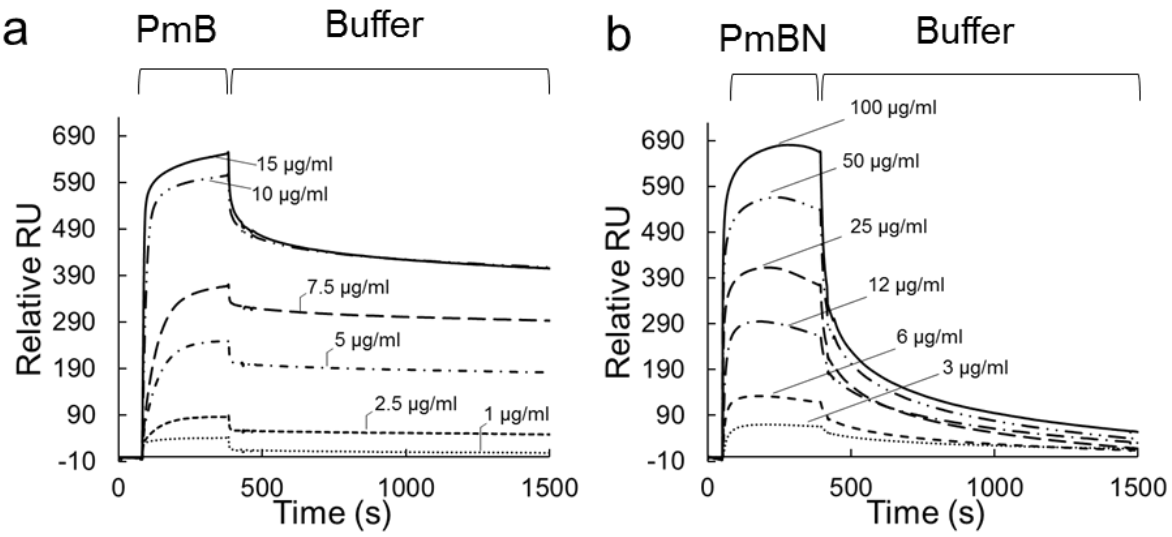

Figure 3.7 | SPR sensorgrams of PmB and PmBN binding to $_{LPS}$HBM.

Concentration dependent binding of PmB (**a**) and PmBN (**b**) to $_{LPS}$HBM measured by SPR. Buffer consisted of 150 mM NaCl, 1 mM CaCl2 and 20 mM HEPES pH 7.4. PmB and PmBN were injected on the $_{LPS}$HBM for 300s at different concentrations followed by 1200s of buffer to monitor the dissociation. The bound antimicrobial was removed with 100 mM NaOH after each injection.

The structural aspects of PmB binding to the $_{LPS}$HBM were investigated by NR (**Fig. 3.8**). Adding a concentration of 100 µg/ml PmB to the $_{LPS}$HBM resulted in a significant shift of the Kiessig fringe, measured against a D_2O solution background, towards lower values of Q (**Fig. 3.8b**). As discussed previously, the Kiessig fringe is most sensitive to changes in the low-SLD hydrogenous acyl tails of LPS as the dOTS SAM has an SLD nearly matched to the bulk D_2O solution. The inverse relationship between Q and real space distances, implies that a shift of the reflectivity towards lower Q is related to an increase in thickness of the interfacial structure, particularly of the hydrogenous LPS acyl tail region. The LPS monolayer was modelled as two layers as described earlier, with the only difference that the SLD of the LPS head group region was not fixed to its calculated value but was allowed to vary to account for the possible intercalation of the peptide moiety of PmB into the core region. The SLD of the layer modelling the tails was kept fixed to that calculated for hydrocarbons as the potential intercalation of PmB acyl tail into the hydrophobic core of the monolayer would not affect significantly the overall chemical composition and hence the SLD of this region. As suggested by the shift of the Kiessig fringe, the fit to the reflectivity data confirmed the increased thickness of the LPS tails which changed from ~11 Å to ~15 Å (**Table 3.2**).

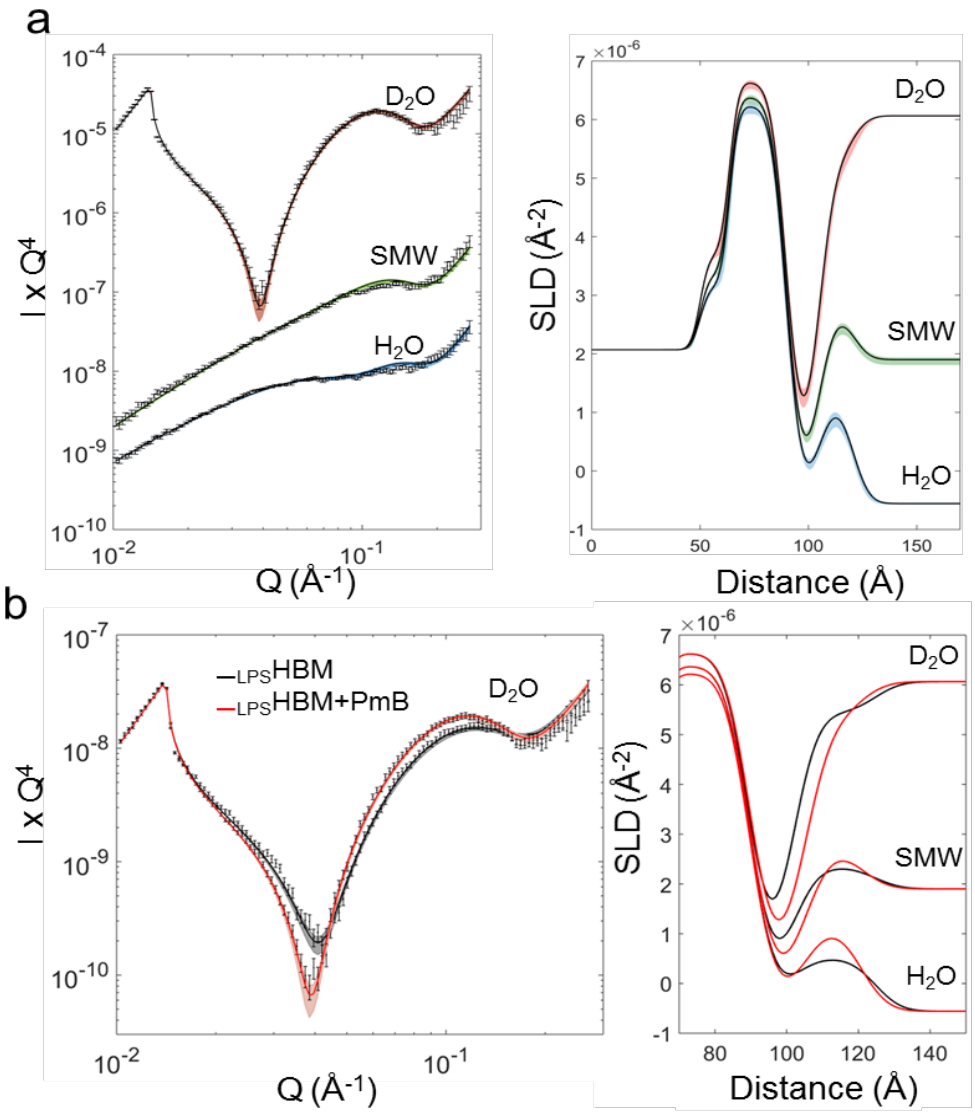

Figure 3.8 | NR of PmB interaction with $_{LPS}$HBM.

(**a**) Neutron reflectivity data points, best fit lines (left) and corresponding SLD profiles (right) for the $_{LPS}$HBM after the addition of 100 µg/ml PmB. Reflectivity curves are offset vertically for clarity. (**b**) Kiessig fringe measured in D_2O and SLD profiles of the $_{LPS}$HBM before (black) and after (red) the interaction with PmB.

Table 3.2 | Parameters derived from the fitting of the reflectivity data from the $_{LPS}$HBM after the addition of PmB

The parameters describing the substrate are shown in table 3.1. The parameters fixed to the SLD value calculated from the chemical composition of the component in the layer are shaded in grey. In brackets are the 95% confidence intervals derived from the Bayesian error analysis. HG = head group.

LPS+PmB parameter	Fitted value
LPS+PmB tails thickness (Å)	15.3 (14.6 16.0)
LPS+PmB tails SLD ($Å^{-2}x10^{-6}$)	-0.39
LPS+PmB tails coverage (%)	90.4 (86.7 94.2)
LPS+PmB HG thickness (Å)	15.5 (15.1, 16.7)
LPS+PmB HG coverage (%)	59.9 (56.0, 65.7)
LPS+PmB HG SLD in D_2O ($Å^{-2}x10^{-6}$)	4.87 (4.50, 5.26)
LPS+PmB roughness (Å)	6.0 (5.5 6.4)

On the other hand, PmB binding caused a thinning of the headgroup region of ~8 Å and a reduction of ~22% of the volume of water associated with the core oligosaccharide. The coverage of the LPS monolayer also decreased by ~7% indicating the partial removal of RaLPS by PmB. The structural changes measured by NR indicated an expansion of the hydrophobic core of the monolayer, in agreement with the proposed intercalation of PmB tail into the acyl tails of LPS, supported also by the increased disorder measured by FTIR. Concomitantly, the displacement of bound water from LPS head groups suggested binding of the cationic peptide moiety of PmB. Interestingly, although the calculated SLD of peptides is lower than that of carbohydrates, the SLD of the head group region was found to be higher following binding of PmB compared to the carbohydrate region alone (**Table 3.2**).

This apparent contradiction, however, might be explained by an increase in the density of the core oligosaccharide region which would in turn raise the SLD of the layer. The concomitant reduction in thickness supported this interpretation in which the electrostatic binding of the cationic peptide induced a collapse of the head group into a thinner and denser layer. This is in agreement with the observation that divalent cations induce a collapse of the LPS head group region resulting in an increase in density and decrease in overall thickness of the LPS oligosaccharide (Schneck *et al.*, 2009). Considering the affinity of PmB for divalent cations binding sites on LPS (Moore *et al.*, 1986; Zhang *et al.*, 2000) and its high positive charge density, it is plausible that PmB binding affected the structure of the LPS monolayer in a similar fashion to that of divalent cations.

Taken together, the results from ATR-FTIR, SPR and NR revealed the binding of PmB to the self-assembled $_{LPS}$HBM by highlighting different aspects of the PmB-LPS interaction. SPR measured the concentration dependent binding of PmB to LPS and indicated the critical role of PmB hydrophobic moiety for the binding stability of the cationic peptide. The combination of FTIR and NR confirmed the intercalation of PmB acyl tail into the hydrophobic core of the LPS monolayer which resulted in a decrease of the ordering of the LPS tails region and a concomitant expansion of the volume occupied by the hydrocarbon chains. PmB binding also caused the partial removal of LPS from the monolayer as indicated by the increase in water penetration in the hydrophobic region of the bilayer, after interaction with the antimicrobial as measured by NR.

3.2.2 Isotopically asymmetric OM model bilayers ($_{dPL/hLPS}$OMM)

A way to overcome the shortcomings of LPS monolayers and produce a more realistic asymmetric lipid bilayer, is to use Langmuir-Blodgett (LB) and Langmuir-Schaefer (LS) deposition techniques. LB and LS depositions were used to sequentially transfer a monolayer of tail deuterated 1,2-dipalmitoyl-sn-glycero-3-phosphocholine (d_{62}DPPC), followed by a hydrogenous RaLPS monolayer, from the air-water interface onto a solid substrate (Clifton *et al.*, 2013b; Clifton *et al.*, 2015a). The monolayers were first subject to two sequential compression-decompression isotherm cycles between 0 and 38 mN/m to evaluate monolayer stability and finally compressed and held at a surface pressure of 37 mN/m for the LB and LS transfer as described in the Methods. The procedure yielded an isotopically asymmetric phospholipid-LPS OM model ($_{dPL/hLPS}$OMM) with the advantage of affording total control of the packing and lipid composition of each leaflet of the bilayer. The use of tail deuterated DPPC provided the contrast necessary to resolve the structure of each individual leaflet by NR. The neutron reflectivity curves from the $_{dPL/hLPS}$OMM were collected at three solution contrasts as described above for the $_{LPS}$HBM. **Figure 3.9** shows the NR data, best fit lines and SLD profile of the $_{dPL/hLPS}$OMM collected in H_2O, D_2O and SMW. The data was fitted to a model of the interface composed of five layers, representing, from the substrate to the bulk solution: a silicon oxide layer, the d_{62}DPPC head groups, d_{62}DPPC tails, LPS tails and LPS head groups. The SLD profile obtained from the fits, described a highly asymmetric bilayer with less than 1% of the hydrophobic core volume fraction occupied by water, indicating comprehensive coverage (**Table 3.3**). The fits indicated a high level of asymmetry with an inner leaflet containing 83% DPPC and the outer leaflet of 97% RaLPS. The

estimation of the asymmetry was done according to the calculated SLD of hydrogenous and deuterated hydrocarbons, -0.39 x10^{-6}Å^{-2} and 7.45 x10^{-6}Å^{-2} respectively, which assumes 100% deuteration of d_{62}DPPC and a density of the tail region of 1 g/cm^3 (Clifton *et al*., 2013b; Clifton *et al*., 2015a). The structure of the LPS leaflet revealed a ~16 Å thick tail region and a ~27 Å thick core oligosaccharide, for a total LPS thickness of ~43 Å in excellent agreement with previously reported values on these systems (Clifton *et al*., 2013b; Clifton *et al*., 2015b). This value was closer to the 48 Å measured by X-ray diffraction (Snyder *et al.*, 1999) compared to the ~35 Å of the $_{LPS}$HBM, indicating a more upright orientation and suggesting a tighter lipid packing of LPS in the OM model assembled via LB/LS depositions.

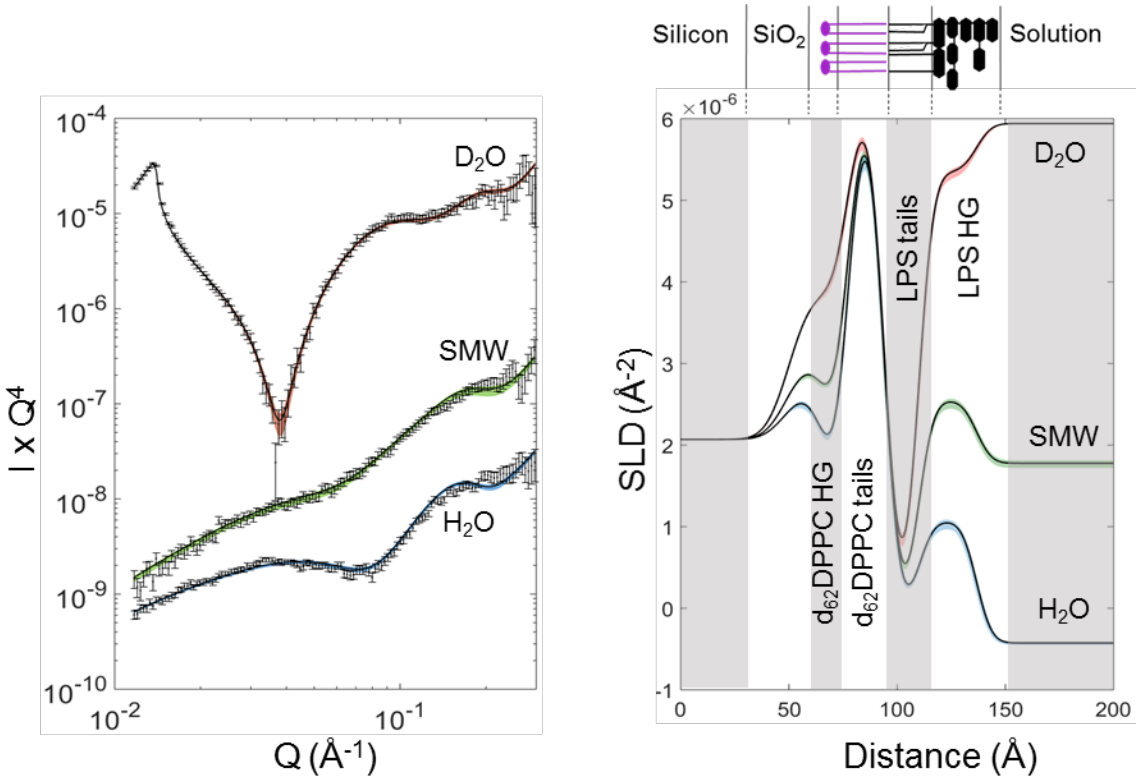

Figure 3.9 | NR of $_{dPL/hLPS}$OMM at room temperature.

Neutron reflectivity data points, best fit lines (left) and corresponding SLD profiles (right) for the $_{dPL/hLPS}$OMM at RT. A cartoon of the interface is shown above the SLD profile displaying deuterated phospholipids in purple and RaLPS in black. Alternate shading indicates adjacent layers used in the model to fit the data. Reflectivity curves are offset vertically for clarity

3.2.2.1 Interaction of PmB with $_{dPL/hLPS}$OMM

As done for the $_{LPS}$HBM, PmB 100 µg/ml dissolved in a D_2O buffer solution containing 5 mM $CaCl_2$, 20 mM HEPES, pD 7.4 was added to the $_{dPL/hLPS}$OMM while monitoring the Kiessig fringe.

Surprisingly, in sharp contrast with what observed under the same conditions with the $_{LPS}$HBM, the reflectivity from $_{dPL/hLPS}$OMM remained completely unaffected by the addition of the antimicrobial (**Fig. 3.10**). This lack of interactions indicated the possibility that the controlled assembly afforded by the Langmuir-Blodgett and Schaefer depositions prevented the intercalation of PmB within the model membrane, likely due to the tighter molecular arrangement. Based on previous data which indicated an increase in PmB efficacy as a function of temperature (Teubner and Bader, 1977; Hodate and Bito, 1982; Katsu *et al.*, 1984), the same interaction was investigated at human physiological temperature of 37ºC.

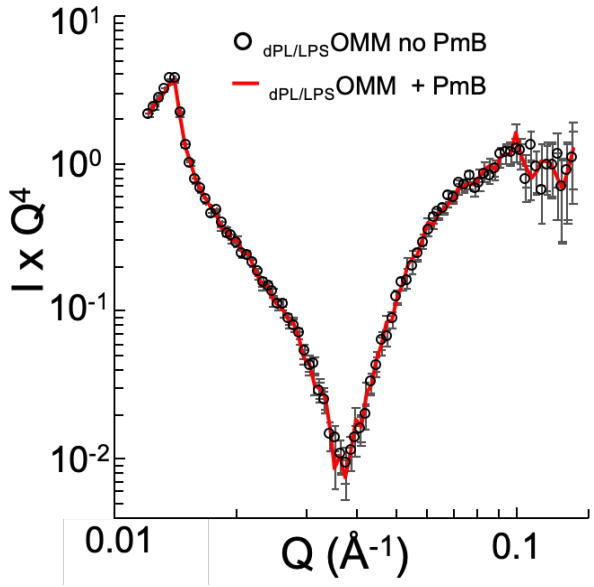

Figure 3.10 | Lack of PmB effects on $_{dPL/hLPS}$OMM at RT.

Addition of 100 µg/ml PmB to the $_{dPL/hLPS}$OMM caused no changes in the Kiessig fringe of the reflectivity profile measured in D_2O. The reflectivity was measured at a single incident angle of 0.9° to have the peak flux in correspondence of the sharp dip of the Kiessig fringe, yielding better statistics but a smaller Q range.

Heating the $_{dPL/hLPS}$OMM to 37°C, in the absence of PmB, caused the Kiessig fringe to shift towards higher values of Q which corresponded to a decrease in total thickness of the model membrane, from ~68 Å to ~60 Å (**Fig 3.11a**, **Table 3.3**) as described by the parameters obtained from the fits to the data. The contrast provided by the asymmetric isotopic distribution in the hydrophobic region of the bilayer enabled the assignment of the main thickness changes to the LPS outer leaflet, which decreased by ~6 Å. The $_{dPL/hLPS}$OMM maintained a high level of lipid asymmetry upon heating to 37°C and no deuterated material was detected in the LPS outer leaflet as indicated by its fitted SLD value.

Contrary to what observed at room temperature, the addition of PmB to the $_{dPL/hLPS}$OMM at 37°C caused a prominent shift of the Kiessig fringe towards higher Q values (**Fig. 3.11b**). The comparison between the SLD profiles of the $_{dPL/hLPS}$OMM at 37°C before and after the addition of PmB indicated a substantial disruption of the bilayer with a significant loss of lipid asymmetry and a further decrease in total thickness from ~60 Å to ~53 Å. The final isotopic composition of the hydrophobic core of the PmB-treated bilayer, described by its SLD, showed ~30% of hydrogenous hydrocarbons (LPS and PmB tails) penetrating in the inner leaflet while the outer leaflet gained ~27% of deuterated material (phospholipids tails). The inner and outer bilayer head groups exhibited a concomitant loss of asymmetry revealed by the convergence in size and SLD of these regions to values intermediate between those of LPS and phospholipids as a result of the leaflet mixing (**Table 3.3**). The picture that emerges from the fits to the data indicates that PmB was able to cause the lipids in the outer leaflet and those in the inner leaflet to lose the initial asymmetric distribution yielding a more symmetric, mixed bilayer. Although the lipids underwent a profound rearrangement within the bilayer, the water content within the hydrophobic region did not change after the antimicrobial interaction (**Table 3.3**). Although PmB has detergent-like properties, this did not result in a major removal of lipids from the silicon substrate. The presence, within the $_{dPL/hLPS}$OMM, of both hydrogenous and deuterated material did not make it possible to clearly understand the extent of PmB insertion in the model membrane, which is examined later on in the chapter when discussing the results on a fully deuterated OMM.

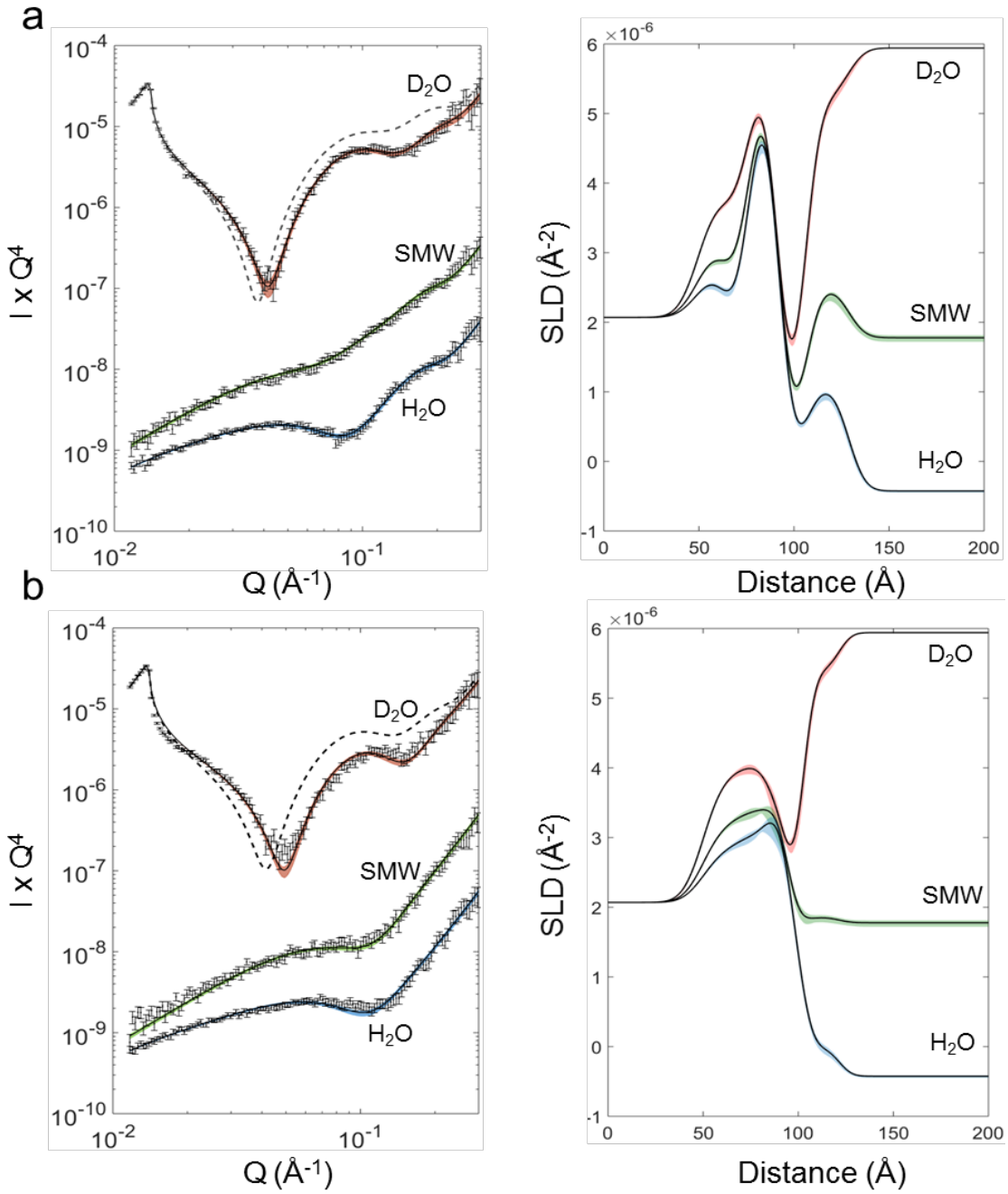

Figure 3.11 | PmB effect on $_{dPL/hLPS}$OMM at 37°C.

Neutron reflectivity data points, best fit lines (left) and corresponding SLD profiles (right) from the $_{dPL/hLPS}$OMM at 37°C before (**a**) and after (**b**) the addition of 100 µg/ml PmB. The dashed lines in **a** and **b** represent the reflectivity measured at room temperature and at 37°C respectively, to highlight the effect of heating and PmB addition on the shift of the Kiessig fringe measured in D_2O. Reflectivity curves are offset vertically for clarity

Table 3.3 | Parameters derived from the fitting of the reflectivity data from the $_{dPL/hLPS}$OMM.

The substrate parameters describe the silicon surface and are assumed not to vary with temperature or PmB addition. The total bilayer thickness is calculated by summing the thickness of the various components of the bilayer. The SLD of the silicon oxide is fixed to that of its calculated value. In brackets are the 95% confidence intervals derived from the Bayesian error analysis.

Substrate parameters	Fitted value
Substrate roughness (Å)	8.5 (8.2, 8.8)
Silicon oxide SLD ($Å^{-2}x10^{-6}$)	3.41
Silicon oxide thickness (Å)	18.9 (18.5, 19.3)
Silicon oxide hydration (%)	16.7 (16.0, 17.3)

Bilayer parameters	Fitted value at RT	Fitted value at 37°C	Fitted value at 37°C+PmB
dDPPC HG thickness (Å)	8.0 (7.8, 8.1)	7.2 (7.0, 7.6)	15.0 (14.7, 15.55)
dDPPC HG SLD ($Å^{-2}x10^{-6}$)	1.82 (1.76, 1.89)	1.76 (1.59, 1.95)	3.71 (3.62, 3.83)
dDPPC HG coverage (%)	50.9 (48.9, 53.4,)	64.2 (61.3, 66.5)	84.5 (83.4, 85.4)
dDPPC tails thickness (Å)	17.3 (16.8 18.0)	16.0 (15.7, 16.5)	10.6 (10.1, 11.2)
dDPPC tails SLD ($Å^{-2}x10^{-6}$)	6.13 (6.00 6.26)	5.84 (5.68, 5.99)	3.47 (3.16, 3.69)
LPS tails thickness (Å)	15.6 (15.4, 15.8)	12.6 (12.4, 12.9)	7.5 (6.8, 8.1)
LPS tails SLD ($Å^{-2}x10^{-6}$)	-0.08 (-0.08, -0.07)	-0.39 (-0.4, -0.39)	1.71 (1.52, 1.93)
LPS HG thickness (Å)	26.9 (26.1, 27.6)	23.9 (23.1, 24.7)	19.6 (18.7, 20.0)
LPS HG SLD in D_2O ($Å^{-2}x10^{-6}$)	4.92 (4.8, 5)	4.72 (4.57, 4.85)	2.87 (2.65, 3.11)
LPS HG coverage (%)	51.0 (49.5, 52.6)	53.3 (51.7, 54.7)	17.2 (15.2, 19.3)
Bilayer coverage (%)	99.3 (98.1, 100)	99.3 (97.9, 100)	98.7 (96.6, 100)
Bilayer roughness (Å)	5.5 (5.3, 5.6)	6.9 (6.7, 7.1)	5.2 (5.0, 5.4)
Tot. bilayer thickness	67.8	59.7	52.7

The critical temperature effect was confirmed by stepwise heating the model membrane in the presence of the antibiotic while monitoring the neutron reflectivity from the bilayer in D_2O (**Fig. 3.12a**). Stepwise increases in temperature caused the Kiessig fringe to progressively shift to higher values of Q. The plot of the barycentric mean of the Kiessig fringe revealed a sigmoidal trend of the shift with a mid-point at 36.5°C (see section 2.7.4 for details on barycentric mean calculations) (**Fig. 3.12b**). In the presence of the lipopeptide, minor changes occurred between 20°C and 28°C, while between 32°C and 40°C the reflectivity altered significantly. The concentration dependency of PmB effects at physiological temperature was assessed by adding increasing amounts of PmB to the $_{dPL/hLPS}$OMM at 37°C (**Fig. 3.12c**).

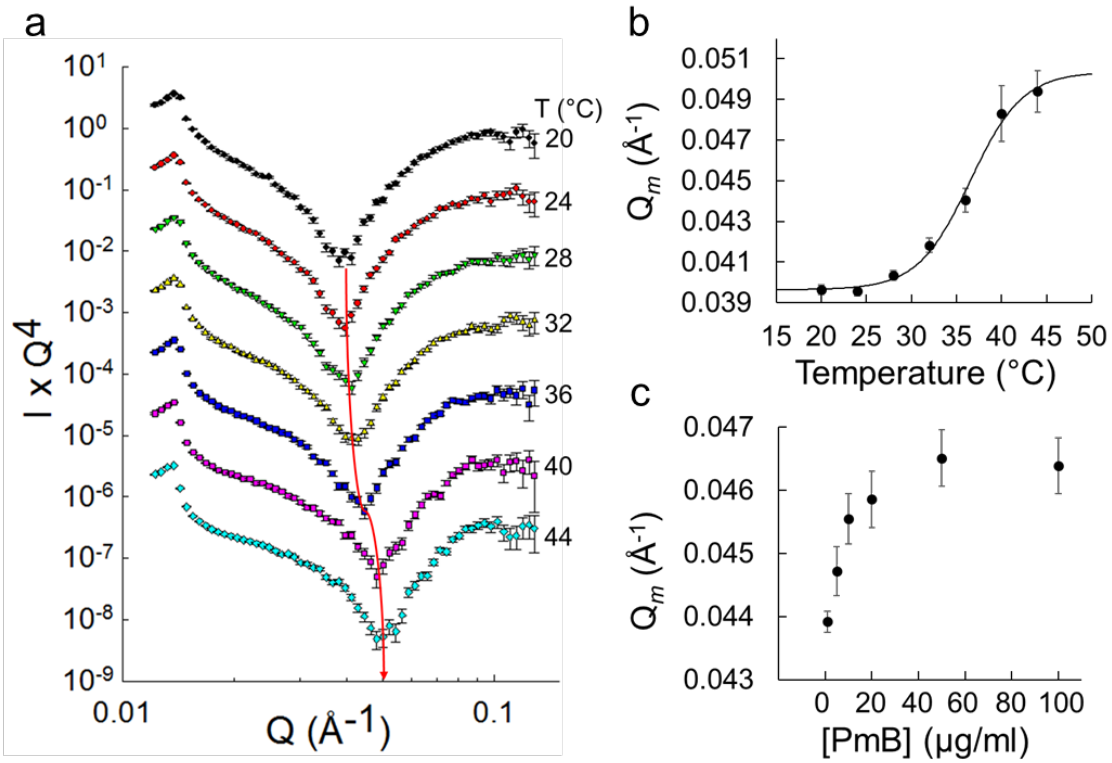

Figure 3.12 | Temperature and concentration dependence of PmB effects on $_{dPL/hLPS}$OMM.

(**a**) Reflectivity profile measured in D_2O from the $_{dPL/hLPS}$OMM in the presence of 100 μg/ml PmB at increasing temperature. The red arrow is a guide to the eye and follows the shift of the Kiessig fringe. Reflectivity curves are offset vertically for clarity (**b**) Plot of the shift in Q of the fringe shown in **a** quantified as the barycentric mean of the data (see Methods). (**c**) Shift in barycentric mean Q of the Kiessig fringe from a $_{dPL/hLPS}$OMM sample titrated with increasing amounts of PmB at 37°C. The error bars in **b** and **c** indicate the error of the respective neutron intensity profiles.

The effects of the antimicrobial on the reflectivity from the model OM were already evident at 5 μg/ml and reached saturation at 50 μg/ml. Increasing the concentration from 50 μg/ml to 100 μg/ml did not cause any significant further change in the reflectivity signal (**Fig. 3.12c**).

Contrary to what observed with PmB, when the model membrane was treated with PmB deacylated analogue, PmBN, this did not cause any observable effects on the membrane asymmetry as shown by the SLD profiles (**Fig. 3.13**). Only the thinning of the membrane caused by the heating was evident at 37°C in the presence of PmBN.

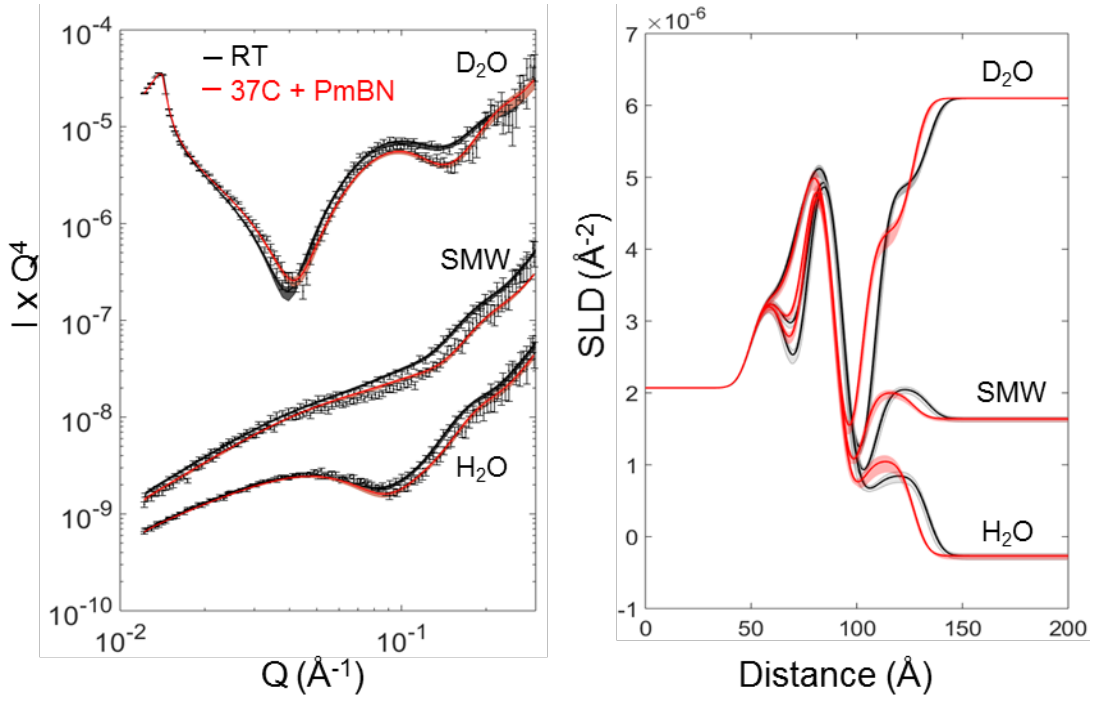

Figure 3.13 | Effects of PmBN on $_{dPL/LPS}$OMM.

Neutron reflectivity data points, best fit lines (left) and corresponding SLD profiles (right) from the $_{dPL/hLPS}$OMM at RT (black) and after heating to 37°C in the presence of 100 µg/ml PmBN (red). Reflectivity curves are offset vertically for clarity

3.2.3 Fully deuterated OM model bilayers ($_{dPL/dLPS}$OMM)

The disruption of the $_{dPL/hLPS}$OMM by PmB was accompanied by a substantial loss of lipid asymmetry upon binding of the antimicrobial to the model OM at body temperature. The isotopic contrast between the d_{62}DPPC and RaLPS enabled the determination of critical aspects of the PmB-LPS interaction but at the same time presented one drawback. It was not possible to determine whether the hydrogenous PmB had penetrated into the inner leaflet, or if the reduction in the SLD of the deuterated layer was solely due to the mixing of LPS. The similar SLD of PmB and hydrogenous LPS prevented the determination of the relative position of PmB and LPS tails into the mixed bilayer. To provide complementary information to the data obtained with the $_{dPL/hLPS}$OMM, the effects of PmB were studied on a fully deuterated OM model ($_{dPL/dLPS}$OMM), in which both phospholipids and LPS were labelled with deuterium, leaving PmB the only hydrogenous component in the system.

3.2.3.1 Characterisation of deuterium labelled LPS

Creating a $_{dPL/dLPS}$OMM required the production of deuterium labelled RaLPS (dRaLPS), which, unlike some phospholipids, is not available commercially. A rough *E. coli* strain (BW25113), which produces rough LPS with a complete core oligosaccharide (Chang *et al.*, 2010), was therefore adapted to grow into 98% D_2O in order to replace the majority of hydrogen atoms with deuterium in its cellular components. The use of hydrogenous carbon source in the culture media, means that the components are not fully deuterated. dRaLPS was extracted and purified according to (Le Brun *et al.*, 2013) as described in the Methods and the final product was characterised by TLC, DOC PAGE and FTIR. Migration of dRaLPS extract on DOC PAGE showed no differences from commercial hydrogenous RaLPS and from the RaLPS fraction of wild type smooth LPS (**Fig. 3.14a**). Similarly, no differences were detected in the TLC elution profile of the lipid A moiety of hydrogenous and dRaLPS obtained by mild acid hydrolysis (**Fig. 3.14b**). Although RaLPS and dRaLPS appeared identical by TLC and DOC PAGE, when characterised by FTIR spectroscopy, the absorption spectra of the two lipids confirmed the major difference in hydrogen and deuterium contents. RaLPS showed the peaks characteristic of the C-^{1}H stretching vibrations between 3000 and 2800 cm^{-1}, whilst the spectra of dRaLPS displayed a much weaker signal in the C-^{1}H stretching vibration region and an additional intense set of peaks in the C-^{2}H stretching vibration region (2000-2300 cm^{-1}), indicating the successful replacement of hydrogen by deuterium in the molecule (**Fig. 3.14c**). Based on the reduction in area under the peaks of the C-^{1}H signal in the spectra of dRaLPS, the level of deuteration was estimated to be ~93%.

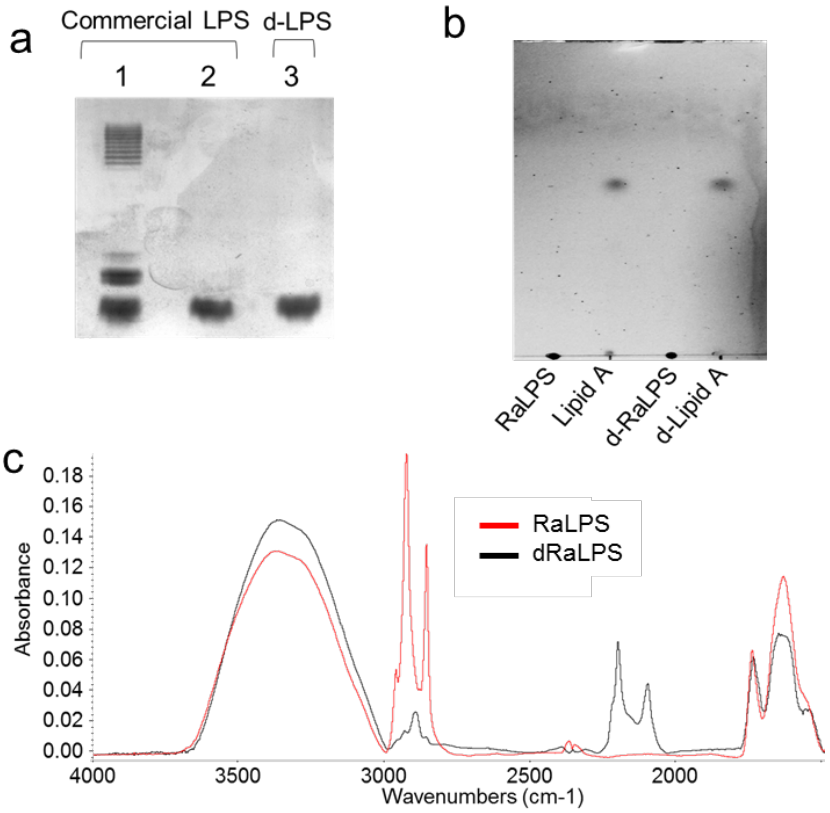

Figure 3.14 | Characterisation of deuterium labelled RaLPS.

(**a**) Silver stained DOC PAGE of wild type smooth LPS (lane 1), RaLPS (lane 2) and dRaLPS (lane 3) showing no difference in the migration of RaLPS band between the three species (**b**) TLC of dRaLPS and RaLPS and respective lipid A moieties obtained by mild acid hydrolysis showing no difference in the migration of the lipid A moiety. No migration is expected for RaLPS before hydrolysis in the mobile phase containing chloroform, methanol and water (60:39:1 v:v:v) due to high hydrophilicity of the LPS head group. (**c**) FTIR spectra of hydrogenous (red) and deuterated (black) RaLPS.

3.2.3.2 Characterisation of $_{dPL/dLPS}$OMM

The purified dRaLPS was used to produce a perdeuterated $_{dPL/dLPS}$OMM using the same LB/LS deposition described earlier for its isotopically asymmetric counterpart $_{dPL/hLPS}$OMM. **Figure 3.15** shows the NR data, best fit lines and SLD profile of the $_{dPL/dLPS}$OMM collected in H_2O, D_2O and SMW. The thickness of each region of the bilayer was in agreement with that measured for the $_{dPL/hLPS}$OMM in section 3.2.2, however, the SLD of the LPS leaflet was substantially higher, in line with the high deuterium content measured by FTIR. The SLD of the dRaLPS acyl tails was found to be $6.23*10^{-6}$ Å^{-2}, indicating a similar level of deuteration to that of commercial d_{62}DPPC which yielded an SLD of the tail region of $6.37*10^{-6}$ Å^{-2}.

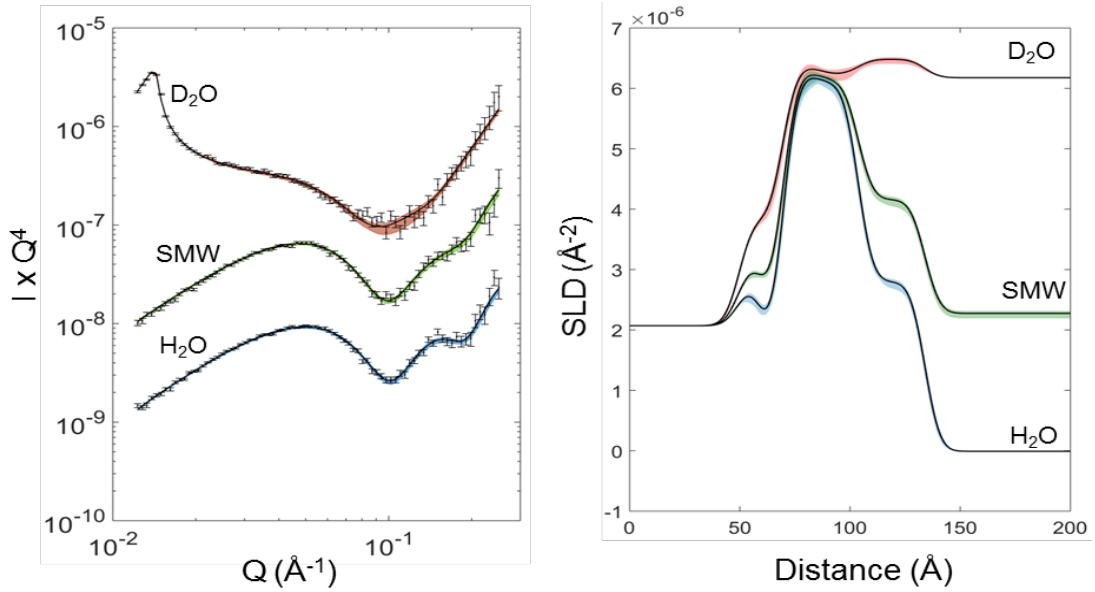

Figure 3.15 | NR of $_{dPL/dLPS}$OMM at RT.

Neutron reflectivity data points, best fit lines (left) and corresponding SLD profiles (right) for the $_{dPL/dLPS}$OMM. Reflectivity curves are offset vertically for clarity

3.2.3.3 Interaction of PmB with $_{dPL/dLPS}$OMM

As in the case of the isotopically asymmetric bilayer, addition of 100 µg/ml PmB to the $_{dPL/dLPS}$OMM at room temperature, left the reflectivity unaffected, indicating the same lack of interactions measured earlier (**Fig. 3.16**). Heating the $_{dPL/dLPS}$OMM to 37°C in the absence of PmB had a similar effect on the membrane structure to that observed on the isotopically asymmetric model as the overall thickness of the dRaLPS leaflet decreased by ~7 Å (**Fig. 3.17a**, **Table 3.4**). Together with the thickness reduction, the SLD of the outer leaflet also decreased from ~6.22 *10^{-6} Å^{-2} to ~5.61*10^{-6} Å^{-2} whilst that of the d_{62}DPPC inner leaflet remained largely unchanged. Unlike in the case of the $_{dPL/hLPS}$OMM, the changes in SLD observed upon heating the $_{dPL/dLPS}$OMM could not be caused by the mixing of hydrogenous and deuterated material given the absence of hydrogenous molecules. Thus the ~10% reduction in the dRaLPS tails SLD could only be due to a decrease in the density of the acyl chain region of LPS of a similar magnitude. The reduction in thickness and density observed in the RaLPS leaflet upon heating, both pointed to a potential phase transition from the gel to the liquid phase.

Contrary to the $_{dPL/hLPS}$OMM, the absence of a hydrogenous layer in the $_{dPL/dLPS}$OMM does not give rise to a Kiessig fringe in the D_2O contrast. The high deuterium content of the lipid bilayer however, makes the H_2O data very sensitive to alterations of the membrane structure.

In H_2O, the intensity of the reflected signal is proportional to the difference in SLD between the deuterium rich lipid layer and the hydrogen rich solution. The reduction in SLD and thickness of the LPS leaflet, translated to a lowered overall reflectivity signal in H_2O (**Fig. 3.17a**). Upon addition of PmB at 37°C a further reduction in the intensity of the reflectivity in H_2O indicated an additional reduction in thickness and SLD of the bilayer (**Fig. 3.17b**).

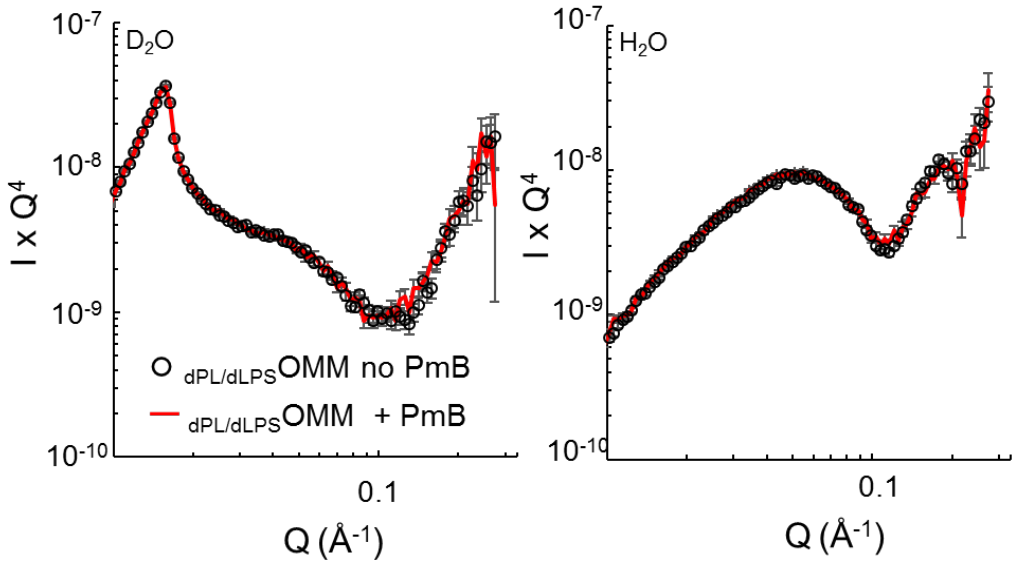

Figure 3.16 | Lack of PmB effect on $_{dPL/dLPS}$OMM at RT.

Addition of 100 µg/ml PmB to the $_{dPL/dLPS}$OMM at RT caused no changes in the reflectivity profiles measured in D_2O (left) and in H_2O (right)

The fit to the data revealed a decrease in the total bilayer thickness of 15 Å. Interestingly, only the SLD of the LPS leaflet decreased from 5.61 $*10^{-6}$ $Å^{-2}$ to 4.23 $*10^{-6}$ $Å^{-2}$ whilst that of the inner leaflet remained unchanged suggesting that the hydrogen rich PmB penetrated almost exclusively into the LPS outer leaflet. The information provided by the structural changes in the head group regions however, indicated mixing of lipids of the two leaflets. As for the $_{dLP/hLPS}$OMM, the convergence in size and SLD of the head group regions to values intermediate between those of LPS and phospholipids confirmed the mixing of the leaflets (**Table 3.4**). Using a similar approach to that employed previously with the isotopically asymmetric membranes shown in **Fig. 3.12**, the effect of stepwise heating the membrane in the presence of PmB and that of titrating the bilayer with increasing antibiotic concentration at 37°C was examined (**Fig. 3.18**).

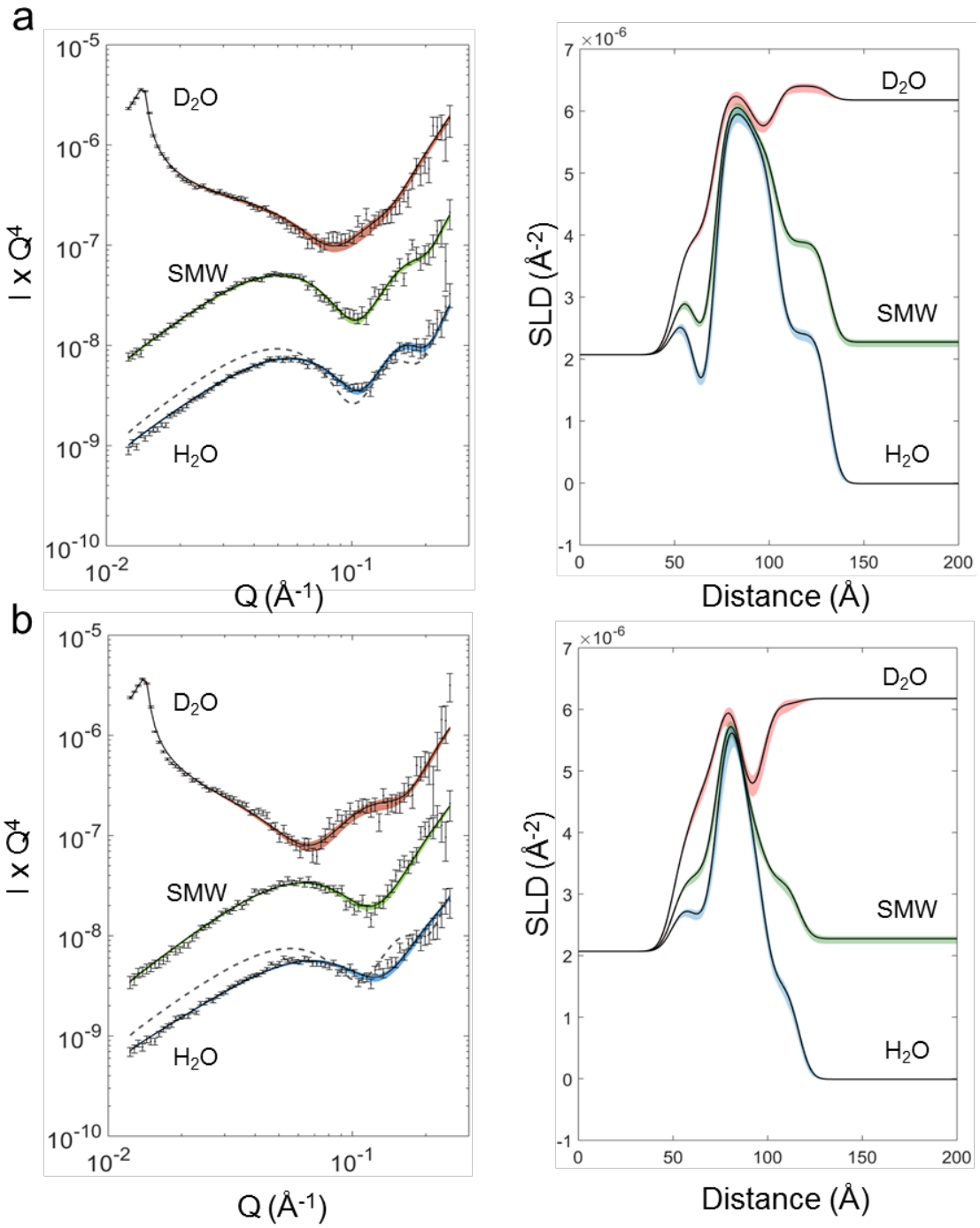

Figure 3.17 | PmB effect on $_{dPL/dLPS}$OMM at 37°C.

Neutron reflectivity data points, best fit lines (left) and corresponding SLD profiles (right) from the $_{dPL/dLPS}$OMM at 37°C before (**a**) and after (**b**) the addition of 100 µg/ml PmB. The dashed lines in **a** and **b** represent the reflectivity measured at room temperature and at 37°C respectively, to show the effect of heating and PmB addition on the reduction in the reflected intensity measured in H_2O. Reflectivity curves are offset vertically for clarity

Table 3.4 | Parameters derived from the fitting of the reflectivity data from the $_{dPL/dLPS}$OMM. The substrate parameters describe the silicon surface and are assumed not to vary with temperature or PmB addition.

The substrate parameters describe the silicon surface and are assumed not to vary with temperature or PmB addition. The total bilayer thickness is calculated by summing the thickness of the various components of the bilayer. The SLD of the silicon oxide is fixed to that of its calculated value. In brackets are the 95% confidence intervals derived from the Bayesian error analysis.

Substrate parameters	Fitted value
Substrate roughness (Å)	5.4 (5.1, 5.7)
Silicon oxide thickness (Å)	11.2 (10.4, 11.9)
Silicon oxide SLD ($Å^{-2}x10^{-6}$)	3.41
Silicon oxide hydration (%)	16.6 (15.9, 17.3)

Bilayer parameters	Fitted value at RT	Fitted value at 37°C	Fitted value at 37°C + PmB
dDPPC HG thickness (Å)	8.0 (7.8, 8.2)	9.9 (9.5, 10.4)	12.3 (12.0, 12.8)
dDPPC HG SLD ($Å^{-2}x10^{-6}$)	1.91 (1.78, 2.08)	1.50 (1.44, 1.56)	3.99 (3.80, 4.18)
dDPPC HG coverage (%)	59.7 (56.2, 63.0)	46.0 (43.9, 48.0)	61.7 (60.5, 63.2)
dDPPC tails thickness (Å)	17.3 (16.0, 18.4)	19.7 (19.2, 20.0)	12.6 (11.9, 13.4)
dDPPC tails SLD ($Å^{-2}x10^{-6}$)	6.37 (6.21, 6.52)	6.29 (6.19, 6.40)	6.31 (6.11, 6.49)
dLPS tails thickness (Å)	17.2 (16.5, 18.0)	12.6 (12.2, 13.0)	11.0 (10.5, 11.4)
dLPS tails SLD ($Å^{-2}x10^{-6}$)	6.23 (6.15, 6.33)	5.61 (5.51, 5.72)	4.23 (3.98, 4.46)
dLPS HG thickness (Å)	30.3 (29.8, 30.9)	27.9 (27.4, 28.4)	19.2 (17.8, 20.4)
dLPS HG SLD in D_2O ($Å^{-2}x10^{-6}$)	6.64 (6.58, 6.70)	6.58 (6.50, 6.65)	6.06 (5.87, 6.27)
dLPS HG coverage (%)	80.5 (79.8, 81.2)	74.0 (72.2, 76.2)	50.4 (47.1, 54.0)
Bilayer coverage (%)	97.6 (98.1, 100)	95.7 (95.0, 96.6)	98.1 (95.9, 99.8)
Bilayer roughness (Å)	5.4 (5.0, 5.7)	4.7 (4.6, 4.9)	5.0 (4.8, 5.4)
Tot. bilayer thickness	72.8	70.1	55.1

Due to the absence of the Kiessig fringe in the fully deuterated OM model, changes in the reflectivity were quantified by the reduction in intensity of the reflected signal in H_2O. In particular the area under each curve was taken as a measure of the total reflected intensity. In the presence of 100 µg/ml of PmB, stepwise increases in temperature caused the reflected intensity to progressively attenuate. The plot of the area under the curves revealed a sigmoidal trend of the shift, with a mid-point at 33.3°C (**Fig. 3.18a**).

The concentration dependency of PmB effects was assessed by adding increasing amounts of PmB to the $_{dPL/dLPS}$OMM at 37°C whilst monitoring the reflectivity in H_2O (**Fig. 3.18b**). The progressive attenuation of the reflectivity was significant between 0 and 20 µg/ml whilst only minor changes occurred by increasing the concentration to 50 µg/ml and 100 µg/ml. Comparing the relative trend of attenuation of the reflected intensity reported here (**Fig. 3.18**) to that of the Kiessig fringe shift described in section 3.2.2.1 (**Fig. 3.12**) highlights the similarities in the changes measured. For the $_{dPL/hLPS}$OMM the barycentric mean of the Kiessig fringe shifted to higher values of Q whilst in the $_{dPL/dLPS}$OMM the reflectivity shifted

to lower values of intensity giving rise to the opposite trends. However, in both cases, the temperature ramps followed a sigmoidal trend with a mid-point of 36.5°C for the isotopically asymmetric membrane (**Fig. 3.12b)** and 33.3°C for the fully deuterated OM model (**Fig. 3.18a**).

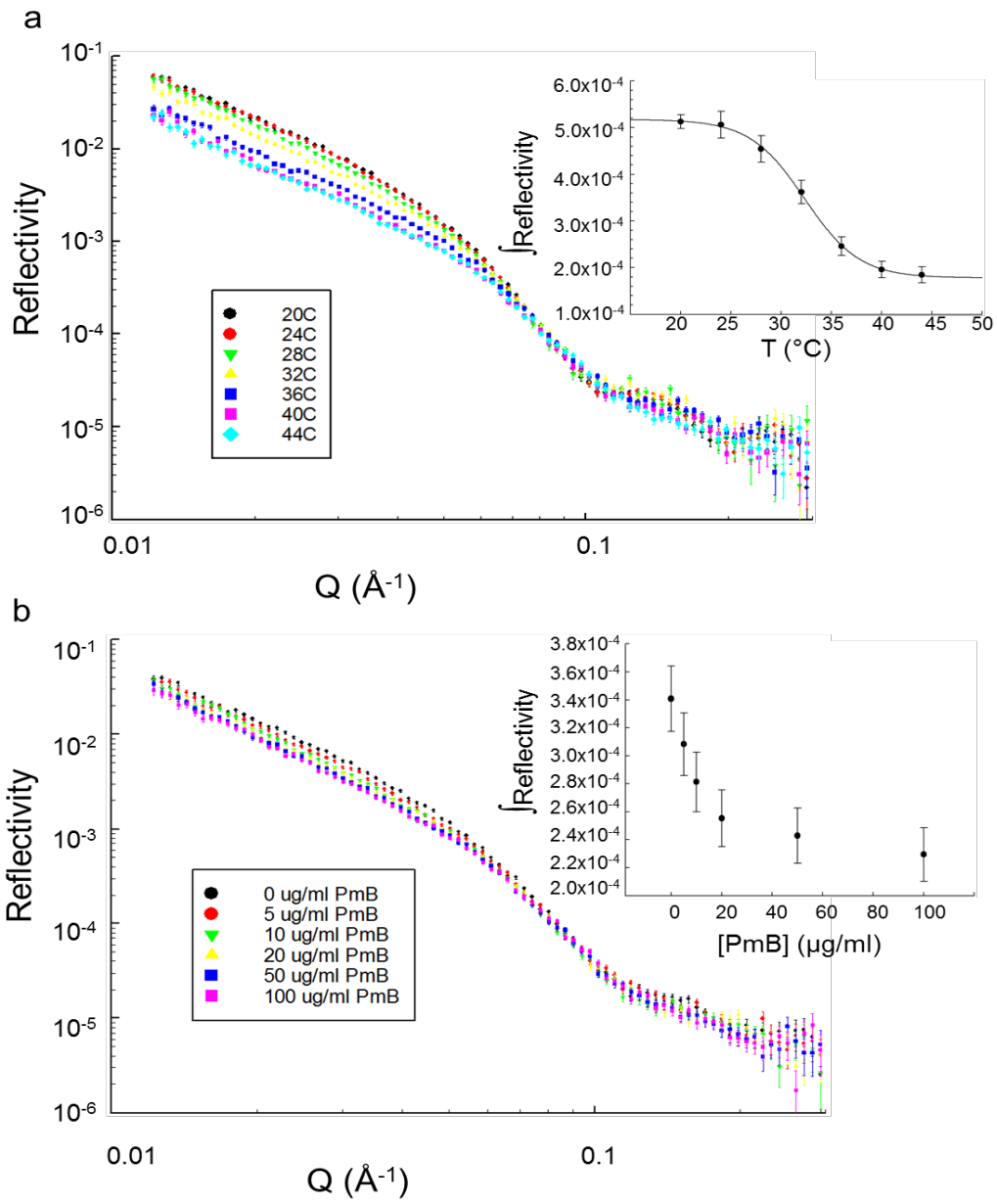

Figure 3.18 | Temperature and concentration dependence of PmB effects on $_{dPL/dLPS}$OMM.

(**a**) Reflectivity profile measured in H_2O for the $_{dPL/dLPS}$OMM in the presence of 100 µg/ml PmB at increasing temperature. The inset shows the plot of the reduction in the intensity of the reflectivity measured in H_2O and quantified as the area under each curve by the integral between Q values of 0.012 $Å^{-1}$ and 0.3 $Å^{-1}$. (**b**) Reflectivity profile measured in H_2O for the $_{dPL/dLPS}$OMM titrated with increasing amounts of PmB at 37°C. The inset shows the plot of the reduction in the intensity of the reflectivity measured in H_2O quantified as the area under each curve. The error bars in the plots shown in the insets indicated the error of the respective neutron intensity profiles.

Similarly, the plot of the titration curves displayed a similar concentration dependence with major shifts between 0 and 20 μg/ml of PmB and only minor changes upon increasing the antimicrobial concentration to 50 and 100 μg/ml (**Fig. 3.12c** and **3.18b**).

3.2.4 Phase behaviour of OM models

To complement the structural data obtained by NR on the model membranes, the dynamics of the systems were investigated by ATR-FTIR. ATR-FTIR can be used to measure the transition of lipids from the liquid to gel state thanks to the difference in the IR absorption characteristic of fluid-like and solid-like hydrocarbons (Coates, 2006). The isotopically asymmetric leaflets (^{1}H vs.^{2}H) of the $_{dPL/hLPS}$OMM generate distinct IR signals that enable differentiation between the acyl chains of the phospholipids and those of the LPS allowing monitoring of the dynamics of each leaflet independently. The IR spectrum of the $_{dPL/hLPS}$OMM clearly displayed the distinct LPS C-^{1}H stretching vibrations between ~3000 cm^{-1} and ~2800 cm^{-1} and the deuterated phospholipid C-^{2}H stretching vibrations between ~2250 cm^{-1} and ~2050 cm^{-1} (**Fig. 3.19a**). The peak absorbance of the H-C-H symmetric bond stretching is strongly affected by the ordering of the aliphatic hydrocarbons and undergoes an abrupt 3-4 cm^{-1}shift as the acyl chains undergo the gel to liquid phase transition (**Fig. 3.19b**) (Brandenburg and Seydel, 1990). As the temperature of the $_{dPL/hLPS}$OMM was gradually increased from 20°C to 55°C, both leaflets of the bilayer changed from gel to liquid disordered states (**Fig. 3.19c**). As expected, the synthetic phospholipid displayed a sharp transition while the chemically heterogeneous, RaLPS extract displayed a more gradual peak shift. The mid-points (T_m) calculated from non-linear regressions of data from two independent samples showed a T_m of 36.2 ±1.6°C and 39.3 ± 0.4°C for RaLPS and tail d_{62}DPPC respectively, in good agreement with data published for the two separate lipids in suspension (Guard-Friar *et al.*, 1985; Brandenburg and Seydel, 1990). Cooling down the lipids at room temperature caused the peaks to return to the original position, confirming the reversibility of the measured phase transition (**Fig. 3.19d**). The same experiment on the $_{LPS}$HBM, showed a similar transition to the liquid crystalline phase upon heating to physiological temperature (**Fig. 3.19e**). This implies that PmB disruption of the self-assembled model membrane took place in the gel phase, rather than requiring a liquid crystalline phase as observed with the $_{dPL/hLPS}$OMM and the $_{dPL/dLPS}$OMM. Lastly, to further test the hypothesis on the critical role of controlled molecular assembly in regulating PmB penetration of OM models, the interaction of the antibiotic with the $_{dPL/hLPS}$OMM was

investigated using ATR-FTIR. Unlike with the $_{LPS}$HBM, no PmB binding was detected until the $_{dPL/hLPS}$OMM was taken through its thermal phase transition (**Fig. 3.19f**), in line with the NR data.

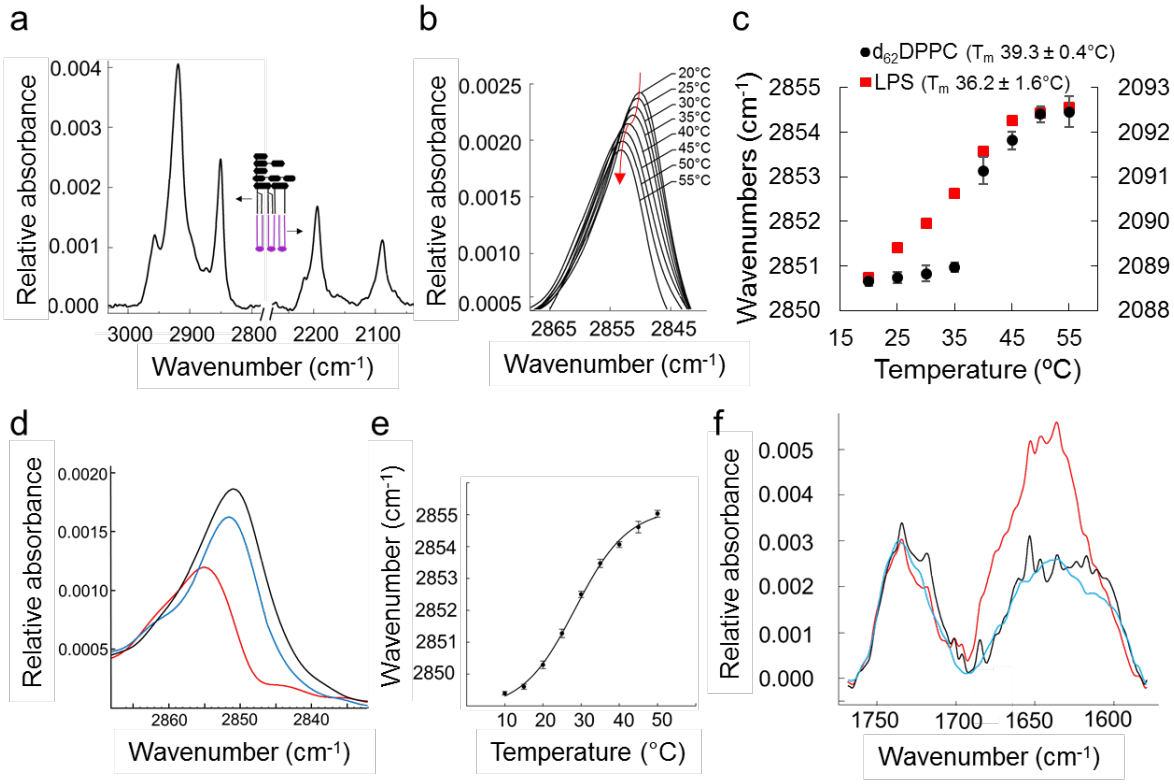

Figure 3.19 | Phase transition of OM models measured by ATR-FTIR.

(**a**) ATR-FTIR absorption spectra of a $_{dPL/LPS}$OMM. The two main peaks on the left are the C-^{1}H bond vibrations of the asymmetric (~2920 cm^{-1}) and symmetric (~2850 cm^{-1}) ^{1}H-C-^{1}H stretching modes, arising from the acyl chains of LPS. On the right, the asymmetric (~2193 cm^{-1}) and symmetric (~2088 cm^{-1}) ^{2}H-C-^{2}H stretching modes of the tail deuterated phospholipids (**b**) Peak absorption of the LPS ^{1}H-C-^{1}H symmetric stretching vibration measured between 20°C and 55°C. The red arrow follows the shift and is only a guide to the eye (**c**) Phase transition of RaLPS (red squares, left Y axis) and d_{62}DPPC (black circles, right Y axis) measured by the peak shift of the symmetric ^{1}H-C-^{1}H and ^{2}H-C-^{2}H stretching modes as a function of temperature (mean and SE of 5 measurements).T_m are calculated from the standard error of two independent samples, only one of which is shown here (**d**) CH_2 symmetric vibration signal before heating (black) at 55°C (red) and after cooling back to room temperature (blue) indicating the reversibility of the phase transition in the $_{dPL/hLPS}$OMM (**e**) Phase transition of RaLPS in the $_{LPS}$HBM showing a similar transition displayed by the $_{dPL/hLPS}$OMM (**f**) Infrared spectra of a $_{dPL/hLPS}$OMM before (black) and after (blue) the addition of PmB at RT and after cycling the bilayer once through its phase transition (red). The increase in the amide band signal at 1650 cm^{-1}, characteristic of the PmB binding, becomes apparent only after the phase transition has occurred.

3.3 DISCUSSION

Generally, a drug's cell membrane permeability is simply related to its hydrophobicity or LogP (octanol/water partition coefficient) but antibiotics are more polar than other drug categories (O'Shea and Moser, 2008). For Gram-negative bacteria this is because the majority of antibiotics enter via water filled pores within OM proteins that only allow diffusion of small (<600 Da), water soluble molecules (Nikaido, 1993). Although antibiotics following this route are numerous and chemically varied, their common pathway gives them a shared vulnerability to simple mutations in the pore proteins (Pages *et al.*, 2008). The only large, polar antibiotic used against Gram-negative infections is PmB (1.2 kDa) which directly targets LPS in the OM to promote its uptake and currently provides the clearest model for the development of new molecules that can avoid the limitations of the OM restricted access (Velkov *et al.*, 2014). A better understanding of the physical chemistry of the OM and its interactions with PmB is thus critical to open up the non-protein pore route into Gram-negative bacteria.

Here, the interaction of the last resort antibiotic PmB with the Gram-negative cell envelope was studied using two types of *in vitro* models of the OM. The first model was an RaLPS monolayer self-assembled on a hydrophobic surface ($_{LPS}$HBM). After characterising the formation of the $_{LPS}$HBM, the effects of the antimicrobial were investigated by SPR, ATR-FTIR and NR at room temperature. The biophysical characterisation of the LPS assembly by vesicle fusion indicated the formation of high coverage monolayers on the hydrophobic substrates (**Fig. 3.2a, 3.4** and **3.5b**). SPR revealed the concentration dependent binding of PmB to the $_{LPS}$HBM, which occurred between 0 and 10 µg/ml, in line with the antibiotic minimum inhibitory concentrations (MIC) of ~2 µg/ml effective *in vivo* (**Fig. 3.7a**) (Velkov *et al.*, 2014). PmB deacylated analogue PmBN, displayed unstable binding and no saturation of the $_{LPS}$HBM, indicating the critical role of PmB hydrophobic tail in the specific interaction with LPS (**Fig. 3.7b**). The increased disorder of the acyl chain region of LPS measured by ATR-FTIR upon binding of the antimicrobial, suggested the intercalation of PmB disordered acyl tail into the LPS hydrophobic region (Meredith *et al.*, 2009) (**Fig. 3.6a**). This was supported also by the induced expansion of the hydrocarbon region detected by NR (**Fig. 3.8, Table 3.1** and **3.2**). Overall, the combined biophysical analysis clearly revealed binding of the antimicrobial to the LPS monolayer at room temperature, indicating a stable interaction and the intercalation of PmB in the $_{LPS}$HBM. The data outlined the formation of

a PmB-LPS complex which is in line in with molecular models based on NMR data, where the antimicrobial binds LPS with its acyl tail intercalated in the LPS hydrophobic region and the peptide moiety bound to the anionic inner core oligosaccharide (Pristovsek and Kidric, 1999; Mares *et al.*, 2009). However, as suggested by the lower than expected SPR response, the structural analysis by NR showed that self-assembly did not yield an optimal arrangement of LPS in the monolayer indicating a sub optimal packing of the leaflet which would facilitate PmB penetration.

Studying the same interaction using a more realistic asymmetric OM model ($_{PL/LPS}$OMM) assembled via controlled deposition through sequential Langmuir-Blodgett and Langmuir-Schaefer monolayer transfers, revealed a radically different picture. Addition of PmB (100 µg/ml) to the $_{dPL/LPS}$OMMs, under the same conditions of the $_{LPS}$HBM, did not have any detectable effects on the model membrane as shown by NR and ATR-FTIR (**Fig 3.10, 3.16** and **3.19f**). This result was rather surprising as the concentration used was ~100 times higher than the MIC of the antibiotic, which is known to promote release of a substantial amount of periplasmic and cytoplasmic protein from *E. coli* at a concentration of 5 µg/ml (Sahalan and Dixon, 2008). Only heating the bilayer through its thermal phase transition enabled PmB to cause a substantial disruption of the membrane structure which resulted in thinning of the membrane and loss of lipid asymmetry as shown by the NR experiments on the $_{dPL/hLPS}$OMM and the $_{dPL/dLPS}$OMM, summarised in **Figure 3.20**. It was clear from the NR experiments that PmB was able to disrupt the asymmetric OM models only when the LPS was in the fluid state whilst having no effect on the OM model in the gel phase. In particular the model independent analysis of the NR data showed that the temperature dependent interaction of PmB with both the $_{dPL/hLPS}$OMM and the $_{dPL/dLPS}$OMM followed a sigmoidal trend which closely resembled the trend of the phase transition measured by ATR-FTIR (**Fig. 3.12a** and **b**, **3.18a**). The mid-point of the phase transition of the LPS leaflet in the $_{dPL/hLPS}$OMM was found to be 36.2°C which corresponded almost exactly to the mid-point of the fringe shift describing PmB disruption on the same model which was 36.5°C (**Fig. 3.18a**). The same sigmoidal trend was observed for the disruption of the $_{dPL/dLPS}$OMM, although with a slightly lower mid-point at 33.3°C, a difference which is likely due to the lower phase transition temperature of deuterated lipids compared to their hydrogenous analogues (Guard-Friar *et al.*, 1985).

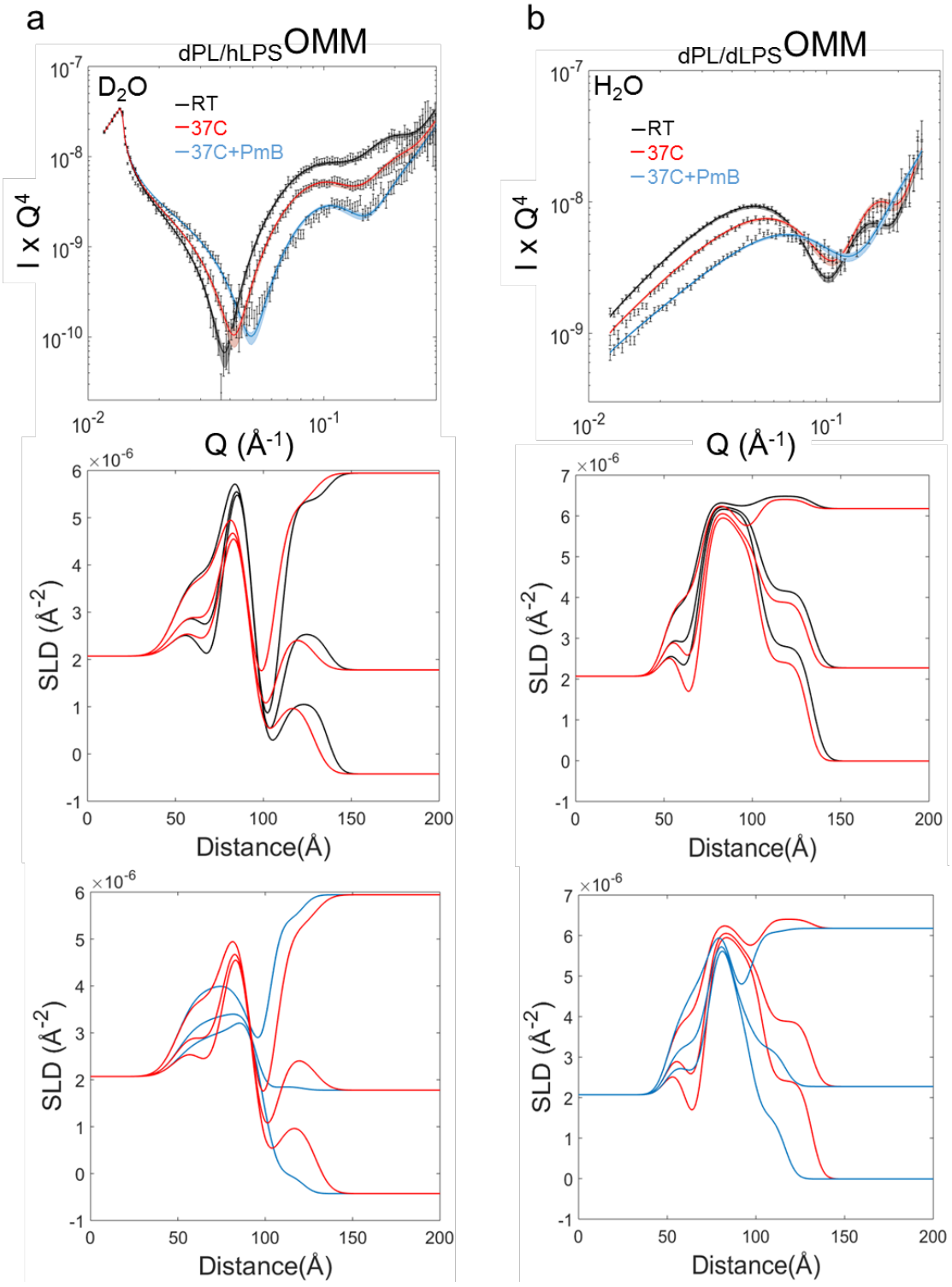

Figure 3.20 | Summary of PmB effects at 37°C.

Effects of sequentially heating to 37°C and adding PmB (100 μg/ml) to asymmetric OM models containing tail deuterated phospholipids and hydrogenous RaLPS (**a**) or deuterated RaLPS (**b**). Changes in the reflectivty upon heating and PmB addition (top), comparison of SLD profiles at RT, in black, and 37°C, in red, (middle) and comparison of SLD profiles at 37°C before and after PmB addition in red and blue respectively (bottom).

Although it is well established that plasma membranes are maintained in a liquid crystalline state in most organisms, the physical state of the OM remains unclear. Whilst some studies on isolated LPS showed a transition to a liquid crystalline phase at physiological temperature (Brandenburg and Seydel, 1990) others suggested that the structured OM remains in a gel-like state on the basis of its observed low permeability (Nikaido, 2003).

However, *in vivo,* the toxic effects of PmB have been shown to be highly dependent on temperature indicating a nearly all-or-none toxic effect on E. *coli* between 20°C and 35°C which has been suggested to depend on the transition of the OM from the gel to the fluid phase (Teubner and Bader, 1977; Hodate and Bito, 1982; Katsu *et al.*, 1984). The data reported here clearly shows the dependence of PmB effects on the phase transition of a realistic *in vitro* model of the OM, providing the first direct evidence of the substantial relevance of the liquid-crystalline state of the OM for the susceptibility towards a last resort drug such as PmB. It was previously believed that millimolar levels of divalent cations would raise the transition temperature of LPS well above physiological levels, therefore excluding the relevance of a liquid crystalline state under physiological conditions (Nikaido, 2003). The data shown here proved that even in the presence of 5 mM Ca^{2+} ions, LPS underwent a phase transition below 37°C.

Crucially, the critical effect of temperature on the interaction was only revealed by the experiments on the more accurate asymmetric OM model, whereas the self-assembled LPS monolayer displayed significant PmB binding in the gel phase at room temperature (**Fig. 3.8** and **3.19e**). These results highlighted the importance of using realistic OM models in order to replicate the behaviour of the natural OM and obtain biologically relevant information through biophysical investigation.

The highly cationic nature of PmB is regarded as its main driving force in the interaction with LPS and the first step of the binding is thought to be mediated by the electrostatic interaction (Velkov *et al.*, 2010; Yu *et al.*, 2015). This is also exemplified by the fact that the most well studied mechanisms of resistance towards PmB involve the reduction of LPS negative charge to prevent PmB binding (Gunn *et al.*, 1998; Trent *et al.*, 2001; Zhou *et al.*, 2001). However, the deacylated analogue of PmB, PmB nonapeptide (PmBN), which preserves the cationic nature of PmB but lacks the hydrophobic tail, is known to lack toxicity towards *E. coli* and only affects OM permeability at concentrations hundreds of times higher compared to PmB (Vaara, 1992). As shown here, PmBN only transiently binds LPS (**Fig.**

3.7b) and does not possess any membrane active properties under the conditions studied (**Fig. 3.13**). Therefore, the role of hydrophobic interactions is critical for the effects of PmB on the OM, as demonstrated by the crucial role of the OM phase transition for PmB activity.

As pan-resistant Gram-negative infections continue to spread, so does the use of last resort drugs such as PmB. This unavoidably leads to development of PmB resistant bacteria which in turn require development of PmB analogues capable of overcoming the resistance. In an effort to develop new effective PmB analogues, Velkov *et al* designed and synthesised PmB derivatives which were able to regain toxicity even towards organisms that had developed a high level of resistant against PmB (Velkov *et al.*, 2014). Interestingly, their strategy was based on the modification of the PmB scaffold with additional hydrocarbon moieties in order to potentiate the hydrophobic interaction with LPS. Following this strategy led to the identification of PmB analogues which were active against PmB resistant strains of *P. aeruginosa*, *A. baumannii* and *K. pneumoniae* with an MIC of 2-8 μg/ml, whereas PmB was not inhibitory evet at 128 μg/ml. These observations, together with the data presented here, indicate that hydrophobic forces are a crucial aspect of PmB mode of action and play a fundamental role in the development of new, much needed, effective antibiotics.

4 INTERACTION OF COLICIN N WITH OUTER MEMBRANE MODELS

4.1 INTRODUCTION

Colicins are antimicrobial proteins released by *E. coli* to kill closely related competing strains (Kim *et al.*, 2014). Their lethal function relies on the ability of these toxins to cross the Gram-negative outer membrane (OM), the largely impermeable and asymmetric lipid bilayer protecting Gram-negative bacteria which comprises an inner leaflet of phospholipids and an outer leaflet of lipopolysaccharides (LPS). Members of the colicin family are arranged in three structural and functional domains. The N-terminal translocation domain (T-domain) usually contains a disordered region that can interact with periplasmic proteins of the Tol or Ton families and often contains a terminal amino acid sequence that recognises a specific outer membrane protein that enables the trans-OM transport step (Raggett *et al.*, 1998; Housden *et al.*, 2010; Johnson *et al.*, 2013). The central domain is the receptor binding domain (R-domain) which usually binds tightly to an outer membrane protein and is assumed to be responsible for initially targeting the colicin to the OM (Kurisu *et al.*, 2003; Buchanan *et al.*, 2007).The C-terminal domain carries the toxic function which can be either plasma membrane pore-formation, nucleic acid degradation or peptidoglycan synthesis inhibition (Cascales *et al.*, 2007).

Colicin N (ColN) (**Fig. 4.1a**), is the smallest pore forming colicin (42 kDa) and translocates across the OM via the interaction of its T-domain with the OM protein F (OmpF) and the Tol pathway (Kim *et al.*, 2014). Interestingly, its outer membrane receptor was also thought to be OmpF until Sharma *et al* discovered that ColN only killed cells with a complete LPS core structure (Sharma *et al.*, 2009). Johnson *et al* were then able to show that this depended upon a precise recognition by ColN R-domain of the heptose (III) and glucose units at the boundary between the inner and outer core regions of the LPS oligosaccharide head group (**Fig. 4.1b**) (Johnson *et al.*, 2014). So far ColN is the only colicin that has been shown to use LPS as its primary receptor, whilst all other colicins exploit OM proteins in both the recognition and the translocation steps.

The aim of this study was to investigate the interaction of ColN with LPS in order to better understand the first steps of the antimicrobial's translocation through the Gram-negative cell envelope. To do so, the structural features of ColN binding to asymmetric OM models containing either LPS with the complete core oligosaccharide (RaLPS) or a truncated version missing the ColN binding epitope (RdLPS) (**Fig. 4.1b**), were studied by neutron

reflectometry (NR). Due to the elongate shape of ColN, the thickness of the protein layer adsorbed on the membrane provided information on the orientation of the protein bound to OM models under different conditions of accessibility its binding sites. The toxicity of ColN mutants bearing mutations in a region within the R-domain, which was shown by preliminary data to be important for ColN activity, was tested using a liquid culture assay. Finally, the LPS-binding ability of ColN proteins with reduced antibacterial activity was assessed by surface plasmon resonance (SPR) which confirmed that a short amino acid sequence was critical for both toxicity and LPS-binding. The initial measurements on the interaction of ColN with Ra and Rd LPS OM models were carried out by Dr. Luke Clifton and Dr. Max Skoda and the data have been published during the course of my PhD (Clifton *et al.*, 2016). The data shown here has been re-analysed by me in order for it to be coherent with the rest of this work. The purification and characterisation of most ColN mutants discussed here was carried out by Tonia Konstantinou under the supervision of Dr. Helen Waller.

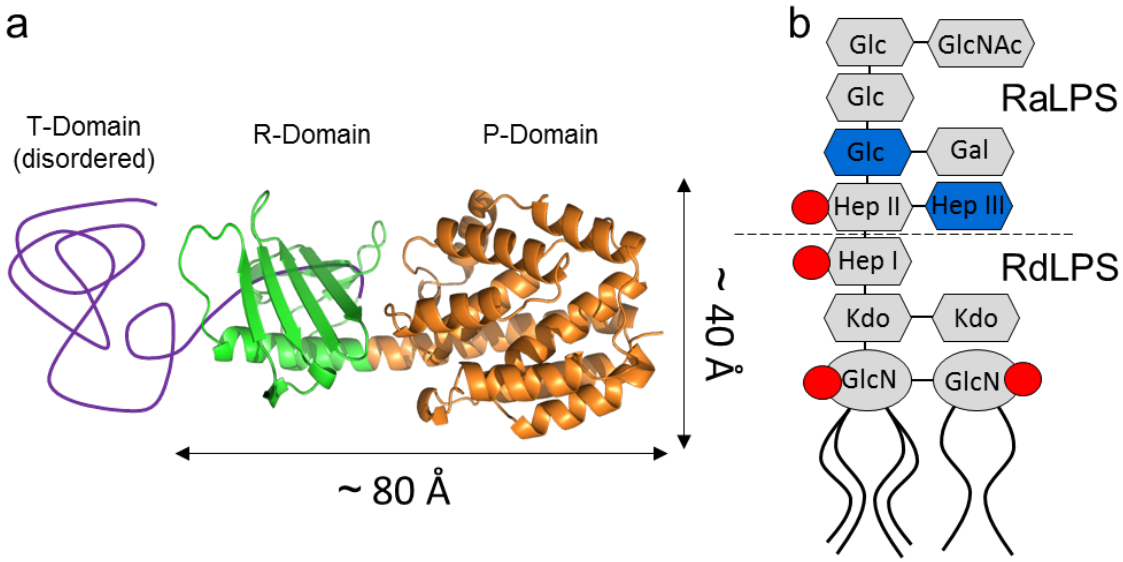

Figure 4.1 | Structure of ColN and LPS.

(**a**) Crystal structure of colicin N. The R-domain (green) is the region previously shown to recognise specific sugars in the RaLPS oligosaccharide. The P-domain (orange) carries the lethal activity by forming a pore in the cytoplasmic membrane. The T-domain (purple) is drawn as a cartoon since it is absent in the crystal structure (PDB 1A87) due to its disordered nature. It is responsible for the translocation step and it interacts with the OM protein OmpF (**b**) Structures of LPS used in this study. The dashed line separates the structure of RdLPS (from *E. coli* strain F583) from RaLPS (from *E. coli* strain EH100) which contains the additional sugars above the line. Highlighted in blue are the main sugars recognised by ColN R-domain as shown by (Johnson *et al.*, 2014), in red the anionic phosphate groups.

4.2 RESULTS

4.2.1 Effect of core oligosaccharide size on electrostatic binding of ColN to asymmetric OM models

Asymmetric outer membrane models containing deuterated phospholipids in the inner leaflet and hydrogenous rough LPS in the outer leaflet were assembled using Langmuir-Blodgett and Langmuir-Schaefer deposition techniques as described in the Methods chapter (Clifton *et al.*, 2013b; Clifton *et al.*, 2015a). Two models, containing different types of LPS were used to mimic the OM of bacteria sensitive and resistant to ColN. LPS which confers sensitivity to ColN *in vivo* (RaLPS) and LPS which is resistant to the antimicrobial protein (RdLPS) differ in their oligosaccharide head groups and, in the case of RdLPS, this is shorter, missing the sugars responsible for the specific recognition of ColN (**Fig. 4.1b**) (Sharma *et al.*, 2009). The OM models were thus characterised by NR before and after the interaction with ColN, under three isotopic solution contrasts.

The structure of both bilayers before addition of the antimicrobial protein showed the successful assembly of highly asymmetric model membranes comprising, in both cases, an outer leaflet containing >95% LPS (**Fig. 4.2** and **Table 4.1**). The coverage of the bilayers was >98%, indicating the lack of major defects as shown by the negligible water penetration in the hydrophobic core of the membrane. As expected, the main difference in the bilayer structures was the size of the LPS head groups which was ~27 Å in the case of RaLPS and ~18 Å for RdLPS. This reflects the shorter oligosaccharide headgroup present in RdLPS compared to RaLPS with the respective thickness in agreement with X-ray lamellar diffraction data from LPS bilayer stacks (Snyder *et al.*, 1999)

Addition of ColN to the bilayers significantly affected the reflectivity of both samples (**Fig. 4.3**). The Kiessig fringe arising from isotopically asymmetric bilayers in D_2O, shifted significantly towards lower Q values upon addition of 0.07 mg/ml ColN in both cases, indicating an increased overall thickness of the interfacial structures caused by the adsorption of the protein on the membrane. To fit the reflectivity from the bilayer-ColN complex, an additional layer was added between the LPS oligosaccharide and the bulk solution to model the adsorbed protein. The SLD of the protein layer in D_2O was fixed to 3.33×10^{-6} Å^{-2} calculated for the ColN chemical composition using the online Bio Molecular Scattering Length Density Calculator (http://psldc.isis.rl.ac.uk/Psldc/) (**Table 2.11**)

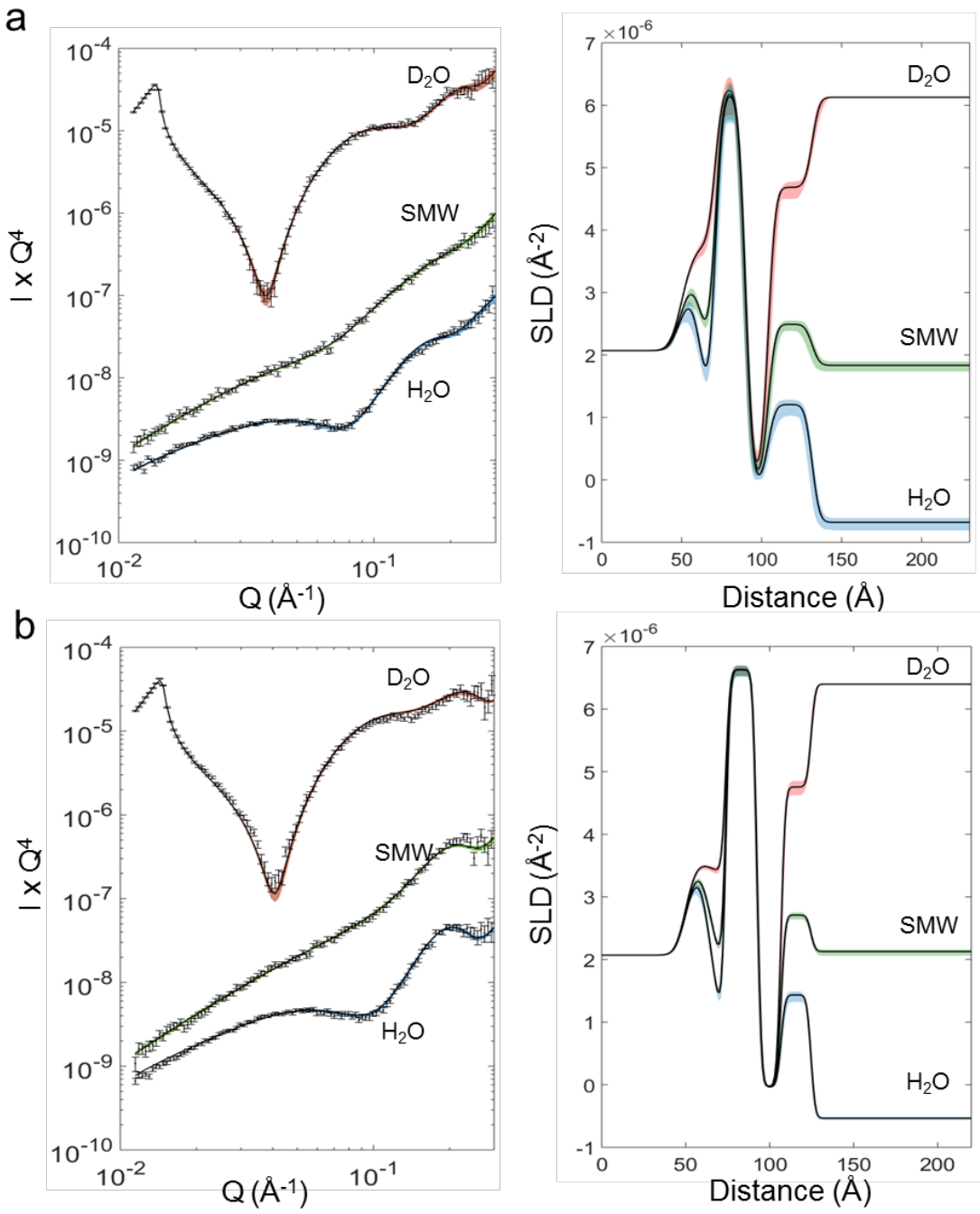

Figure 4.2 | NR of OM models containing Ra and RdLPS.

Neutron reflectivity data points, best fit lines (left) and corresponding SLD profiles (right) for asymmetric OM models containing tail deuterated DPPC in the inner leaflet and hydrogenous RaLPS (**a**) and RdLPS (**b**) in the outer leaflet. Data was collected in three isotopic contrasts: D_2O, H_2O and SMW and constrained to fit a common model of the interface. The coloured shading around the lines represents the 95% confidence intervals obtained from the Bayesian error analysis. Reflectivity curves are offset vertically for clarity

On the OM model containing RaLPS, the adsorbed ColN layer was found to be ~44 Å thick, with a coverage of ~28%. Notably, the protein adsorption did not affect the structure of the

bilayer which could be modelled with the same parameters before and after ColN addition (**Table 4.1**). This indicated that the protein remained bound to the membrane surface without disrupting or penetrating into the bilayer. Unexpectedly, ColN bound significantly also to the OM model containing RdLPS, despite the lack of specific binding sites. On the RdLPS model membrane the adsorbed layer of ColN was found to be ~40 Å thick and with a coverage of ~39%. Beside a minor reduction of the LPS headgroup thickness of ~5 Å, the addition of ColN to the RdLPS membrane resulted in no further changes in the membrane structure, indicating lack of penetration of the protein or disruption of the lipid bilayer. (**Table 4.1**) The protein coverage indicated by neutrons refers to the volume occupied by the dry protein fraction within the respective layers, not accounting for the intrinsic hydration associated with proteins. Therefore, the reported "dry coverage" underestimates the actual volume of hydrated protein adsorbed on the surface. The volume fraction occupied by water molecules in a packed three-dimensional lattice corresponding to 100% "wet coverage" of protein was estimated using MD simulation software by Dr. Philip Ciesielski (see method section 2.7.4). An atomistic model obtained from ColN crystal structure (PDB 1A87) was placed in a box of minimum dimensions and solvated with water molecules. Within the box, the volume fraction occupied by water molecules was 60%. Thus, the dry coverage of ~39% found adsorbed on the surface of the RdLPS OM model, likely corresponded to a near total wet coverage of ColN molecules whilst on RaLPS the actual volume occupied by the hydrated protein amounted to 70% when the protein's intrinsic hydration was taken into account.

Unexpectedly, although bacteria producing RdLPS are resistant to ColN *in vivo*, the higher protein coverage measured indicated that more ColN was able to bind to RdLPS compared to the membrane containing RaLPS. However RdLPS lacks the specific binding sites for ColN (Johnson *et al.*, 2014) suggesting that the interaction relied on non-specific electrostatic attraction between the anionic LPS and the cationic antibacterial protein which has an isoelectric point of 10.2 (Lakey *et al.*, 1994). The prolate shape of ColN revealed by its crystal structure, shows a major axis of ~80 Å and a minor axis of ~40 Å (**Fig. 4.1a**). This suggested that the measured thickness of the adsorbed ColN layer, of 40 Å and 44 Å on Rd and RaLPS respectively, corresponded to the protein oriented with its major axis parallel to the membrane plane. In this "side-on" conformation, the electrostatic interactions between the protein and the anionic LPS are likely to be maximised due to the larger area of contact between the ColN and the membrane.

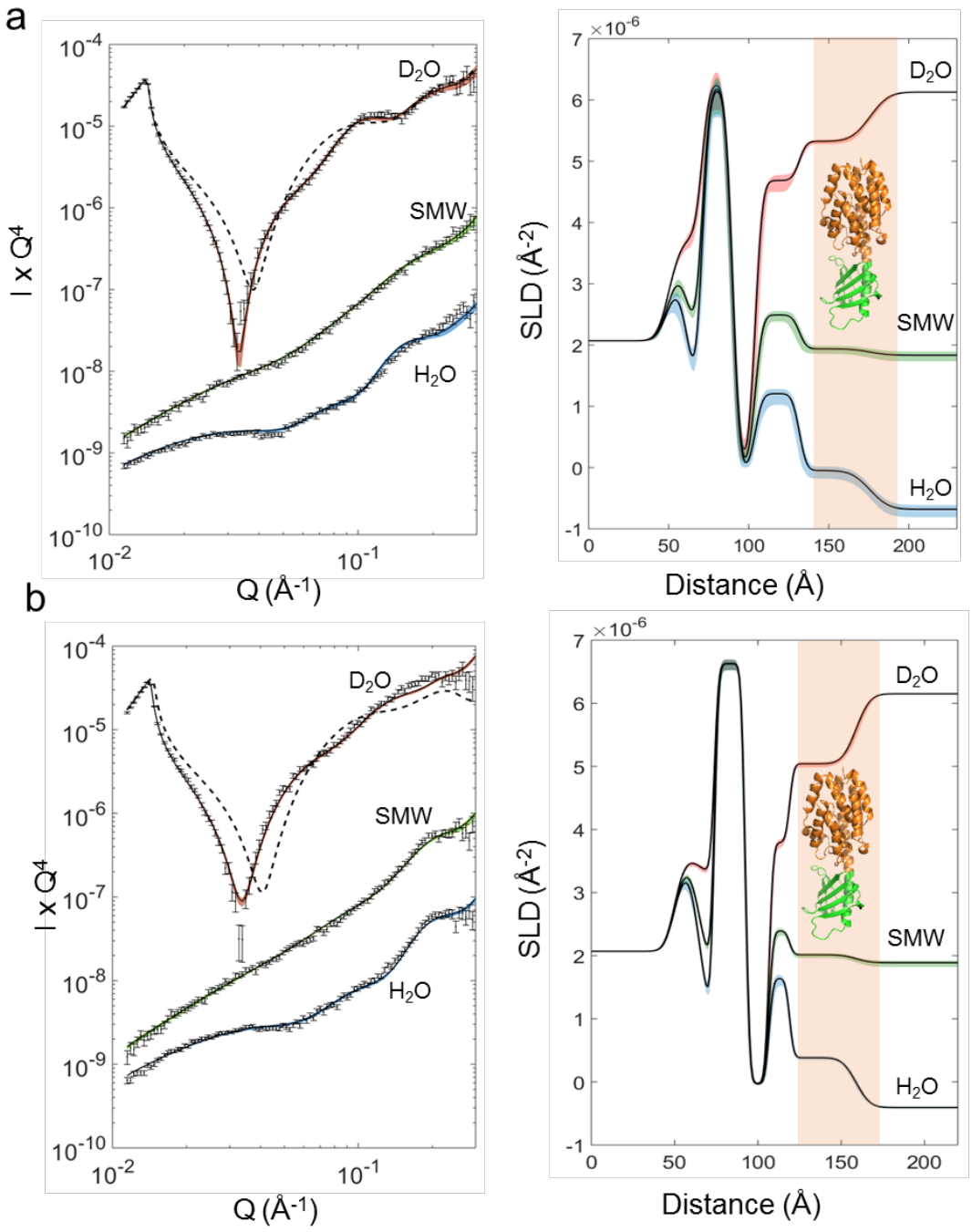

Figure 4.3 | NR of ColN binding to OM models containing Ra and RdLPS.

Neutron reflectivity data points, best fit lines (left) and corresponding SLD profiles (right) for asymmetric OM models containing RaLPS (**a**) and RdLPS (**b**) in the presence of 0.07 mg/ml ColN. Reflectivity curves are offset vertically for clarity. The dashed reflectivity curves are from the respective OM models in D_2O before the addition of the protein. In both cases the shift of the data to lower Q upon addition of ColN is evident. The highlighted areas in the SLD profiles correspond to the layer of protein adsorbed onto the model membranes and the ColN structure is superimposed in its side on orientation

Table 4.1 | Parameters derived from the fitting of the NR data from the Ra and RdLPS OM models and corresponding adsorbed ColN layers.

In brackets, the 95% confidence interval relative to each parameter obtained from the Bayesian error analysis. The bilayer parameters describe the OM models both before and after the addition of the protein with the exception of the RdLPS head group which was affected by the protein adsorption and required a separate set of parameters shown under "bilayer+ColN parameters". a, b and c indicate that for the RaLPS bilayer, the same LPS head group parameters used before ColN also described the head group structure and physical state after the addition of the protein. Substrate parameters are omitted for simplicity.

Bilayer parameters	Fitted value (RaLPS)	Fitted value (RdLPS)
dDPPC HG thickness (Å)	8.4 (7.4, 9.5)	8.9 (8.7, 9.0)
dDPPC HG SLD ($Å^{-2}x10^{-6}$)	1.88 (1.62, 2.15)	1.74 (1.70, 1.82)
dDPPC HG coverage (%)	54.2 (49.1, 59.2)	35.4 (33.5, 37.1)
dDPPC tails thickness (Å)	18.9 (17.4, 20.3)	18.7 (18.5, 19.0)
dDPPC tails SLD ($Å^{-2}x10^{-6}$)	6.28 (5.97, 6.63)	6.63 (6.57, 6.71)
LPS tails thickness (Å)	14.3 (13.7, 15.1)	14.1 (14.0, 14.2)
LPS tails SLD ($Å^{-2}x10^{-6}$)	-0.04 (-0.05, -0.03)	-0.04 (-0.04, -0.03)
LPS HG thickness (Å)	27.4 (26.5, 28.2)[a]	17.9 (17.4, 18.4)
LPS HG SLD in D_2O ($Å^{-2}x10^{-6}$)	4.53 (4.36, 4.79)[b]	4.15 (4.03, 4.29)
LPS HG coverage (%)	69.7 (66.8, 72.6)[c]	73.5 (71.8, 75.3)
Bilayer coverage (%)	98.7 (97.2, 99.9)	99.8 (99.4, 100)
Bilayer roughness (Å)	3.6 (3.0, 4.2)	2.0 (2.0, 2.1)

Bilayer+ColN parameters	Fitted value (RaLPS)	Fitted value (RdLPS)
LPS HG thickness (Å)	a	12.4 (11.9, 12.8)
LPS HG SLD in D_2O ($Å^{-2}x10^{-6}$)	b	3.57 (3.50, 3.65)
LPS HG coverage (%)	c	89.6 (89.3, 90)
ColN thickness (Å)	44.2 (42.8, 45.8)	40.0 (39.0, 40.1)
ColN SLD D_2O ($Å^{-2}x10^{-6}$)	3.33	
ColN coverage (%)	28.1 (27.0, 29.2)	38.6 (37.5, 40.0)
ColN roughness (Å)	9.2 (8.2, 9.9)	6.7 (6.5, 6.9)

The larger amount of ColN adsorbed onto RdLPS compared to the RaLPS model OM suggested a stronger electrostatic interaction of the antimicrobial protein with the LPS bearing a truncated core oligosaccharide. The additional sugars present in the RaLPS oligosaccharide, despite containing ColN binding sites, might have therefore played a role in screening the non-specific electrostatic interaction between the protein and the negative charges present on LPS, which are located in the innermost region of the LPS head group.

4.2.1.1 Charge screening study

In order to compare the strength of the membrane-protein interaction, the ColN-OM model complexes were measured in the presence of increasing concentrations of NaCl with the goal of screening the electrostatic forces between ColN and the two LPS species. The effect of increasing concentrations of monovalent ions on the amount of ColN adsorbed onto the membranes was analysed by NR. During the NaCl titration measurements, ColN concentration in the solution was kept constant (at 0.07 mg/ml) to ensure equilibrium between the membrane-bound and the soluble state. Reflectivity data were collected in D_2O, which displayed a sharp Kiessig fringe and provided the strongest contrast with the hydrogen rich protein. Reflectivity curves measured under increasing salt concentrations were constrained to fit to a common model of the interface in which the parameters describing the bilayer remained constant across all salt concentrations whilst the only variable parameter was the volume fraction of the protein adsorbed.

Adsorption of ColN in the absence of NaCl resulted in a protein volume fraction comparable to that measured in the previous experiments (**Table 4.1**) with a dry coverage of ~43% on RdLPS and ~28% on RaLPS (**Table 4.2**). As the amounts of monovalent ions dissolved in the solution increased, the volume fraction of the protein gradually decreased, until no protein was left bound to the surface of both model membranes (**Fig. 4.4**). In the case of the ColN-RaLPS complex the complete removal of the protein was achieved in the presence of 100 mM NaCl (**Fig. 4.4a**). In contrast, when the same titration was carried out on the ColN-RdLPS complex, the complete removal of the bound protein required a concentration of 350 mM NaCl (**Fig 4.4b**). The volume fractions of the protein at each corresponding NaCl concentration are listed in **table 4.2** for the models containing the two LPS types. The significantly higher concentration of salt necessary to remove ColN from the RdLPS membrane, compared to RaLPS, confirmed the stronger nature of the electrostatic interaction suggested by the higher volume fraction of protein initially adsorbed on the bilayers. The strength of the ColN-LPS interaction appeared to be inversely proportional to the length of the LPS oligosaccharide region, despite the ColN binding sites being present only in the thicker oligosaccharide of RaLPS (**Fig 4.5**)

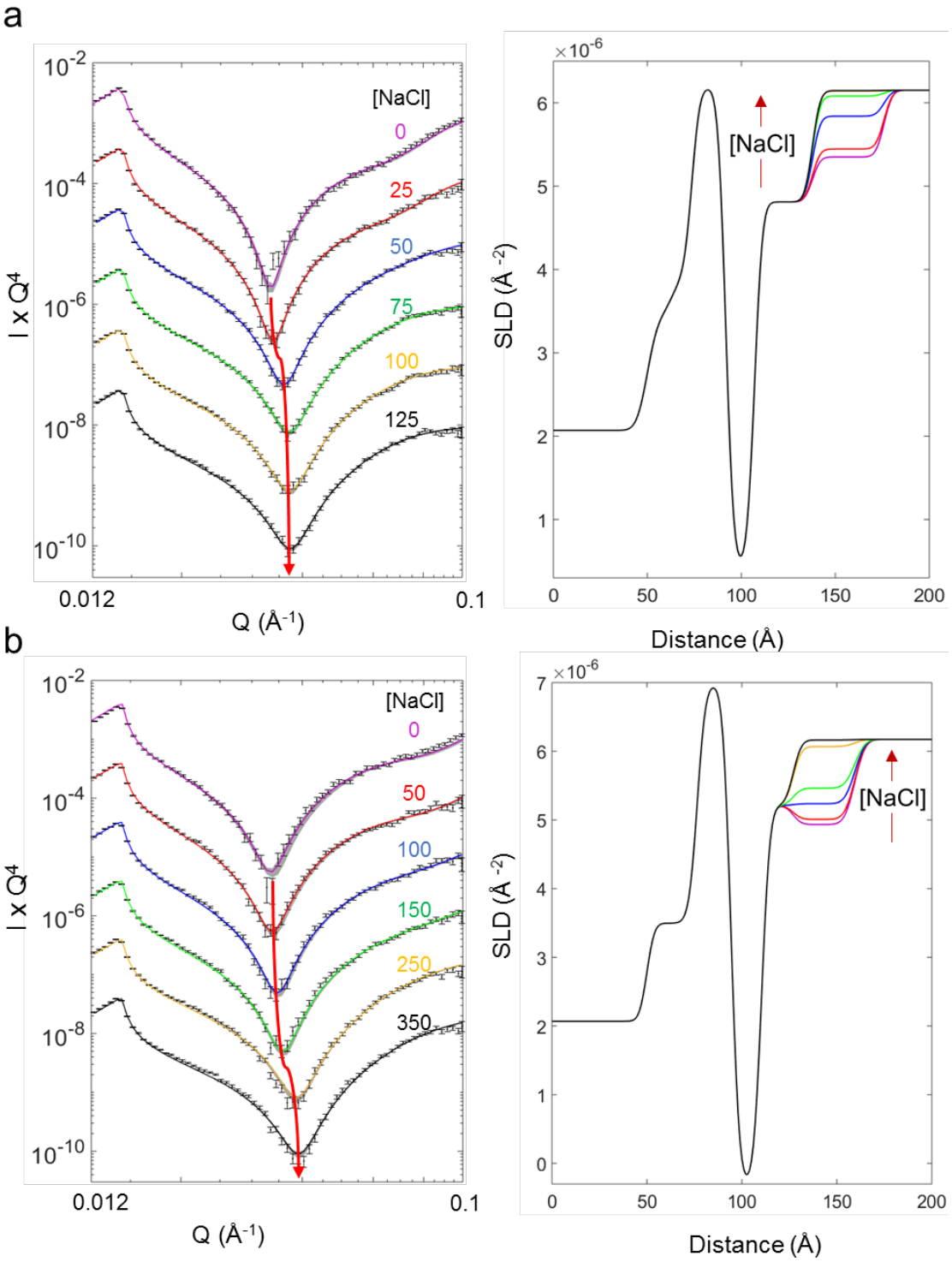

Figure 4.4 | NaCl titration of the LPS-ColN complexes.

Neutron reflectivity data points, best fit lines (left) and corresponding SLD profiles (right) for asymmetric OM models containing RaLPS (**a**) and RdLPS (**b**) measured in D_2O in the presence of 0.07 mg/ml ColN at different NaCl concentrations. Reflectivity curves are offset vertically for clarity. The red arrows are a guide to the eye following the shift of the fringe to higher Q values as the protein is removed from the membrane surface. The corresponding SLD profiles display the gradual removal of ColN as [NaCl] (mM) increases.

Table 4.2 | Volume fractions of ColN adsorbed on Ra and RdLPS OM models as a function of [NaCl] calculated from the fitted SLD of the protein layer under each salt condition

In brackets the 95% confidence interval relative to each parameter obtained from the Bayesian error analysis. N.A = not assigned.

[NaCl] (mM)	ColN coverage on RaLPS (%)	ColN coverage on RdLPS (%)
0	28.2 (26.1, 30.4)	43.4 (38.6, 48.33)
20	24.8 (23.4, 26.1)	43.3 (39.2, 47.32)
50	11.0 (10.0, 12.0)	40.8 (37.1, 45.0)
75	2.5 (1.5, 3.5)	35.8 (32.4, 40.0)
100	<1	32.8 (29.4, 36.4)
125	<1	28.74 (31.9, 25.5)
150	N.A.	24.9 (22.3, 27.8)
175	N.A.	20.4 (17.8, 23.1)
200	N.A.	15.1 (12.5, 17.8)
250	N.A.	3.7 (2.0, 5.7)
300	N.A.	<1
350	N.A.	<1

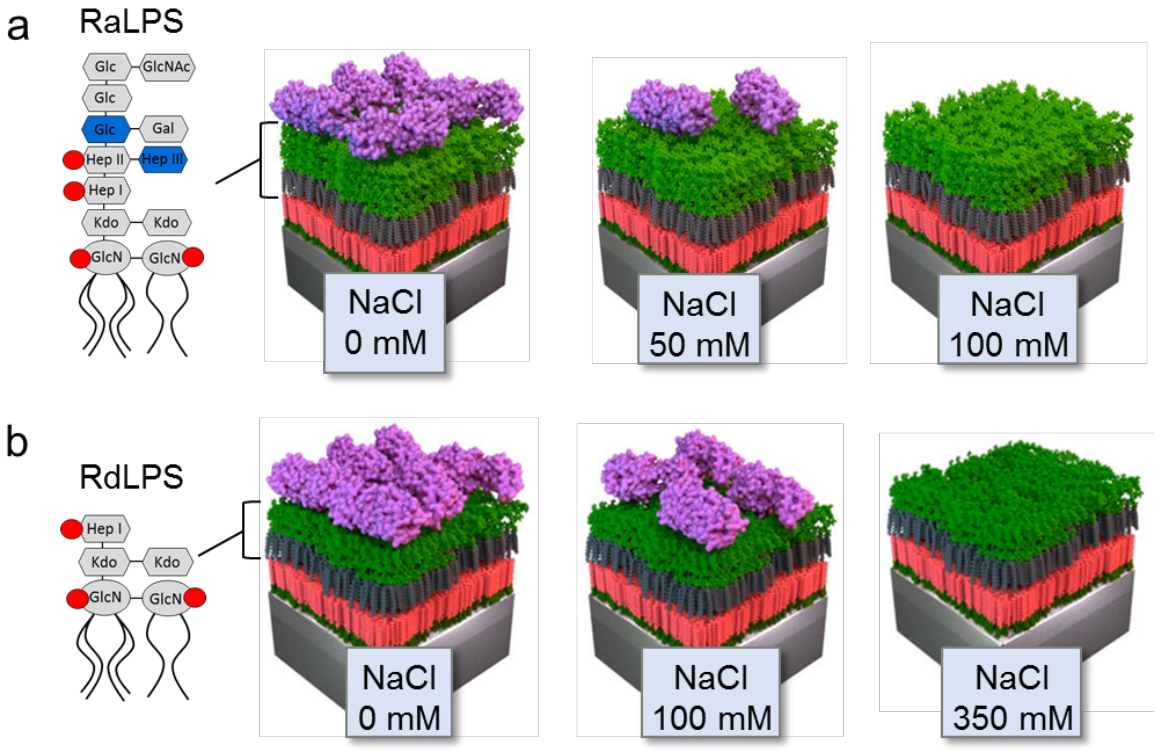

Figure 4.5 | Cartoon representation of the salt dependent binding of ColN from asymmetric OM models.

Removal of ColN from OM models containing Ra (**a**) and RdLPS (**b**). The position of the main negative charges within the LPS molecules, represented by the phosphate groups of the lipid A moiety are shown in red. The RaLPS oligosaccharide recognised by ColN is highlighted in blue.

4.2.2 Core oligosaccharide packing affects specific ColN binding

The additional sugars in the oligosaccharide head group of RaLPS reduced the ability of ColN to bind to the asymmetric model OM, despite containing the known ColN binding sites, absent in RdLPS. However, the specific sugars recognised by the protein on RaLPS are not exposed on the surface of the molecule but rather buried under an additional oligosaccharide (**Fig. 4.5a**). The accessibility of ColN R-domain to its binding sites could have thus been prevented by the tight LPS packing afforded by the LB/LS controlled deposition techniques.

To test this hypothesis, ColN binding was assessed on OM models treated with EDTA. EDTA is known to destabilise the OM in *vivo* (Vaara, 1992) and was shown to induce mixing of phospholipids and LPS in OM models by removing the stabilising Ca^{2+} ions (Clifton *et al.*, 2015b). The EDTA induced mixing of phospholipids in the outer leaflet was exploited here to loosen the packing of RaLPS molecules and expose the buried head group region. EDTA treatment of the asymmetric RaLPS OM model reduced the overall lipid asymmetry, yielding an outer leaflet containing ~35% phospholipids (**Fig. 4.6a**, **Table 4.3**), compared to the ~5% content of the untreated membrane described in section **4.2.1** (**Table 4.1**). The 3 mM EDTA solution was then replaced by the initial buffer containing 5 mM Ca^{2+} and 20 mM HEPES pH 7.4. Adsorption of ColN on the mixed bilayer revealed a different picture from that observed on the highly asymmetric OM model. Rather than a single layer of protein observed on the untreated bilayer, fitting the data from the EDTA treated OM model required a model that included 2 layers of protein (**Fig. 4.6b**). The ColN layer proximal to the membrane was ~45 Å thick, with a dry coverage of ~26% (65% total wet coverage), nearly identical to the protein layer measured on the untreated RaLPS membrane. The additional distal layer was thicker and sparser, measuring ~78 Å and with a dry coverage of ~6% (15% total wet coverage) (**Table 4.3**).

The addition of 100 mM NaCl to the membrane-ColN complex, which earlier removed all ColN electrostatically bound to the asymmetric RaLPS bilayer (**Fig. 4.4a**), affected significantly only the protein layer proximal to the membrane, which decreased in coverage from ~26% to ~10% (from 65% to 25% wet coverage). The amount of protein forming the distal layer remained largely unchanged, going from a dry coverage of ~6% in the absence of salt, to ~7% in the presence of 100 mM NaCl, respectively 15% and 17.5% wet coverage (**Fig. 4.6c**). Nor the adsorption of ColN or the addition of NaCl affected the structure of the OM model itself, which was modelled by the same set of parameters under all conditions.

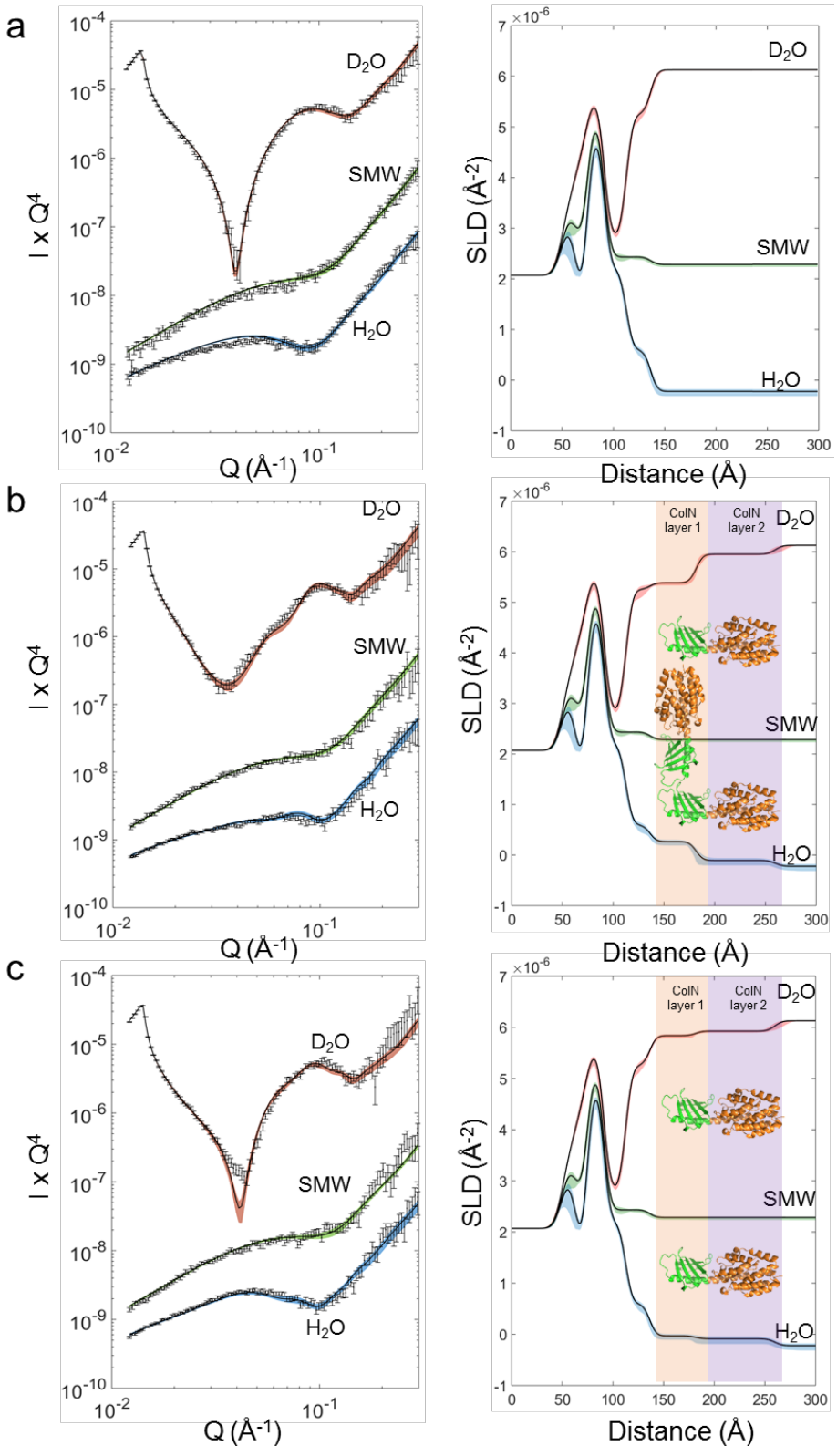

Figure 4.6 | NR of ColN binding to EDTA treated RaLPS OM model.

Neutron reflectivity data points, best fit lines (left) and corresponding SLD profiles (right) for EDTA treated RaLPS OM model in the absence of protein (**a**), in the presence of 0.07 mg/ml ColN (**b**), and in the presence of 0.07 mg/ml ColN and 100 mM NaCl (**c**). The protein layers detected are highlighted in orange and purple and ColN structure is superimposed in its side-on and end-on orientations.

Table 4.3 | Parameters derived from the fitting of the NR data from the EDTA treated RaLPS OM model and associated ColN layers in the absence and the presence of NaCl.

In brackets, the 95% confidence interval relative to each parameter obtained from the Bayesian error analysis. Substrate parameters are omitted for simplicity.

Bilayer parameters	Fitted value
dDPPC HG thickness (Å)	10.6 (10.1, 11.3)
dDPPC HG SLD ($Å^{-2}x10^{-6}$)	3.34 (3.19, 3.47)
dDPPC HG coverage (%)	40.2 (36.3, 44.8)
dDPPC tails thickness (Å)	16.8 (16.2, 17.3)
dDPPC tails SLD ($Å^{-2}x10^{-6}$)	5.77 (5.70, 5.83)
LPS tails thickness (Å)	19.4 (18.5, 20.8)
LPS tails SLD ($Å^{-2}x10^{-6}$)	1.88 (1.79, 1.99)
LPS HG thickness (Å)	21.7 (20.0, 23.3)
LPS HG SLD in D_2O ($Å^{-2}x10^{-6}$)	4.53 (4.36, 4.79)
LPS HG coverage (%)	39.3 (34.0, 43.0)
Bilayer coverage (%)	93.5 (91.8, 95.2)
Bilayer roughness (Å)	8.4 (8.0, 8.8)

ColN parameters	Fitted value No salt	Fitted value @ 100 mM NaCl
ColN SLD D_2O ($Å^{-2}x10^{-6}$)	3.33	
ColN layer 1 thickness (Å)	45.6 (41.9, 48.9)[a]	a+b
ColN layer 1 coverage (%)	74.1 (72.8, 75.5)	91.7 (91.1, 92.3)
ColN layer 1 roughness (Å)	6.8 (6.1, 7.4)	9.2 (8.3, 9.9)
ColN layer 2 thickness (Å)	73.8 (69.1, 78.0)[b]	N.A.
ColN layer 2 coverage (%)	93.2 (92.2, 94.1)	N.A.
ColN layer 2 roughness (Å)	7.7 (7.3, 8.0)	N.A.

The two protein layers detected suggested a scenario in which ColN adopted two different conformations on the EDTA treated OM model. The first, represented by the ~45 Å thick protein layer proximal to the membrane, corresponded to the thickness of ColN in its side-on conformation. This closely resembled the protein arrangement detected on the asymmetric bilayer before the EDTA treatment (**Fig 4.3, Table 4.1**) in terms of both thickness and coverage. In both cases, addition of 100 mM NaCl significantly affected the coverage of the side-on ColN by substantially reducing the amount of protein adsorbed.

The second conformation, ~78 Å thicker that the first one, measured a total of ~123 Å from the membrane surface and was only detected on the EDTA treated OM model. This second protein layer was not sensitive to the presence of NaCl like the first one, suggesting a stronger interaction with the OM model. Based on the thicker nature of the salt resistant protein layer and the prolate shape of ColN shown by its crystal structure (**Fig 4.1b**), a possible interpretation of the data was that of an "end-on" conformation of ColN bound to the membrane with its major axis normal to the membrane plane. The absence of this protein layer on the untreated asymmetric OM model and the higher stability of its binding to LPS, compared to the side-on bound ColN, suggested that the end-on conformation of ColN was the result of the specific recognition of LPS by the R-domain. This specific interaction was made possible only by the increased accessibility to the core oligosaccharide region caused by the EDTA treatment. The total thickness of the end-on protein layer measured by NR (~123 Å) (**Table 4.3**), compared with the size of ColN major axis in its crystal structure (~80 Å) (**Fig. 4.1a**), indicated that the protein could have potentially lost its compact structure, possibly due to partial unfolding of the P-domain.

4.2.3 LPS binding and toxicity of ColN are regulated by a loop region within the R-domain

To further investigate the binding of the R-domain to LPS and its importance for ColN activity, a series of ColN proteins containing mutations in the R-domain region were generated and tested for bactericidal activity and LPS binding. Mutants were designed by Dr. C. Johnson to disrupt a loop region contained in the R-domain between amino acids N162 and K171, referred to as loop^{R}, which scored highly in structural similarity with the proposed LPS-binding motif of the bactericidal permeability-increasing (BPI) protein and the LPS binding protein (LPB) (Berbee *et al.*, 2010) (**Fig 4.7**). Preliminary results in our group, from experiments performed by Dr. H. Waller, also suggested this region to be important for ColN toxicity.

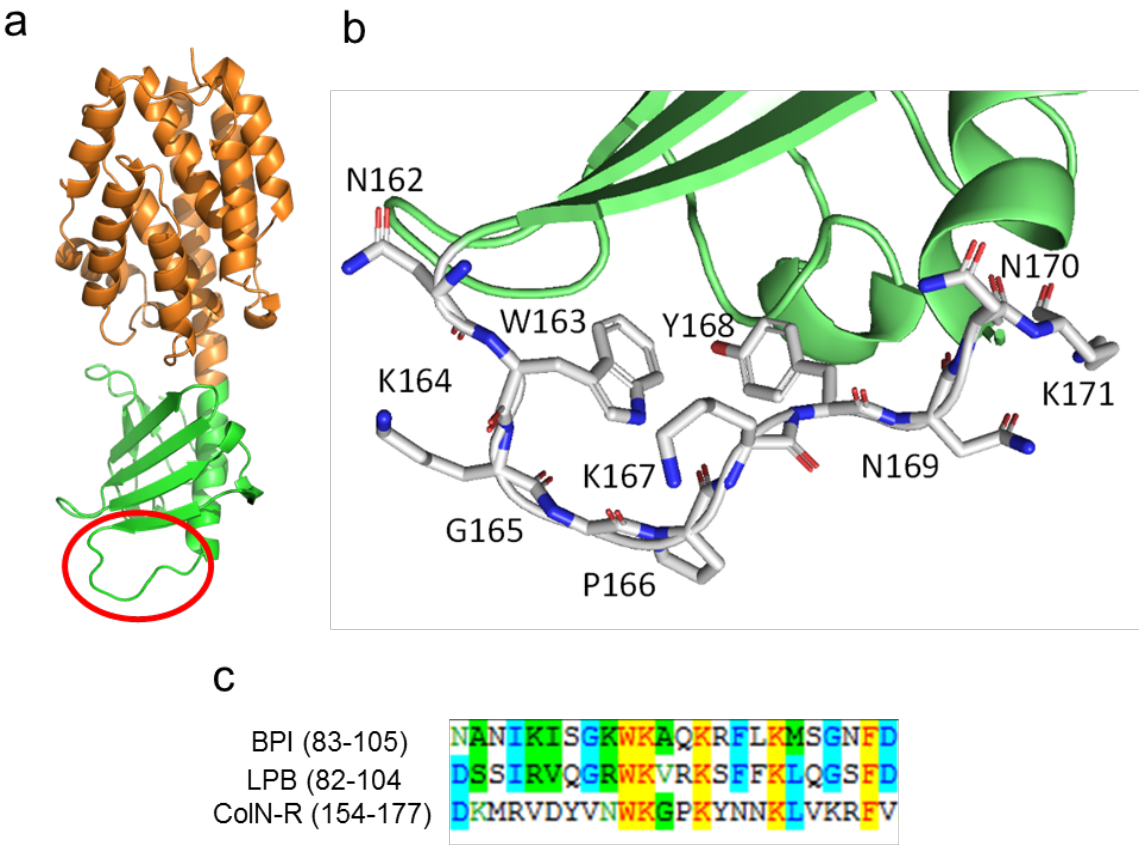

Figure 4.7 | Structure and localisation of loop^R within ColN.

(**a**) Localisation of loop^R (red circle) within the R-domain of ColN (green) (**b**) Amino acid composition of the loop^R region. (**c**) Sequence similarity between the proposed binding sites of the two LPS binding proteins (BPI and LPB) and ColN R-domain. In red the conserved residues

4.2.3.1 ColN mutants production and characterisation

Site directed mutagenesis was used to target both single amino acids and groups of residues in the loop^R region that could potentially be involved in the interaction with the negatively charged LPS. A list of the mutants successfully purified is given in **table 4.5**. The ColN loop^R mutants were expressed with a C-terminal hexahistidine tag in *E. coli* BL21-AI cells and purified by immobilised metal affinity chromatography as described in the Methods. Protein expression and purification were followed by Coomassie stained SDS-PAGE which showed the arabinose induced expression of the proteins and the successful purification by affinity chromatography (**Fig. 4.8a** and **b**). The correct folding of the mutants was assessed by circular dichroism (CD) and compared to that of wild type (WT) ColN. CD spectra were collected in the far-UV region between 185 and 245 nm and the signal normalised to the amount of protein present. All mutants displayed folded and predominantly α-helical spectra resembling WT ColN (**Fig. 4.8c**). Small deviations in the spectra of different mutants are

likely dependent on differences in sample concentrations due to errors associated with the short path length of the Nanodrop spectrometer (LabTech). The stability of the mutants was then assessed by determining the melting point of the proteins by following the changes in the CD signal at 222 nm as the samples were heated from 25°C to 95°C.

Table 4.4 | List of Colicin N mutants produced and characterised by CD and SDS-PAGE.

The mutants were designed to introduce single point charge reversal of the three lysines highlighted by the alignment (K171E, K167E and K164E), neutralisation of the positive charges of all three lysines by substitution with alanines ($ColN^{3A}$), neutralisation of lysine positive charges and asparagine polar side chains by substitution with alanines ($ColN^{6A}$), triple charge reversal of all the three lysines ($ColN^{3E}$) and partial deletion of the loop ($ColN^{\Delta 6}$).

Mutant name	Mutations
K171E	K171E
K167E	K167E
K164E	K164E
$ColN^{3A}$	K171A, K167A, K164A
$ColN^{6A}$	K171A, K167A, K164A, N162A, N169A, N170A
$ColN^{3E}$	K171E, K167E, K164E
$ColN^{\Delta 6}$	Deletion of N162 to K167 (inclusive)

The first order derivative of the change in the CD signal was calculated using the spectrometer software (Jasco Spectra Manager) to extract the melting temperature of each mutant (**Fig 4.8d**). WT ColN displayed the highest melting temperature at 73°C whilst all the mutants displayed slightly lower melting temperatures. The largest differences, of 5.4°C and 4.8°C, were recorded for the constructs containing a 6 amino acid substitution ($ColN^{6A}$) and a 6 amino acid deletion ($ColN^{\Delta 6}$) suggesting that the thermal stability was mainly affected by the number of mutations in the region. In general, the thermal stability of the mutants was comparable to that of ColN WT allowing for further biophysical characterisation and assessment of their bactericidal activity.

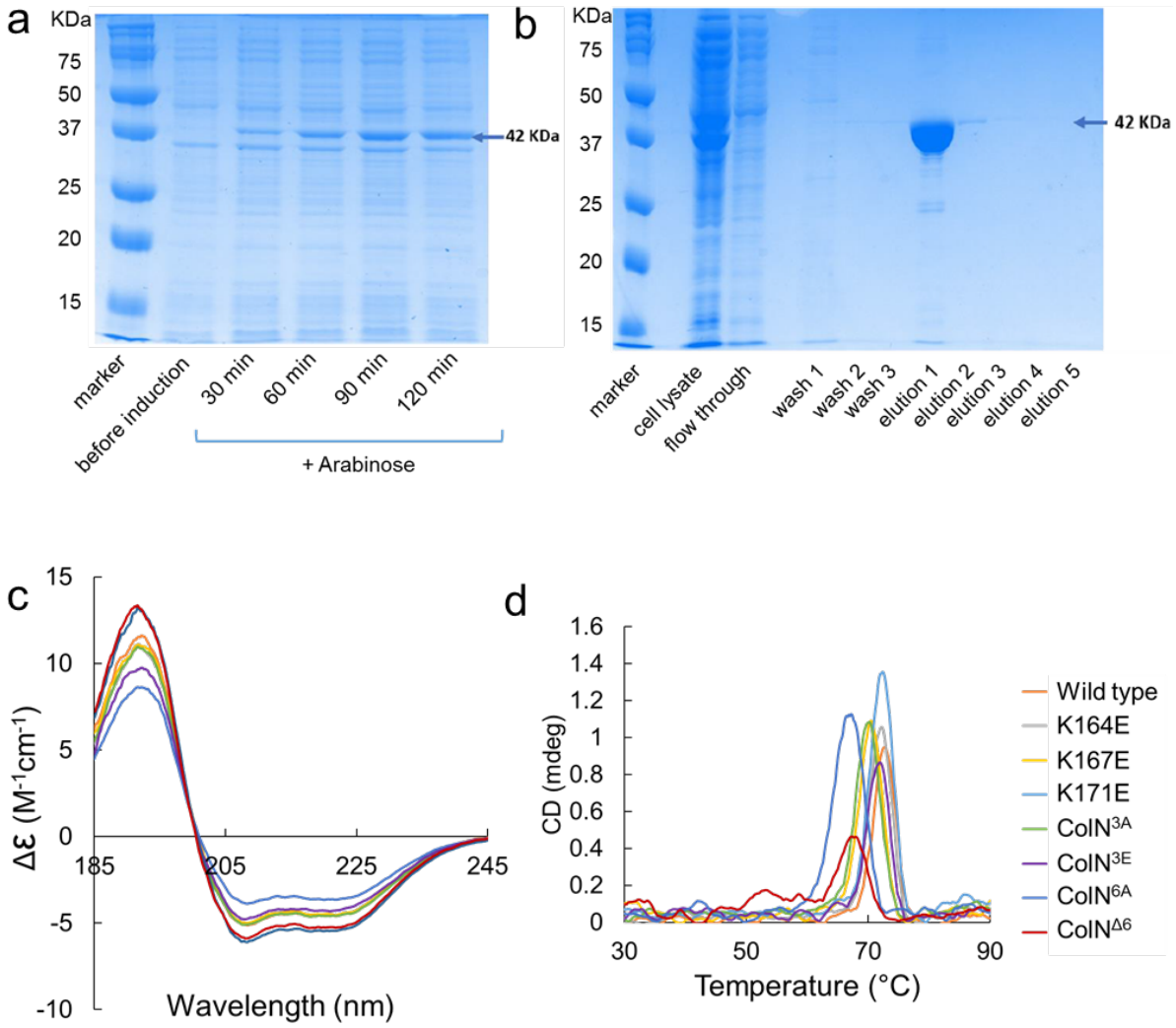

Figure 4.8 | Characterisation of ColN loop^R mutants.

Representative SDS PAGE characterisation of the K171E loop^R mutant showing (**a**) the expression and (**b**) the purification by immobilised metal affinity chromatography. The band at 42 KDa is the ColN protein which in **a**, appears only after protein expression is induced by arabinose. Far UV circular dichroism spectra (**c**) and melting temperatures (**d**) of all the purified loop^R mutants.

4.2.3.2 Toxicity of ColN mutants

The effect of the loop^R mutations on the antibacterial activity of the proteins was tested using a liquid culture cell survival assay. Overnight liquid cultures of *E. coli* BE3000 cells were diluted to an OD_{600} of 0.5, aliquoted in a 96 well plate and treated for 30 minutes with ColN mutants at a concentration of 10 nM. The content of the wells was then diluted 1:100, inoculated in a 96 well plate containing fresh media and incubated at 37°C for 20 h. The regrowth of the cells was monitored by measuring the OD_{600} overtime and the lag phase between the inoculation and the rise in OD_{600} indicated the relative toxicity of the mutants (**Fig 4.9**). The single charge reversal mutants K164E K167E and K171E did not show any

reduction in activity under these conditions. Similarly, ColN^{3A}, which had K164, K167 and K171 replaced by alanines, did not show any reduction in toxicity compared to the wild type. When K164, K167 and K171 were all simultaneously changed to glutamates as in ColN^{3E}, the bactericidal activity of the protein was drastically reduced. Following on the WT-like behaviour of ColN^{3A}, the effect of a further reduction in overall polarity of loop^{R} was tested by replacing N162, N169 and N170 with alanines in addition to the three lysines of ColN^{3A}, generating the ColN^{6A} construct. Unlike ColN^{3A}, the additional polarity reduction of ColN^{6A} was effective in reducing the toxicity of the protein, although not to the extent of the charge reversal of ColN^{3E}. This indicated that charge reversal was not strictly required for inhibiting ColN antibacterial activity.

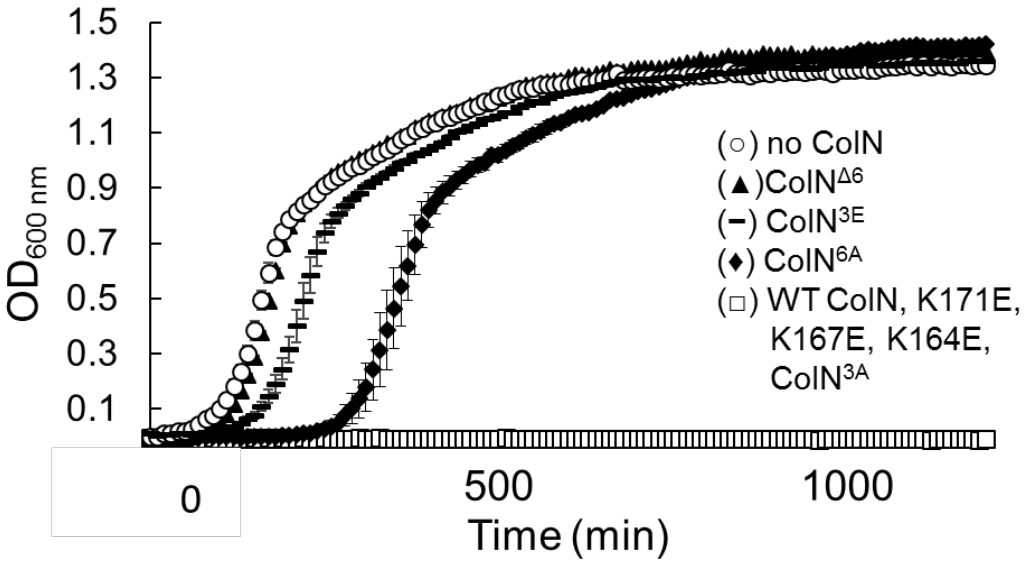

Figure 4.9 | Toxicity of loop^{R} mutants tested by liquid culture killing assay.

Growth of *E. coli* BE3000 cells after the 30 min treatment with ColN WT and mutants at a concentration of 10 nM. The delay in the rise of the OD_{600} (lag phase) is proportional to the killing efficiency of the proteins. A flat signal means no viable bacteria were left after the treatment with ColN. This was the case for WT ColN and mutants K171E, K167E, K162E and ColN^{3A} whilst ColN$^{\Delta 6}$ ColN^{3E} and ColN^{6A} all displayed a reduced toxicity. Error bars are the standard error of triplicate experiments

Since loop^{R} is not involved in any secondary structure, it presents several exposed peptide bonds capable of making polar contact with LPS. Thus, to conclusively test the role of loop^{R} in ColN toxicity, the ColN$^{\Delta 6}$ construct was generated, containing a 6 amino acid deletion within the loop, from N162 to K167 inclusive. ColN$^{\Delta 6}$ displayed the greatest reduction in toxicity within this series of mutants, displaying a complete loss of activity. Overall ColN^{6A},

ColN^{3E} and ColN$^{\Delta 6}$ all showed a decreased activity which largely correlated to the degree of disruption of the loop^{R} region.

4.2.3.3 LPS binding of ColN mutants

The results obtained from the killing assay showed the importance of loop^{R} for the toxic activity of ColN. However, whether this reduction in toxicity was linked to the impaired binding of the R-domain to LPS remained unclear. Surface plasmon resonance (SPR) was used to screen the LPS binding ability of the mutants. The C-terminally histidine-tagged ColN mutants were immobilised on a Ni^{2+} charged NTA surface and a suspension of 10 µM LPS was flowed over the immobilised proteins while monitoring the SPR response. The binding of LPS was then normalised to the amount of protein present on the surface, in order to compare the binding ability of each mutant.

The mutants which displayed a decreased toxicity *in vivo* displayed a weaker interaction with RaLPS (**Fig. 4.10a**) compared to the mutants that retained WT *in vivo* toxicity (**Fig 4.10b**). The RaLPS binding of the mutants was normalised against the WT result and expressed as a percentage of WT binding capacity (**Fig. 4.10c**). The strongest decrease in the ability to bind LPS was observed for ColN^{3E} and ColN$^{\Delta 6}$ which, compared to the wild type, retained 12.1% ± 0.6% and 15.2 ± 0.8% of the LPS binding capacity followed by ColN^{6A} with 51.8% ± 0.6%. In contrast, the remaining constructs all displayed higher levels of RaLPS binding. Interestingly ColN^{3A} and the single mutants K164E and K167E also exhibited a significantly reduced response to RaLPS, retaining 57.1% ± 0.9%, 53.5% ± 3.7% and 69.3% ± 0.2% binding capacity respectively. K171E was the least affected mutant and bound 94.2% ± 5.8% of the RaLPS bound by the WT. Finally, to test the specificity of the measured ColN-LPS interaction the experiment was repeated for all mutants with RdLPS which lacks the sugars recognised by the R-domain. As expected, in all cases the binding of RdLPS was significantly lower than the response obtained with RaLPS (**Fig 4.11**), confirming that the interaction was dominated by the specific LPS recognition of the R-domain. However, although to a much reduced extent, RdLPS was still able to display some residual binding to the ColN mutants.

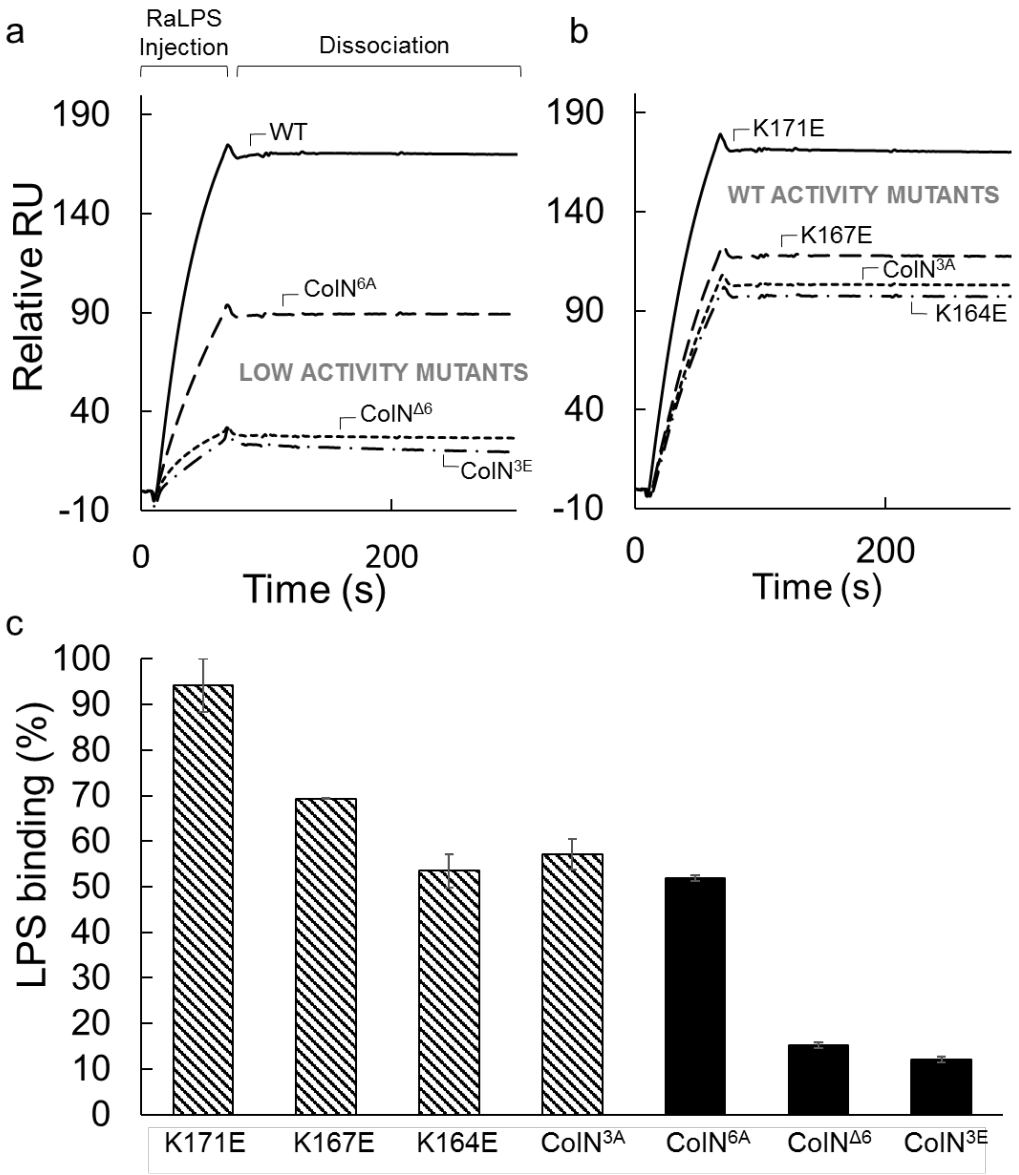

Figure 4.10 | RaLPS binding ability of loop^R mutants.

SPR signal from RaLPS binding to ColN WT and mutants immobilised on a gold surface. RaLPS was injected for 60s followed by 240s of buffer. Sensograms of RaLPS binding to WT and mutants with reduced toxicity (**a**) and to mutant with WT activity (**b**). The responses are normalised to the amount of protein immobilised on the surface. (**c**) LPS binding ability of loop^R mutants relative to WT. Black bars represent mutants with reduced toxicity and striped bars, mutants with WT toxicity. Error bars are the standard error of duplicate independent measurements

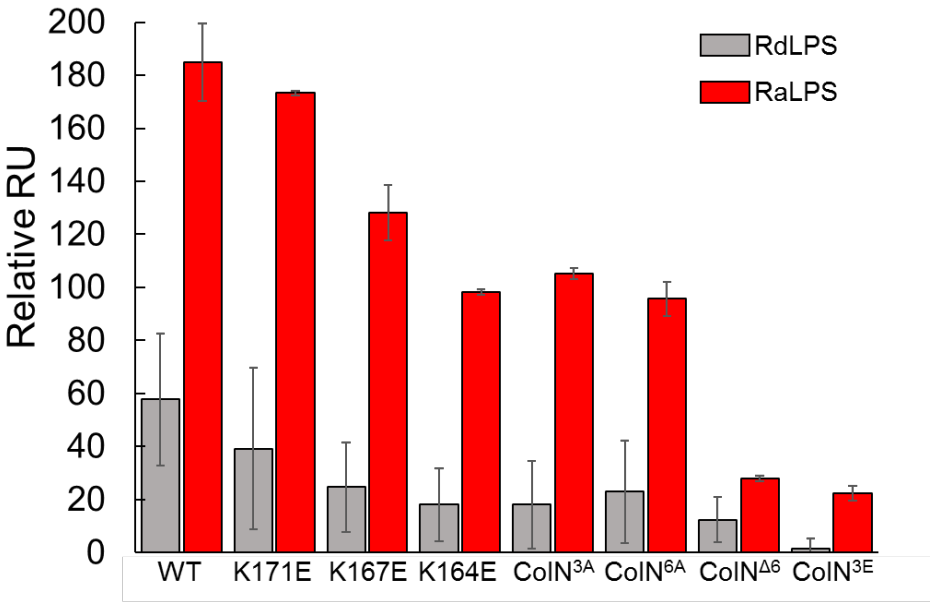

Figure 4.11 | Specificity of ColN WT and mutants binding to Ra and RdLPS.

SPR response of RdLPS (grey) and RaLPS (red) binding to ColN WT and mutants immobilised on a gold surface. Error bars are the standard error of duplicate independent measurements

4.3 Discussion

Unlike most colicins, which target outer membrane proteins such as BtuB and Cir (colicin interacting receptor) (Kurisu *et al.*, 2003) ColN is the only member of the family to exploit LPS as the primary receptor to recognise the Gram-negative target cells. Johnson *et al* previously demonstrated that ColN binds LPS via its R-domain, which was shown to recognise specific heptose and glucose residues contained in the LPS head group oligosaccharide (Sharma *et al.*, 2009). The work by Johnson et al was able to explain the molecular basis behind the resistance towards ColN of *E. coli* strains that produced a truncated version of LPS (RdLPS) lacking ColN target residues (Johnson *et al.*, 2014). However, the mechanism behind the first steps of ColN translocation through the OM and the LPS binding sites within ColN R-domain, remained unclear.

Here, the interaction of ColN with LPS was investigated from a biophysical point of view using neutron reflectometry (NR), surface plasmon resonance (SPR) and the results compared with an *in vivo* toxicity assay. The NR experiments showed that the binding of ColN to asymmetric OM models containing Ra or RdLPS was not dependent on the presence of the known ColN binding sites on LPS. Higher amounts of ColN bound to the OM model containing RdLPS compared to RaLPS (**Fig. 4.3** and **Table 4.1**). The interaction was shown

to be purely electrostatic in nature and could be completely reversed by the addition of monovalent ions (NaCl) which screened the attraction between the negatively charged LPS and the cationic ColN (**Fig 4.4** and **Table 4.2**). Within the LPS molecule, the negatively charged moieties, such as phosphates and anionic sugars, are concentrated in the inner oligosaccharide region whilst the outer region present in RaLPS, is mainly composed of non-charged sugars (Heinrichs *et al.*, 1998b). This led to the idea that the additional sugars present in RaLPS, although containing the ColN binding sites, weakened the electrostatic interaction by forming a tightly packed insulating layer between the cationic ColN and the anionic LPS inner head group region.

The restricted accessibility to the LPS head group region was one of the possible causes that prevented ColN specific recognition of RaLPS, thus the same interaction was investigated using an OM model in which the packing of RaLPS had been compromised by EDTA treatment (Clifton *et al.*, 2015b). NR data revealed that in addition to the side-on oriented protein, already observed on the unperturbed asymmetric OM model (**Fig 4.3**), a second species of ColN bound to the EDTA-treated RaLPS model OM adopting a conformation that more closely resembled an end-on orientation of ColN with the major axis normal to the membrane plane. Contrary to the side-on bound ColN, the end-on conformation was shown to remain stably anchored to RaLPS in the presence of 100 mM NaCl which removed the majority of the side-on bound ColN (**Fig 4.6** and **Table 4.3**), indicating a stronger, and more specific interaction.

In vivo, the process of ColN translocation through the OM requires the presence of both RaLPS and OmpF. Whilst RaLPS mediates the anchoring of ColN, by interacting with the R-domain, the actual translocation across the OM involves the formation of a ColN-OmpF complex via the T-domain (Raggett *et al.*, 1998; Housden *et al.*, 2010; Johnson *et al.*, 2013). Baboolal *et al* showed that addition of ColN to OmpF-LPS complexes displaced OmpF-bound LPS and resulted in the formation of an OmpF-ColN complex, indicating that ColN becomes closely associated with the protein-lipid interface (Baboolal *et al.*, 2008). More recently, Clifton *et al* reported the low resolution structure of the ColN-OmpF complex in solution, using small angle neutron scattering (Clifton *et al.*, 2012). In the complex, ColN was shown to unfold and occupy the clefts on the outside of the OmpF trimers, which constitute the protein-LPS interface of OmpF. The high resolution structure of the first porin-LPS complex was also recently elucidated (Arunmanee *et al.*, 2016). It revealed that LPS molecules adjacent to porins, such as OmpF, are anchored to the side of protein for the entire

length of the RdLPS molecule (**Fig. 4.12**) leaving the additional sugars of the RaLPS oligosaccharide, which include ColN binding sites, exposed above the protein lumen. The importance of the exposure of buried oligosaccharide residues for the specific ColN-LPS binding observed here by NR, together with the role of OmpF in ColN translocation, suggests that the exposed sugars of LPS bound to OmpF would constitute the ideal binding site for ColN in the OM.

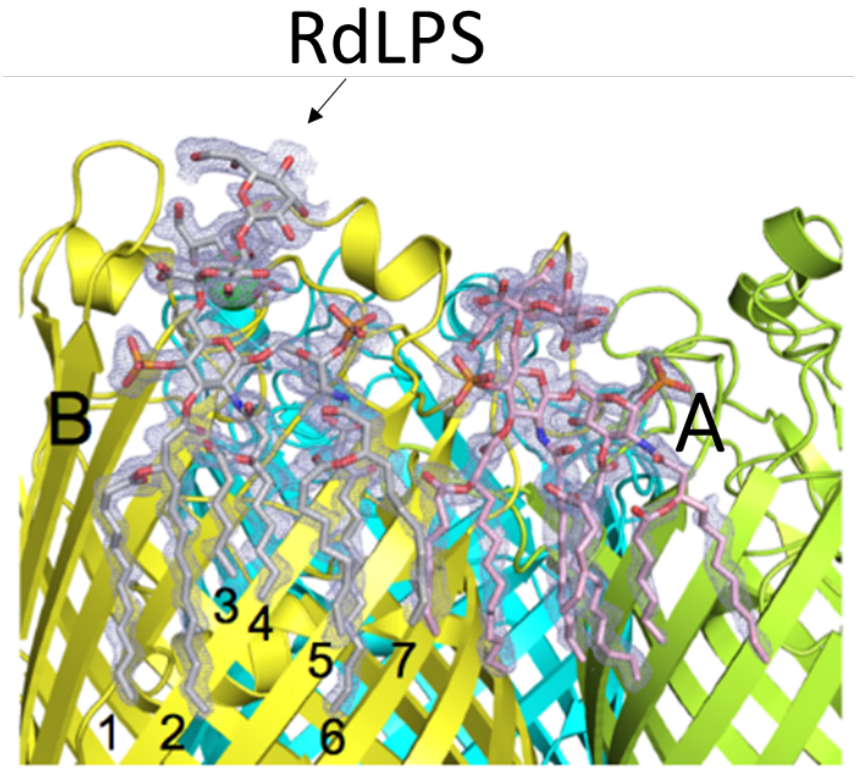

Figure 4.12 | X-ray structure of a porin-RdLPS complex.

Two LPS molecules labelled A and B were resolved in the crystal structure of the LPS-OmpE36 complex described by Arunmanee *et al*. The LPS molecules were hepta-acylated and the seven acyl chains of LPS B are numbered for clarity. LPS B represents the complete RdLPS structure and the arrow indicates the terminal heptose residue of the oligosaccharide. The structure shows how the head group of RdLPS reaches the same height of the protein top. The additional sugar residues of RaLPS, including those recognised by ColN, protrude above the protein lumen providing a suitable site of access for the binding of ColN R-domain. Figure adapted from (Arunmanee *et al.*, 2016)

As shown in **Figure 1.10**, the R-domains of other members of the colicin family are much longer and flexible structures compared to ColN, leaving the other domains projecting from the bacterial surface upon binding of the R-domain to its target OM protein receptor. This would appear to enable subsequent fishing for the translocator protein (Kleanthous, 2010).

By contrast, ColN R-domain, which recognises the LPS core, is a shorter, compact β-rich domain. Anchoring the R-domain to OmpF-bound LPS would in turn bring the T-domain in close contact with its protein target, facilitating the subsequent translocation step.

Although the recognition of the specific sugars present in RaLPS oligosaccharide by the R-domain of ColN had been proven (Johnson *et al.*, 2014), the LPS binding site within the R-domain remained unknown. Previous results in our lab identified a terminal loop region of the R-domain (loop^{R}) which scored highly in structural similarity with the carbohydrate binding motif of the bactericidal permeability-increasing (BPI) protein (**Fig. 4.7**). Therefore, a mutagenesis study was carried out in order to probe the role of loop^{R} in ColN activity. The mutants were tested for toxicity and LPS binding ability (**Fig 4.9** and **4.10**) revealing that disruption of loop^{R} was able to compromise both ColN ability to bind LPS and its toxicity. The greatest reduction in both toxicity and LPS binding was displayed by a six amino acids deletion (ColN$^{\Delta 6}$) and by the charge reversal of the three lysines highlighted in the sequence alignment (ColN^{3E}). A drastic reduction in the polarity of the loop by replacement of three lysines and three asparagines by alanines (ColN^{6A}) also led to a decrease in toxicity and LPS binding, although not to the extent of ColN$^{\Delta 6}$ and ColN^{3E} (**Table 4.5**). None of the single point mutations K171E, K167E, K164E nor the triple charge neutralisation of ColN^{3A} resulted in a decrease in toxicity under the conditions studied here. However K167E, K164E and ColN^{3A} displayed a partial reduction in LPS binding. This indicated that none of the lysines of loop^{R} constitutes, alone, a critical residue for ColN toxicity and even when all three were changed to alanines simultaneously the toxicity was conserved. The higher level of loop^{R} disruption required to abolish ColN toxicity indicated that the RaLPS binding site contained in the R-domain involves the cooperative contribution of several amino acids within the loop^{R} region. This not surprising considering the size of the oligosaccharide involved in the interaction. Furthermore, in addition to the amino acid side chains, the amide bonds of the loop backbone might also play a role in hydrogen bond formation with the target oligosaccharide due to the lack of secondary structure of loop^{R}.

Table 4.5 | List of mutants tested in this study showing the effects on toxicity and LPS binding.

Mutant name	Mutations	Toxicity	LPS binding relative to WT
K171E	K171E	WT	94.2± 5.8%
K167E	K167E	WT	69.3± 0.2%
K164E	K164E	WT	53.5± 3.7%
ColN^{3A}	K171A, K167A, K164A	WT	57.1± 0.9%
ColN^{6A}	K171A, K167A, K164A, N162A, N169A, N170A	Reduced	51.8± 0.6%
ColN^{3E}	K171E, K167E, K164E	Greatly reduced	12.1± 0.6%
ColN$^{\Delta 6}$	Deletion of N162 to K167 (inclusive)	Abolished	15.2± 0.8%

Taken together, the mutagenesis study revealed that loop^{R} plays a crucial role in both ColN toxicity and LPS recognition. Compared to other colicins, the much shorter R-domain of ColN indicates that the T-domain is likely to initiate ColN translocation in the near vicinity of the proposed LPS binding site. In light of the terminal positioning of loop^{R} within the R-domain, the re-orientation of ColN observed by NR upon binding RaLPS, could therefore be functional to bring the T-domain in close contact with its OmpF target, facilitating ColN translocation through the OM (**Fig. 4.13**).

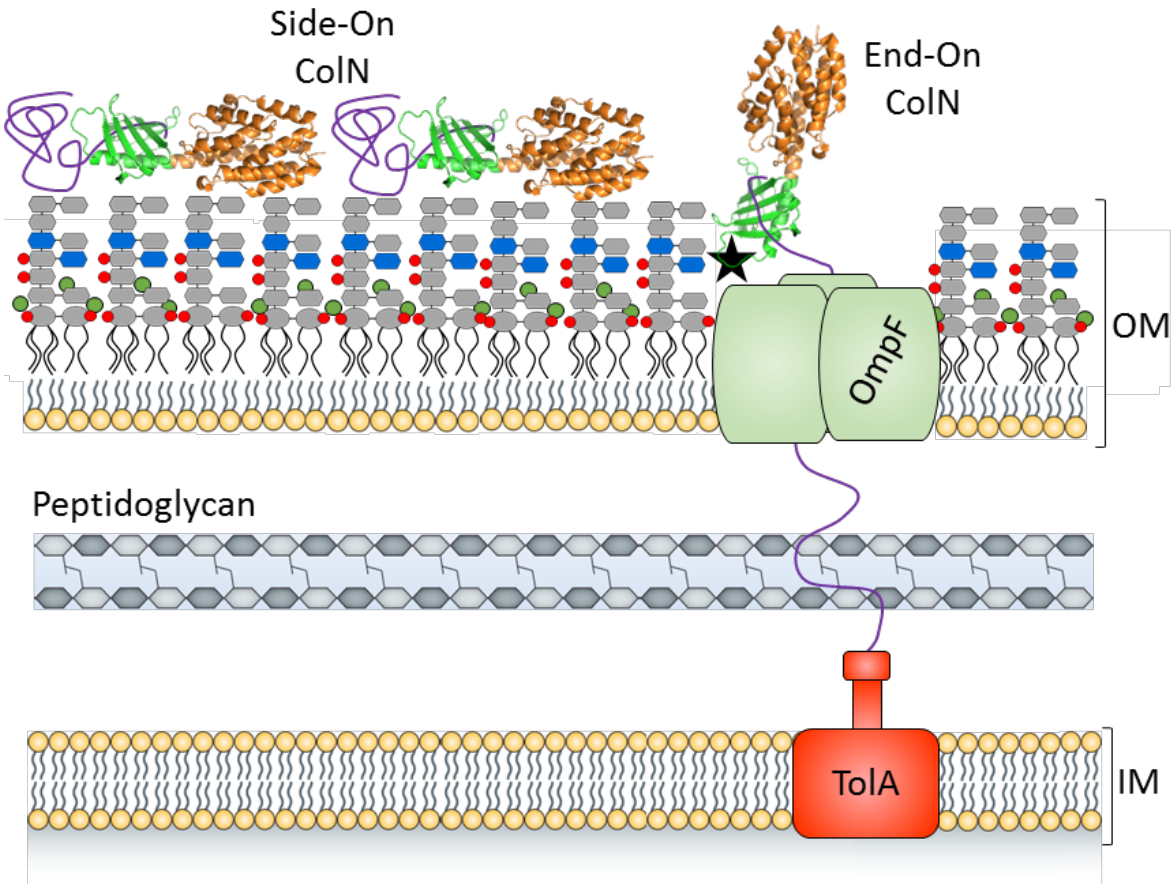

Figure 4.13 | Cartoon of the proposed role of loop^{R} in the first steps of ColN binding.

Schematic cartoon of the Gram-negative cell envelope showing phospholipids in yellow, LPS in grey and calcium as green dots. Highlighted in blue, the sugars recognised by the R-domain of ColN. The two ColN orientations detected by NR are shown in the cartoon. On the left, the side-on oriented ColN which results from non-specific electrostatic interactions with the anionic cell envelope due to lack of accessibility to the LPS-ColN binding sites. On the right, the end-on orientation induced by the specific recognition by the R-domain of the ColN-LPS binding site exposed next to OmpF (★). The T-domain is shown in purple, translocating across the OM via OmpF and binding to its target periplasmic protein TolA. This then leads to P-domain translocation and the pore formation in the IM.

5 Development of Novel Outer Membrane Models

5.1 INTRODUCTION

In the previous two chapters of this thesis, the use of asymmetric outer membrane (OM) models has been central to understand biophysical properties of the OM and its interaction with antimicrobial molecules. However, creating a realistic *in vitro* replica of a complex biological structure like the OM, does not end with reproducing the high levels of lipid asymmetry and tight lipid packing. This chapter describes three types of novel OM models for neutron reflectometry (NR) studies (i) silicon supported smooth LPS OM models (ii) floating smooth LPS OM models (iii) OM models containing the OmpF porin and LPS. The OM models of chapters three and four only contained rough LPS (Ra and Rd types). Rough LPS contains a head group made of a core oligosaccharide which in RdLPS is truncated and in RaLPS is present in its complete form. On the other hand, smooth LPS, contains additional sugars in the head group in the form of a repeating oligosaccharide termed the O-antigen (**Fig 1.2**). Although the majority of strains used in laboratories express a rough form of LPS, this is not the case for strains living in their natural environment such as enteric *E. coli*. This is due to the protected and stress-free environment offered by laboratory conditions, which allows laboratory adapted strains to lose the ability to synthesise the O-antigen (Nikaido, 2003). The O-antigen is formed by a repeating oligosaccharide made of two to six monosaccharide units, which caps RaLPS and is present in highly variable numbers in wild-type (smooth) Gram-negative strains (Stenutz *et al.*, 2006). One aspect which is therefore important to address in order to pursue the creation of a realistic OM replica *in vitro*, is the possibility of using smooth LPS in the OM models to incorporate the O-antigen into the silicon supported asymmetric bilayers (**Fig. 5.1a**).

A second aspect which differentiates biological membranes from supported bilayer models is the interaction of the latter with the underlying solid interface. The presence of substrates such as the silicon wafers used so far in NR experiments, in direct contact with the inner leaflet of the bilayer, can affect the bilayer's behaviour and provide a stabilising effect, due to the restricted mobility of the lipids, which is absent in the biological system due to the restricted mobility of the lipids (Feng *et al.*, 2005; Alessandrini and Facci, 2014; Wu *et al.*, 2016). *In vivo*, the inner phospholipid leaflet of the OM faces the periplasm, an aqueous compartment which contains proteins and the thin peptidoglycan layer of the cell wall. A way to mimic the periplasm in OM models is to include an aqueous compartment between the solid substrate and the inner leaflet, creating a free standing bilayer (FSB) that floats

above a 10-20 Å layer of water (**Fig. 5.1b**) (Hughes *et al.*, 2008; Hughes *et al.*, 2014). FSB can be produced by depositing a lipid bilayer via Langmuir-Blodgett (LB) and Langmuir-Schaefer (LS) techniques onto a substrate coated with a self-assembled monolayer (SAM) which allows the trapping of a water layer below the model membrane. The presence of a water gap between the bilayer and the substrate reduces the interactions between the model membrane and the solid support. The possibility of assembling floating asymmetric OM models was demonstrated recently by Clifton *et al* using 1-oleoyl-2-(16-thiopalmitoyl)-sn-glycero-3-phosphocholine (ω-thioPC) (**Fig. 5.1d**) to create the SAM which provided the substrate for the formation of the floating bilayer (Clifton *et al.*, 2015a). One of the drawbacks of this approach is the limited availability and complex assembly of the ω-thioPC SAM. Here, novel free standing OM models were assembled using N-(2-hydroxyethyl)-16-mercaptohexadecanamide (C16NEtOH) (**Fig. 5.1e**), a less complex, easier to handle and more stable thiolated compound that provides consistently high quality, well characterised SAMs on gold surfaces (Lee *et al.*, 2009; Lee *et al.*, 2018). These, novel, C16NEtOH SAMs were used to support the first floating OM models containing smooth LPS.

Lastly, maybe the clearest difference between the natural OM and the models described so far is the lack of membrane proteins in the *in vitro* models. The natural OM contains a variety of membrane proteins which play a fundamental role in the transport of molecules, including nutrients and most antibiotics (Nikaido, 1992; Pages *et al.*, 2008). Among the most abundant integral membrane proteins that populate the OM are protein channels known as porins which passively regulate the influx and efflux of small water soluble molecules (Nikaido, 1993). The incorporation of oriented proteins in asymmetric phospholipid/LPS bilayers assembled by LB/LS deposition remains a problem that has not yet been solved. However, the trimeric porin OmpF has been successfully reconstituted in phospholipid bilayers grafted to a gold surface (Cisneros *et al.*, 2006; Holt *et al.*, 2009). This has been achieved by Holt *et al* by exploiting the thiol gold chemistry to immobilise OmpF bearing a cysteine mutation (E183C) on the bottom of the barrel in position 183 of its periplasmic β-turn linking β-strand 9 and 10, onto a gold substrate (Terrettaz *et al.*, 2002). Following the protein immobilisation, the gaps between the grafted proteins were filled with 1,2-dipalmitoyl-sn-glycero-3-phosphothioethanol (DPPTE) (**Fig. 5.1f**), a phospholipid bearing a thiol-containing head group, creating a chemically grafted mimic of the inner leaflet.

An outer leaflet was assembled on the OmpF containing bilayer by depositing phospholipids from an ethanolic solution (**Fig 5.1c**).

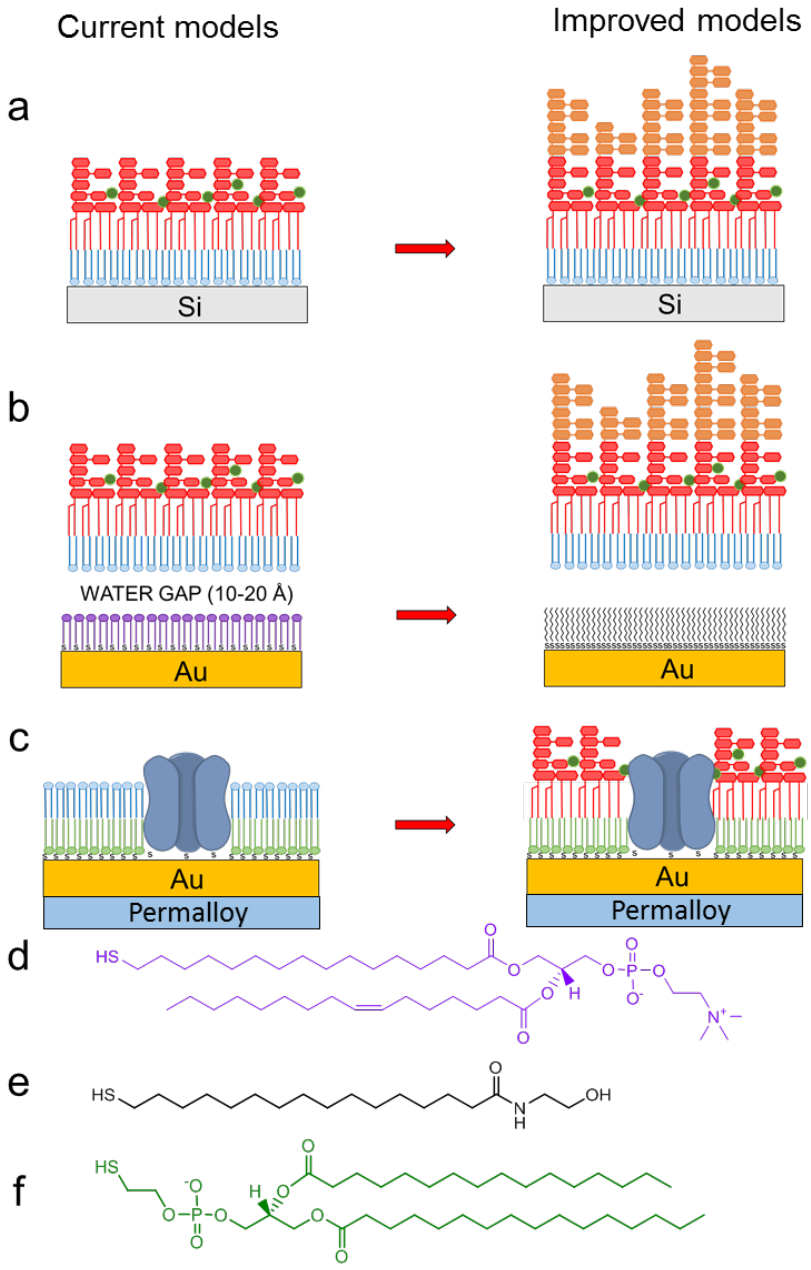

Figure 5.1 | Schematic cartoon of current OM models and novel versions described in this chapter.

(**a**) Asymmetric silicon supported bilayer containing rough (left) and smooth LPS (right). Rough LPS is shown in red, calcium ions are green dots, phospholipids in blue and the O-antigen in orange. (**b**) On the left, the floating OM model containing RaLPS developed by Clifton *et al* by using a SAM of ω-thioPC (purple) floating on a 10-20 Å water layer. On the right a floating OM model containing smooth LPS and assembled on a SAM of C16NEtOH (black) (**c**) On the left, the OmpF containing HBM developed by Holt *et al* composed of a chemically grafted inner leaflet of DPPTE (green), cys-OmpF and a DMPC outer leaflet (blue). On the right the chemically grafted cys-OmpF/DPPTE layer surrounded by RaLPS. (**d**) ω-thioPC (**e**) C16NEtOH (**f**) DPPTE.

The model developed by Holt *et al*, although containing OmpF, lacked LPS, which is a fundamental component of the OM. Here, the approach developed by Holt *et al* was used to create an OmpF-containing HBM which included an LPS outer leaflet (**Fig 5.1c**). The chemically grafted OmpF-DPPTE inner leaflet was used as a platform on which LPS could be introduced from self-assembly. The advantage that this model provides is the possibility to remove LPS from the model using detergents and re-assemble a different type of LPS in situ on the OmpF-DPPTE inner leaflet grafted on gold. This was done here as a proof of principle by assembling the outer leaflet of the protein-containing OM model using hydrogenous RaLPS and then exchanging it for deuterated RaLPS. The NR data on this system was collected using the magnetic contrast technique previously described by Holt *et al* (Holt *et al.*, 2009). Briefly, this approach exploits the magnetic properties of neutrons to generate additional reflectivity curves in the NR experiment. Neutrons have a magnetic moment which contributes to their scattering when they interact with a magnetic material. In the absence of magnetic fields, the spin state of neutrons in a neutron beam is randomly oriented and the magnetic interaction is averaged out. However, in magnetic contrast neutron reflectometry (MCNR) the neutron beam is polarised to select a defined orientation of the neutrons spin state. A magnetic field is then set up across the sample to magnetize a ferromagnetic layer within the sample. This will scatter neutrons with different magnitudes depending if its magnetisation is parallel (↑↑) or antiparallel (↑↓) with the spin state of the beam. Biological samples do not generally display magnetic properties which can be exploited in MCNR. However, if a magnetic layer, such as the ferromagnetic permalloy layer shown in **Figure 5.1c**, is present within the substrate, the SLD of this layer will vary depending on the polarisation of the neutron beam. Thus, measuring the same sample using neutrons polarised parallel or antiparallel to the permalloy layer will generate two different reflectivity curves. This is analogous to exchanging H_2O with D_2O in the sample sub-phase to obtain multiple contrasts that are then used to constrain the fitting of the data. Magnetic contrast and solution contrast can then be combined so that each dataset measured in a certain solution (e.g. D_2O) turns into two datasets, one measured with the neutron beam parallel ($D_2O^{\uparrow\uparrow}$) and one antiparallel ($D_2O^{\uparrow\downarrow}$) with respect to the permalloy layer. Here the OmpF-LPS OM model was characterised with the classic three solution contrasts used so far, but with each contrast measured twice, once with a beam polarised parallel to the permalloy and

once antiparallel, doubling the amount of contrasts to 6, which were then constrained to fit the same model of the interface.

5.2 RESULTS

5.2.1 Asymmetric OM models containing smooth LPS

Four commercially available smooth LPS types from different enteropathogenic serotypes of *E. coli* (O26, O55, O111 and O127) were analysed by DOC PAGE to characterise their LPS content (**Fig. 5.2**). The banding profiles indicated that all smooth LPS types contained a considerable fraction of rough LPS and LPS containing 1 O-antigen unit, referred to as semi-rough LPS or lipooligosaccharide (LOS). Serotype O26 only displayed a clear band corresponding to RaLPS whilst a high molecular weight (MW) component was visible at the top of the gel for serotypes O55, O111 and O127, although less pronounced in the case of the latter. The LOS fractions displayed similar banding patterns in O55 and O111 whilst O127 displayed a fainter band corresponding to RaLPS and the RaLPS+1 O-antigen unit seemed to account for the largest fraction of the LOS. The LPS from serotypes O55, O111 and O127 was chosen for the reconstitution experiments as it showed a visible high MW LPS fraction which suggested the presence of long O-antigen chains.

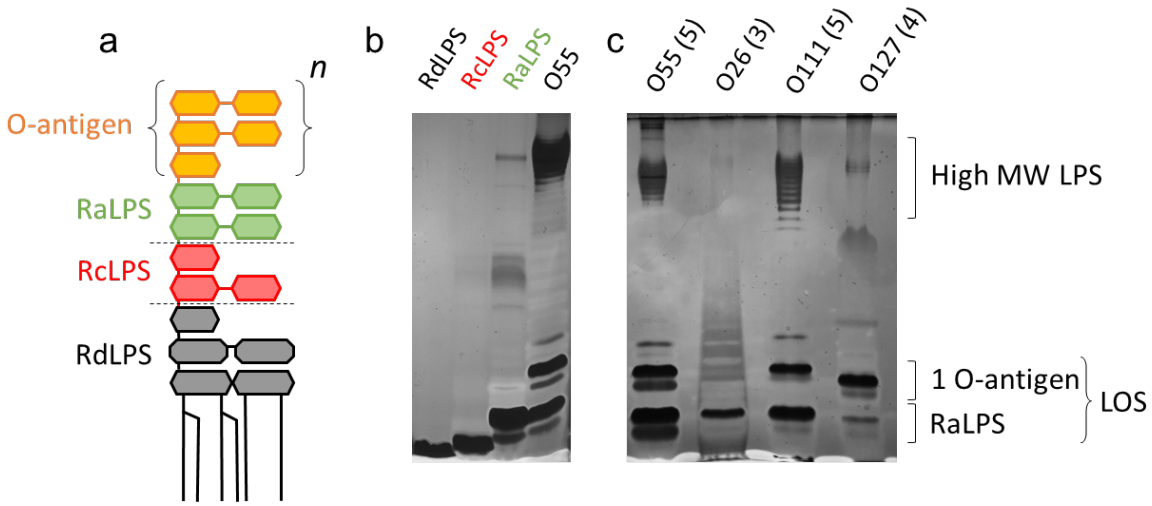

Figure 5.2 | DOC PAGE banding pattern of LPS.

(**a**) Schematic representation of LPS and its carbohydrate head group sections. In black RdLPS, in red the extra sugars present in RcLPS, in green the additional sugars present in the complete core oligosaccharide of RaLPS. In orange a single unit of O-antigen (**b**) Effect of oligosaccharide size on the DOC PAGE banding pattern of rough and smooth LPS visualised by silver staining. Comparison between truncated rough LPS (Rd and RcLPS), complete core RaLPS and smooth LPS. (**c**) Comparison of smooth LPS from enteropathogenic *E. coli* serotypes O55, O26, O111 and O127. In brackets the number of monosaccharides present in a single O-antigen unit of each LPS species.

The method used for the deposition of rough LPS monolayers at the air-water interface did not yield stable smooth LPS monolayers until the organic solvent used to solubilise smooth LPS was changed from $CHCl_3$, MeOH, H_2O (60:39:1, v:v:v) to phenol:$CHCl_3$:petroleum ether 2:5:8 (v:v:v) (PCP). The choice of PCP as the solvent for the deposition was based on a recent paper by Miciulla *et al* who used the PCP solvent mixture to spread stable smooth LPS monolayers at the air-water interface (Micciulla *et al.*, 2019). Other than the change in the LPS solvent, the procedure described for the assembly of the asymmetric OM models containing rough LPS remained the same for smooth LPS. The OM models containing smooth LPS were thus characterised by NR. **Figure 5.3** shows the reflectivity curves, fits and corresponding SLD profiles from the OM models reconstituted using the LPS from enteropathogenic bacteria whilst the parameters derived from the fits are listed in **Table 5.1**. Except for the O-antigen region, the bilayers were modelled using the same approach used in the previous chapters. The O-antigen however, due to its elongated nature and highly variable chain length does not lend itself to be represented as a stack of well-defined layers. The volume fraction of the long carbohydrate chains as a function of the distance from the bilayer (x) was thus modelled using the decay function described by **Equation 5.1**:

$$\Phi_{(x)} = \alpha e^{-\left(\frac{x}{\gamma}\right)^{\beta}} \quad (5.1)$$

Where $\Phi_{(x)}$ is the volume fraction of O-antigen as a function of distance, α defines the maximum volume fraction, β describes how steep is the decay whilst γ relates to the length of the O-antigen layer. This was the same approach used previously to model the O-antigen region of smooth LPS monolayers (Rodriguez-Loureiro *et al.*, 2018; Micciulla *et al.*, 2019). All three types of smooth LPS yielded high quality asymmetric OM models with coverages between 92% and 98%. The levels of asymmetry were also high and comparable to those obtained with rough LPS, displaying outer leaflets containing between 89% and 91% of LPS and inner leaflets containing between 88% and 96% d_{62}DPPC. Overall the three OM models reconstituted using O-antigen containing LPS species yielded highly asymmetric OM models comparable to those obtained with rough LPS.

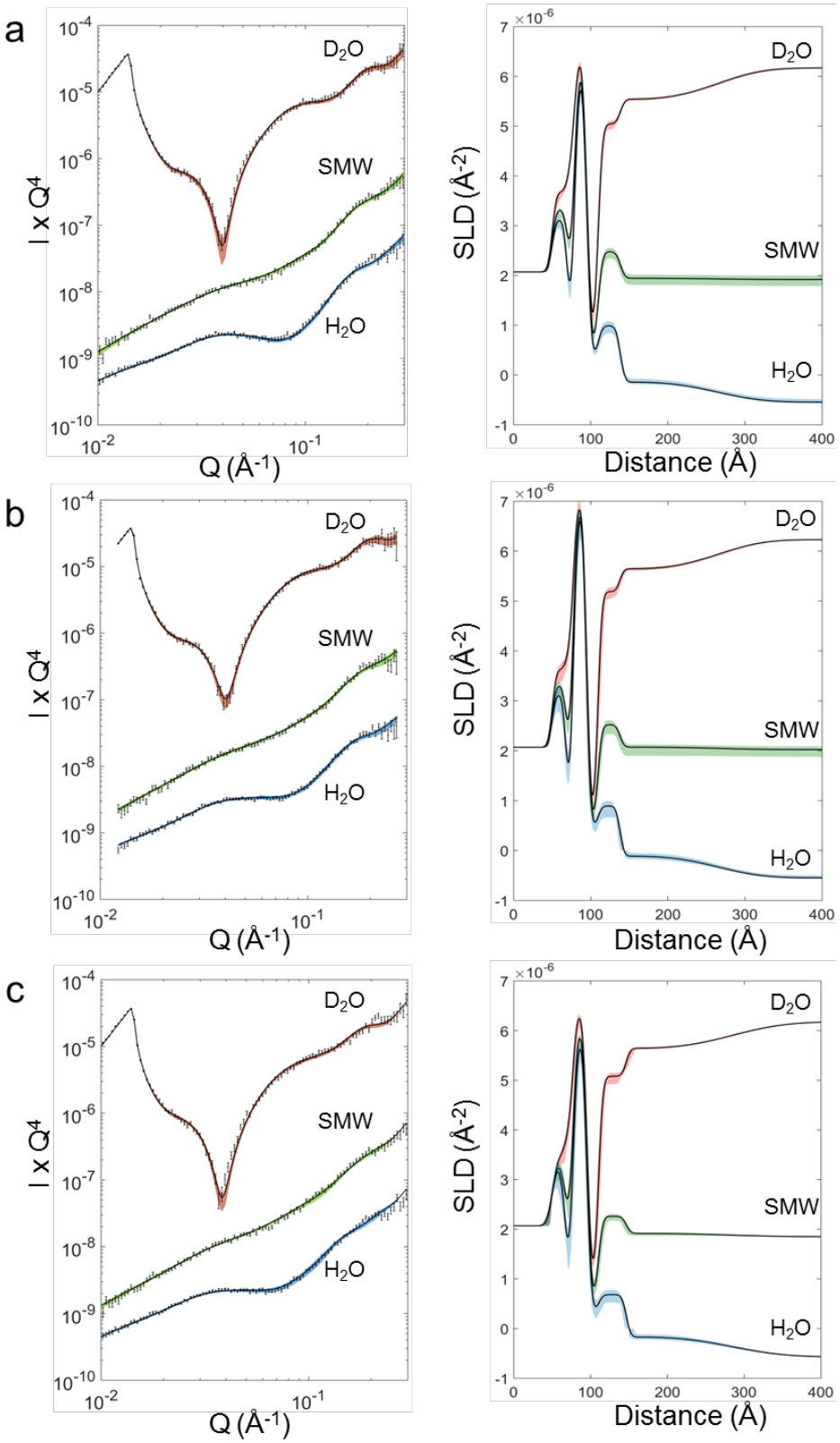

Figure 5.3 | NR of asymmetric OM models containing smooth LPS.

Neutron reflectivity data points, best fit lines (left) and corresponding SLD profiles (right) for OM models reconstituted using (**a**) O55 (**b**) O111 and (**c**) O127 LPS. Reflectivity curves are offset vertically for clarity.

Table 5.1 | Parameters derived from the fitting of the NR data from the O-antigen containing OM models assembled from smooth LPS.

In brackets, the 95% confidence interval derived from the Bayesian error analysis. Substrate parameters are omitted for simplicity

Bilayer parameters	Fitted value O55	Fitted value O111	Fitted value O127
dDPPC HG thickness (Å)	8.4 (8.0, 9.0)	9.2 (8.3, 10.0)	9.5 (8.9, 10.1)
dDPPC HG SLD ($Å^{-2}x10^{-6}$)	1.82 (1.71, 1.90)	1.82 (1.71, 1.90)	1.79 (1.70, 1.89)
dDPPC HG coverage (%)	45.5 (41.7, 50.0)	51.7 (45.0, 58.5)	49.2 (44.5, 54.1)
dDPPC tails thickness (Å)	16.3 (16.0, 17.0)	17.4 (16.2, 18.6)	18.5 (17.5, 19.0)
dDPPC tails SLD ($Å^{-2}x10^{-6}$)	6.52 (6.35, 6.72)	7.06 (6.75, 7.37)	6.44 (6.26, 6.70)
LPS tails thickness (Å)	14.2 (14.0, 14.5)	14.5 (14.0, 15.2)	14.7 (14.0, 15.3)
LPS tails SLD ($Å^{-2}x10^{-6}$)	0.31 (0.24, 0.36)	0.42 (0.22, 0.63)	0.38 (0.06 0.65)
LPS HG thickness (Å)	29.1 (27.8, 30.0)	28.7 (26.7, 30.9)	36.2 (34.4, 38.0)
LPS HG SLD in D_2O ($Å^{-2}x10^{-6}$)	4.16 (4.01, 4.38)	4.43 (4.19, 4.63)	4.14 (4.00, 4.31)
LPS HG coverage (%)	54.6 (51.3, 58.9)	56.6 (50.0, 62.2)	52.4 (46.7, 57.9)
O-antigen SLD in D_2O ($Å^{-2}x10^{-6}$)	3.0 (2.73, 3.4)	3.29 (2.73, 3.87)	3.21 (2.39 3.81)
α	0.20 (0.18, 0.22)	0.20 (0.17, 0.24)	0.18 (0.18 0.29)
β	3.05 (2.86, 3.15)	3.08 (3.04, 3.10)	3.00 (2.89, 3.10)
γ	141.9 (138.5, 145.4)	143.5 (140.3, 146.7)	157.4 (153.8, 161.8)
Bilayer coverage (%)	95.8 (93.3 97.9)	97.9 (95.1 99.9)	92.1 (90.2, 94.2)
Bilayer roughness (Å)	4.8 (4.3, 5.3)	4.4 (3.8, 4.9)	4.7 (4.3, 5.1)

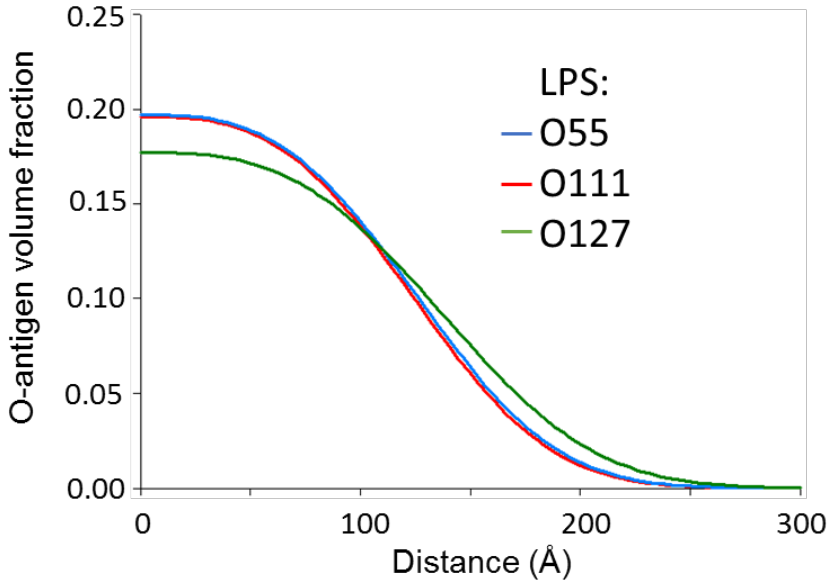

Figure 5.4 | Distribution of O-antigen chains of the OM models containing smooth LPS.

Exponential functions describing the decay of the volume fraction of O-antigen from the end of the core oligosaccharide region which represents the origin of the x axis in the graph.

For O55 and O111 LPS, the structure of the core oligosaccharide region was in line with that of RaLPS measured in the previous chapters displaying a length of 29 Å and a coverage of ~55%. However, in the case of O127 LPS the core oligosaccharide region was ~7 Å thicker compared to the other two LPS species. This is in agreement with the DOC PAGE banding profile of O127 (**Fig. 5.2**) which indicates that the LOS of this LPS species contains a high fraction of LPS with 1 O-antigen and lower amounts of RaLPS, implying an increased minimal length of the LPS head group.

The O-antigen region was similar across the three OM models (**Fig. 5.4**). The difference between the structures of O55 and O111 O-antigen layers was almost indistinguishable both in terms of length (~ 250 Å) and volume fractions. O127 displayed a marginally more extended ensemble of carbohydrate chains with a slightly different distribution of the volume fraction which was lower in the proximity of the core oligosaccharide but decayed more gently as a function of distance. The value of α, which describes the maximum volume fraction of the O-antigen (i.e. the value of the function at the origin in **Fig. 5.4**) indicated a starting coverage of 18%-20% of the carbohydrate chains of the O-antigen which projected from a core oligosaccharide of 52%-57% coverage. An exact value for the thickness of the O-antigen cannot be obtained from the function, which asymptotically tends to zero. However, evaluating the function at an arbitrary low coverage is useful to compare the extension of the three functions. For example, at 0.1% coverage of the O-antigen chains the O-antigen chain length is 247.2 Å, 250.8 Å and 273.3 Å from the core oligosaccharide for O111, O55 and O127 respectively.

5.2.1.1 Smooth LPS fractionation and purification

Unlike for rough LPS, it is not possible to obtain smooth LPS with a defined length of the O-antigen by mutating genes involved in LPS synthesis (Samuel and Reeves, 2003). Therefore, in order to achieve some degree of control on the amount of O-antigen in the OM models, one approach is to separate heterogeneous smooth LPS in fractions containing different numbers of O-antigen units and use these fractions to reconstitute different OM models. Size exclusion chromatography (SEC) was used to fractionate LPS containing different amounts of O-antigen by exploiting the different size of the smooth LPS molecules, following a modified version of the protocol illustrated by Peterson and McGroarty and

described in the Methods (Peterson and McGroarty, 1985). LPS from *E. coli* O111:B4 (Sigma Aldrich) was dissolved in a buffer containing 0.25% deoxycholate (DOC) and 1 mM EDTA to dissociate the LPS molecules which otherwise form large aggregates, due to their amphiphilic nature, that elute in the void volume. Considering the molecular weight (MW) of RaLPS of ~4 kDa, the column used for the purification was a size exclusion chromatography column (Generon) with an optimal resolution for molecules between 3 and 70 kDa. Since LPS does not absorb in the UV spectrum, detection of the eluted species was done by running the content of each fraction collected on DOC PAGE and staining using silver staining. The separation by size of the species contained in the commercially available smooth LPS from *E. coli* serotype O111 is shown in **Figure 5.5**. Separation of monodisperse species containing an exact number of O-antigen units could not be achieved. However, the fractionation allowed the successful separation of fractions of LPS species with increasing amounts of O-antigen. Three sets of fractions were pooled together: a low-MW fraction, containing RaLPS and LPS with up to 3 O-antigen units, a mid-MW fraction of LPS containing between 1 and 10 O-antigen units and a high-MW fraction containing only LPS with more than 5 O-antigen units. The pooled fractions were and extensively dialysed in Nanopure water to remove all components of the SEC buffer and freeze dried.

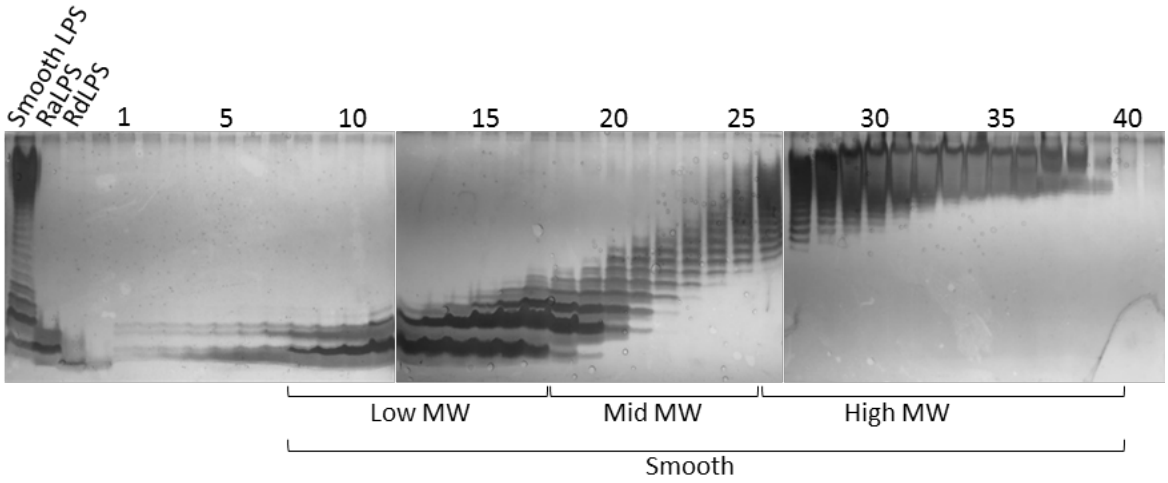

Figure 5.5 | DOC PAGE of fractions collected from SEC from the separation of LPS O111.

On the left side the different types of LPS available commercially which differ in the size of the oligosaccharide head group. On the right the fractions (1-40) collected from the SEC experiment containing increasing amounts of O-antigen. The fractions were pooled according to the grouping indicated below the gel and used in the reconstitution of the OM models. The low-MW fractions (fr. 8-17) contained between 0 and 3 O-antigen units, the mid-MW (fr. 18-25) between 1 and 10 and the high-MW more than 5 O-antigen units (fr. 26-38).

5.2.1.2 NR characterisation of OM models containing fractionated LPS

The freeze-dried pooled fractions of LPS were used to reconstitute asymmetric OM models. The high-MW fraction, containing only the long-chain O-antigen component of smooth LPS did not form stable monolayers suitable for the LS assembly of the model membranes probably due to the high water solubility of these molecules. Therefore, asymmetric OM models were assembled using only the low and mid MW fractions and characterised by NR. The NR data and the corresponding SLD profiles from two OM models containing low and mid MW fractions are shown in **Figure 5.6** and the parameters relative to the fits in **Table 5.2**. The coverage of the bilayers was ~87% and ~94% for the low-MW and the mid-MW respectively. The asymmetry level was high with the low-MW LPS models containing ~98% d_{62}DPPC and ~92% LPS in the inner and outer leaflet respectively whilst the he mid-MW fraction model was composed of ~86% d_{62}DPPC and ~89% LPS in the inner and outer leaflets. The low-MW LPS model was found to have a ~29 Å thick core oligosaccharide region, in line with that of RaLPS whilst the mid-MW had a substantially thicker core oligosaccharide layer measuring a total of ~44 Å. As shown by the banding pattern of the mid-MW LPS in the DOC PAGE, nearly all RaLPS was removed from this fraction, thus increasing the minimal length of the oligosaccharide to that of LPS bearing 1 O-antigen units. The region modelled by the exponential function showed also two very different regions of the sparse carbohydrate chains. For the low-MW LPS the function described a dense and short layer, with an initial volume fraction of ~29% that quickly decayed below 0.1% coverage at 44.6 Å from the core oligosaccharide. The model containing the mid-MW fraction LPS had longer but much sparser O-antigen layer with an initial volume fraction of ~5% and an extension of 130.8 Å at 0.1% coverage (**Fig. 5.6c**)

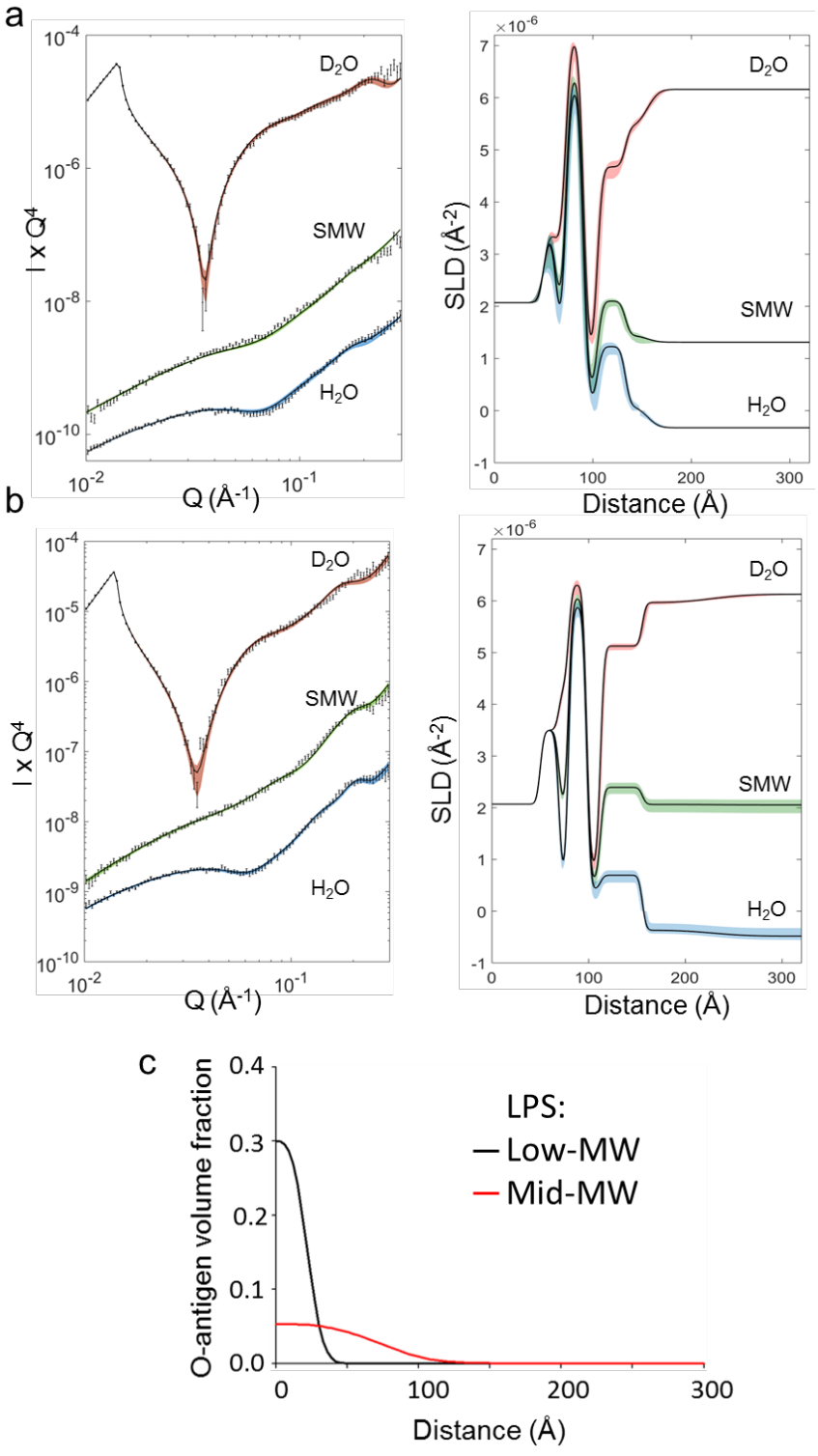

Figure 5.6 | NR of O-antigen containing asymmetric OM models.

NR data points, best fit lines (left) and corresponding SLD profiles (right) for OM models reconstituted using (**a**) low-MW fraction and (**b**) mid-MW fraction of O111 LPS. (**c**) Exponential functions describing the decay of the volume fraction of O-antigen from the end of the core oligosaccharide region for the low-MW LPS (black) and the mid-MW LPS (red). Reflectivity curves are offset vertically for clarity.

Table 5.2 | Parameters derived from the fitting of the NR data from the OM models containing fractionated smooth LPS.

In brackets, the 95% confidence interval derived from the Bayesian error analysis. Substrate parameters are not shown for simplicity.

Bilayer parameters	Fitted value Low-MW	Fitted value Mid-MW
dDPPC HG thickness (Å)	9.0 (8.3, 9.7)	9.8 (9.6, 9.9)
dDPPC HG SLD ($Å^{-2}x10^{-6}$)	1.79 (1.71, 1.89)	1.81 (1.71, 1.89)
dDPPC HG coverage (%)	67.8 (65.2, 70.0)	42.0 (40.2, 44.6)
dDPPC tails thickness (Å)	18.0 (17.2, 18.8)	18.7 (18.2, 19.0)
dDPPC tails SLD ($Å^{-2}x10^{-6}$)	7.31 (7.14, 7.39)	6.32 (6.20, 6.46)
LPS tails thickness (Å)	14.1 (14.0, 14.3)	14.3 (14.0 14.6)
LPS tails SLD ($Å^{-2}x10^{-6}$)	0.23 (-0.16, 0.58)	0.48 (0.30, 0.63)
LPS HG thickness (Å)	28.6 (27.1, 30.2)	43.5 (42.3, 44.7)
LPS HG SLD in D_2O ($Å^{-2}x10^{-6}$)	4.18 (4.02, 4.30)	4.05 (4.00, 4.13)
LPS HG coverage (%)	71.5 (69.8, 72.9)	46.9 (44.8, 49.1)
O-antigen SLD in D_2O ($Å^{-2}x10^{-6}$)	3.79 (3.05, 4.51)	3.22 (2.55, 3.81)
α	0.29 (0.21, 0.4)	0.05 (0.04, 0.06)
β	3.01 (2.78, 3.26)	2.97 (2.82, 3.14)
γ	25.2 (22.9, 27.6)	83.8 (70.0, 102.6)
Bilayer coverage (%)	86.9 (85.0 88.7)	93.6 (91.8, 95.6)
Bilayer roughness (Å)	4.2 (3.7, 4.7)	3.2 (3.0, 3.5)

Overall, these results showed that it is possible to reconstitute smooth LPS in high coverage asymmetric OM models. Moreover, the separation of LPS by size allowed to achieve some degree of control on the amount of O-antigen contained in the model membranes.

5.2.2 Floating OM models

The possibility of creating floating OM models containing RaLPS have been recently demonstrated on a SAM made of phospholipids functionalised with a terminal thiol group on one of the two alkyl chains (ω-thioPC) (**Fig. 5.1d**) (Clifton *et al.*, 2015a). The high cost and low availability of the ω-thioPC significantly limited the use of these model membranes. Therefore, to overcome issues related to the use of ω-thioPC, here floating OM models were deposited above a SAM made of N-(2-Hydroxyethyl)-16-mercaptohexadecanamide (C16NEtOH). These thiols are much simpler molecules (**Fig. 5.1e**), are commercially

available and known to form high quality monolayers on gold surfaces which make them suitable for supporting the formation of the floating membranes (Lee *et al.*, 2009; Lee *et al.*, 2018). Gold coated silicon wafers were functionalised with a C16NEtOH SAM as described in the Methods and used as substrates for the LB/LS deposition of asymmetric OM models containing tail deuterated DPPC in the inner leaflet and RaLPS on the outer leaflet. The model membranes were then characterised by NR. Due to the higher complexity of the system, the samples were measured under four rather than three solution contrasts by adding a dataset collected in a mixture of H_2O and D_2O 1:3 (v:v) which matches the SLD of gold (gold matched water, AuMW). Furthermore, the C16NEtOH coated gold substrates were also characterised in H_2O and D_2O in the absence of the lipid bilayer and added to the list of datasets used in the model to constrain the fitting of the substrates structure. The SAM layer was modelled by fitting an area per molecule (APM) to the C16NEtOH layer in order to constrain the headgroup region and the tail region to be consistent with being part of the same molecule. **Figure 5.7a** shows the set of all reflectivity datasets used to obtain the structure of the sample assembled using the low-MW LPS O111 obtained as described in section 5.2.1.1. The first two curves (labelled D_2O* and H_2O*) were obtained from the gold coated substrate functionalised with the C16NEtOH SAM in the absence of the lipid bilayer and describe the structure of the substrate alone shown in **Figure 5.7b**. The curves 3 to 6 describe the complete sample, after the deposition of the asymmetric bilayer which is described by the SLD profile shown in **Figure 5.7c**. The parameters obtained from the fits are displayed in **Table 5.3**. All the curves were fitted to a common model of the interface and shared the same parameters for the substrate, composed of silicon oxide, permalloy, gold, C16NEtOH tails and C16NEtOH head group layers. On top of the substrate layers, the asymmetric bilayer was modelled as described earlier, with the addition of a layer of water between the C16NEtOH head group and the bilayer. The parameters obtained from the fits to the data are shown in **Table 5.3** and indicated the formation of a high coverage C16NEtOH SAM on the gold surface, with a coverage of ~97% and a small APM ~22 $Å^2$, indicating the formation of a tightly packed monolayer on the gold surface. The bilayer data described an asymmetric OM model containing 88% d_{62}DPPC in the inner leaflet and 89% LPS in the outer leaflet, with a total coverage of 79%. A ~10 Å water gap was found to separate the substrate and the bilayer indicating the successful formation of a floating OM model.

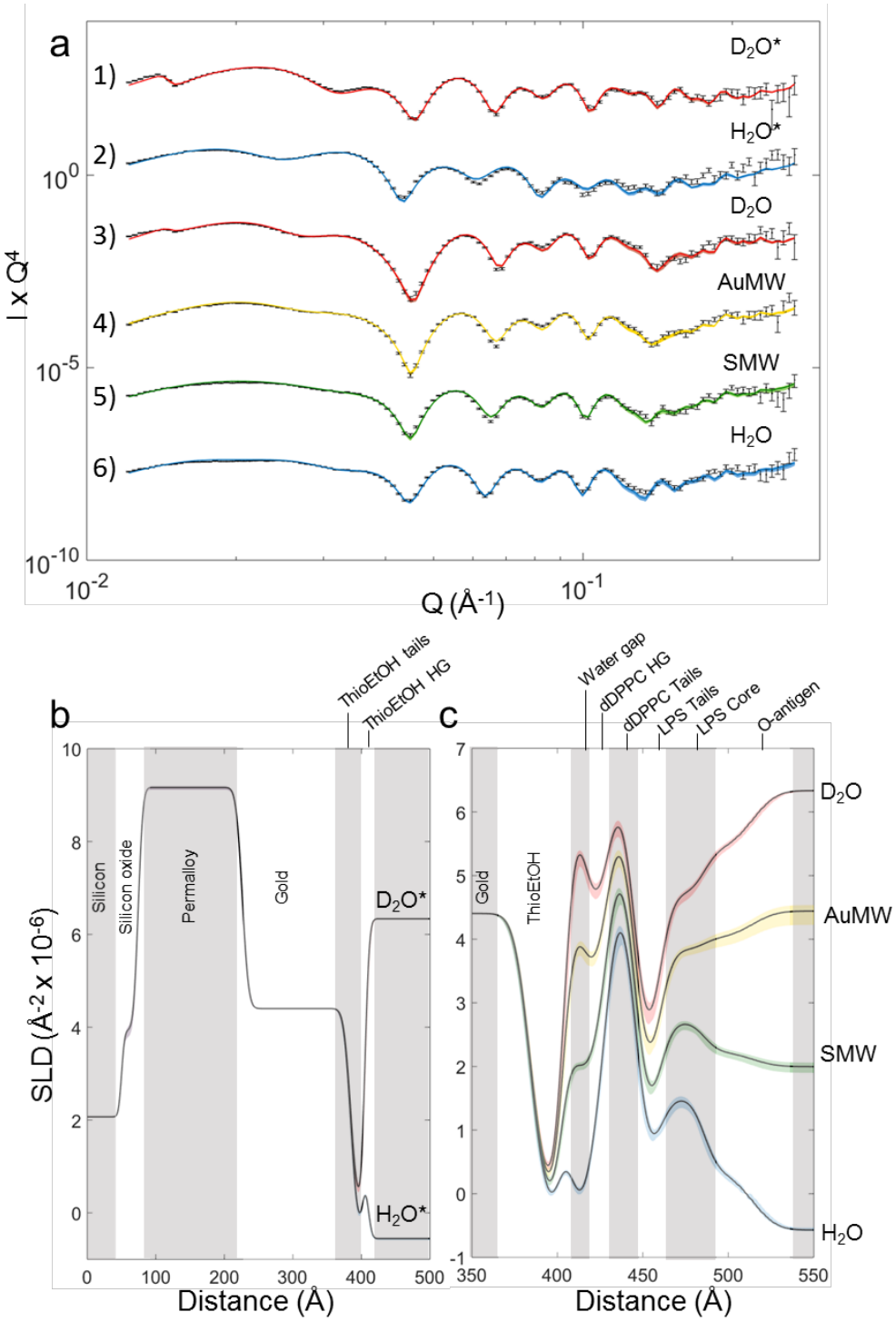

Figure 5.7 | NR of floating OM model containing low-MW fraction LPS.

(**a**) Neutron reflectivity curves from the C16NEtOH coated gold substrate alone (curves 1-2) and from the same substrate in the presence of the floating OM model containing the low-MW fraction of smooth LPS O111 (curves 3-6). Reflectivity curves are offset vertically for clarity (**b**) SLD profile of the gold coated substrate functionalised with the C16NEtOH SAM without bilayer. All 6 curves in **a,** were constrained to fit to this structure of the substrate and SAM. The layers of the model are labelled and shaded in grey (**c**) SLD profile of the floating OM model containing the low-MW fraction of smooth LPS.

Using the same approach, unfractionated smooth LPS O111 was also reconstituted in a floating OM model (**Fig. 5.8** and **Table 5.3**).

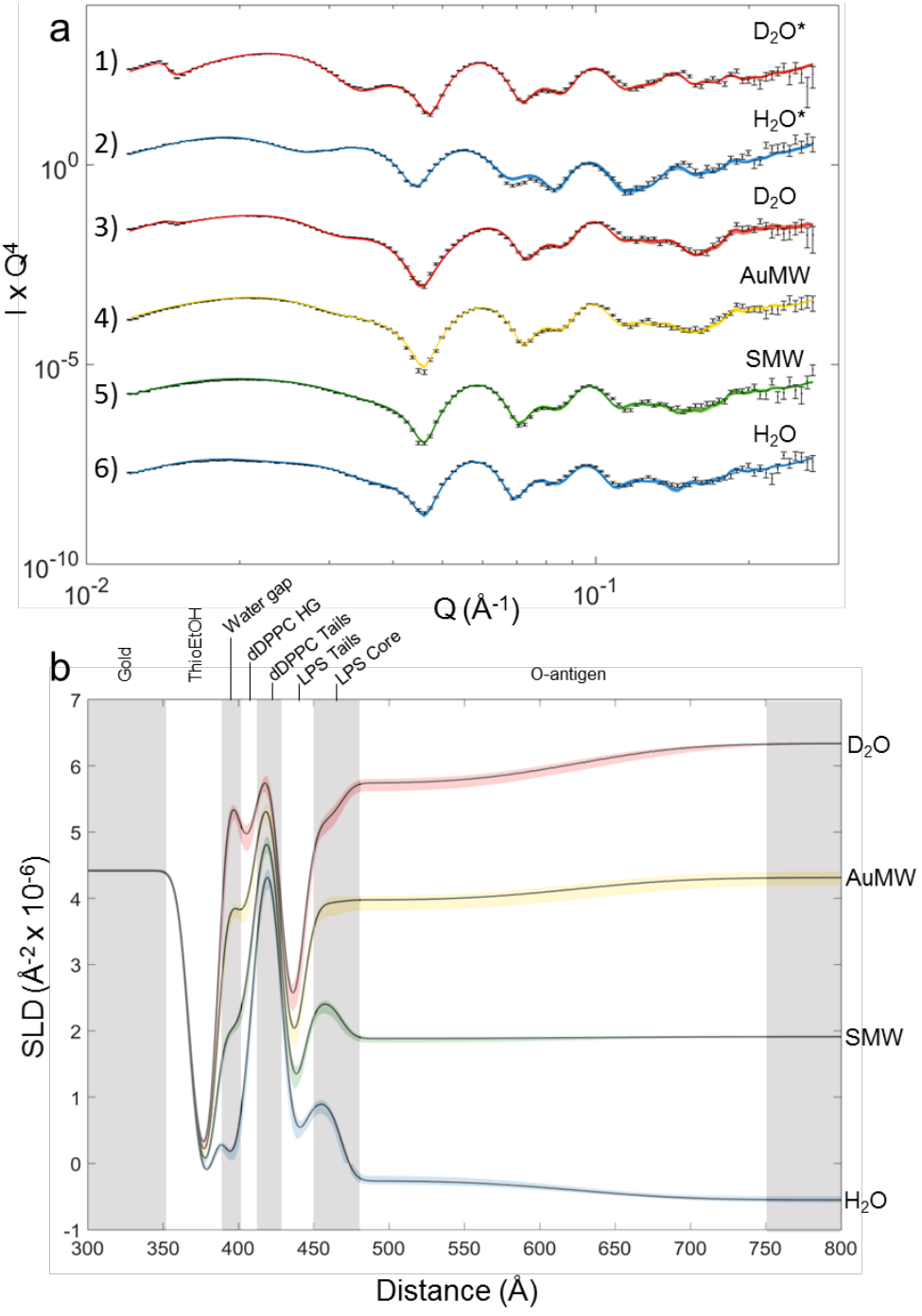

Figure 5.8 | NR of floating OM model containing smooth LPS.

(**a**) Neutron reflectivity curves from the C16NEtOH coated gold substrate alone (curves 1-2) and from the same substrate in the presence of the floating OM model containing smooth LPS O111 (curves 3-6). Reflectivity curves are offset vertically for clarity (**b**) SLD profile of the floating OM model containing smooth LPS O111. The layers of the model are labelled and shaded in grey. The structure of the underlying substrate is omitted for simplicity.

The structure and coverage of the C16NEtOH SAM were almost indistinguishable from those of the substrate measured earlier indicating the consistent formation of high coverage monolayer.

Table 5.3 | Parameters derived from the fitting of the NR data from the floating OM models containing low-MW fractionated and smooth O111 LPS.

In brackets the 95% confidence interval derived from the Bayesian error analysis. Shaded parameters were fixed to their calculated value.

Bilayer parameters	Fitted value Low-MW	Fitted value Smooth
Substrate roughness (Å)	3.0 (3.0, 3.1)	3.0 (3.0, 3.1)
Oxide thickness (Å)	23.1 (22.6, 23.8)	27.9 (27.1, 28.5)
Silicon oxide SLD ($Å^{-2}x10^{-6}$)	3.41	
Silicon oxide roughness (Å)	6.2 (5.7, 6.7)	8.2 (7.7, 8.7)
Permalloy thickness (Å)	152.8 (152.3 153.4)	155.3 (154.9, 155.7)
Permalloy SLD ($Å^{-2}x10^{-6}$)	9.17 (9.14, 9.21)	8.86 (8.82, 8.91)
Permalloy roughness (Å)	9.1 (8.7, 9.5)	8.8 (8.6, 9.1)
Gold thickness (Å)	158.2 (157.9, 158.5)	136.6 (136.3, 137.0)
Gold SLD ($Å^{-2}x10^{-6}$)	4.41 (4.40, 4.42)	4.27 (4.23, 4.32)
Gold roughness (Å)	7.5 (7.1, 7.9)	7.4 (7.2, 7.6)
ThioEtOH APM ($Å^2$)	22.0 (21.6, 22.3)	21.8 (21.5, 22.2)
ThioEtOH coverage (%)	96.5 (96.4, 96.6)	96.8 (96.7, 96.9)
ThioEtOH roughness (Å)	5.1 (4.9, 5.3)	6.2 (6.0, 6.4)
Central water thickness (Å)	9.9 (9.2, 10.4)	10.2 (9.8, 10.5)
dDPPC HG thickness (Å)	11.4 (10.9, 11.9)	10.8 (10.5, 11.2)
dDPPC HG SLD ($Å^{-2}x10^{-6}$)	1.62 (1.51, 1.77)	2.44 (2.31, 2.57)
dDPPC HG coverage (%)	54.0 (51.0, 57.1)	68.5 (67.3, 69.7)
dDPPC tails thickness (Å)	17.3 (16.6, 18.1)	18.9 (18.6, 19.0)
dDPPC tails SLD ($Å^{-2}x10^{-6}$)	6.43(6.22, 6.64)	6.06 (6.00, 6.17)
LPS tails thickness (Å)	13.2 (12.6, 13.7)	14.0 (13.5, 14.7)
LPS tails SLD ($Å^{-2}x10^{-6}$)	0.48 (0.46, 0.50)	-0.05 (-0.06, -0.05)
LPS HG thickness (Å)	27.2 (26.1, 28.6)	25.6 (24.2, 26.9)
LPS HG SLD in D_2O ($Å^{-2}x10^{-6}$)	4.00 (3.90, 4.10)	4.93 (4.83, 4.99)
LPS HG coverage (%)	69.3 (68.2, 70)	52.0 (49.9, 54.2)
O-antigen SLD in D_2O ($Å^{-2}x10^{-6}$)	3.83 (3.71, 3.96)	3.73 (3.50, 3.87)
α	0.36 (0.35, 0.38)	0.24 (0.23, 0.25)
β	2.96 (2.90, 3.04)	2.92 (2.90, 2.98)
γ	32.0 (31.2, 32.8)	138.12 (132.8, 143.3)
Bilayer coverage (%)	79.0 (76.7, 81.2)	87.1 (84.9, 89.6)
Bilayer roughness (Å)	6.6 (6.1, 7.0)	7.2 (7.0, 7.5)

The bilayer obtained from smooth LPS displayed a high coverage (~87%) and asymmetry (~83% d_{62}DPPC in the inner leaflet and ~96% LPS in the outer leaflet). The O-antigen layer of the floating smooth LPS OM model was also in line with that of the same LPS reconstituted onto silicon, with an initial volume fraction of 24% in the proximity of the core oligosaccharide and an extension of 243.3 Å at 0.1% coverage.

5.2.3 Effect of EDTA on floating and silicon supported smooth LPS OM models

The purpose of introducing a water cushion between the solid substrate and the OM model addressed in the previous section, was to avoid any artefactual effects on the behaviour of the bilayer, resulting from the interaction of the inner leaflet with the underlying solid interface. To better understand to what extent the presence of a solid support stabilises the OM models, the effect of the chelating agent EDTA on the models assembled using smooth LPS O111 on silicon was compared to that of the same model floating above the C16NEtOH SAM. EDTA is known to disrupt the OM both *in vivo* (Vaara, 1992) and *in vitro* (Clifton *et al.*, 2015b). In chapter 4, it was used to destabilise an RaLPS silicon-supported OM model, resulting in an increase of the phospholipid content in the outer leaflet from ~5% to ~28%. The NR data and the corresponding SLD profile of the silicon supported smooth LPS OM model treated with 3 mM EDTA are shown in **Figure 5.9** and the relative parameters are listed in **Table 5.4**. The OM model directly assembled on silicon displayed minimal changes after the EDTA treatment (**Fig. 5.9a**). Comparing the parameters before EDTA treatment (**Table 5.1**) and after (**Table 5.4**), indicates that the overall structure of the bilayer remained largely unaffected both in terms of coverage and characteristics of the layers, including the O-antigen region. The main change was a minor mixing of the two leaflets with the d_{62}DPPC content of the LPS leaflet going from ~10% to ~14% whilst the LPS content of the d_{62}DPPC leaflet increased from ~4% to ~9%. ETDA treatment of the floating version of the same OM model, containing smooth LPS O111, had a substantially different effect (**Fig 5.9b**). EDTA completely removed the bilayer from the surface of the substrate leaving only unstructured remnants with a coverage of ~7% on the surface (the parameters of the fits are not shown as the SLD clearly shows that no layer model would give any relevant information). Considering the identical lipid composition of the two bilayers, the only difference between the two OM models was the interaction with the underlying substrate. When in direct contact

with the silicon solid substrate, the effects of removing stabilising Ca^{2+} ions from the OM model were barely noticeable. On the contrary when Ca^{2+} ions were removed from the same OM model floating above the ~10 Å water gap, the bilayer was completely solubilised.

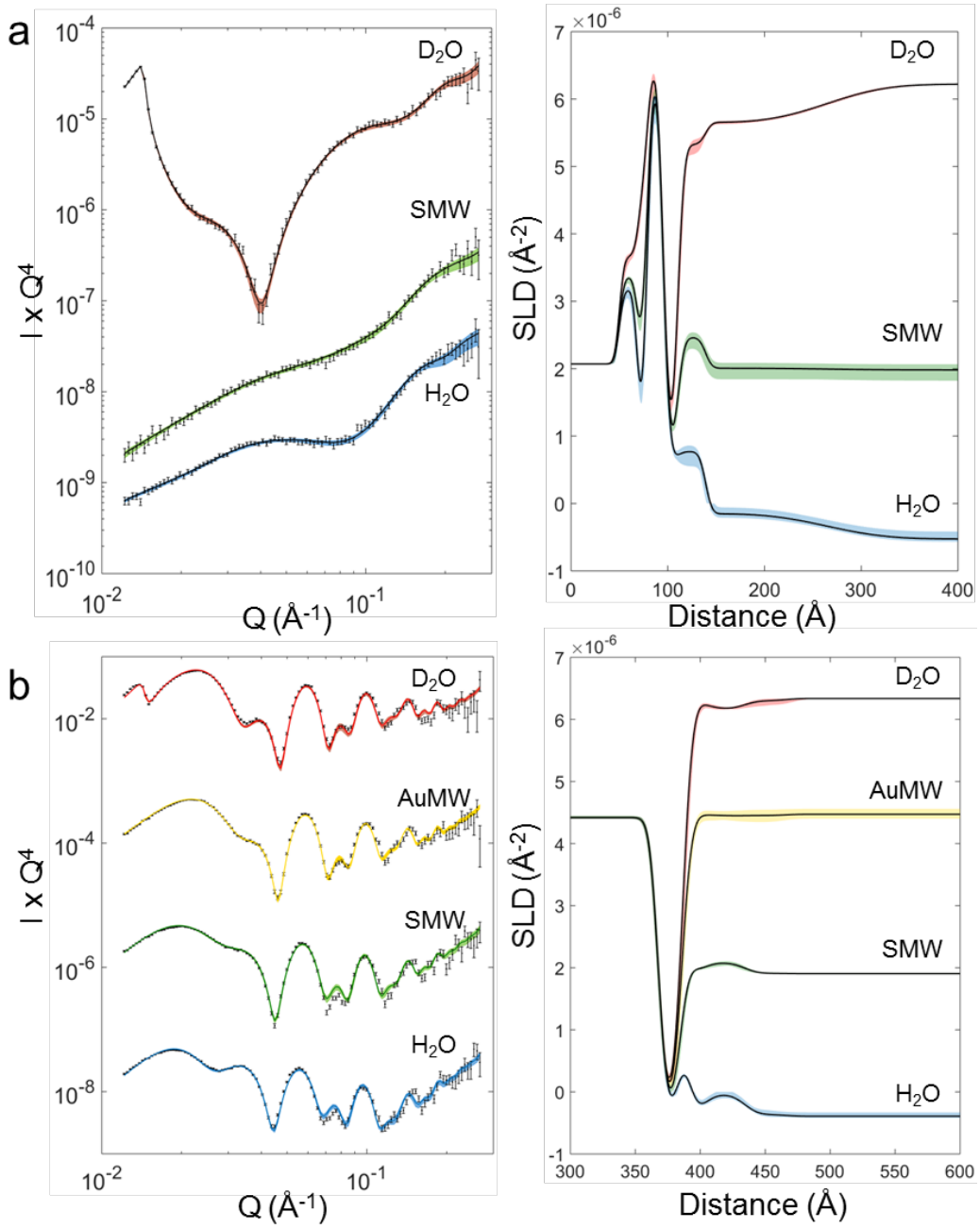

Figure 5.9 | Effect of EDTA on floating and silicon supported OM model containing smooth LPS.

Neutron reflectivity data points, best fit lines (left) and corresponding SLD profiles (right) for (**a**) silicon supported OM model containing O111 smooth LPS and (**b**) floating OM containing O111 smooth LPS both in the presence of 3 mM EDTA. In **b**, the strong features in the reflectivity data are due to the Permalloy/gold/SAM substrate. Reflectivity curves are offset vertically for clarity.

Table 5.4 | Parameters derived from the fitting of the NR data from the silicon supported OM model containing O111 LPS in the presence of 3 mM EDTA.

In brackets the 95% confidence interval derived from the Bayesian error analysis. The parameters describing the bilayer before EDTA treatment are shown in **Table 5.1**, central column.

Bilayer parameters	Fitted value O111 on silicon
dDPPC HG thickness (Å)	9.3 (8.6, 9.9)
dDPPC HG SLD ($Å^{-2}x10^{-6}$)	1.82 (1.71, 1.90)
dDPPC HG coverage (%)	41.8 (40.1, 45.1)
dDPPC tails thickness (Å)	16.9 (16.1, 18.0)
dDPPC tails SLD ($Å^{-2}x10^{-6}$)	6.67 (6.42, 6.90)
LPS tails thickness (Å)	15.0 (14.5, 15.6)
LPS tails SLD ($Å^{-2}x10^{-6}$)	0.67 (0.60, 0.70)
LPS HG thickness (Å)	28.6 (27.2, 29.9)
LPS HG SLD in D_2O ($Å^{-2}x10^{-6}$)	4.40 (4.18, 4.63)
LPS HG coverage (%)	48.2 (41.5, 56.2)
O-antigen SLD in D_2O ($Å^{-2}x10^{-6}$)	3.23 (3.00, 3.50)
α	0.19 (0.17, 0.21)
β	3.02 (2.90, 3.10)
γ	142.7 (139.3, 146.6)
Bilayer coverage (%)	99.1 (97.4 100.0)
Bilayer roughness (Å)	5.3 (5.0, 5.6)

5.2.4 OM model containing LPS and OmpF

None of the OM models described so far included OM proteins. However, porins are significant components of the OM and their reconstitution in OM models has been addressed by several studies (Terrettaz *et al.*, 2002; Cisneros *et al.*, 2006; Hsia *et al.*, 2016). Holt *et al* used NR to characterise a porin containing lipid bilayer in which OmpF was immobilised on a gold surface via a cysteine residue introduced by mutagenesis on the bottom of the β-barrel generating the mutant OmpF E183C (^{cys}OmpF) (Holt *et al.*, 2009). A phospholipid bilayer was then assembled around the protein by using DPPTE to create a gold grafted inner leaflet and DMPC to create the outer leaflet (**Fig 5.1c**). Here the same approach was used to create the chemically grafted ^{cys}OmpF-DPPTE monolayer on a gold substrate on top of which an RaLPS outer leaflet was introduced by self-assembly. The NR data was collected using the magnetic contrast approach by exploiting the magnetised permalloy layer buried beneath the

gold and measuring the sample with a polarised neutron beam. The combination of three solution contrasts, each measured with two neutron spin states, yielded 6 scattering curves for each sample that were constrained to fit the same model of the interface.

^{cys}OmpF was expressed and purified from *E. coli* BZB1107 cells as described in the Methods. **Figure 5.10** shows the steps of the protein production and purification followed by SDS PAGE. The expression of the protein was induced by addition of IPTG and is visible in the gel as an intense band appearing at ~37 kDa, the MW corresponding to an OmpF monomer (lanes 2-4). After separating the membrane pellets by ultra-centrifugation these were washed twice with a detergent solution containing 2% SDS to remove contaminants (lanes 5-8). The membrane fraction was again pelleted by ultra-centrifugation and the protein extracted from the pellet in a 2% SDS solution containing 0.5 M NaCl. The unboiled extract lane shows the OmpF trimer (apparent MW ~75 kDa) which remains intact in the SDS PAGE buffer but dissociates into monomers when the sample is heated to 95°C (lanes 9-10) (Arunmanee *et al.*, 2016).

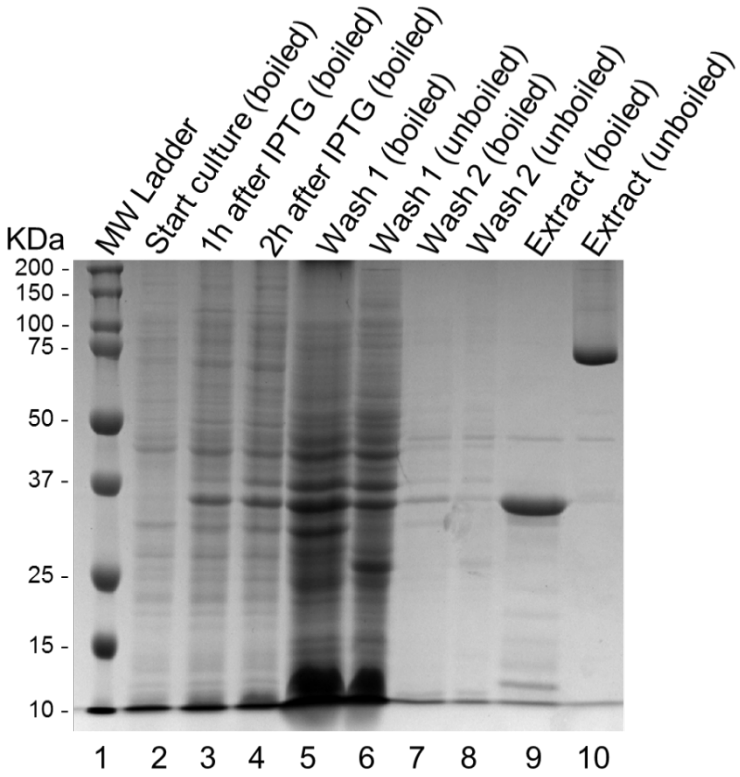

Figure 5.10 | SDS PAGE of the purification of ^{cys}OmpF from *E. coli* BZB1107 cells.

^{cys}OmpF monomer bands migrate at 37 kDa whilst the trimer migrates at 75 kDa.

The components of the OM model were assembled from solution via self-assembly as described in the Methods. Initially, a permalloy/gold substrate was treated with β-mercaptoethanol to passivate the gold surface, in order to reduce its tendency to denature proteins (Terrettaz *et al.*, 2002). The gold surface was then incubated with ^{cys}OmpF solubilised in detergent and the protein solution was flushed repeatedly onto the surface followed by detergent washes to remove non-specifically adsorbed protein. Following the protein immobilisation, DPPTE was deposited in a similar fashion to fill in the gaps between the proteins, creating a chemically grafted mimic of the inner leaflet. **Figure 5.11a** shows the reflectivity curves measured by MCNR from the ^{cys}OmpF-DPPTE monolayer assembled on the gold substrate. Each solution contrast yielded two different reflectivity curves afforded by the two polarisations of the neutron beam used to measure the sample. The SLD profiles of **Figure 5.10b** shows the two different SLD values of the permalloy layer as seen by neutrons polarised parallel (↑↑) or antiparallel (↑↓) with regards to the magnetic field in the permalloy. As a result of the higher constraints on the fits, afforded by the doubling of the three solution contrasts datasets by MCNR, the errors associated with the parameters obtained after the Bayesian error analysis were smaller than those obtained from regular NR experiments (**Table 5.5**).

The monolayer was divided into three layers, in order from the gold surface to the solution: (i) DPPTE head group, (ii) DPPTE tails and (iii) OmpF protruding from the monolayer (**Fig 5.10b**). The DPPTE layer was modelled by fitting an area per molecule (APM) in order to constrain the headgroup region and the tail region to be consistent with being part of the same molecule (described in the Methods, section 2.7.4) Since OmpF spans the head group and tail regions of the DPPTE monolayer, the SLD of these two regions was modelled to take into account the volume fraction of protein present in the DPPTE layers. The volume fraction of protein was then set to be constant across the three layers spanned by ^{cys}OmpF.

The APM of DPPTE obtained from the fits was ~48 Å^2 in agreement with the APM reported for saturated phospholipids in the literature (Hughes *et al.*, 2002), and the lipid had a coverage of ~54% as estimated from the tail region of the monolayer. The APM translates to a thickness of the monolayer of 24.1 Å given a calculated molecular volume of DPPTE of 1155 Å^3 which is also in line with the thickness of DPPC measured so far in this thesis.

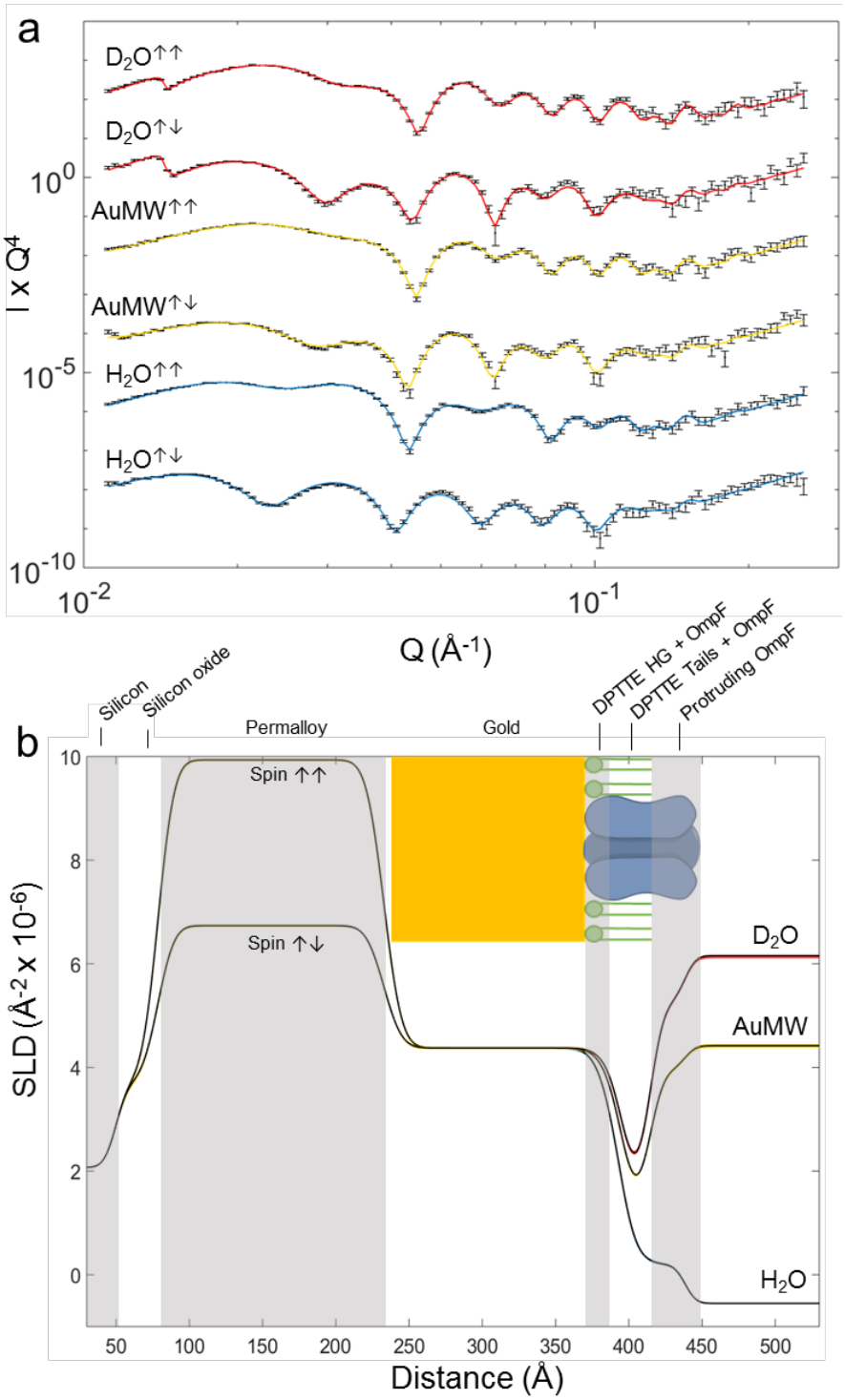

Figure 5.11 | MCNR characterisation of a ^{cys}OmpF-DPPTE monolayer adsorbed on gold.

(**a**) Neutron reflectivity data points and best fit lines for a ^{cys}OmpF-DPPTE monolayer measured under three solution contrasts (D_2O in red, AuMW in yellow and H_2O in blue), each one using two neutron spin states parallel (↑↑) or antiparallel (↑↓). Reflectivity curves are offset vertically for clarity. (**b**) SLD profiles obtained from the fits shown in **a**. The layers of the model are labelled above the SLD and highlighted by alternate shading. A model of the ^{cys}OmpF-DPPTE monolayer at the gold interface is shown in correspondence of its SLD profile.

Table 5.5 | Parameters derived from the fitting of the MCNR data from the ^{cys}OmpF-DPPTE monolayer assembled on the gold substrate.

In brackets the 95% confidence interval derived from the Bayesian error analysis. Shaded parameters were fixed to their calculated value.

Substrate + ^{Cys}OmpF-DPPTE monolayer parameters	Fitted value
Substrate roughness (Å)	6.5 (6.5, 6.6)
Oxide thickness (Å)	28.5 (28.3, 28.7)
Oxide SLD ($Å^{-2}x10^{-6}$)	3.41
Oxide roughness (Å)	8.9 (8.8, 9.0)
Permalloy thickness (Å)	154.3 (154.2, 154.5)
Permalloy SLD ↑↑ ($Å^{-2}x10^{-6}$)	9.94 (9.92, 9.95)
Permalloy SLD ↑↓ ($Å^{-2}x10^{-6}$)	6.73 (6.72, 6.74)
Permalloy roughness (Å)	9.6 (9.5, 9.7)
Gold thickness (Å)	156.9 (156.7, 157.0)
Gold SLD ($Å^{-2}x10^{-6}$)	4.38 (4.36, 4.39)
Gold roughness (Å)	10.8 (10.7, 10.9)
DPPTE APM ($Å^2$)	48.0 (47.7, 48.2)
DPPTE HG coverage (%)	46.4 (46.1, 46.8)
DPPTE Tails coverage (%)	54.2 (53.9, 54.6)
DPPTE roughness (Å)	7.5 (7.4, 7.6)
Protruding OmpF thickness (Å)	23.9 (23.7, 24.0)
OmpF SLD in D_2O ($Å^{-2}x10^{-6}$)	3.21
OmpF roughness (Å)	5.9 (5.8, 6.0)
OmpF coverage (%)	29.4 (29.1, 29.8)

Protruding from the DPPTE monolayer, the SLD profiles revealed a ~24 Å thick layer of protein with a coverage of ~29%. This estimate of the protein's coverage however only represents the dry volume occupied by the proteins mass, underestimating the real area coverage of OmpF as it does not account for the hollow region of its channel which is filled with water. The total thickness of OmpF obtained by summing the DPPTE monolayer thickness to the protein layer was 48 Å in reasonable agreement with the 55±13 Å thickness of OmpF measured by AFM on the same system (Cisneros *et al.*, 2006). Overall the combined protein-lipid coverage of the ^{cys}OmpF-DPPTE monolayer was ~83% of the analysed area, which, considering the intrinsic water contained in the OmpF channel, is likely to be close to a near total coverage of the surface. The ^{cys}OmpF-DPPTE layer was then incubated with a suspension of hydrogenous RaLPS in order to deposit the outer leaflet to complete the model membrane. After an 8 h incubation, the excess LPS was flushed with buffer and the sample measured again by MCNR. The six additional datasets obtained after

the addition of the RaLPS outer leaflet were constrained to fit to the same parameters used for the substrate and the ^{cys}OmpF-DPPTE layer in addition to a set of parameters describing the newly added RaLPS layer.

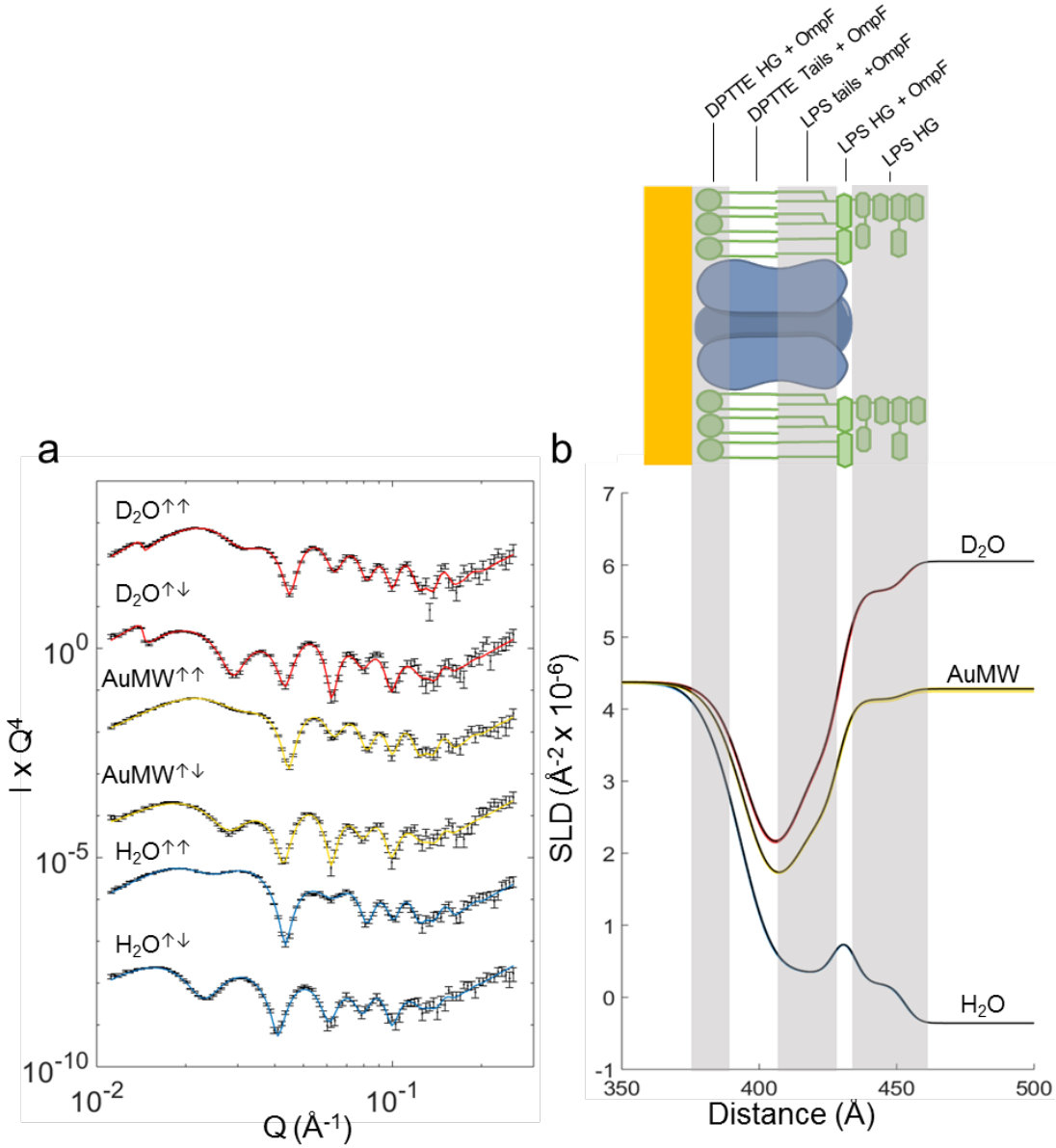

Figure 5.12 | MCNR characterisation of the ^{cys}OmpF-DPPTE monolayer after the assembly of a hydrogenous RaLPS outer leaflet.

(**a**) Neutron reflectivity data points and best fit lines from the ^{cys}OmpF-DPPTE monolayer after incubation with hydrogenous RaLPS. The reflectivity was measured under three solution contrasts (D_2O in red, AuMW in yellow and H_2O in blue), each one using two neutron spin states parallel (↑↑) or antiparallel (↑↓). Reflectivity curves are offset vertically for clarity. (**b**) SLD profiles obtained from the fits shown in **a**. A model of the membrane is shown above the SLD profile corresponding to the layers described by the SLD. Substrate layers are omitted for simplicity as they are the same as those shown in **Figure 5.11b**.

Once the LPS leaflet is added to the model, the proteins vertical profile is entirely within the lipid region, and its volume fraction can only be inferred from relating it to the data obtained before the addition of the outer leaflet, making it important to constrain the fits to the datasets obtained without LPS. The LPS layer was modelled with three layers, on top of the DPPTE monolayer, corresponding to: (i) LPS tails, (ii) LPS inner head group and (iii) LPS outer head group. The SLD of the LPS tails and the inner head group layers also took into account the contribution of the SLD of OmpF as the protein spanned these layers whereas the outer head group projected above the protein. The fits revealed a thickness of the LPS tails of ~14 Å and a coverage of ~26% (**Table 5.6**). The inner head group was ~5 Å whilst the outer head group was ~19 Å adding up to a total of ~24 Å, slightly shorter than the core oligosaccharide measured on the asymmetric bilayers. However self-assembly was shown in chapter 3 to yield an LPS monolayer with a shorter core oligosaccharide than LB/LS models (**Table 3.1**) likely due to tilted orientation. The LPS coverage was also found to be sub-optimal, covering only roughly half the area occupied by the tails of the DPPTE inner leaflet suggesting only a partial assembly of the outer leaflet. The LPS outer leaflet was removed by washing the sample with a detergent solution and the sample was incubated with a suspension of deuterated RaLPS (dRaLPS) for 8 h to replace the hydrogenous outer leaflet with a different RaLPS layer. As with the previous sample the data was fitted to the same structure of the substrate and the ^{cys}OmpF-DPPTE by constraining the fits with those shown in **Figure 5.11a.** The dRaLPS layer was modelled with the same three layers described for hydrogenous RaLPS. The thickness obtained from the dRaLPS tail and head group regions was almost identical to that obtained for hydrogenous RaLPS showing good reproducibility of the assembly procedure (**Table 5.6**). As shown by the change in SLD of the tails region not only all the hydrogenous LPS was replaced by dRaLPS but the new outer leaflet reached a higher coverage of ~35% of the surface, indicating the formation of a more complete LPS layer which coated the ^{cys}OmpF-DPPTE monolayer and embedded the protein. Overall the results showed that the ^{cys}OmpF-DPPTE monolayer provided a versatile platform for the reconstitution of surfaces which contain both LPS and porins like OmpF, with the possibility of using the same grafted protein-lipid substrate to assemble and remove the outer leaflet multiple times.

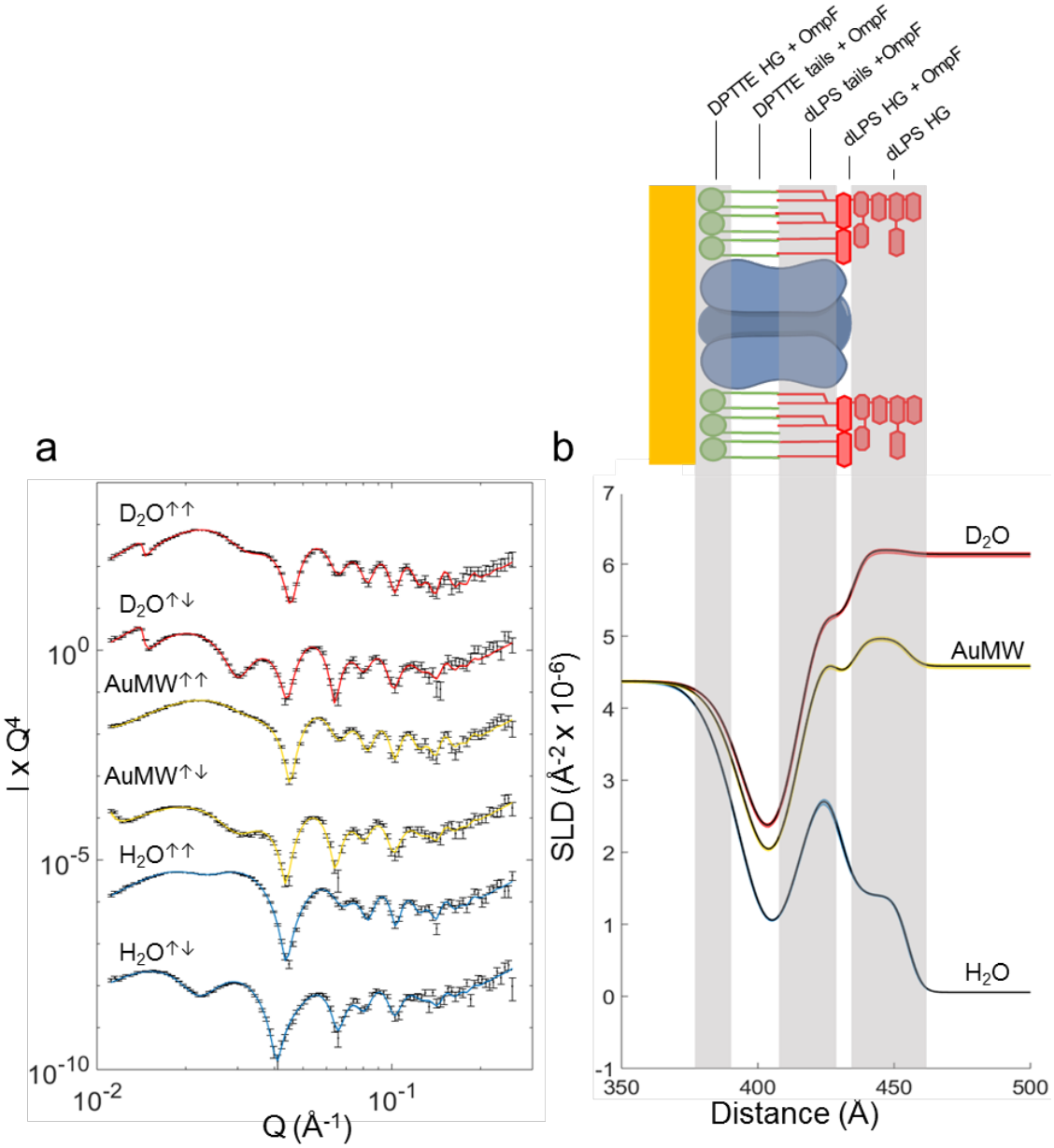

Figure 5.13 | MCNR characterisation of the ^{cys}OmpF-DPPTE monolayer after the assembly of a deuterated RaLPS outer leaflet.

(**a**) Neutron reflectivity data points and best fit lines from the ^{cys}OmpF-DPPTE monolayer after removal of hydrogenous RaLPS and incubation with deuterated RaLPS. The reflectivity was measured under three solution contrasts (D_2O in red, AuMW in yellow and H_2O in blue), each one using two neutron spin states parallel (↑↑) or antiparallel (↑↓). Reflectivity curves are offset vertically for clarity. (**b**) SLD profiles obtained from the fits shown in **a**. The layers of the model are labelled above the SLD and highlighted by alternate shading. A model of the model membrane is shown above the SLD profile (deuterated LPS is shown in red). Substrate layers are omitted for simplicity as they are the same as those shown in **Figure 5.11b**.

Table 5.6 | Parameters derived from the fitting of the MCNR data from the ^{cys}OmpF-DPPTE monolayer assembled on the gold substrate in the presence of hydrogenous and deuterated RaLPS outer leaflets.

In brackets the 95% confidence interval derived from the Bayesian error analysis. Shaded parameters were fixed to their calculated value.

RaLPS parameters	Fitted value Hydrogenous RaLPS	Fitted value Deuterated RaLPS
LPS tails thickness(Å)	14.0 (13.9, 14.1)	14.6 (14.5, 14.7)
LPS tails SLD ($Å^{-2}x10^{-6}$)	-0.39	7.10 (7.04, 7.14)
LPS coverage (%)	26.3 (26.0, 26.5)	34.8 (34.5, 35.1)
LPS inner HG thickness (Å)	5.1 (5.0, 5.2)	5.2 (5.1, 5.3)
LPS inner HG SLD in D_2O ($Å^{-2}x10^{-6}$)	4.88 (4.84, 4.92)	5.04 (5.01, 5.07)
LPS outer HG thickness (Å)	19.3 (19.2, 19.5)	20.6 (20.5, 20.8)
LPS outer HG SLD in D_2O ($Å^{-2}x10^{-6}$)	4.06 (4.03, 4.10)	6.39 (6.34, 6.45)
LPS HG coverage (%)	19.8 (19.6, 20.0)	25.7 (25.5, 26.0)
LPS roughness (Å)	3.96 (3.93, 4.00)	

5.3 DISCUSSION

Planar OM models reconstituted using bacterial LPS can provide a useful tool to understand the biophysical properties of the Gram-negative cell envelope while also offering a platform to study its interactions with antimicrobial compounds (Clifton *et al.*, 2015a; Clifton *et al.*, 2015b). The reliability of the information obtained from these models however depends on how closely these can reproduce the natural OM. The primary feature of the OM, which distinguishes it from other biological membranes, is the presence of LPS and its confinement to the outer leaflet of the lipid bilayer (Nikaido, 2003). Therefore the initial efforts to develop realistic OM models focused on achieving high levels of lipid asymmetry and incorporating rough LPS, which represents the minimal LPS structure that allows normal bacterial growth (Clifton *et al.*, 2013b). Rough LPS is the obvious candidate to reconstitute in OM models for NR studies for two main reasons: (i) It is widely conserved across Gram-negatives, making the models representative of a large family of bacteria and (ii) it has a well-defined structure which can be modelled as a tail region and a head group with a well-defined size. Smooth LPS on the other hand does not have a well-defined size as it is a mixture of widely polydisperse molecules. The data presented here, demonstrates for the first time that it is possible to reconstitute smooth LPS from various strains of the Gram-negative bacterium *E.*

coli into asymmetric bilayers with results comparable to those obtained using the simpler rough LPS, in terms of both coverage and asymmetry (**Fig. 5.3**). The first accurate structural characterisation of a smooth LPS monolayer deposited onto a hydrophobic substrate was reported recently by Rodriguez-Loureiro *et al* which were able to reconstitute LPS from *E. coli* O55 onto an OTS monolayer (Rodriguez-Loureiro *et al.*, 2018). They introduced the use of an exponential decay function employed here to model the O-antigen volume fraction distribution. A comparison between their results with those reported here indicates that the structure of the O-antigen from the asymmetric model membranes is very similar to that displayed by LPS reconstituted on OTS. The parameters of the exponential function reported by Rodriguez-Loureiro *et al* are $\alpha = 0.22$ $\beta = 2.5$ $\gamma = 145$ which compare well with those obtained here for LPS O55 ($\alpha = 0.20$ $\beta = 3.05$ $\gamma = 141.9$) (**Table 5.1**) indicating a comparable volume fraction (α), distribution (β) and extension (γ) of the carbohydrate chains.

In order to then achieve some degree of control on the amount of O-antigen reconstituted in the models described here, smooth LPS fractionated according to the size of its carbohydrate head group by SEC (**Fig 5.5**) was also successfully reconstituted into asymmetric OM models (**Fig. 5.6**). This approach allowed the creation of OM models with different morphologies of the O-antigen region (**Fig. 5.14**). Notably, only the low and mid-MW fractions of LPS yielded stable enough monolayers for the assembly of the model membranes whilst the isolated high-MW component could not be reconstituted due to its highly soluble nature. It is interesting to notice that the DOC PAGE analysis of all smooth LPS types reported here (**Fig 5.2**) indicated the presence of a significant amount of lipooligosaccharide (LOS) in the smooth LPS mixtures, and when this was removed, as in the high-MW fraction, no stable LPS layers could be achieved. On the other hand, the whole unfractionated smooth LPS yielded stable monolayers and high-quality OM models which incorporated the highly hydrophilic LPS displaying extended O-antigen chains of up to ~250 Å. This indicates that the presence of the more hydrophobic LOS fraction is necessary for the stability of monolayers containing the high-MW component characterised by long hydrophilic O-antigen chains. These observations suggest that the significant LOS content of bacteria displaying smooth LPS, could play an important role in the integrity of the OM by stabilising the highly soluble long O-antigen chains and anchoring them on the outer leaflet of the OM.

Compared to smooth LPS monolayers on OTS, a second important advantage offered by asymmetric phospholipid/smooth LPS bilayers, is the possibility to be assembled on substrates different than silicon. This allowed the creation of smooth OM models on functionalised gold surfaces that yielded the first floating asymmetric bilayers containing the O-antigen (**Fig. 5.7** and **5.8**). The floating smooth OM models were assembled on top of a C16NEtOH monolayer which yielded high coverage SAMs on gold and was shown to be a valid replacement for the less practical ω-thioPC used previously floating OM models containing RaLPS (Clifton *et al.*, 2015a). The smooth LPS floating bilayers were shown to be separated from the underlying SAM by a ~10 Å water gap. In comparison the water gap obtained with ω-thioPC was about twice as big, averaging around 20 Å. The presence of a water reservoir between the bilayer and the underlying substrate is important for recreating a more realistic dynamic of the membrane as the restricted lipid mobility caused by the direct contact with a solid substrate can produce artefacts.

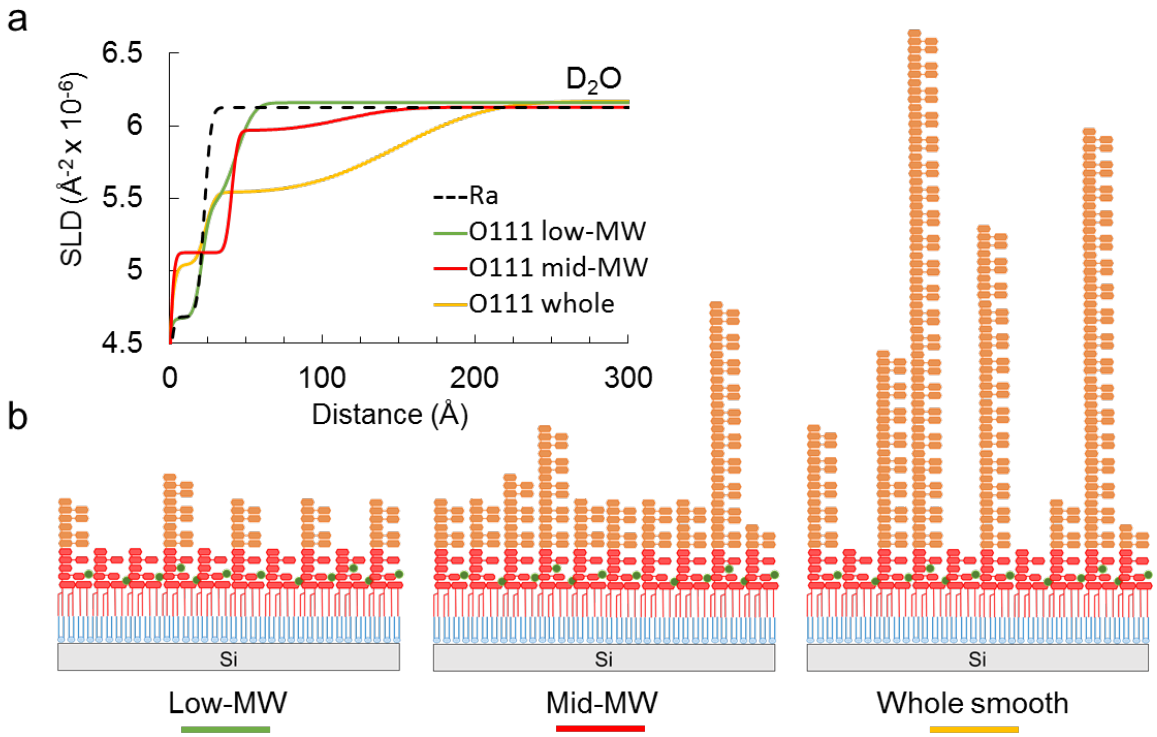

Figure 5.14 | O-antigen structures characterised by NR.

(**a**) Comparison of the carbohydrate region of various model membranes differing in the size of their LPS head group as described by their SLD profiles measured in D_2O. RaLPS (black dashed) only contains the core oligosaccharide. O111 low-MW (green) contains the LOS fraction of smooth LPS, O111 mid-MW (red) only contains LPS with the O-antigen (i.e. no RaLPS) and the unfractionated O111 (yellow) contains the natural mixture of the LPS extract. (**b**) Cartoon representation of the reconstituted smooth LPS OM models on silicon containing different populations of smooth LPS as described by the SLD profiles in **a**. The O-antigen chains are shown as rigid vertical structures for clarity but they are more likely to resemble entangled polymers

The difference in behaviour between the silicon supported and the floating models was exemplified when both systems were subject to EDTA treatment. EDTA chelates the Ca^{2+} required for OM stability and causes the release of large quantity of LPS *in vivo* (Vaara, 1992). EDTA treatment only caused minor changes in the asymmetry levels of the silicon supported model without affecting the coverage and integrity of the bilayer (**Fig. 5.9a**, and **Table 5.4**). On the other hand, it completely solubilised the floating smooth LPS OM model (**Fig. 5.9b**). The leaflet mixing effect of EDTA on the silicon supported smooth OM model was much smaller than those shown in chapter 4 on the membrane containing RaLPS, with the phospholipid content of the outer leaflet increasing by just 4% compared to the 30% measured for RaLPS. This suggests that for models assembled on silicon, the steric effects

of the bulkier smooth LPS molecules makes it less likely to flip into the inner leaflet reducing the destabilising effects of EDTA. Clifton *et al* investigated the effect of EDTA on floating OM models containing RaLPS (Clifton *et al.*, 2015b). They showed how EDTA induced mixing of the inner and outer leaflet to a similar extent to that measured on the silicon supported RaLPS model, affecting the coverage of the bilayer only marginally. In sharp contrast, essentially no bilayer was left after the addition of EDTA to the floating OM model containing smooth LPS described here. The substantial difference between the behaviour of floating bilayers containing rough and smooth LPS suggests that the high hydrophilicity of the long carbohydrate chains of the O-antigen promoted the solubilisation of the smooth LPS OM model whilst the more hydrophobic RaLPS remained assembled in a bilayer structure even after Ca^{2+} removal. These observations suggest that for silicon supported OM models, the large nature of the smooth LPS head group further restricts lipid mobility stabilising the bilayer in the presence of EDTA. On the other hand, in floating models, the hydrophilicity of the large O-antigen chains greatly increases the susceptibility of the bilayer to EDTA causing the release of LPS from the model, similar to that observed *in vivo* (Marvin *et al.*, 1989).

This has important consequences on the choice of OM models when designing biophysical experiments to investigate the OM. The higher susceptibility of floating membranes containing smooth LPS can be beneficial to understand subtle effects but can also be detrimental due to the more delicate nature of the system and the extra steps required for its preparation. Silicon supported models offer a robust and reliable OM mimic which has been shown to provide a biologically relevant platform to study the biophysics of the OM (Clifton *et al.*, 2013b; Clifton *et al.*, 2015b). However, the stabilising effects of the solid substrate could represent an obstacle in situations where a close resemblance of the dynamics of the natural OM are central to the problem being investigated.

Lastly, the use of the grafted ^{cys}OmpF-DPPTE monolayer on gold as a platform to reconstitute different types of LPS was also shown to be a viable option to recreate a porin-LPS surface which imitates the composition of the Gram-negative cell envelope. LPS was shown to assemble around the immobilised OmpF (**Fig. 5.12**) and could be removed and replaced by a different LPS species on the same substrate (**Fig 5.13**). However, comparing the maximum coverage of the LPS outer leaflet achieved here (~35%) with that of the phospholipid outer leaflet assembled by Holt *et al* (~73%) shows that LPS self-assembly is

less straight forward than that of phospholipids, as also indicated by the results of Chapter 3. More work is therefore needed to optimise the creation of LPS monolayers from self-assembly which could be improved by using conditions different to those used here to achieve closer results to the high coverage and tight packing of the models assembled by LB/LS.

6 CONCLUSIONS AND FUTURE WORK

6.1 CONCLUSIONS

The results presented in this thesis describe the use of realistic OM models as platforms to understand the properties of the natural OM and its interactions with antibacterial molecules. The combination of realistic models with the use of NR and selective deuteration was shown to be a successful approach to understand properties of the Gram-negative cellular envelope and obtain structural information on its interaction with antibiotics, under near-physiological conditions.

In the case of the antibiotic polymyxin B (PmB), the temperature dependent disruption of the OM described *in vivo* (Teubner and Bader, 1977; Hodate and Bito, 1982; Katsu *et al.*, 1984) was reproduced on asymmetric OM models assembled by LB/LS deposition. The onset of membrane damage occurred in a temperature range similar to that reported *in vivo*, specifically, the effects were substantial between room temperature (20°C) and physiological temperature (37°C). In the same range, both leaflets of the OM model were shown to undergo the transition from the gel to the fluid state. NR allowed to monitor the change in the bilayer structure as a function of temperature and the change in the data closely resembled the sigmoidal shift typical of the phase transition of lipids indicating a substantial correlation between PmB effects and phase state of the model membrane. This provided the first direct evidence of the relevance of the disputed liquid crystalline state of the OM (Nikaido, 2003). PmB caused major mixing of the bilayer components, which prevented the clear identification of PmB final location in the system. This led to the development of a new OM model created by using deuterated LPS and deuterated phospholipids, which highlighted the localisation of the hydrogenous antimicrobial within the deuterium rich bilayer. These novel OM models have potentially broad applications in the study of antibiotic interactions, since they provide contrast between the deuterated OM with hydrogenous components, reducing the need for deuterated antibiotics which are costly and difficult to obtain.

The study on ColN allowed to directly measure for the first time the protective effects of the outer core oligosaccharide, which screened the electrostatic attraction between LPS and a cationic antimicrobial protein. NR revealed for the first time the salt dependent binding of ColN to OM models, providing data on the relative strength of the interaction with LPS containing a complete (Ra) and a truncated core (Rd). Moreover, the structural data provided information on different orientations of the protein at the membrane interface, an aspect that is particularly challenging to characterise by any other biophysical technique. ColN adsorbed on the membranes containing tightly packed RaLPS in a side-on conformation, with its major axis parallel to the membrane plane. Increasing accessibility to the known ColN binding sites by disrupting LPS packing via EDTA treatment, revealed a second protein orientation which more closely resembled ColN bound with its major axis normal to the interface. This second protein conformation bound more stably to the OM model indicating a stronger interaction, which suggested a specific recognition by ColN of its binding sites on LPS. The molecular basis of the ColN-LPS interaction was then investigated by mutagenesis and the results outlined the crucial role of a defined loop region within ColN R-domain ($loop^R$) which substantially impacted on the protein's ability to bind LPS and its toxic effects on *E. coli*. ColN uses LPS as a receptor and OmpF as a translocator (Buchanan *et al.*, 2007; Sharma *et al.*, 2009) and the porin lipid interface has been suggested to be the path followed by ColN in its translocation (Baboolal *et al.*, 2008; Clifton *et al.*, 2012; Johnson *et al.*, 2014). The compact structure of ColN together with the combined requirement for OmpF and LPS for its activity indicate that LPS bound to OmpF would be an ideal receptor for the antimicrobial protein, especially in light of OmpF potential role in exposing the core oligosaccharide to ColN R-domain.

Lastly the novel OM models developed and characterised in the final chapter demonstrated for the first time the possibility to create high coverage asymmetric bilayers which contain LPS from pathogenic bacteria. Both silicon supported bilayers and floating bilayers, decoupled from the substrate by a 10 Å water gap, could be used to reconstitute smooth LPS and purified lipooligosaccharide (LOS) species into asymmetric OM mdoels. The presence of the water gap between the solid substrate and the inner leaflet of the bilayer was shown to have substantial effects on the susceptibility of the OM model to the permeabilising agent EDTA. Moreover, in addition to the novel smooth LPS OM models, the previously

developed ^{cys}OmpF-DPPTE monolayer (Holt *et al*., 2009) was shown to be a suitable platform for the reconstitution of a surface that displayed oriented porins and LPS.

6.2 FUTURE WORK

The use of models of the OM has already shown significant potential to reveal important information about the complex Gram-negative cell envelope. The next steps in this research area should focus on the following aspects:

Polymyxin B

The next step in using OM models to uncover the details of the PmB-LPS interaction is to analyse the interaction of PmB with LPS produced by resistant bacteria, to better understand how LPS modifications affect the binding of the antimicrobial to the OM. For this purpose, OM models are well suited and can provide important information on the structural aspects of the interaction. It would also be informative to analyse the effect of the substrate on PmB interaction with OM models, especially considering the effects that the substrate can have on the phase transition of the lipids (Feng *et al.*, 2005; Alessandrini and Facci, 2014; Wu *et al.*, 2016). Analysing the effects of PmB on floating OM models would be the next step in this direction.

Colicin N

ColN mutants that were shown not to bind LPS in the SPR assay would provide an interesting system to better understand the non-specific interactions observed between ColN and LPS. Considering the critical role of the outer core oligosaccharide in preventing the interaction of ColN with its OM receptor leaves questions open about the role of the O-antigen in this interaction. Now that the reconstitution of smooth LPS has been shown to produce high quality OM models, and importantly with control over the length of O-antigen, this enables the investigation of the role of the O-antigen in the ColN-OM interaction. Furthermore, given the important role of OmpF in the ColN interaction, the binding of ColN on model membranes containing OmpF should also be explored, as this will provide information on the role of ColN translocon on its interaction with the cellular envelope.

Improved OM models

The next step to further improve current OM models is to incorporate OmpF into asymmetric phospholipid/LPS bilayers that are not covalently grafted to the substrate like the ^{cys}OmpF-DPPTE model described here. As a first step, the structure of OmpF-LPS monolayers at the air water interface should be investigated and grazing incidence diffraction measurements could provide relevant insights in the lateral organisation of the porin-LPS matrix, which is known to contain highly ordered regions of porins (Jaroslawski *et al.*, 2009)

6.3 Final Remarks

The OM constitutes one of the major obstacles to the development of new antibiotics active against Gram-negative bacteria and resistance to existing drugs is rapidly becoming a worldwide urgent health issue. The protective function of this effective biological barrier is what gives Gram-negatives a critical advantage when it comes to preventing harmful compounds from entering the cytoplasm and cause cell damage. The work presented in this thesis has focused on *in vitro* models of the OM as tools to understand the properties of this biological barrier and its interaction with two antimicrobials: polymyxin B and colicin N. One of the crucial aspects of using *in vitro* model membranes to answer biologically relevant questions is the impossibility of these models to entirely replicate the complex biomolecular assembly found in biological membranes. This constitutes both the main shortcoming and at the same time the main advantage of this approach. The high complexity of biological membranes is reduced in the models, leaving out a large fraction of its original components. However, this allows the investigation of membrane properties from a reductionist perspective, with important advantages in structural studies such as those presented in this thesis. Care must be taken thus when generalising results obtained *in vitro* to explain the behaviour of the complex systems that these should represent. This makes the choice of an appropriate model membrane crucial to obtain reliable information on the natural cell envelope, and as the model membrane toolbox expands, so does the number of questions this approach can contribute to answer.

7 BIBLIOGRAPHY

Abeles, F. (1950) 'Recherches theoriques sur les proprietesoptiques des lames minces', *J Phys Radium*, 22, pp. 307-309.

Abellon-Ruiz, J., Kaptan, S.S., Basle, A., Claudi, B., Bumann, D., Kleinekathofer, U. and van den Berg, B. (2017) 'Structural basis for maintenance of bacterial outer membrane lipid asymmetry', *Nat Microbiol*, 2(12), pp. 1616-1623.

Abuillan, W., Schneck, E., Korner, A., Brandenburg, K., Gutsmann, T., Gill, T., Vorobiev, A., Konovalov, O. and Tanaka, M. (2013) 'Physical interactions of fish protamine and antisepsis peptide drugs with bacterial membranes revealed by combination of specular x-ray reflectivity and grazing-incidence x-ray fluorescence', *Phys Rev E Stat Nonlin Soft Matter Phys*, 88(1), p. 012705.

Alessandrini, A. and Facci, P. (2014) 'Phase transitions in supported lipid bilayers studied by AFM', *Soft Matter*, 10(37), pp. 7145-7164.

Amor, K., Heinrichs, D.E., Frirdich, E., Ziebell, K., Johnson, R.P. and Whitfield, C. (2000) 'Distribution of core oligosaccharide types in lipopolysaccharides from Escherichia coli', *Infect Immun*, 68(3), pp. 1116-24.

Armen, R.S., Uitto, O.D. and Feller, S.E. (1998) 'Phospholipid Component Volumes: Determination and Application to Bilayer Structure Calculations', *Biophysical Journal*, 75(2), pp. 734-744.

Arnold, O., Bilheux, J.C., Borreguero, J.M., Buts, A., Campbell, S.I., Chapon, L., Doucet, M., Draper, N., Ferraz Leal, R., Gigg, M.A., Lynch, V.E., Markvardsen, A., Mikkelson, D.J., Mikkelson, R.L., Miller, R., Palmen, K., Parker, P., Passos, G., Perring, T.G., Peterson, P.F., Ren, S., Reuter, M.A., Savici, A.T., Taylor, J.W., Taylor, R.J., Tolchenov, R., Zhou, W. and Zikovsky, J. (2014) 'Mantid—Data analysis and visualization package for neutron scattering and μ SR experiments', *Nuclear Instruments and Methods in Physics Research Section A: Accelerators, Spectrometers, Detectors and Associated Equipment*, 764, pp. 156-166.

Arteta, M.Y., Berti, D., Montis, C., Campbell, R.A., Eriksson, C., Clifton, L.A., Skoda, M.W., Soltwedel, O., Koutsioubas, A., Baglioni, P. and Nylander, T. (2015) 'On the formation of dendrimer/nucleolipids surface films for directed self-assembly', *Soft Matter*, 11(10), pp. 1973-90.

Arunmanee, W., Pathania, M., Solovyova, A.S., Le Brun, A.P., Ridley, H., Basle, A., van den Berg, B. and Lakey, J.H. (2016) 'Gram-negative trimeric porins have specific LPS binding sites that are essential for porin biogenesis', *Proc Natl Acad Sci U S A*, 113(34), pp. E5034-43.

Baboolal, T.G., Conroy, M.J., Gill, K., Ridley, H., Visudtiphole, V., Bullough, P.A. and Lakey, J.H. (2008) 'Colicin N binds to the periphery of its receptor and translocator, outer membrane protein F', *Structure (London, England : 1993)*, 16(3), pp. 371-379.

Bainbridge, G., Armstrong, G.A., Dover, L.G., Whelan, K.F. and Lakey, J.H. (1998) 'Displacement of OmpF loop 3 is not required for the membrane translocation of colicins N and A in vivo', *FEBS Lett*, 432(3), pp. 117-22.

Bayer, M.E. and Leive, L. (1977) 'Effect of ethylenediaminetetraacetate upon the surface of Escherichia coli', *J Bacteriol*, 130(3), pp. 1364-81.

Berbee, J.F., Coomans, C.P., Westerterp, M., Romijn, J.A., Havekes, L.M. and Rensen, P.C. (2010) 'Apolipoprotein CI enhances the biological response to LPS via the

CD14/TLR4 pathway by LPS-binding elements in both its N- and C-terminal helix', *J Lipid Res*, 51(7), pp. 1943-52.

Bladen, H.A. and Mergenhagen, S.E. (1964) 'Ultrastructure of Viellonella and morphological correlation of an outer membrane with particles associated with endotoxic activity', *J Bacteriol*, 88, pp. 1482-92.

Bolam, D.N. and van den Berg, B. (2018) 'TonB-dependent transport by the gut microbiota: novel aspects of an old problem', *Curr Opin Struct Biol*, 51, pp. 35-43.

Boll, J.M., Tucker, A.T., Klein, D.R., Beltran, A.M., Brodbelt, J.S., Davies, B.W. and Trent, M.S. (2015) 'Reinforcing Lipid A Acylation on the Cell Surface of Acinetobacter baumannii Promotes Cationic Antimicrobial Peptide Resistance and Desiccation Survival', *MBio*, 6(3), pp. e00478-15.

Born, M. and Wolf, E. (1970) 'Principles of Optics', *Pergamon*.

Brandenburg, K., Arraiza, M.D., Lehwark-Ivetot, G., Moriyon, I. and Zähringer, U. (2002) 'The interaction of rough and smooth form lipopolysaccharides with polymyxins as studied by titration calorimetry', *Thermochimica Acta*, 394(1), pp. 53-61.

Brandenburg, K., David, A., Howe, J., Koch, M.H., Andra, J. and Garidel, P. (2005) 'Temperature dependence of the binding of endotoxins to the polycationic peptides polymyxin B and its nonapeptide', *Biophys J*, 88(3), pp. 1845-58.

Brandenburg, K. and Seydel, U. (1990) 'Investigation into the fluidity of lipopolysaccharide and free lipid A membrane systems by Fourier-transform infrared spectroscopy and differential scanning calorimetry', *Eur J Biochem*, 191(1), pp. 229-36.

Brandenburg, K. and Seydel, U. (1991) 'A comment on the preparation of liposomes from and on the beta in equilibrium alpha acyl chain melting behaviour of rough mutant lipopolysaccharide', *Biochim Biophys Acta*, 1069(1), pp. 1-4.

Buchanan, S.K., Lukacik, P., Grizot, S., Ghirlando, R., Ali, M.M., Barnard, T.J., Jakes, K.S., Kienker, P.K. and Esser, L. (2007) 'Structure of colicin I receptor bound to the R-domain of colicin Ia: implications for protein import', *Embo j*, 26(10), pp. 2594-604.

Cascales, E., Buchanan, S.K., Duche, D., Kleanthous, C., Lloubes, R., Postle, K., Riley, M., Slatin, S. and Cavard, D. (2007) 'Colicin biology', *Microbiol Mol Biol Rev*, 71(1), pp. 158-229.

Chalton, D.A. and Lakey, J.H. (2010) 'Simple detection of protein soft structure changes', *Anal Chem*, 82(7), pp. 3073-6.

Chang, V.C., Chen, L., Wang, A.X. and Yuan, X. (2010) 'The Effect of Lipopolysaccharide Core Structure Defects on Transformation Efficiency in Isogenic Escherichia coli BW 25113 rfaG , rfaP , and rfaC Mutants', *Journal of Experimental Microbiology and Immunology*, 14, pp. 101-107.

Cisneros, D.A., Muller, D.J., Daud, S.M. and Lakey, J.H. (2006) 'An approach to prepare membrane proteins for single-molecule imaging', *Angew Chem Int Ed Engl*, 45(20), pp. 3252-6.

Clifton, L.A., Ciesielski, F., Skoda, M.W., Paracini, N., Holt, S.A. and Lakey, J.H. (2016) 'The Effect of Lipopolysaccharide Core Oligosaccharide Size on the Electrostatic Binding of Antimicrobial Proteins to Models of the Gram Negative Bacterial Outer Membrane', *Langmuir*, 32(14), pp. 3485-94.

Clifton, L.A., Holt, S.A., Hughes, A.V., Daulton, E.L., Arunmanee, W., Heinrich, F., Khalid, S., Jefferies, D., Charlton, T.R., Webster, J.R., Kinane, C.J. and Lakey, J.H.

(2015a) 'An accurate in vitro model of the E. coli envelope', *Angew Chem Int Ed Engl*, 54(41), pp. 11952-5.

Clifton, L.A., Johnson, C.L., Solovyova, A.S., Callow, P., Weiss, K.L., Ridley, H., Le Brun, A.P., Kinane, C.J., Webster, J.R., Holt, S.A. and Lakey, J.H. (2012) 'Low resolution structure and dynamics of a colicin-receptor complex determined by neutron scattering', *J Biol Chem*, 287(1), pp. 337-46.

Clifton, L.A., Neylon, C. and Lakey, J.H. (2013a) 'Examining protein-lipid complexes using neutron scattering', *Methods Mol Biol*, 974, pp. 119-50.

Clifton, L.A., Skoda, M.W., Daulton, E.L., Hughes, A.V., Le Brun, A.P., Lakey, J.H. and Holt, S.A. (2013b) 'Asymmetric phospholipid: lipopolysaccharide bilayers; a Gram-negative bacterial outer membrane mimic', *J R Soc Interface*, 10(89), p. 20130810.

Clifton, L.A., Skoda, M.W., Le Brun, A.P., Ciesielski, F., Kuzmenko, I., Holt, S.A. and Lakey, J.H. (2015b) 'Effect of divalent cation removal on the structure of gram-negative bacterial outer membrane models', *Langmuir*, 31(1), pp. 404-12.

Coates, J. (2006) 'Interpretation of Infrared Spectra, A Practical Approach', *Encyclopedia of Analytical Chemistry*.

Cooper, M.A., Try, A.C., Carroll, J., Ellar, D.J. and Williams, D.H. (1998) 'Surface plasmon resonance analysis at a supported lipid monolayer', *Biochimica et Biophysica Acta (BBA) - Biomembranes*, 1373(1), pp. 101-111.

Cowan, S.W., Schirmer, T., Rummel, G., Steiert, M., Ghosh, R., Pauptit, R.A., Jansonius, J.N. and Rosenbusch, J.P. (1992) 'Crystal structures explain functional properties of two E. coli porins', *Nature*, 358(6389), pp. 727-33.

Dalgliesh, R.M., Langridge, S., Plomp, J., de Haan, V.O. and van Well, A.A. (2011) 'Offspec, the ISIS spin-echo reflectometer', *Physica B: Condensed Matter*, 406(12), pp. 2346-2349.

De Mot, R. and Vanderleyden, J. (1994) 'The C-terminal sequence conservation between OmpA-related outer membrane proteins and MotB suggests a common function in both gram-positive and gram-negative bacteria, possibly in the interaction of these domains with peptidoglycan', *Mol Microbiol*, 12(2), pp. 333-4.

Delcour, A.H. (2009) 'Outer membrane permeability and antibiotic resistance', *Biochim Biophys Acta*, 1794(5), pp. 808-16.

Deris, Z.Z., Swarbrick, J.D., Roberts, K.D., Azad, M.A., Akter, J., Horne, A.S., Nation, R.L., Rogers, K.L., Thompson, P.E., Velkov, T. and Li, J. (2014) 'Probing the penetration of antimicrobial polymyxin lipopeptides into gram-negative bacteria', *Bioconjug Chem*, 25(4), pp. 750-60.

Dong, C., Beis, K., Nesper, J., Brunkan-Lamontagne, A.L., Clarke, B.R., Whitfield, C. and Naismith, J.H. (2006) 'Wza the translocon for E. coli capsular polysaccharides defines a new class of membrane protein', *Nature*, 444(7116), pp. 226-9.

Duwe, A.K., Rupar, C.A., Horsman, G.B. and Vas, S.I. (1986) 'In vitro cytotoxicity and antibiotic activity of polymyxin B nonapeptide', *Antimicrob Agents Chemother*, 30(2), pp. 340-1.

Efron, B. (1979) 'Bootstrap Methods: Another Look at the Jackknife', *The Annals of Statistics*, 7(1), pp. 1-26.

Fahey, P.F. and Webb, W.W. (1978) 'Lateral diffusion in phospholipid bilayer membranes and multilamellar liquid crystals', *Biochemistry*, 17(15), pp. 3046-53.

Falagas, M.E. and Kasiakou, S.K. (2005) 'Colistin: the revival of polymyxins for the management of multidrug-resistant gram-negative bacterial infections', *Clin Infect Dis*, 40(9), pp. 1333-41.

Feng, Z.V., Spurlin, T.A. and Gewirth, A.A. (2005) 'Direct Visualization of Asymmetric Behavior in Supported Lipid Bilayers at the Gel-Fluid Phase Transition', *Biophysical Journal*, 88(3), pp. 2154-2164.

Ferguson, A.D., Hofmann, E., Coulton, J.W., Diederichs, K. and Welte, W. (1998) 'Siderophore-mediated iron transport: crystal structure of FhuA with bound lipopolysaccharide', *Science*, 282(5397), pp. 2215-20.

Foglia, F., Lawrence, M.J. and Barlow, D.J. (2015) 'Studies of model biological and bio-mimetic membrane structure: Reflectivity vs diffraction, a critical comparison', *Current Opinion in Colloid & Interface Science*, 20(4), pp. 235-243.

Forst, D., Welte, W., Wacker, T. and Diederichs, K. (1998) 'Structure of the sucrose-specific porin ScrY from Salmonella typhimurium and its complex with sucrose', *Nat Struct Biol*, 5(1), pp. 37-46.

Fragneto, G., Delhom, R., Joly, L. and Scoppola, E. (2018) 'Neutrons and model membranes: Moving towards complexity', *Current Opinion in Colloid & Interface Science*, 38, pp. 108-121.

Galanos, C., Luderitz, O. and Westphal, O. (1969) 'A new method for the extraction of R lipopolysaccharides', *Eur J Biochem*, 9(2), pp. 245-9.

Garavito, R.M., Jenkins, J., Jansonius, J.N., Karlsson, R. and Rosenbusch, J.P. (1983) 'X-ray diffraction analysis of matrix porin, an integral membrane protein from Escherichia coli outer membranes', *J Mol Biol*, 164(2), pp. 313-27.

Gidalevitz, D., Ishitsuka, Y., Muresan, A.S., Konovalov, O., Waring, A.J., Lehrer, R.I. and Lee, K.Y. (2003) 'Interaction of antimicrobial peptide protegrin with biomembranes', *Proc Natl Acad Sci U S A*, 100(11), pp. 6302-7.

Glenwright, A.J., Pothula, K.R., Bhamidimarri, S.P., Chorev, D.S., Basle, A., Firbank, S.J., Zheng, H., Robinson, C.V., Winterhalter, M., Kleinekathofer, U., Bolam, D.N. and van den Berg, B. (2017) 'Structural basis for nutrient acquisition by dominant members of the human gut microbiota', *Nature*, 541(7637), pp. 407-411.

Goose, J.E. and Sansom, M.S. (2013) 'Reduced lateral mobility of lipids and proteins in crowded membranes', *PLoS Comput Biol*, 9(4), p. e1003033.

Guard-Friar, D., Chen, C.H. and Engle, A.S. (1985) 'Deuterium isotope effect on the stability of molecules: phospholipids', *The Journal of Physical Chemistry*, 89(9), pp. 1810-1813.

Guard-Petter, J., Lakshmi, B., Carlson, R. and Ingram, K. (1995) 'Characterization of lipopolysaccharide heterogeneity in Salmonella enteritidis by an improved gel electrophoresis method', *Appl Environ Microbiol*, 61(8), pp. 2845-51.

Gunn, J.S., Lim, K.B., Krueger, J., Kim, K., Guo, L., Hackett, M. and Miller, S.I. (1998) 'PmrA-PmrB-regulated genes necessary for 4-aminoarabinose lipid A modification and polymyxin resistance', *Mol Microbiol*, 27(6), pp. 1171-82.

Han, M.L., Shen, H.H., Hansford, K.A., Schneider, E.K., Sivanesan, S., Roberts, K.D., Thompson, P.E., Le Brun, A.P., Zhu, Y., Sani, M.A., Separovic, F., Blaskovich, M.A.T., Baker, M.A., Moskowitz, S.M., Cooper, M.A., Li, J. and Velkov, T. (2017) 'Investigating the Interaction of Octapeptin A3 with Model Bacterial Membranes', *ACS Infect Dis*, 3(8), pp. 606-619.

Han, M.L., Velkov, T., Zhu, Y., Roberts, K.D., Le Brun, A.P., Chow, S.H., Gutu, A.D., Moskowitz, S.M., Shen, H.H. and Li, J. (2018) 'Polymyxin-Induced Lipid A

Deacylation in Pseudomonas aeruginosa Perturbs Polymyxin Penetration and Confers High-Level Resistance', *ACS Chem Biol*, 13(1), pp. 121-130.

Heinrichs, D.E., Yethon, J.A., Amor, P.A. and Whitfield, C. (1998a) 'The assembly system for the outer core portion of R1- and R4-type lipopolysaccharides of Escherichia coli. The R1 core-specific beta-glucosyltransferase provides a novel attachment site for O-polysaccharides', *J Biol Chem*, 273(45), pp. 29497-505.

Heinrichs, D.E., Yethon, J.A. and Whitfield, C. (1998b) 'Molecular basis for structural diversity in the core regions of the lipopolysaccharides of Escherichia coli and Salmonella enterica', *Mol Microbiol*, 30(2), pp. 221-32.

Henderson, J.C., O'Brien, J.P., Brodbelt, J.S. and Trent, M.S. (2013) 'Isolation and chemical characterization of lipid A from gram-negative bacteria', *J Vis Exp*, (79), p. e50623.

Henderson, J.C., Zimmerman, S.M., Crofts, A.A., Boll, J.M., Kuhns, L.G., Herrera, C.M. and Trent, M.S. (2016) 'The Power of Asymmetry: Architecture and Assembly of the Gram-Negative Outer Membrane Lipid Bilayer', *Annu Rev Microbiol*, 70, pp. 255-78.

Herrmann, M., Schneck, E., Gutsmann, T., Brandenburg, K. and Tanaka, M. (2015) 'Bacterial lipopolysaccharides form physically cross-linked, two-dimensional gels in the presence of divalent cations', *Soft Matter*, 11(30), pp. 6037-44.

Hitchcock, P.J., Leive, L., Mäkelä, P.H., Rietschel, E.T., Strittmatter, W. and Morrison, D.C. (1986) 'Lipopolysaccharide nomenclature--past, present, and future', *J Bacteriol*, 166(3), pp. 699-705.

Hodate, K. and Bito, Y. (1982) 'Temperature dependence of bactericidal action of polymyxin B', *Microbiol Immunol*, 26(8), pp. 737-40.

Holt, S.A., Le Brun, A.P., Majkrzak, C.F., McGillivray, D.J., Heinrich, F., Losche, M. and Lakey, J.H. (2009) 'An ion-channel-containing model membrane: structural determination by magnetic contrast neutron reflectometry', *Soft Matter*, 5(13), pp. 2576-2586.

Housden, N.G., Wojdyla, J.A., Korczynska, J., Grishkovskaya, I., Kirkpatrick, N., Brzozowski, A.M. and Kleanthous, C. (2010) 'Directed epitope delivery across the Escherichia coli outer membrane through the porin OmpF', *Proc Natl Acad Sci U S A*, 107(50), pp. 21412-7.

Howe, J., Andrä, J., Conde, R., Iriarte, M., Garidel, P., Koch, M.H., Gutsmann, T., Moriyón, I. and Brandenburg, K. (2007) 'Thermodynamic analysis of the lipopolysaccharide-dependent resistance of gram-negative bacteria against polymyxin B', *Biophys J*, 92(8), pp. 2796-805.

Hsia, C.-Y., Chen, L., Singh, R.R., DeLisa, M.P. and Daniel, S. (2016) 'A Molecularly Complete Planar Bacterial Outer Membrane Platform', *Scientific Reports*, 6, p. 32715.

Hughes, A.V. (2013) 'Rascal', *Sourceforge*.

Hughes, A.V., Holt, S.A., Daulton, E., Soliakov, A., Charlton, T.R., Roser, S.J. and Lakey, J.H. (2014) 'High coverage fluid-phase floating lipid bilayers supported by ω-thiolipid self-assembled monolayers', *J R Soc Interface*, 11(98), p. 20140245.

Hughes, A.V., Howse, J.R., Dabkowska, A., Jones, R.A., Lawrence, M.J. and Roser, S.J. (2008) 'Floating lipid bilayers deposited on chemically grafted phosphatidylcholine surfaces', *Langmuir*, 24(5), pp. 1989-99.

Hughes, A.V., Roser, S.J., Gerstenberg, M., Goldar, A., Stidder, B., Feidenhans'l, R. and Bradshaw, J. (2002) 'Phase Behavior of DMPC Free Supported Bilayers Studied by Neutron Reflectivity', *Langmuir*, 18(21), pp. 8161-8171.

Hwang, H., Paracini, N., Parks, J.M., Lakey, J.H. and Gumbart, J.C. (2018) 'Distribution of mechanical stress in the Escherichia coli cell envelope', *Biochim Biophys Acta Biomembr*, 1860(12), pp. 2566-2575.

Jaroslawski, S., Duquesne, K., Sturgis, J.N. and Scheuring, S. (2009) 'High-resolution architecture of the outer membrane of the Gram-negative bacteria Roseobacter denitrificans', *Mol Microbiol*, 74(5), pp. 1211-22.

Jeong, J.Y., Yim, H.S., Ryu, J.Y., Lee, H.S., Lee, J.H., Seen, D.S. and Kang, S.G. (2012) 'One-step sequence- and ligation-independent cloning as a rapid and versatile cloning method for functional genomics studies', *Appl Environ Microbiol*, 78(15), pp. 5440-3.

Jeworrek, C., Evers, F., Howe, J., Brandenburg, K., Tolan, M. and Winter, R. (2011) 'Effects of specific versus nonspecific ionic interactions on the structure and lateral organization of lipopolysaccharides', *Biophys J*, 100(9), pp. 2169-77.

Johnson, C.L., Ridley, H., Marchetti, R., Silipo, A., Griffin, D.C., Crawford, L., Bonev, B., Molinaro, A. and Lakey, J.H. (2014) 'The antibacterial toxin colicin N binds to the inner core of lipopolysaccharide and close to its translocator protein', *Mol Microbiol*, 92(3), pp. 440-52.

Johnson, C.L., Ridley, H., Pengelly, R.J., Salleh, M.Z. and Lakey, J.H. (2013) 'The unstructured domain of colicin N kills Escherichia coli', *Mol Microbiol*, 89(1), pp. 84-95.

Kamio, Y. and Nikaido, H. (1976) 'Outer membrane of Salmonella typhimurium: accessibility of phospholipid head groups to phospholipase c and cyanogen bromide activated dextran in the external medium', *Biochemistry*, 15(12), pp. 2561-70.

Katsu, T., Yoshimura, S., Tsuchiya, T. and Fujita, Y. (1984) 'Temperature dependence of action of polymyxin B on Escherichia coli', *J Biochem*, 95(6), pp. 1645-53.

Kern, W. (1990) 'The Evolution of Silicon Wafer Cleaning Technology', *Journal of The Electrochemical Society*, 137(6), pp. 1887-1892.

Kim, Y.C., Tarr, A.W. and Penfold, C.N. (2014) 'Colicin import into E. coli cells: a model system for insights into the import mechanisms of bacteriocins', *Biochim Biophys Acta*, 1843(8), pp. 1717-31.

Kleanthous, C. (2010) 'Swimming against the tide: progress and challenges in our understanding of colicin translocation', *Nat Rev Microbiol*, 8(12), pp. 843-8.

Koebnik, R. (1996) 'In vivo membrane assembly of split variants of the E.coli outer membrane protein OmpA', *Embo j*, 15(14), pp. 3529-37.

Koebnik, R., Locher, K.P. and Van Gelder, P. (2000) 'Structure and function of bacterial outer membrane proteins: barrels in a nutshell', *Mol Microbiol*, 37(2), pp. 239-53.

Koike, M., Iida, K. and Matsuo, T. (1969) 'Electron microscopic studies on mode of action of polymyxin', *J Bacteriol*, 97(1), pp. 448-52.

Kurisu, G., Zakharov, S.D., Zhalnina, M.V., Bano, S., Eroukova, V.Y., Rokitskaya, T.I., Antonenko, Y.N., Wiener, M.C. and Cramer, W.A. (2003) 'The structure of BtuB with bound colicin E3 R-domain implies a translocon', *Nat Struct Biol*, 10(11), pp. 948-54.

Laemmli, U.K. (1970) 'Cleavage of structural proteins during the assembly of the head of bacteriophage T4', *Nature*, 227(5259), pp. 680-5.

Lakey, J.H. (2009) 'Neutrons for biologists: a beginner's guide, or why you should consider using neutrons', *J R Soc Interface*, 6 Suppl 5(Suppl 5), pp. S567-73.

Lakey, J.H. (2019) 'Recent advances in neutron reflectivity studies of biological membranes', *Current Opinion in Colloid & Interface Science*, 42, pp. 33-40.

Lakey, J.H., Parker, M.W., Gonzalez-Manas, J.M., Duche, D., Vriend, G., Baty, D. and Pattus, F. (1994) 'The role of electrostatic charge in the membrane insertion of colicin A. Calculation and mutation', *Eur J Biochem*, 220(1), pp. 155-63.

Le Brun, A.P., Clifton, L.A., Halbert, C.E., Lin, B., Meron, M., Holden, P.J., Lakey, J.H. and Holt, S.A. (2013) 'Structural characterization of a model gram-negative bacterial surface using lipopolysaccharides from rough strains of Escherichia coli', *Biomacromolecules*, 14(6), pp. 2014-22.

Lee, H.-H., Gavutis, M., Ruželė, Ž., Valiokas, R.n. and Liedberg, B. (2018) 'Mixed Self-Assembled Monolayers with Terminal Deuterated Anchors: Characterization and Probing of Model Lipid Membrane Formation', *The Journal of Physical Chemistry B*, 122(34), pp. 8201-8210.

Lee, H.H., Ruzele, Z., Malysheva, L., Onipko, A., Gutes, A., Bjorefors, F., Valiokas, R. and Liedberg, B. (2009) 'Long-chain alkylthiol assemblies containing buried in-plane stabilizing architectures', *Langmuir*, 25(24), pp. 13959-71.

Li, Y., Powell, D.A., Shaffer, S.A., Rasko, D.A., Pelletier, M.R., Leszyk, J.D., Scott, A.J., Masoudi, A., Goodlett, D.R., Wang, X., Raetz, C.R. and Ernst, R.K. (2012) 'LPS remodeling is an evolved survival strategy for bacteria', *Proc Natl Acad Sci U S A*, 109(22), pp. 8716-21.

Liang, C.Y., Lytton, M.R. and Boone, C.J. (1960) 'Infrared spectra of crystalline and stereoregular polymers. II. Carbon—hydrogen and carbon—deuterium stretching frequencies of polypropylene and deuterated polypropylenes', *Journal of Polymer Science*, 47(149), pp. 139-148.

Lopes, J. and Inniss, W.E. (1969) 'Electron microscopy of effect of polymyxin on Escherichia coli lipopolysaccharide', *J Bacteriol*, 100(2), pp. 1128-9.

Louise Meyer, R., Zhou, X., Tang, L., Arpanaei, A., Kingshott, P. and Besenbacher, F. (2010) 'Immobilisation of living bacteria for AFM imaging under physiological conditions', *Ultramicroscopy*, 110(11), pp. 1349-57.

Lounatmaa, K., Mäkelä, P.H. and Sarvas, M. (1976) 'Effect of polymyxin on the ultrastructure of the outer membrane of wild-type and polymyxin-resistant strain of Salmonella', *J Bacteriol*, 127(3), pp. 1400-7.

Lu, J.R., Thomas, R.K. and Penfold, J. (2000) 'Surfactant layers at the air/water interface: structure and composition', *Adv Colloid Interface Sci*, 84(1-3), pp. 143-304.

Mares, J., Kumaran, S., Gobbo, M. and Zerbe, O. (2009) 'Interactions of lipopolysaccharide and polymyxin studied by NMR spectroscopy', *J Biol Chem*, 284(17), pp. 11498-506.

Marsh, D. (2007) 'Lateral pressure profile, spontaneous curvature frustration, and the incorporation and conformation of proteins in membranes', *Biophys J*, 93(11), pp. 3884-99.

Marvin, H.J., ter Beest, M.B. and Witholt, B. (1989) 'Release of outer membrane fragments from wild-type Escherichia coli and from several E. coli lipopolysaccharide mutants by EDTA and heat shock treatments', *Journal of bacteriology*, 171(10), pp. 5262-5267.

May, K.L. and Silhavy, T.J. (2018) 'The Escherichia coli Phospholipase PldA Regulates Outer Membrane Homeostasis via Lipid Signaling', *MBio*, 9(2).

Meilleur, F., Weiss, K.L. and Myles, D.A. (2009) 'Deuterium labeling for neutron structure-function-dynamics analysis', *Methods Mol Biol*, 544, pp. 281-92.

Meredith, J.J., Dufour, A. and Bruch, M.D. (2009) 'Comparison of the Structure and Dynamics of the Antibiotic Peptide Polymyxin B and the Inactive Nonapeptide in Aqueous Trifluoroethanol by NMR Spectroscopy', *The Journal of Physical Chemistry B*, 113(2), pp. 544-551.

Mergenhagen, S.E., Bladen, H.A. and Hsu, K.C. (1966) 'Electron microscopic localization of endotoxic lipopolysaccharide in gram-negative organisms', *Ann N Y Acad Sci*, 133(2), pp. 279-91.

Metcalf, T.N., Wang, J.L. and Schindler, M. (1986) 'Lateral diffusion of phospholipids in the plasma membrane of soybean protoplasts: Evidence for membrane lipid domains', *Proc Natl Acad Sci U S A*, 83(1), pp. 95-9.

Mi, W., Li, Y., Yoon, S.H., Ernst, R.K., Walz, T. and Liao, M. (2017) 'Structural basis of MsbA-mediated lipopolysaccharide transport', *Nature*, 549(7671), pp. 233-237.

Micciulla, S., Gerelli, Y. and Schneck, E. (2019) 'Structure and Conformation of Wild-Type Bacterial Lipopolysaccharide Layers at Air-Water Interfaces', *Biophys J*, 116(7), pp. 1259-1269.

Milne, J.L. and Subramaniam, S. (2009) 'Cryo-electron tomography of bacteria: progress, challenges and future prospects', *Nat Rev Microbiol*, 7(9), pp. 666-75.

Moffatt, J.H., Harper, M., Harrison, P., Hale, J.D., Vinogradov, E., Seemann, T., Henry, R., Crane, B., St Michael, F., Cox, A.D., Adler, B., Nation, R.L., Li, J. and Boyce, J.D. (2010) 'Colistin resistance in Acinetobacter baumannii is mediated by complete loss of lipopolysaccharide production', *Antimicrob Agents Chemother*, 54(12), pp. 4971-7.

Molinaro, A., Holst, O., Di Lorenzo, F., Callaghan, M., Nurisso, A., D'Errico, G., Zamyatina, A., Peri, F., Berisio, R., Jerala, R., Jimenez-Barbero, J., Silipo, A. and Martin-Santamaria, S. (2015) 'Chemistry of lipid A: at the heart of innate immunity', *Chemistry*, 21(2), pp. 500-19.

Moore, R.A., Bates, N.C. and Hancock, R.E. (1986) 'Interaction of polycationic antibiotics with Pseudomonas aeruginosa lipopolysaccharide and lipid A studied by using dansyl-polymyxin', *Antimicrob Agents Chemother*, 29(3), pp. 496-500.

Nakajima, H., Kiyokawa, N., Katagiri, Y.U., Taguchi, T., Suzuki, T., Sekino, T., Mimori, K., Ebata, T., Saito, M., Nakao, H., Takeda, T. and Fujimoto, J. (2001) 'Kinetic analysis of binding between Shiga toxin and receptor glycolipid Gb3Cer by surface plasmon resonance', *J Biol Chem*, 276(46), pp. 42915-22.

Needham, B.D. and Trent, M.S. (2013) 'Fortifying the barrier: the impact of lipid A remodelling on bacterial pathogenesis', *Nat Rev Microbiol*, 11(7), pp. 467-81.

Nelder, J.A. and Mead, R. (1965) 'A Simplex Method for Function Minimization', *The Computer Journal*, 7(4), pp. 308-313.

Neville, F., Hodges, C.S., Liu, C., Konovalov, O. and Gidalevitz, D. (2006) 'In situ characterization of lipid A interaction with antimicrobial peptides using surface X-ray scattering', *Biochim Biophys Acta*, 1758(2), pp. 232-40.

Nevot, L. and Croce, P. (1980) 'Caractérisation des surfaces par réflexion rasante de rayons X. Application à l'étude du polissage de quelques verres silicates', *Rev. Phys. Appl. (Paris)*, 15(3), pp. 761-779.

Nguyen, H.H., Park, J., Kang, S. and Kim, M. (2015) 'Surface plasmon resonance: a versatile technique for biosensor applications', *Sensors (Basel, Switzerland)*, 15(5), pp. 10481-10510.

Nieba, L., Nieba-Axmann, S.E., Persson, A., Hamalainen, M., Edebratt, F., Hansson, A., Lidholm, J., Magnusson, K., Karlsson, A.F. and Pluckthun, A. (1997) 'BIACORE analysis of histidine-tagged proteins using a chelating NTA sensor chip', *Anal Biochem*, 252(2), pp. 217-28.

Nikaido, H. (1992) 'Porins and specific channels of bacterial outer membranes', *Mol Microbiol*, 6(4), pp. 435-42.

Nikaido, H. (1993) 'Transport across the bacterial outer membrane', *J Bioenerg Biomembr*, 25(6), pp. 581-9.

Nikaido, H. (2003) 'Molecular basis of bacterial outer membrane permeability revisited', *Microbiol Mol Biol Rev*, 67(4), pp. 593-656.

Noinaj, N., Gumbart, J.C. and Buchanan, S.K. (2017) 'The beta-barrel assembly machinery in motion', *Nat Rev Microbiol*, 15(4), pp. 197-204.

O'Shea, R. and Moser, H.E. (2008) 'Physicochemical properties of antibacterial compounds: implications for drug discovery', *J Med Chem*, 51(10), pp. 2871-8.

Okuda, S., Sherman, D.J., Silhavy, T.J., Ruiz, N. and Kahne, D. (2016) 'Lipopolysaccharide transport and assembly at the outer membrane: the PEZ model', *Nature reviews. Microbiology*, 14(6), pp. 337-345.

Oliveira, R.G., Schneck, E., Quinn, B.E., Konovalov, O.V., Brandenburg, K., Gutsmann, T., Gill, T., Hanna, C.B., Pink, D.A. and Tanaka, M. (2010) 'Crucial roles of charged saccharide moieties in survival of gram negative bacteria against protamine revealed by combination of grazing incidence x-ray structural characterizations and Monte Carlo simulations', *Phys Rev E Stat Nonlin Soft Matter Phys*, 81(4 Pt 1), p. 041901.

Oliveira, R.G., Schneck, E., Quinn, B.E., Konovalov, O.V., Brandenburg, K., Seydel, U., Gill, T., Hanna, C.B., Pink, D.A. and Tanaka, M. (2009) 'Physical mechanisms of bacterial survival revealed by combined grazing-incidence X-ray scattering and Monte Carlo simulation', *Comptes Rendus Chimie*, 12(1-2), pp. 209-217.

Orwa, J.A., Govaerts, C., Busson, R., Roets, E., Van Schepdael, A. and Hoogmartens, J. (2001) 'Isolation and structural characterization of polymyxin B components', *J Chromatogr A*, 912(2), pp. 369-73.

Pages, J.M., James, C.E. and Winterhalter, M. (2008) 'The porin and the permeating antibiotic: a selective diffusion barrier in Gram-negative bacteria', *Nat Rev Microbiol*, 6(12), pp. 893-903.

Paracini, N., Clifton, L.A., Skoda, M.W.A. and Lakey, J.H. (2018) 'Liquid crystalline bacterial outer membranes are critical for antibiotic susceptibility', *Proceedings of the National Academy of Sciences*, 115(32), p. E7587.

Parratt, L.G. (1954) 'Surface Studies of Solids by Total Reflection of X-Rays', *Physical Review*, 95(2), pp. 359-369.

Penfold, J., Richardson, R.M., Zarbakhsh, A., Webster, J.R.P., Bucknall, D.G., Rennie, A.R., Jones, R.A.L., Cosgrove, T., Thomas, R.K., Higgins, J.S., Fletcher, P.D.I., Dickinson, E., Roser, S.J., McLure, I.A., Hillman, A.R., Richards, R.W., Staples, E.J., Burgess, A.N., Simister, E.A. and White, J.W. (1997) 'Recent advances in the study of chemical surfaces and interfaces by specular neutron reflection', *Journal of the Chemical Society, Faraday Transactions*, 93(22), pp. 3899-3917.

Penfold, J. and Thomas, R.K. (1990) 'The application of the specular reflection of neutrons to the study of surfaces and interfaces', *Journal of Physics: Condensed Matter*, 2(6), pp. 1369-1412.

Penfold, J., Ward, R.C. and Williams, W.G. (1987) 'A time-of-flight neutron reflectometer for surface and interfacial studies', *Journal of Physics E: Scientific Instruments*, 20(11), pp. 1411-1417.

Perez, F. (2004) 'Serial Cloner', *Available from: http://serialbasics.free.fr/Home/Home.html*.

Peterson, A.A. and McGroarty, E.J. (1985) 'High-molecular-weight components in lipopolysaccharides of Salmonella typhimurium, Salmonella minnesota, and Escherichia coli', *J Bacteriol*, 162(2), pp. 738-45.

Plant, A.L., Brighamburke, M., Petrella, E.C. and Oshannessy, D.J. (1995) 'Phospholipid/Alkanethiol Bilayers for Cell-Surface Receptor Studies by Surface Plasmon Resonance', *Analytical Biochemistry*, 226(2), pp. 342-348.

Plesiat, P., Aires, J.R., Godard, C. and Kohler, T. (1997) 'Use of steroids to monitor alterations in the outer membrane of Pseudomonas aeruginosa', *J Bacteriol*, 179(22), pp. 7004-10.

Plesiat, P. and Nikaido, H. (1992) 'Outer membranes of gram-negative bacteria are permeable to steroid probes', *Mol Microbiol*, 6(10), pp. 1323-33.

Pothula, K.R., Solano, C.J.F. and Kleinekathöfer, U. (2016) 'Simulations of outer membrane channels and their permeability', *Biochimica et Biophysica Acta (BBA) - Biomembranes*, 1858(7, Part B), pp. 1760-1771.

Pristovsek, P. and Kidric, J. (1999) 'Solution structure of polymyxins B and E and effect of binding to lipopolysaccharide: an NMR and molecular modeling study', *J Med Chem*, 42(22), pp. 4604-13.

Raetz, C.R., Reynolds, C.M., Trent, M.S. and Bishop, R.E. (2007) 'Lipid A modification systems in gram-negative bacteria', *Annu Rev Biochem*, 76, pp. 295-329.

Raetz, C.R. and Whitfield, C. (2002) 'Lipopolysaccharide endotoxins', *Annu Rev Biochem*, 71, pp. 635-700.

Raggett, E.M., Bainbridge, G., Evans, L.J., Cooper, A. and Lakey, J.H. (1998) 'Discovery of critical Tol A-binding residues in the bactericidal toxin colicin N: a biophysical approach', *Mol Microbiol*, 28(6), pp. 1335-43.

Rice, L.B. (2008) 'Federal funding for the study of antimicrobial resistance in nosocomial pathogens: no ESKAPE', *J Infect Dis*, 197(8), pp. 1079-81.

Rodriguez-Loureiro, I., Latza, V.M., Fragneto, G. and Schneck, E. (2018) 'Conformation of Single and Interacting Lipopolysaccharide Surfaces Bearing O-Side Chains', *Biophys J*, 114(7), pp. 1624-1635.

Rosenbusch, J.P. (1974) 'Characterization of the major envelope protein from Escherichia coli. Regular arrangement on the peptidoglycan and unusual dodecyl sulfate binding', *J Biol Chem*, 249(24), pp. 8019-29.

Ruiz, N., Kahne, D. and Silhavy, T.J. (2009) 'Transport of lipopolysaccharide across the cell envelope: the long road of discovery', *Nat Rev Microbiol*, 7(9), pp. 677-83.

Sahalan, A.Z. and Dixon, R.A. (2008) 'Role of the cell envelope in the antibacterial activities of polymyxin B and polymyxin B nonapeptide against Escherichia coli', *Int J Antimicrob Agents*, 31(3), pp. 224-7.

Saner, C.K., Lusker, K.L., Lejeune, Z.M., Serem, W.K. and Garno, J.C. (2012) 'Self-assembly of octadecyltrichlorosilane: Surface structures formed using different protocols of particle lithography', *Beilstein journal of nanotechnology*, 3, pp. 114-122.

Schindler, M., Osborn, M.J. and Koppel, D.E. (1980) 'Lateral diffusion of lipopolysaccharide in the outer membrane of Salmonella typhimurium', *Nature*, 285(5762), pp. 261-3.

Schindler, M. and Rosenbusch, J.P. (1984) 'Structural transitions of porin, a transmembrane protein', *FEBS Lett*, 173(1), pp. 85-9.

Schirmer, T., Keller, T.A., Wang, Y.F. and Rosenbusch, J.P. (1995) 'Structural basis for sugar translocation through maltoporin channels at 3.1 A resolution', *Science*, 267(5197), pp. 512-4.

Schneck, E., Papp-Szabo, E., Quinn, B.E., Konovalov, O.V., Beveridge, T.J., Pink, D.A. and Tanaka, M. (2009) 'Calcium ions induce collapse of charged O-side chains of lipopolysaccharides from Pseudomonas aeruginosa', *J R Soc Interface*, 6 Suppl 5(Suppl 5), pp. S671-8.

Schneck, E., Schubert, T., Konovalov, O.V., Quinn, B.E., Gutsmann, T., Brandenburg, K., Oliveira, R.G., Pink, D.A. and Tanaka, M. (2010) 'Quantitative determination of ion distributions in bacterial lipopolysaccharide membranes by grazing-incidence X-ray fluorescence', *Proc Natl Acad Sci U S A*, 107(20), pp. 9147-51.

Schroeder, G., Brandenburg, K. and Seydel, U. (1992) 'Polymyxin B induces transient permeability fluctuations in asymmetric planar lipopolysaccharide/phospholipid bilayers', *Biochemistry*, 31(3), pp. 631-638.

Shands, J.W. (1965) 'Localization of Somatic Antigen on Gram-Negative Bacteria by Electron Microscopy', *J Bacteriol*, 90(1), pp. 266-70.

Sharma, O., Datsenko, K.A., Ess, S.C., Zhalnina, M.V., Wanner, B.L. and Cramer, W.A. (2009) 'Genome-wide screens: novel mechanisms in colicin import and cytotoxicity', *Mol Microbiol*, 73(4), pp. 571-85.

Sherman, D.J., Xie, R., Taylor, R.J., George, A.H., Okuda, S., Foster, P.J., Needleman, D.J. and Kahne, D. (2018) 'Lipopolysaccharide is transported to the cell surface by a membrane-to-membrane protein bridge', *Science*, 359(6377), pp. 798-801.

Singer, S.J. and Nicolson, G.L. (1972) 'The fluid mosaic model of the structure of cell membranes', *Science*, 175(4023), pp. 720-31.

Sivia, D.S. and Webster, J.R.P. (1998) 'The Bayesian approach to reflectivity data', *Physica B: Condensed Matter*, 248(1), pp. 327-337.

Snyder, S., Kim, D. and McIntosh, T.J. (1999) 'Lipopolysaccharide bilayer structure: effect of chemotype, core mutations, divalent cations, and temperature', *Biochemistry*, 38(33), pp. 10758-67.

Sonntag, I., Schwarz, H., Hirota, Y. and Henning, U. (1978) 'Cell envelope and shape of Escherichia coli: multiple mutants missing the outer membrane lipoprotein and other major outer membrane proteins', *J Bacteriol*, 136(1), pp. 280-5.

Stahelin, R.V. (2013) 'Surface plasmon resonance: a useful technique for cell biologists to characterize biomolecular interactions', *Mol Biol Cell*, 24(7), pp. 883-6.

Stefaniu, C., Brezesinski, G. and Mohwald, H. (2014) 'Langmuir monolayers as models to study processes at membrane surfaces', *Adv Colloid Interface Sci*, 208, pp. 197-213.

Stenutz, R., Weintraub, A. and Widmalm, G. (2006) 'The structures of Escherichia coli O-polysaccharide antigens', *FEMS Microbiol Rev*, 30(3), pp. 382-403.

Stevenson, G., Neal, B., Liu, D., Hobbs, M., Packer, N.H., Batley, M., Redmond, J.W., Lindquist, L. and Reeves, P. (1994) 'Structure of the O antigen of Escherichia coli K-12 and the sequence of its rfb gene cluster', *J Bacteriol*, 176(13), pp. 4144-56.

Strong, L. and Whitesides, G.M. (1988) 'Structures of self-assembled monolayer films of organosulfur compounds adsorbed on gold single crystals: electron diffraction studies', *Langmuir*, 4(3), pp. 546-558.

Terrettaz, S., Ulrich, W.P., Vogel, H., Hong, Q., Dover, L.G. and Lakey, J.H. (2002) 'Stable self-assembly of a protein engineering scaffold on gold surfaces', *Protein Sci*, 11(8), pp. 1917-25.

Teubner, M. and Bader, J. (1977) 'Resistance to polymyxin B at low temperature: A function of the outer membrane in gram-negative bacteria', *FEMS Microbiology Letters*, 1(2), pp. 75-77.

Thomas, C.J., Surolia, N. and Surolia, A. (1999) 'Surface plasmon resonance studies resolve the enigmatic endotoxin neutralizing activity of polymyxin B', *J Biol Chem*, 274(42), pp. 29624-7.

Tommasi, R., Brown, D.G., Walkup, G.K., Manchester, J.I. and Miller, A.A. (2015) 'ESKAPEing the labyrinth of antibacterial discovery', *Nat Rev Drug Discov*, 14(8), pp. 529-42.

Trent, M.S., Ribeiro, A.A., Lin, S., Cotter, R.J. and Raetz, C.R. (2001) 'An inner membrane enzyme in Salmonella and Escherichia coli that transfers 4-amino-4-deoxy-L-arabinose to lipid A: induction on polymyxin-resistant mutants and role of a novel lipid-linked donor', *J Biol Chem*, 276(46), pp. 43122-31.

Tristram-Nagle, S., Liu, Y., Legleiter, J. and Nagle, J.F. (2002) 'Structure of gel phase DMPC determined by X-ray diffraction', *Biophys J*, 83(6), pp. 3324-35.

Vaara, M. (1992) 'Agents that increase the permeability of the outer membrane', *Microbiol Rev*, 56(3), pp. 395-411.

Velkov, T., Roberts, K.D., Nation, R.L., Wang, J., Thompson, P.E. and Li, J. (2014) 'Teaching 'old' polymyxins new tricks: new-generation lipopeptides targeting gram-negative 'superbugs'', *ACS Chem Biol*, 9(5), pp. 1172-7.

Velkov, T., Thompson, P.E., Nation, R.L. and Li, J. (2010) 'Structure--activity relationships of polymyxin antibiotics', *J Med Chem*, 53(5), pp. 1898-916.

Ventola, C.L. (2015) 'The antibiotic resistance crisis: part 1: causes and threats', *P t*, 40(4), pp. 277-83.

Vila-Farres, X., Ferrer-Navarro, M., Callarisa, A.E., Marti, S., Espinal, P., Gupta, S., Rolain, J.M., Giralt, E. and Vila, J. (2015) 'Loss of LPS is involved in the virulence and resistance to colistin of colistin-resistant Acinetobacter nosocomialis mutants selected in vitro', *J Antimicrob Chemother*, 70(11), pp. 2981-6.

Wacklin, H.P. (2010) 'Neutron reflection from supported lipid membranes', *Current Opinion in Colloid & Interface Science*, 15(6), pp. 445-454.

Webster, J., Holt, S. and Dalgliesh, R. (2006) 'INTER the chemical interfaces reflectometer on target station 2 at ISIS', *Physica B: Condensed Matter*, 385-386, pp. 1164-1166.

Webster, J.R.P., Langridge, S., Dalgliesh, R.M. and Charlton, T.R. (2011) 'Reflectometry techniques on the Second Target Station at ISIS: Methods and science', *The European Physical Journal Plus*, 126(11), p. 112.

Welbourn, R.J.L. and Clarke, S.M. (2019) 'New insights into the solid–liquid interface exploiting neutron reflectivity', *Current Opinion in Colloid & Interface Science*, 42, pp. 87-98.

Wu, H.L., Tong, Y., Peng, Q., Li, N. and Ye, S. (2016) 'Phase transition behaviors of the supported DPPC bilayer investigated by sum frequency generation (SFG) vibrational spectroscopy and atomic force microscopy (AFM)', *Phys Chem Chem Phys*, 18(3), pp. 1411-21.

Yamashita, H., Taoka, A., Uchihashi, T., Asano, T., Ando, T. and Fukumori, Y. (2012) 'Single-molecule imaging on living bacterial cell surface by high-speed AFM', *J Mol Biol*, 422(2), pp. 300-9.

Yu, Z., Qin, W., Lin, J., Fang, S. and Qiu, J. (2015) 'Antibacterial Mechanisms of Polymyxin and Bacterial Resistance', *BioMed Research International*, 2015, p. 11.

Zavascki, A.P., Goldani, L.Z., Li, J. and Nation, R.L. (2007) 'Polymyxin B for the treatment of multidrug-resistant pathogens: a critical review', *J Antimicrob Chemother*, 60(6), pp. 1206-15.

Zhang, G., Meredith, T.C. and Kahne, D. (2013) 'On the essentiality of lipopolysaccharide to Gram-negative bacteria', *Curr Opin Microbiol*, 16(6), pp. 779-85.

Zhang, L., Dhillon, P., Yan, H., Farmer, S. and Hancock, R.E. (2000) 'Interactions of bacterial cationic peptide antibiotics with outer and cytoplasmic membranes of Pseudomonas aeruginosa', *Antimicrob Agents Chemother*, 44(12), pp. 3317-21.

Zhou, Z., Ribeiro, A.A., Lin, S., Cotter, R.J., Miller, S.I. and Raetz, C.R. (2001) 'Lipid A modifications in polymyxin-resistant Salmonella typhimurium: PMRA-dependent 4-amino-4-deoxy-L-arabinose, and phosphoethanolamine incorporation', *J Biol Chem*, 276(46), pp. 43111-21.